Technische Universität München

Department Chemie

Fachgebiet für Theoretische Chemie

Quantum Chemical Studies Related to Biomass Conversion by Heterogeneous Catalysis

Cheng-chau Chiu

Vollständiger Abdruck der von der Fakultät für Chemie der Technischen Universität München zur Erlangung des akademischen Grades eines

Doktors der Naturwissenschaften (Dr. rer. nat)

genehmigten Dissertation.

Vorsitzender:		Univ.-Prof. Dr. Dr. h.c. Bernhard Rieger
Prüfer der Dissertation:	1.	Univ.-Prof. Dr. Dr. h.c. Notker Rösch, i.R.
	2.	Univ.-Prof. Dr. Klaus Köhler
	3.	Hon.-Prof. Dr. Dr. h.c. Hans-Joachim Freund (schriftliche Beurteilung)
		Univ.-Prof. Dr. Ville R. I. Kaila (mündliche Prüfung)

Die Dissertation wurde am 7. Januar 2015 bei der Technischen Universität München eingereicht und durch die Fakultät für Chemie am 18. Februar 2015 angenommen.

Acknowledgments

I want to start this page with expressing my gratitude to my PhD advisor, Professor Notker Rösch, for giving me the opportunity to study this interesting topic in his group as well as for the guidance of my scientific work.

Special appreciation further goes to Dr. Alexander Genest, who literally took care of everything, starting from scientific discussions, to providing solutions to computer problems and even administrative support. Another person who deserves an extra mention is Dr. Sven Krüger who provided assistance with both scientific as well as administrative issues.

I want to thank all external collaborators who were involved in my studies for their contribution to the success of the projects. I should mention here Professor Georgi Vayssilov and Dr. Armando Borgna for their participation in the zeolite project and the guaiacol project, respectively. I also thank Dr. Michael Sullivan for administrative support during my stay at the Institute of High Performance Computing (IHPC) in Singapore.

Furthermore, I want to thank my colleagues Dr. Duygu Başaran and Dr. Zhijian Zhao for the daily discussions on our works on heterogeneous catalysis and various other things. I also thank Dr. Lili Zhao for the good cooperation on our joint project on mixed metal oxides. Special thanks also go to Thomas Soini, who was always ready to help, also for issues beyond our scientific works.

I thank all present and past colleagues I have encountered during my time at the Technische Universität München (TUM) and at the Catalysis Modelling Group at IHPC, Benjamin Chen, Dr. Ion Chiorescu, Dr. Konstantina Damianos, Dr. Shrabani Dinda, Dr. Wilhelm Eger, Dr. Agalya Govindasamy, Bo Li, Dr. Virve Kartunen, Stefan Kienzle, Dr. Alena Kremleva, Dr. Xiufang Ma, Dr. Remi Marchal, Dr. Alexei Matveev, Dr. Astrid Nikodem, Dr. Suwit Suthirakun, Dr. Yin Wu, for the good working atmosphere.

Apart from those persons, which I have encountered at the university, I want to mentioned and thank a special group of person, which have awaken my interest for chemistry: my high school chemistry teachers Volker Lang, Hartmut Volke, Klaus Lorbach and Heiner Greis.

I also thank the International Graduate School of Science and Engineering at the TUM and the A*STAR Graduate Academy for their generous scholarships. Furthermore, I thank the Leibniz-Rechenzentrum of the Bayerische Akademie der Wissenschaften and the A*STAR Computing Resource Center for providing the computing resources.

Last but not least, I want to thank my family for their unconditional love and support.

Abstract / Zusammenfassung

This thesis deals with the theoretical description of the conversion of biomass derived feedstock in heterogeneously catalyzed reactions as well as related chemical processes. The first part of this work uses periodic DFT methods to study the reaction mechanisms of metal-catalyzed transformations of organic oxygenates, e.g., alcohols and phenols, to unfunctionalized hydrocarbons. This thesis shows that the presence of step sites on a Pt catalyst lowers the barriers associated with the alkane formation from 1-propanol; nevertheless, this reaction path is, consistent with experiment, less favored than the reforming path. This thesis also demonstrates that the preferred decomposition route of ethanol on a close-packed Ru surface leads to the scission of the C-C bond yielding CO and methylene. It is further revealed that the Ru-catalyzed hydrodeoxygenation of guaiacol proceeds via the intermediates catecholate and phenolate and that the availability of step sites determines whether phenol or benzene is formed as the main product. The second part of this work examines two common DFT-based strategies for describing dispersive forces, the DFT-D2 method and the vdW-DF2 functional. Adsorption energies for water, alcohols and alkanes in MFI type zeolites are calculated using the two approaches. Comparison with experimental values shows that both methods are only partially suitable for modeling reactions in zeolites, as they systematically overestimate the exothermicity of alkane adsorption.

Die vorliegende Arbeit beschäftigt sich mit der theoretischen Untersuchung der heterogen katalysierten Umsetzung von biogenen Rohstoffen sowie mit den damit zusammenhängenden chemischen Prozessen. Der erste Teil dieser Arbeit verwendet periodische DFT-Methoden, um die Reaktionsmechanismen der metallkatalysierten Umsetzung von sauerstoffhaltigen, organischen Verbindungen wie Alkohole und Phenole zu nicht funktionalisierten Kohlenwasserstoffen zu untersuchen. Unter anderem zeigt diese Arbeit, dass die Präsenz von Stufen auf einer Pt-Oberfläche die Barrieren für die Alkanbildung aus 1-Propanol herabsetzt. Dennoch ist dieser Reaktionspfad, in

Übereinstimmung mit dem Experiment, energetisch weniger vorteilhaft als die Reformierungsreaktion. Diese Arbeit zeigt auch, dass die bevorzugte Zerfallsroute von Ethanol auf einer dichtest gepackten Ru-Oberfläche zur Spaltung der C-C Bindung und damit zur Bildung von CO und Methylen führt. Zudem wird dargelegt, dass die Ru-katalysierte Hydrodeoxygenierung von Guaiacol über die Intermediate Catecholat und Phenolat verläuft und dass die Verfügbarkeit von Stufen dafür entscheidend ist, ob hauptsächlich Phenol oder Benzol gebildet wird. Im zweiten Teil dieser Arbeit werden zwei gängige, DFT-basierte Methoden zur Beschreibung von Dispersionskräften untersucht, die DFT-D2 Methode und das vdW-DF2 Funktional. Mit beiden Methoden wurden Adsorptionsenergien für Wasser, Alkohole und Alkane in Zeoliten des MFI-Strukturtyps berechnet. Der Vergleich mit experimentellen Werten zeigt, dass beide Methoden nur bedingt für die Modellierung von Reaktionen in Zeoliten geeignet sind, da sie die Exothermizität der Adsorption von Alkanen systematisch überschätzen.

Contents

Acknowledgments **iii**

Abstract / Zusammenfassung **v**

Contents **vii**

Chapter 1 Introduction **1**

Chapter 2 Background **5**

2.1. Aqueous Phase Processing of Biomass 5

2.2. Processing of Aromatic Oxygenates 10

2.3. Conversion of Ethanol to Hydrocarbons 14

Chapter 3 Computational Methods and Models **17**

3.1. Quantum Chemical Methods 17

3.2. Models for Metal-Catalyzed Reactions 19

3.3. Models for Processes in Zeolites 21

3.4. Definition of Reaction Energies and Barriers 23

Chapter 4 Aqueous Phase Processing of 1-Propanol over Pt **25**

4.1. Indroduction 25

4.1.1. Previous Studies 26

4.2. Results and Discussion 30

4.2.1. Effect of Steps on the Propane Formation Pathway 30

4.2.1.1. C-O Cleavage of the Alcohol-Hydrogenolysis Pathway 31

4.2.1.2. Propylene Hydrogenation in the Acidic Dehydration-Hydrogenation Pathway 34

4.3. Conclusion 36

Chapter 5 Decomposition of Ethanol over Ru **39**

5.1. Introduction 39

5.2. Nomenclature 40

5.3. Results and Discussion 41

5.3.1. Adsorption Geometries 41

5.3.2. Reaction Energies 45

5.3.3. Reaction Barriers 47

5.3.4. Reaction Pathways 51

5.4. Conclusions 55

Chapter 6 Hydrodeoxygenation of Guaiacol over Ru 57
6.1. Introduction 57
6.2. Nomenclature 59
6.3. Results and Discussion 60
6.3.1. Adsorption and Reactions on Close-Packed Ru(0001) 62
6.3.1.1. Adsorption Geometries 62
6.3.1.2. Energetics of Reactions 66
6.3.1.3. Comment on the Temperature and Pressure Dependency 71
6.3.1.4. Adsorption Processes 72
6.3.1.5. Reaction Pathways 74
6.3.2. Reaction on Stepped S3-Ru(10$\bar{1}$5) and S3-Ru(10$\bar{1}$5) Surfaces 82
6.3.2.1. Extension to Nomenclature Rules 83
6.3.2.2. Adsorption of Catecholate and Phenolate at Step Sites 85
6.3.2.3. Energetics of the C-O Cleavage Process at Step Sites 87
6.3.2.4. Interpretation of the Experimental Results 91
6.4. Conclusions 92
Chapter 7 Benchmark of DFT Strategies to Address van der Waals Interactions in Zeolites 95
7.1. Introduction 95
7.2. Results and Discussion 96
7.2.1. Adsorption Energies from PBE-D2 Calculations 98
7.2.1.1. Adsorption of Alkanes 98
7.2.1.2. Adsorption of Alcohols and Water 103
7.2.1.3. Comparison of Adsorption Enthalpies and Adsorption Energies 106
7.2.2. Adsorption Energies from vdW-DF2 Calculations 108
7.2.2.1. Adsorption of Alkanes 108
7.2.2.2. Adsorption of Alcohols and Water 109
7.2.3. Comparison of the Two Types of Zeolites 109
7.2.4. Analysis of PBE-D2 Adsorption Energies and Comparison with vdW-DF2 Results 111
7.2.5. General Comments 113
7.3. Conclusions 116
Chapter 8 Summary 119
Appendix: List of Abbreviations 123
References 125

Chapter 1 Introduction

The remaining availability of fossil energy resources as oil, natural gas and coal is disputed in the literature, but it is generally accepted that they *will* be depleted.[1-5] For instance, the rate of petroleum extraction has been predicted to reach its maximum ("peak oil") in the first half of the 21st century.[2,3] However it is still being discussed whether the extraction rate will stay constant at a high level or will decrease after the peak.[2,3] To get a rough idea of the time scales discussed for the depletion of fossil energy, recall that some of the simple forecast models assume the production of oil to continue for 100 years after the peak oil is reached.[2] This is a challenging issue as more than 80% of the world's energy consumption in 2011 was covered by energy sources of fossil origin.[6] The remaining share was covered by hydroelectric, nuclear, and renewable energy sources, although the contribution of the latter is only minor, less than 5%.[6] The up-coming depletion of fossil resources will not only have an impact on the availability of energy, but will also affect the chemical industry, as a large variety of chemicals are produced from fossil resources in petrochemical processes.[7] Thus, it is necessary to reduce the dependency on fossil resources both as energy source and as feedstock for the chemical industry.[8] One possible approach to reach this goal is the usage of renewable resources such as biomass, which has been claimed to be "the only practical source of renewable liquid fuel".[9] Great efforts have been made to establish a biomass based industry that, in analogy to the petrochemical industry, uses a small number of chemicals as building blocks for the synthesis of a large variety of products.[10] For this purpose, various chemical species that may be suitable as building blocks, have been identified, based on their potential for the industrial application, as so-called "platform molecules" for the biomass based industry.[11] The most recent list of platform molecules was proposed in 2010 and contains ten compounds, Figure 1.[11]

A glance at this list of platform molecules provides a hint at the reason, why it is challenging to directly transfer the petrochemical processes to biomass derived feedstocks. Just like the majority of platform molecules, biomass derived materials tend to feature a large number of oxygen containing functional groups, while feedstocks derived from petroleum is

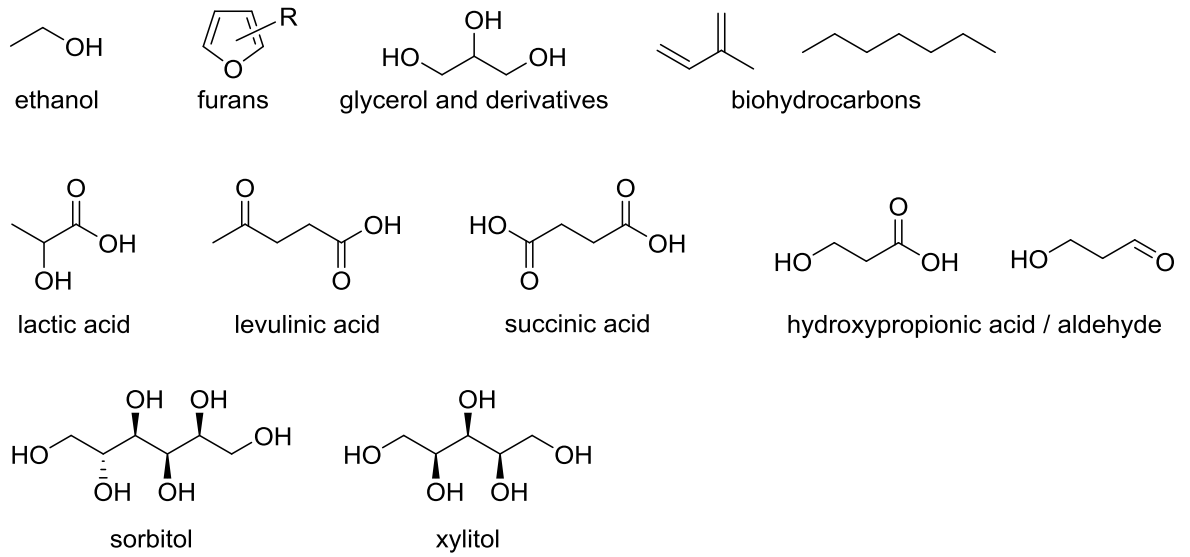

Figure 1: Platform molecules for a biomass based industry according to Ref 11.

generally less strongly functionalized.[10] This issue has a significant impact on the chemical and physical properties of the respective materials, which have to be taken into account when processing them. The large number of functional groups in biomass induces strong intermolecular interactions, which renders many biomass derived molecules to be non-volatile. Such molecules are often soluble in water, making a reaction in the aqueous phase (AP) possible. At variance, the unfunctionalized and thus volatile fossil feed molecules are often hydrophobic. Due to the absence of functional groups, fossil feed molecules are hard to activate and are therefore often processed at high temperature in gas phase.[10] In contrast, functionalized molecules derived from biomass tend to decompose before they evaporate. Therefore, this type of feedstock is best processed in aqueous phase under milder reaction conditions.[10,12]

The difference in the chemistry between petrochemical and biomass derived feedstocks sketched above illustrates the necessity to develop new processes that are tailored to the properties of biomass materials. Quantum chemical studies as carried out in this thesis can assist the development of such new processes, as they can reveal the molecular mechanisms behind a complex reaction network.[13-15] Theoretical methods enable the identification and understanding of the atomic / electronic interactions that are crucial for chemical processes, which is often hard to achieve by experimental methods only. Such information is valuable especially when a process involves complex reaction sequences or networks, as often encountered in catalytic reactions. Applying the additional knowledge about the reactions enables a target driven design and improvement of chemical processes.

Next, the structure of this thesis shall briefly be elucidated. The next chapter after this introduction describes some background information on the utilization of biomass, in order to illustrate the context of the projects in this thesis. In Chapter 3, a short sketch of the applied quantum chemical methods will be provided and various aspects concerning the model building will be addressed.

The results of this thesis will be presented and discussed the Chapters 4 to 7. Chapter 4 deals with the reaction network of 1-propanol over Pt catalysts under AP processing conditions, which has also been studied experimentally.[16] Earlier works at the Fachgebiet für Theoretische Chemie have explored both the reforming[17-19] as well as the alkane formation pathways.[20,21] However, the C-O cleavage pathways leading to alkane formation thus far have been modeled with a close-packed Pt(111) surface only, leaving open the effect of step sites on the alkane formation. This issue will be addressed in this chapter by presenting calculations using a stepped Pt surface to model the catalyst. In combination with the earlier results,[17-21] the new data will be used to derive a complete overview of the reactions of 1-propanol over Pt in AP processing.

Chapter 5 deals with the decomposition of ethanol over Ru catalysts. This chapter can be understood as a complementary study to the contents of Chapter 4, in which reactions catalyzed by a metal favoring the reforming pathway have been investigated. At variance, Ru has been reported to catalyze the formation of alkanes from alcohols.[22,23] A major aspect of this chapter is the competition between the C-O and the C-C cleavage, which is discussed to be crucial for the question whether a catalytic system will favor the formation of alkanes or the reforming pathway.[12,23-25] A second focus of this chapter is put on the mechanism of the C-O and C-C bond cleavages.

Chapter 6 continues with Ru-catalyzed reactions and deals with the hydrodeoxygenation (HDO) process of aromatic oxygenates derived from biomass, e.g. from lignocellulose. Experiments using guaiacol (2-methoxyphenol) as a model feedstock have shown that the oxygen functionalities can (partly) be removed, when the oxygenate is brought to reaction with H_2 over Ru nanoparticles supported on activated carbon.[26-29] Depending on the reaction conditions, in particular on the H_2 pressure, guaiacol can be processed to yield benzene[26] or phenol,[27-29] both chemicals of industrial importance. This chapter will illustrate the calculations to establish, based on the computationally evaluated energetics, a reaction mechanism for the guaiacol HDO on Ru that is consistent with the experimental observations. Furthermore, the calculated results will be used to rationalize why the product selectivity of

the HDO process depends on the H_2 pressure.

The next chapter, Chapter 7, will deal with zeolites. Due to the importance of zeolites for industrial applications, among others as catalysts,[30,31] it is desirable to establish quantum chemical methods that are able to describe accurately molecular processes and interactions in zeolites. However, the proper description of the van der Waals (vdW) interactions, which is known from experimental[32-36] and theoretical studies[35,37-47] to play an important role for the chemistry of zeolites, is a challenge to semi-local DFT approximations.[48] The DFT-D2 method[49] and the non-local correlation density functional of the type vdW-DF2[50] are two approaches, which are claimed to describe the dispersive interactions. This chapter will benchmark the performance of these two methods on the example of the adsorption of water, alcohols and alkanes in Silicalite and H-ZSM5 zeolites.

The final Chapter 8 will present a brief summary of all results, together with some concluding remarks.

Chapter 2 Background

In this chapter, some of the recent developments in biomass processing shall be highlighted. A focus is placed on those processes that are relevant for the reactions studied in this thesis. Earlier approaches to the production of bio-fuels such as the production of bio-diesel from vegetable oil[51] will be omitted here. The aim of this chapter is not only to list promising technologies; the chemical principles behind those processes should also be illustrated here.

2.1. Aqueous Phase Processing of Biomass

In one of the pioneering works on the field of biomass processing, *Dumesic* and co-workers have shown that sugars, e.g. glucose, as well as biomass derived polyols like glycerol can react to form H_2 and alkanes in AP reactions catalyzed by Pt supported on Al_2O_3.[52] Not only alkanes are interesting as an energy carrier, as they can be used as a liquid fuel that is compatible with the current technology, also H_2 is interesting for the energy industry, for instance in fuel cells. A large number of subsequent works have improved the processes for

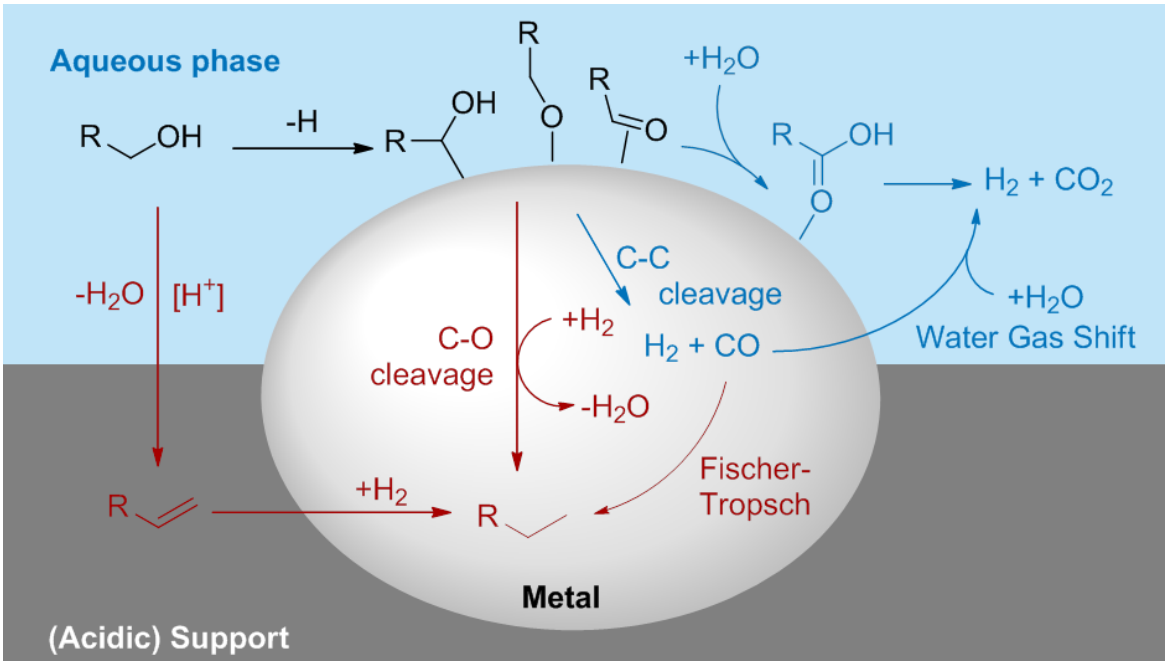

Figure 2: Reaction pathways involved in the catalytic aqueous phase processing of alcohols. The reactions in blue are associated with the reforming pathway; those in red are associated with the formation of alkanes. Ref 52.

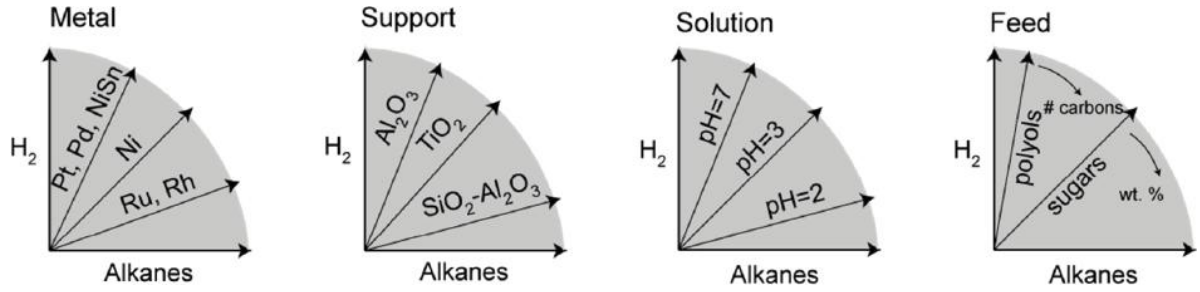

Figure 3: Factors controlling the selectivity of aqueous phase processing of feedstocks derived from starch and sugars as summarized by *Dumesic* and co-workers; adapted from Ref 23.

the production of alkanes or H_2.[12,16,22-24,53-62] In later works, aqueous phase processing has also been developed further to produce structurally more complex chemicals such as γ-valerolactone.[63-65] As this thesis focuses on the reforming pathway and the alkane formation, the production of other (platform) chemicals in AP processing will not be further addressed.

AP processing of sugars or sugar derived alcohols is often performed as a reaction in a single reaction vessel catalyzed by supported metal nanoparticles. The typical reaction conditions are temperatures around 500 K and elevated pressure between 15 and 50 bar. The actual process involves a complex reaction network with reactions that may occur on the metal catalyst, the support and / or in the solvent phase, as shown in Figure 2.[52] The selectivity of this process can for instance be tuned by varying the catalyst / support system. The reforming pathway leading to the formation of H_2 and CO_2 is associated with late, or rather non-oxophilic, transition metal catalysts as Pt or Pd and neutral supports.[23,55,66] At variance, the formation of alkanes is favored by more oxophilic metal catalysts as well as by acidic reaction conditions, which may be induced by an acidic support or by mineral acids in the aqueous phase (Figure 3).[23,55,66]

The impact of the acidic conditions on the selectivity can be easily explained with the acid-catalyzed dehydration, which removes OH groups as water, Figure 2.[24] The preference for alkane formation by catalysts based on more oxophilic metals such as Ni, Ru or Rh,[23,55,66] can be rationalized with the Brønsted-Evans-Polanyi relation (BEP). In this context the BEP relation can be phrased as: the more stable a product state, the lower is the activation barrier for its formation.[67] As oxygen groups are per definition strongly stabilized on the surface of oxophilic metals, barriers associated with C-O bond cleavage reactions yielding a carbon moiety and an oxygen moiety on the metal surface will also be low. Thus oxophilic metals favor the cleavage of C-O bonds, which is necessary for the formation of alkanes.

As discussed in literature, the preference for the formation of either H_2 or alkanes is related to the competition between the C-C and the C-O scission reactions.[12,23-25,68] While it is apparent, why alkane formation is associated with the C-O cleavage, the connection between the preference for the reforming pathway and the C-C cleavage is not so easily accessible and thus shall be elaborated here by a thought experiment. When an alcohol, for instance glycerol ($HOCH_2$-CHOH-CH_2OH), shall be used as feedstock for the production of H_2, it is desirable to turn all H atoms of the alcohol to H_2. If reactions with the aqueous solvent are neglected, the theoretical maximum is four equivalents of H_2 for each glycerol. The removal of all H atoms from glycerol would leave a hypothetical, radical entity "$(CO)_3$" which strongly binds to the catalyst surface and may cause poisoning if not removed. The $(CO)_3$ species can only be removed from the catalyst, if it decomposes via C-C cleavage to non-radical C_1 species such as CO (or CO_2). Of course, there are also other carbonaceous species with more than one C atom that feature a close-shell electron configuration and thus allow for easy desorption, e.g. propane or propylene. However, all these species contain H atoms, i.e., their formation would reduce the H_2 yield. Furthermore, a good reforming catalyst should not favor the C-O cleavage. If a catalyst is active for the C-O scission of CO formed upon C-C cleavage as mentioned above, the CO moiety will be converted into adsorbed C and O. Without the re-formation of the C-O bond, the C and O atoms can only desorb as methane and H_2O, respectively. Hydrogen is consumed in both cases, leading to the undesired reduction of the H_2 yield. Note that CO is normally not observed as a product in aqueous phase processing, as the typical reaction conditions also favor the water gas shift (WGS) reaction (Figure 2). Thus CO reacts with H_2O from the solvent phase to form CO_2 and H_2, which is a desirable side effect that increases the H_2 yield.

There is a large number of theoretical works dealing with the reactions of alcohols or (aliphatic) oxygenates in general on metals surfaces, which partly reflects the success of the aqueous phase processing of biomass.[17,19,25,68-83] On the other hand, reactions of alcohols are not only playing a role in biomass processing, but also in other important processes, such as steam reforming[84] or the methanol synthesis from CO or CO_2.[85] One of the first theoretical studies to address AP processing of alcohols is the work by *Mavrikakis* and co-workers on C-O and C-C cleavage reactions of ethanol on Pt(111).[71] Consistent with the preference of Pt for the H_2 formation, Pt was shown to be more active for the scission of the C-C bonds than for the C-O bond cleavage.[71] The ethanol decomposition on close-packed surfaces of 10 selected transition metals from groups 7−11 has been investigated using BEP relations

derived from DFT calculations.[68] The resulting energetics for the C-C and C-O scission steps was used to predict reaction rates that deviate by 1–2 orders of magnitude from the experimental reference.[68] Note that this agreement between experiment and theory can be considered reasonable for state-of-the-art quantum chemical methods.[68] However, that work[68] did not explicitly consider the dehydrogenation steps and concluded that the rate-limiting steps of ethanol decomposition on the various metals is a C-C cleavage step.[68] It is now known that neglecting hydrogen transfer steps is too strong a simplification when one studies the reaction of alcohols.[86] In fact, the dehydrogenation steps can be more relevant for the kinetics than the C-C and C-O scission steps.[86] Various DFT studies addressing the mechanism of ethanol decomposition on close-packed surfaces of Pt,[87,88] Pd,[75] Rh,[77,80] and Co[89] have demonstrated that dehydrogenation steps often have associated barriers that are comparable or higher than the C-C and C-O scission barriers.

The comparison of the ethanol reforming barriers and the DOS (density of states) of a metal catalyst revealed that those metals featuring a high DOS at around the Fermi level are catalytically more active.[90] A high DOS near the Fermi level can be understood as an indicator for a high redox capability, which benefits the redox steps involved in ethanol reforming, e.g., dehydrogenation, C-C scission etc.[90] Based on this finding, it has been concluded that Rh and Ir should show high catalytic activity for alcohol reforming.[90] However, a high DOS at the Fermi level does not guarantee a high *selectivity* for the reforming pathway as the competing alkane formation also involves redox steps.

As the preceding paragraph shows, many quantum chemical studies focus on the reaction of ethanol, the smallest alcohol containing both a C-O and a C-C bond. Despite of the success of these studies on ethanol, one has to realize that such studies have a certain model character, as mono-ols are not typical for the AP processing of biomass.[23] Thus, various works have studied the reaction of polyols like glycerol on Pt(111).[78,82,91] Similar to the reaction of ethanol, glycerol has to dehydrogenate multiple times before the C-C cleavage becomes kinetically accessible.[82,91] The rate of glycerol reforming on Pt is controlled by the dehydrogenation steps and not the C-C scission.[91] Using the energetics evaluated at the DFT level, BEP relations and linear scaling relations have been derived and applied to investigate the reactions of glycerol on Pd, Rh, Cu and Ni.[92] The linear scaling relations correlate the adsorption energy of an organic species on a given metal surface with the bond strength of atomic C and O centers on the surface. That study showed, consistent with experiment,[22] that Pt and Pd are suitable reforming catalysts.[92] A work on the reforming kinetics of glycol

(ethanediol) over Pt(111) demonstrated that the ideal reforming catalyst should be slightly more oxophilic than Pt,[93] as the better stabilization of O groups would facilitate the rate-limiting dehydrogenation at the OH groups.[93] This finding rationalizes the higher reforming activity of bimetallic NiPt catalysts compared to Pt.[93]

Recall that the typical biomass processing is carried out in aqueous phase, as mentioned at the beginning of this section. Although the solvent likely has an effect on the reaction, the majority of the previously mentioned computational studies do not account for the solvent phase. A first step to overcome this gap between the model and the reality is to consider the reactions of the feedstock with the solvent. DFT calculations on surface reactions on Au,[76] Pt,[19,76,88,94] Pd,[95] Rh,[96] and Co[89] illustrated that an OH group from the solvent phase can react with adsorbed acyl (R-C=O) groups which derive from the dehydrogenation of alcohols. These reactions yield carboxylic acids which are observed as intermediates in AP processing over Pt.[16] Although it is an interesting issue to understand the effect of the aqueous phase on the reactions, only few studies, e.g. Ref 76, account for the solvent by including explicit water molecules to the quantum chemical model. The latter work showed for the ethanol oxidation on Au that the solvent effects are only minor, apart from the reaction of surface acetyl with OH from the solvent.[76]

It is widely accepted that the surface structure of catalysts can have an effect on the reactivity.[97] However, most of the works discussed in the present section rely on modeling metal catalysts with close-packed surfaces. This approximation is often good enough to obtain trends that allow one to rationalize the experimental observations. When studying mechanistic details, one may need to compare the reactions on differently shaped surfaces of a metal. Studies on the alcohol oxidation on Pt[88] and Pd[95] indicate that the open (100) surfaces are catalytically more active than the close-packed (111) surfaces. The presence of step sites can also have an impact on the reaction mechanism. For instance, the decomposition of 1-propanol on Pt(111) can only proceed via decarbonylation; in contrast, two kinetically accessible decomposition pathways have been identified for the stepped Pt(221) surface (cf. Section 4.1.1).[19] Another example is the decomposition of ethanol on Rh: while the reaction on Rh(111) is limited by the dehydrogenation step yielding the surface oxa-metalla-cycle CH_2CH_2O,[77,80] ethanol decomposition at step sites modeled by Rh(211) do not proceed at all via this intermediate.[81,96]

The works discussed thus far focus on the reaction on metal catalysts, although it is known that the support material itself can be catalytically active, as mentioned before. Some

works have addressed the acid-catalyzed alcohol dehydration on typical support materials, like γ-Al_2O_3, used in biomass processing.[98] Suitable models for supported metal catalysts, e.g. Pt/γ-Al_2O_3[99] or Pd/MgO,[100,101] have been reported. These models typically consist of a small metal cluster on a slab model that describes the support material.[99-101] Such more complex models have, for instance, been used to investigate NO activation,[99,100] CO oxidation[100] or the water gas shift reaction,[101] but have yet to be applied in the context of biomass processing.

Summing up the present section, it can stated that the computational studies mentioned above have already been able to reveal various mechanistic details, contributing to the understanding of the reactivity of alcohols on metals. However the reactions of alcohols involving the complex interplay with the metal catalyst, the support and the solvent, still raises questions yet to be explored.

2.2. Processing of Aromatic Oxygenates

The majority of the works introduced in the preceding section deals with the processing of aliphatic alcohols, i.e. species that are derived from sugars or starches. As these parts of biomass are also edible, an unwanted competition between the food production and the biomass based chemical industry can arise, if the latter exclusively focuses on the processing of sugars and starches.[10] Therefore, recent research has also addressed the utilization of feedstocks derived from lignin, one of the inedible main-components of woody biomass.[26-29,102-124] Due to the structure of lignin, which contains aromatic C_6 rings as a repeating structural motif, many molecules derived from processing of lignin are aromatic species. These species display different reactivity than the aliphatic species derived from starches and sugars, which have been mentioned in the preceding section.

One of the typical approaches to process lignin or woody biomass to liquid fuels is pyrolysis, the thermo-chemical decomposition of a feedstock under anaerobic conditions.[24,108,125] The product of this process, referred as “pyrolysis oil” or “bio oil”, contains of a large variety of different aliphatic and aromatic oxygenates.[110,126,127] This mixture of chemicals is not yet suitable for usage as fuel, because it still features various undesired properties like chemical instability, low heating value and high viscosity.[110,128] As these problems are associated with the high oxygen content of the pyrolysis oil,[110,128] (partial) removal of the oxygen functionalities is necessary in order to upgrade the oil and to obtain a product that is compatible with the current petrochemical technology.[128]

The removal of the O groups and the formal replacement by H atoms is referred to as hydrodeoxygenation (HDO). The alkane formation from alcohols or aliphatic oxygenates in

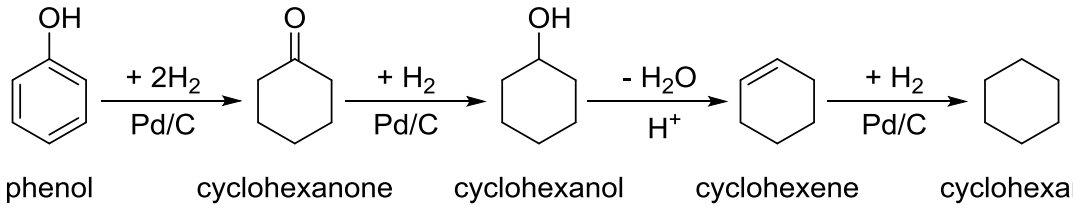

Figure 4: Mechanism for the conversion of phenol to cyclohexane over Pd/C in the presence of H_3PO_4, according to Ref 113.

general as mentioned in Section 2.1 can also be understood as a HDO process. Compared to the reactions of aliphatic oxygenates, the HDO of aromatic species is more challenging due to the stability of the aromatic C-O bonds.[120] There is a large variety of differently designed, catalytic processes for the transformation of aromatic oxygenated, which use metals,[26-29,102-106,111,114-117,120,123,124] metals in conjunction with mineral acids or zeolites,[107,113,122] but also non-metallic materials like carbides, sulfides or oxides as catalysts.[26,112,114,120,121,129] Some of the processes aim at the production of aromatic products,[27-29,102,103,105,106,111,112,114-117,120-124,129] while other variants couple the C-O cleavage with the hydrogenation of the aromatic system yielding cyclic, aliphatic or olefinic products.[104-107,113-115,120,121]

The experimental works on the HDO of aromatics can give a rough idea about the reaction pathways over the various catalytic systems.[26,28,102,103,111,113,114,116-118,130-136] Reactions which combine a metallic hydrogenation catalyst with an acid functionality, typically aim at the production of non-aromatic products.[107,113,122] Such processes start with the hydrogenation of the aromatic ring to yield a saturated system. In a second step, the oxygen group is eliminated in an acid-catalyzed reaction leading to the formation of an olefinic system, which can be re-hydrogenated.[107,113,122] Figure 4 illustrates the reaction mechanism on the example of phenol conversion over Pd/C in the presence of H_3PO_4.[113] In reactions on a metal only, which often target the production of aromatics, the mechanism is slightly different.[26,28,55,102,103,111,116,117] The hydrogenation at the phenyl group is often an unwanted side reaction as it reduces the yield of aromatics. The mechanism for the hydrodeoxygenation of the model molecule guaiacol over CoMo and NiMo catalysts has been proposed to proceed via the intermediates catechol and phenol, leading to the formation of benzene (Figure 5).[102,103] In other words, the aromatic C-O bonds are suggested to be directly cleaved on the metal catalysts. This mechanism has recently also been proposed for that reaction over Ru.[26,28] However, this is not the only pathway under discussion. The direct formation of phenol from guaiacol via the removal of the methoxy group as shown in Figure 5 has also

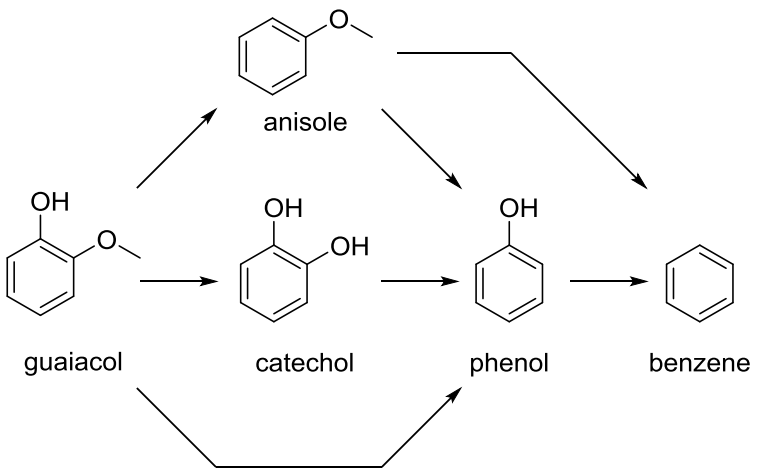

Figure 5: Main reaction pathways discussed for the metal-catalyzed hydrodeoxygenation of guaiacol yielding aromatic products. Alkylation steps catalyzed by the acidic support have been omitted for clarity. Mechanisms taken from Refs 26, 28, 102, 103,111, 116, and 117.

been suggested.[28] Both reaction routes have also been proposed for guaiacol HDO over Pd, Pt, Cu, Fe as well as bimetallic PdFe catalysts.[28] The main difference between the reactions on precious metals (Pd, Pt, Ru) on the one hand and the reactions on base metals (Cu, Fe) or PdFe on the other hand is that only the precious metals are active for the (undesired) hydrogenation of the aromatic ring.[28] Further works suggested that Pt-catalyzed HDO may also proceed via the intermediate anisole which in return can demethylate (removal of CH_3) or demethoxylate (removal of OCH_3) to yield phenol and benzene, respectively (Figure 5).[111,116,117] Despite of these experimental studies, the exact HDO mechanism at an atomistic level and the underlying principles are not as well understood as the reactions of aliphatic oxygenates. This is partly due to the fact that the number of computational works dealing explicitly with the HDO of aromatics is still low.

For a long time, the majority of the computational works on the HDO process only addressed the adsorption of various model substrates on the catalyst surface.[28,112,121,124] Calculations addressing the HDO of *m*-cresol [3-hydroxytoluene, $C_6H_4(OH)(CH_3)$] have demonstrated that the adsorbate only interacts with the C_6 ring with a Ni(111) surface but not via its OH group.[124] In contrast, *m*-cresol also binds via its O center to Fe(110) and NiFe(111) surfaces.[124] The metal-O interaction rationalizes why Fe and NiFe show a high activity for the removal of oxygen yielding toluene while reactions on Ni mainly yield oxygenated products.[124] Different from the "flat" adsorption mode of aromatic oxygenates as found on Ni, Fe and NiFe,[124] such adsorbates only interact via their oxygen center but not their C_6 ring with sulfidic HDO catalysts like MoS_2 or CoMoS.[112,121] It has been speculated that this

interaction mode allows a stronger activation of the C-O bond, thus facilitating the deoxygenation reaction.[112,121]

Some efforts to explore the reaction network of guaiacol HDO on Ru[137,138] and Pt[139] have recently been reported. Although these studies give an overview on large parts of the reaction networks, they still leave some fundamental questions unanswered. For instance, neither the formation of benzene on Ru[26] nor the production of phenol on Pt[28,29,111,116,117] has so far been explained by theory.[137-139] Beside mechanistic studies on guaiacol HDO, it has also been attempted to derive BEP relations for aromatic systems.[139] The reactions of aromatics indeed follow the BEP relations, like the reactions of aliphatic alcohols mentioned in the previous section.[139] However, those parameters derived for aliphatic alcohols are not transferable to aromatics,[139] reflecting the different reactivity of the two classes of reactants. The C-O scission on Fe(110) has been studied for phenol as model;[140] that work showed the direct removal of the OH group to be more favorable than various hydrogen assisted mechanisms.[140] Apart from monocyclic aromatic systems, some computational works evaluated the reactions of larger model molecules like aromatic ethers.[141,142] Studies on the solvent effect illustrate that the C-O bond in benzyl phenyl ether (C_6H_5-CH_2-O-C_6H_5) can be cleaved easily in the presence of acidic protons and a polar solvent.[142] At variance, the reaction in an apolar solvent invokes a radical mechanism that this hardly accessible.[142] Furthermore, the thermodynamics of the transformation of di-arylic ethers (R-C_6H_4-O-C_6H_4-R') on Ni have been explored to clarify why the ether C-O bond can be broken to form (substituted) phenols, whereas the scission of the C-O bond in phenols is inaccessible.[141] The calculations provide as hint that this may be related to the competition between the desorption of the phenols and the C-O cleavage reaction.[141] However, this system needs further investigation as the reported mechanism involves reaction energies of up to 150 kJ mol^{-1}.[141]

Instead of focusing on the reactions, some works addressed the nature of the HDO catalysts, as done for the PdFe bimetallic system.[143] The synergistic effects in that catalyst was related to the partial electron donation from Pd to Fe, resulting in the stabilization of the reduced Fe surface which would otherwise be easily poisoned by oxygen.[143] Before the HDO of aromatics has been studied, most quantum chemical investigations dealing with the reactions of aromatics on metals focused on (de)hydrogenation reactions.[144-151] Among others, transformations of model molecules like benzene,[144-147,149] phenol[148,150,151] or pyridine[149] on Rh, Ni, Pd, Pt, and Cu surfaces have been examined. A recent ab-initio

molecular dynamics study on the hydrogenation of phenol on Pt and Ni revealed that these reactions are both thermodynamically and kinetically significantly easier accessible in aqueous phase than in the gas phase.[151] Also those studies on (de)hydrogenation may contribute to the understanding of the HDO process because hydrogen transfer steps at the aromatic ring are discussed to play a role in HDO.[138,140]

2.3. Conversion of Ethanol to Hydrocarbons

With (bio-)ethanol becoming more abundant since the chemical industry has started to focus on the usage of biomass, there are increased efforts to use ethanol as precursor for the production of higher hydrocarbons, olefins and aromatics.[152-158] Recent works attempted to establish a process catalyzed by pure zeolites[152-154] or by metal modified zeolites.[153,155-158] Due to the different nature of the catalyst, zeolite catalyzed conversion of ethanol invokes a fundamentally different chemistry than the metal-catalyzed reactions introduced in the preceding Sections 2.1 and 2.2.

Although the conversion of ethanol on zeolites has already been mentioned in the 1970's,[160,161] the mechanistic details of this process are not very clear. A very rough reaction scheme as depicted in Figure 6 has been formulated to illustrate the reaction pathways.[159] Based on the analysis of intermediates and products, it has been proposed that the conversion of ethanol on pure zeolites follows a so called "hydrocarbon pool mechanism",[162] similar to the well-studied conversion of methanol on zeolites.[163-166] According to the hydrocarbon pool mechanism for the conversion of methanol to olefins, a large variety of hydrocarbons (olefins, aromatics etc.), referred to as the "hydrocarbon pool", is built up from methanol. These hydrocarbons are methylated in acid-catalyzed steps by methanol to form larger hydrocarbons, which in return can eliminate olefins as products. A variant of the hydrocarbon pool mechanism based on hexamethylbenzene, which has been proposed for the formation of propylene from methanol in H-ZSM5, is exemplarily depicted in Figure 7.[167] As visible from

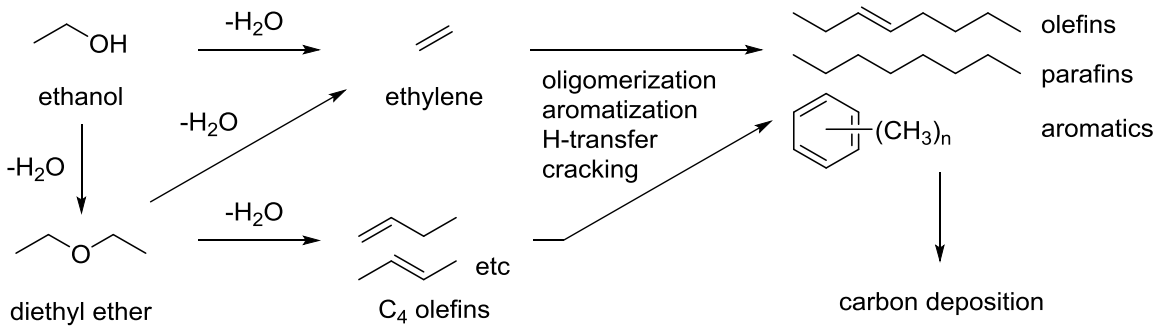

Figure 6: Proposed reaction pathway for ethanol conversion in zeolites according to Ref 159.

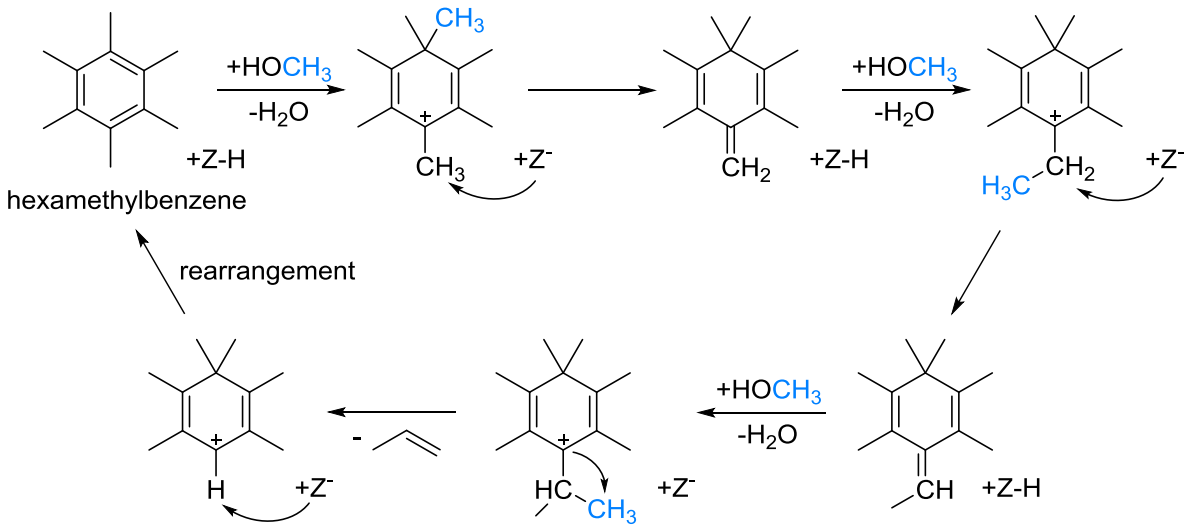

Figure 7: A variant of the hydrocarbon pool mechanism proposed for the zeolite catalyzed conversion of methanol to propylene according to Ref 167. Z-H and Z^- represent the Lewis acid group of the zeolite and the deprotonated zeolite framework, respectively.

the mechanism, the conversion of alcohols in zeolites invokes complex interactions between the actual feedstock (methanol or ethanol), the catalytic active side products (the hydrocarbon pool) and the zeolite. It is known from methanol conversion that the zeolite does not only act as an acid.[165,166] The structure of the zeolite (pore size, pore shape… etc.) has a strong impact on the product distribution. Thus the undirected interactions between the reactant and the walls of the zeolite framework also play an important role.[165,166] The walls of the zeolite framework can introduce steric limitations, which favor the formation of more "compact" products e.g. short, linear hydrocarbons.[165]

The product selectivity of ethanol conversion can be tuned by modifying the zeolite catalysts with metal or metal oxide particles.[155,159] Experiments have demonstrated that Au, Pt, Rh, Pd or Ga can enhance the selectivity for aromatic products to 50–70%.[159] At variance, the incorporation of oxidic clusters as Cr_2O_3, FeO_x and NiO to the catalyst system results in higher selectivity of up to around 30% for C_3 or longer olefins.[155,159] Similar yields for higher olefins have also been reported for reactions over Na, Zr or Sr substituted zeolites.[153,157,158] It is reasonable to assume that the presence of the metal / metal oxides will induce changes to the mechanism, but mechanistic studies on the reactions in such catalytic systems have not been reported yet.

A main focus of the current research is to improve yield and selectivity for the formation of higher olefins,[168] while avoiding the competing coke formation process which ultimately leads to the deactivation of the catalyst.[169]

Chapter 3 Computational Methods and Models

3.1. Quantum Chemical Methods

All results reported in this thesis have been obtained from periodic DFT calculations using the quantum chemistry program Vienna Ab initio Simulation Package (VASP, Version 5.2.12).[170-173] In the following, those parameters that hold for all calculations will be given first. Afterwards, the specific computational parameters employed to study the processes on metals and in zeolites, respectively, will be presented.

All calculations use the projector augmented wave (PAW) method[174,175] in combination with a plane wave basis set characterized by a cut-off energy of 400 eV, if not specified otherwise. The convergence criterion for the evaluation of the electronic structure required the changes of the total energy between two SCF (self-consistent field) iterations to be less than 10^{-6} eV. The optimization of a stationary point structure [i.e. minimum or transition state (TS)] is considered as converged, if the forces on each relaxed atom are below 2×10^{-4} eV/pm.

To identify TS structures, which have only been determined for the systems on metals, pre-optimizations using various implementations of the nudged elastic band method (NEB)[176-183] and the dimer method,[184-187] have been performed. Starting from such an approximate TS structure, a quasi-Newton algorithm was used for the final optimization.

In some cases, the discussion involves enthalpies *H* and Gibbs free enthalpies *G*. Standard methods were used to calculate the thermodynamic corrections to the electronic energy to estimate *H* and *G*.[188,189] The corrections have been calculated from the harmonic vibrational frequencies, evaluated for the adsorbate. The contribution of the metal or of the zeolite framework to the thermodynamic corrections has been largely omitted. Details on the evaluation of the vibrational frequencies are given in the next paragraphs, dealing with the specific computational protocols for the chemical systems on metal and on zeolite, respectively.

Reactions on metals. Reactions on metals are studied with GGA type (generalized gradient approximation) exchange-correlation functionals. The earlier works presented in

Chapter 4 (propanol on Pt) and Chapter 5 (ethanol of Ru) used the functional PW91[190] while the later works in Chapter 6 (guaiacol on Ru) employed the functional PBE.[191,192] The calculations use first-order Methfessel-Paxton smearing,[193] with a smearing width of 0.15 eV (Chapter 4 and Chapter 5) and 0.1 eV (Chapter 6), respectively, to support faster SCF convergence. However, all reported energies refer to values, for which the smearing width is extrapolated to 0. When performing a geometry optimization, a Mockhorst-Pack mesh[194] with 5×5×1 *k*-points is used to sample the Brillouin zone. The energies reported in this thesis are obtained from a single point calculation on the optimized geometry using a denser mesh of 7×7×1 *k*-points. Earlier studies indicate that the chosen *k*-point grid is dense enough to consider the reaction energies to be converged with respect to the density of the grid.[195] The bulk metal-metal distance is determined by varying the unit cell parameters of the close-packed unit cells of Pt and Ru while maintaining the cubic and hexagonal symmetry, respectively. The optimal bulk metal-metal distance corresponds to the distance found in the unit cell with the lowest single point energy. Different to the unit cell optimization for zeolites addressed in the next paragraph, the present approach does not lead to artifacts arising from Pulay-stress. Thus the single point calculations used to determine the metal unit cell sizes are performed with a cut-off energy of 400 eV. All stationary point structures are verified by the evaluation of harmonic vibrational frequencies. To reduce computational costs, only the vibrational modes of the substrate atoms are considered, i.e. the surface metal atoms are fixed during the numerical evaluation of the normal modes. This approximation is possible, as the vibrational modes of the metal surface are typical low lying and are thus not expected to couple strongly with the modes of the organic adsorbate.

Reactions in zeolites. Two functionals have been used to study chemical systems in zeolites: The PBE-D2 functional[49] and the non-local correlation functional of type vdW-DF2.[50,196] The former functional is the PBE functional, as used to study reactions on metal, corrected by an empirical, additive term to account for dispersive interactions.[49] The electronic energies at the PBE-D2 level $E_{\mathrm{PBE\text{-}D2}}$ can be separated into two contributions, the PBE contribution $E_{\mathrm{PBE,}}$ which is the self-consistent GGA-DFT energy, and the empirical correction referred to as the "D2 term" E_{D2}: $E_{\mathrm{PBE\text{-}D2}} = E_{\mathrm{PBE}} + E_{\mathrm{D2}}$.

Calculations on zeolites employ Gaussian smearing with a width of 0.1 eV as proposed for insulators with large unit cells.[197] The Brillouin zone is sampled at the Γ point only. As the MFI type zeolites under study have a lower symmetry than the bulk geometry of close-packed metals, it is difficult to determine the optimal unit cell parameters from a series of

single point calculations. Instead, the unit cell optimization routine as implemented in VASP was used. However, this implementation can suffer from artifacts that arise from Pulay-stress, if the plane wave basis set is too small.[198] Therefore, a cut-off energy of 800 eV is chosen for the optimization of the zeolite unit cells. When evaluating the harmonic vibrational frequencies for adsorption complexes in all-Si zeolites, only the vibrational modes of the adsorbates have been considered, while all atoms of the zeolite framework are fixed during the evaluation of the normal modes. Similar to the situation of adsorption complexes on metal illustrated above, the vibrational modes of the framework are not expected to couple with the adsorbate modes, due to the relatively weak zeolite-adsorbate interaction, which is dominated by dispersive interactions. This circumstance allows neglecting the framework normal modes. For adsorption complexes in Al-substituted zeolites, the vibrational modes of the OH group interacting with the adsorbate are also taken into account.

Species in the gas phase. For the evaluation of adsorption energies, the energies for isolated species in the gas phase are required. These are calculated by placing the molecule under study in a cubic unit cell with edge lengths of 1.5 nm or longer. The Brillouin zone is sampled, similar to the zeolite systems, at the Γ-point only. Spin-polarization is allowed for radical species. All other quantum chemical parameters are identical to the settings used to compute the corresponding adsorption complex on a metal support or in a zeolite cavity.

3.2. Models for Metal-Catalyzed Reactions

The Pt and Ru catalysts are modeled by periodic slabs which are separated by vacuum space of more than 1.5 nm width. The thickness of the slabs corresponds to 5 close-packed layers. The metal centers of the two top layers are allowed to relax, together with the atoms of the substrates, during geometry optimization. The remaining metal centers are fixed at the optimized bulk geometry with Pt-Pt = 282 pm, and Ru-Ru = 270 pm. Note that calculations using the PW91 functional and the PBE functional yield the same bulk metal distance for Ru. Sites on close-packed terraces of the Pt and Ru catalysts are modeled by hexagonal unit cells of the Pt(111) and Ru(0001) surfaces, respectively. The calculations in Chapter 4 and Chapter 5 dealing with 1-propanol and ethanol as substrates use a 3×3 unit cell (9 surface atoms per unit cell). The transformation of the larger substrate guaiacol on Ru described in Chapter 6 is studied with a 5×5 unit cell (25 surface atoms per unit cell).

In addition, the effect of step sites on the metal catalysts has also been considered. In Chapter 4, step sites on Pt are modeled by a monoclinic 3×1 unit cell of the Pt(221) surface with 12 surface atoms (Figure 8). This surface contains step sites of locally three-fold

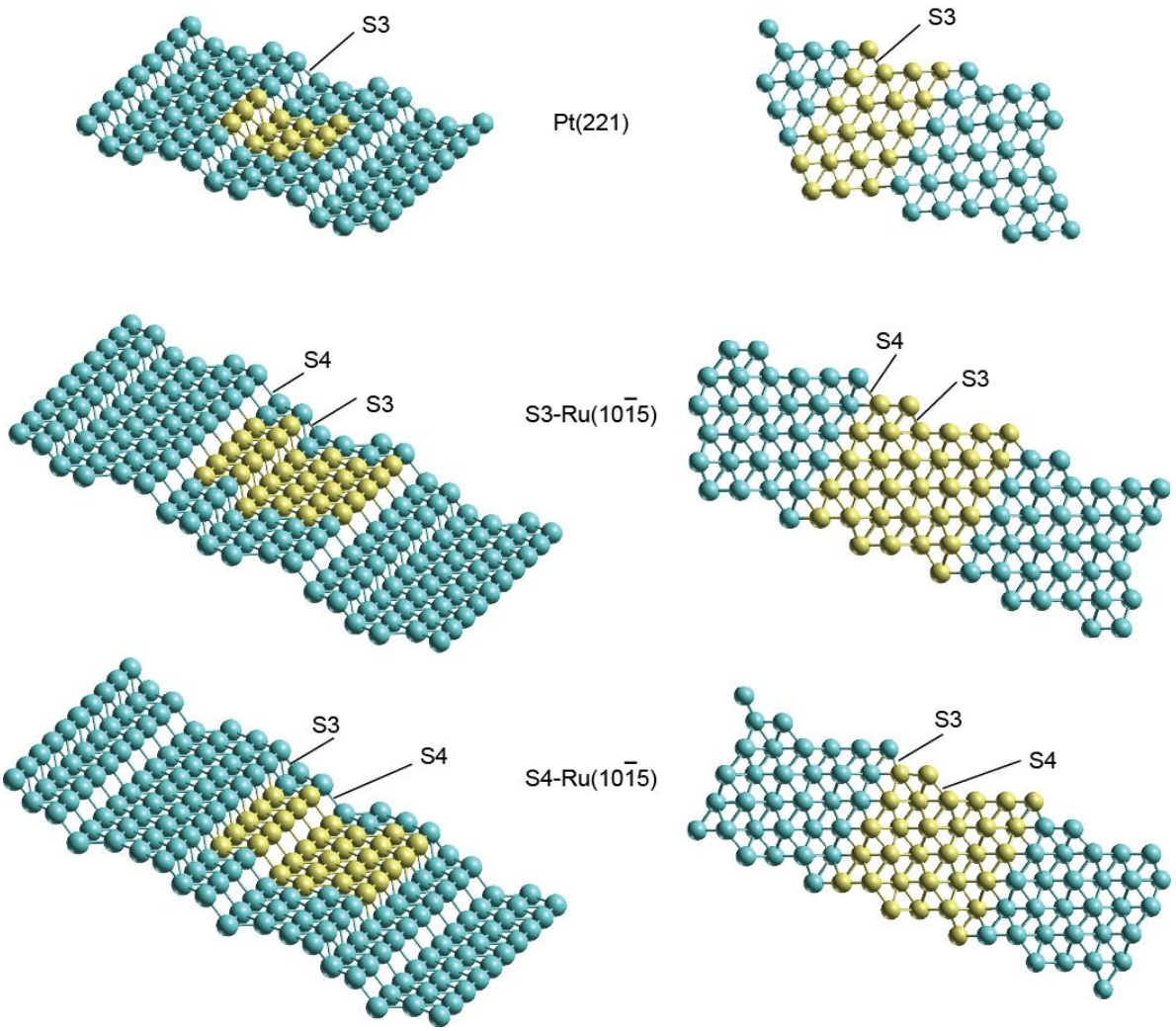

Figure 8: Slab models used to study step sites viewed from top (left) and from side (right). The periodic unit cell is marked in yellow. S3 and S4 type steps are indicated. For clarity, only the top layer is shown in the top view.

coordination ("S3" step) and a three atoms wide terrace (Figure 8). The steps on a Ru surface as studied in Chapter 6 are modeled by Ru slabs derived by cutting the hcp bulk structure of Ru perpendicular to the crystallographic [10$\bar{1}$5] direction. In contrast to an fcc system like Pt, different surfaces can be obtained, by cutting at different positions. Two stepped Ru surfaces have been constructed. Both surfaces contain S3 type steps as well as S4 type steps, i.e. step sites with locally four-fold coordination (Figure 8). Monoclinic 5×1 unit cells of either stepped Ru surface feature 30 surface atoms per unit cell and a terrace that is four atoms wide. The main difference between the two stepped Ru surfaces is the emerging step bordering the three atoms wide terrace. In one case, the emerging step is of S3 type, in the other case of S4 type. Based on this, the surfaces will be referred as S3-Ru(10$\bar{1}$5) and S4-Ru(10$\bar{1}$5), respectively. The former will be used to study reactions at the S3 step and the

latter to model processes at the S4 step.

Note that the model illustrated above formally describes the vacuum-metal interface, although some calculations in this thesis, e.g. those in Chapters 4 and 5, aim at studying processes in aqueous phase. In other words, solvent effects are neglected in this thesis, as the used model approximates the solvent phase by the vacuum phase. This should be kept in mind for the discussion of the Chapters 4 and 5.

3.3. Models for Processes in Zeolites

The unit cell for the periodic models of the MFI type zeolites H-ZSM5 and Silicalite (the all-Si variant of H-ZSM5) are derived from the crystallographic unit cell of the all-Si system which contains 96 T-atoms (Si or Al atoms occupying tetrahedral sites) and two intersections between a strait channel and a sinuidal zig-zag channel (Figure 9).[199] The H-ZSM5 model was constructed by replacing three of the Si centers by Al and adding three H atoms for charge compensation. One Al center is placed at a T12 site, a second Al is at the T8 site of the same channel intersection, the third Al is located at the T7 position of the other channel intersection. The present thesis will only consider the interaction of adsorbates with the aluminol site at T12, similar to various previous theoretical works.[41,43,44] The choice of the T12 site is related to the circumstance that it is easily accessible and allows reactions to occur with low steric constraints. The second Al atom was placed at the T8 position in order to have an O center at the channel intersection, which is coordinated to an Al center but not to the acidic proton. It was assumed that such an O center will show a slight Lewis base character, and that it may play a role in sorption processes. The T7 position for the last Al atom is motivated by the fact that it represents one of the thermodynamically most stable sites for Al in MFI zeolites.[200]

Table 1: Optimized unit cell parameters for Silicalite and H-ZSM.[a]

	Silicalite				H-ZSM5					
	a	*b*	*c*	$\alpha = \beta = \gamma$	*a*	*b*	*c*	α	β	γ
PBE-D2	2027	1992	1333	90.00	2033	1991	1339	89.90	89.88	90.04
vdW-DF2	2050	2006	1356	90.00	2033	2011	1351	90.39	90.03	89.94
Exp.[b]	2009	1974	1314	90.00						

[a] Length of unit cell vectors in pm, angles in degree. [b] Ref 199, values for MFI type zeolites in general.

The unit cell parameters of empty Silicalite and H-ZSM5 have been optimized together with their atomic positions. When studying the interaction of the zeolite framework with adsorbates, the unit cell parameters are fixed to the optimized values for the empty zeolites (Table 1) while all atoms were allowed to relax.

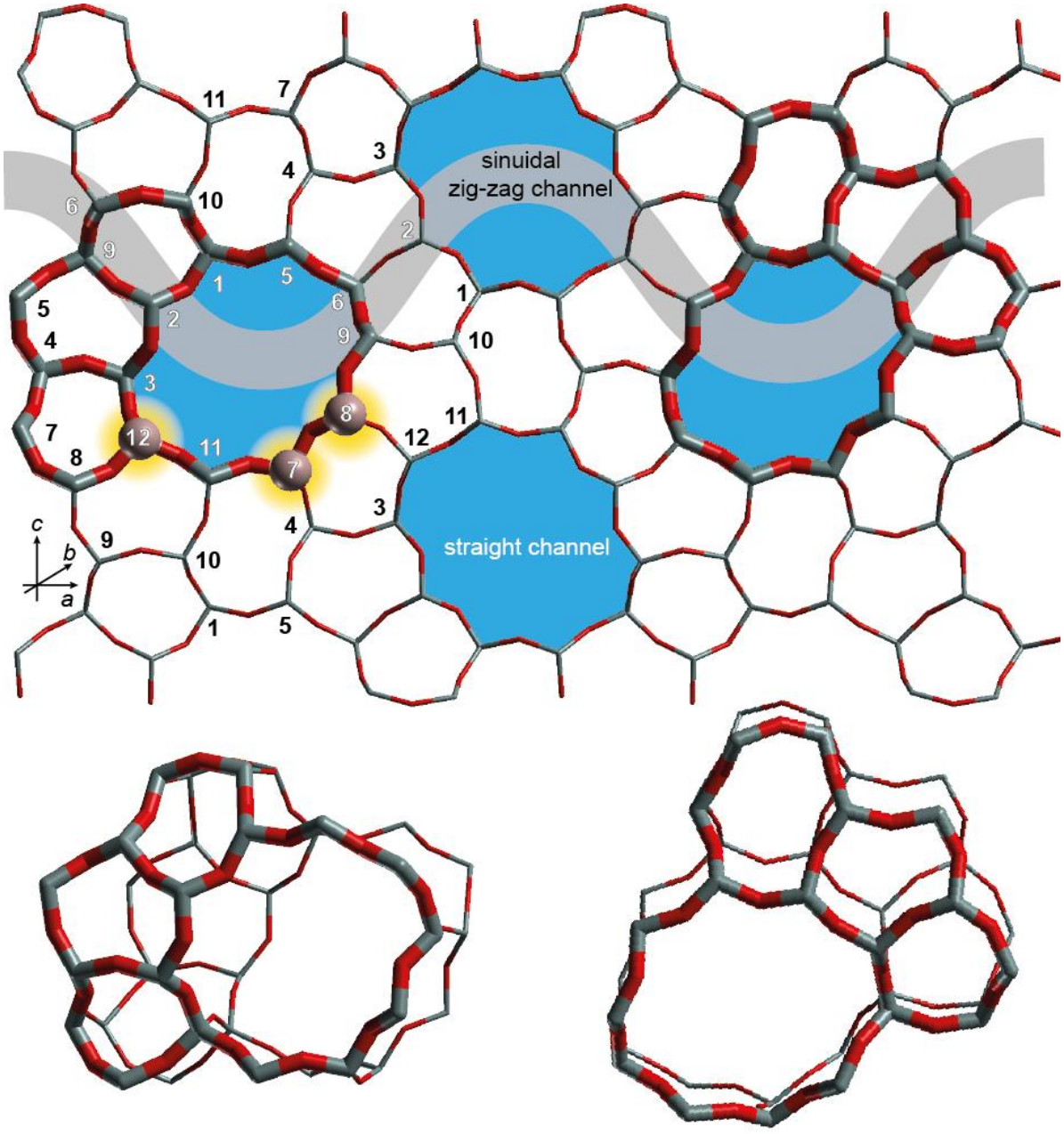

Figure 9: 2×2 super cell of the MFI type zeolites (H-ZSM5 and Silicalite) viewed along the crystallographic *b* direction. O centers are shown in red, Si in gray. The positions considered as Al sites in the H-ZSM5 model are shown as highlighted spheres. The labels of the T-atom sites as well as the straight and sinuidal zig-zag channels are indicated. The cluster cut-outs from the zeolite framework are shown below the super cell. For easier orientation, the front side of the clusters is marked with wide sticks. These cluster extracts will be used in Chapter 7 to illustrate the substrate-zeolite interactions.

3.4. Definition of Reaction Energies and Barriers

Figure 10 gives an overview on the definitions of the reaction energies and barriers as used in this thesis. Figure 10a shows the adsorption of an initial state species **IS** from the gas phase to a surface site **s** (of a metal or a zeolite) to form the adsorption complex **IS-s**. A bond cleavage reaction via the transition state **TS-s** yields the adsorbed products **P1-s** und **P2-s**. The electronic energies of the adsorption complexes are denoted as E(**x**) with **x** being **IS-s**, **TS-s**, **P1-s** and **P2-s**, while E(**s**) and E(**IS**) are the energies associated with the empty surface and the initial state in the gas phase, respectively. The activation energy E_a for the surface reaction is defined as $E_a = E$(**TS-s**) - E(**IS-s**). For the calculation of the reaction energy E_r, it will be assumed that the surface species **P1** and **P2** form adsorption complexes at formally infinite distance, and thus will be calculated as $E_r = [E$(**P1-s**) + E(**P2-s**) - E(**s**)] - E(**IS-s**). This definition neglects that the bond cleavage reaction will first yield an adsorption complex **P1-P2-s,** in which **P1** and **P2** are co-adsorbed in direct vicinity. This intermediate is often neglected, as it is often only a meta-stable, short-lived intermediate that does not affect the reaction kinetics in a significant way. However, in some cases it is desirable to get an overview of the complete potential energy surface. For this purpose, the direct reaction energy $E_{r,d} = E$(**P1-P2-s**) - E(**IS-s**) will be discussed. Following the logic that the direct reaction energy $E_{r,d}$ refers to the minimum states, which are directly connected to the TS, the direct activation barrier $E_{a,d}$ is introduced. $E_{a,d}$ is calculated as the difference between the energy of the transition state and the directly preceding IS state. For a bond dissociation reaction $E_{a,d}$ is equal to E_a.

For the reverse bond formation reaction **P1-s** + **P2-s** → **IS-s** (Figure 10b), E_r and E_a are referred to the **P1-s** and **P2-s** at formally infinite distance, i.e. E_r = E(**IS-s**) - [E(**P1-s**) + E(**P2-s**) - E(**s**)] and $E_a = E$(**TS-s**) - [E(**P1-s**) + E(**P2-s**) - E(**s**)]. At variance, the direct reaction energy and the direct reaction barrier here are defined as $E_{r,d} = E$(**IS-s**) - E(**P1-P2-s**) and $E_{a,d} = E$(**TS-s**) - E(**P1-P2-s**). Note that $E_{a,d}$ is not equal to E_a for a bond formation step.

A special case, which will be encountered in Chapter 4, is the substitution reaction of type **IS-s** + **A-s** → **P-s** + **B-s**, in which a bond formation occurs simultaneously with a bond cleavage (Figure 10c). Such a reaction proceeds via a surface complex **IS-A-s,** in which **IS** and **A** are co-adsorbed. The product of the reaction is a surface complex **P-B-s** with the product species **P** and **B** co-adsorbed. Here the direct reaction energy and the direct barrier are defined as $E_{r,d} = E$(**P-B-s**) - E(**IS-A-s**) and $E_{a,d}$ = E(**TS-s**) - E(**IS-A-s**). At variance, E_r and E_a are calculated as $E_r = E$(**P-s**) + E(**B-s**) - E(**IS-s**) - E(**A-s**) and $E_a = E$(**TS-s**) + [E(**IS-s**) + E(**A-s**) - E(**s**)], respectively.

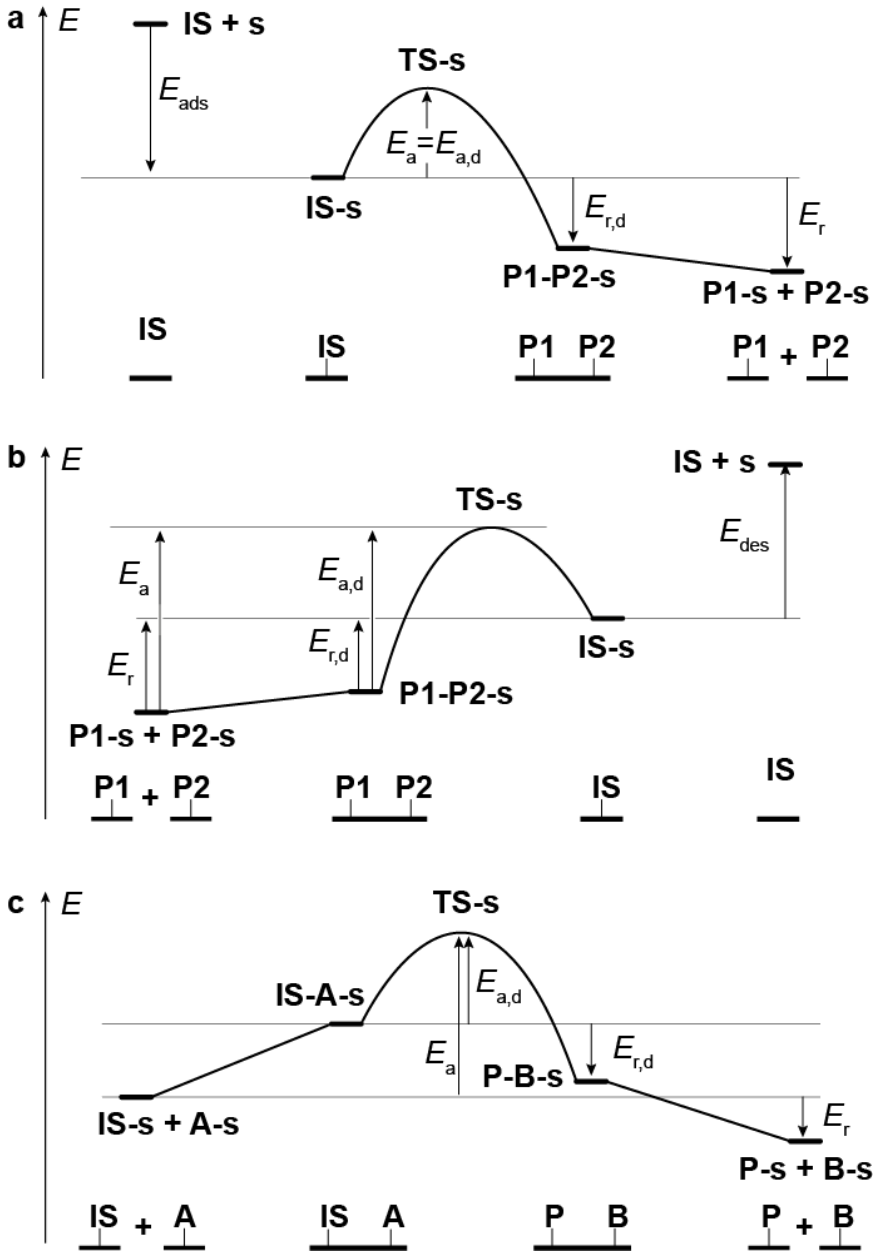

Figure 10: Schematic representation of the definitions for E_r, $E_{r,d}$, E_a, $E_{a,d}$, E_{ads}, and E_{des} for a bond dissociation (a), a bond formation (b), and a substitution reaction (c).

The adsorption energy E_{ads} of a molecule **IS** is defined as $E_{ads} = E(\mathbf{IS\text{-}s}) - E(\mathbf{IS}) - E(\mathbf{s})$, thus a negative values denotes a thermodynamically favorable process. Depending on the context, the desorption energy $E_{des} = - E_{ads}$ will alternatively be reported.

When reaction energies and activation barrier are discussed that depart from the above definition, the definition will be given in the corresponding section.

The corresponding values at the level of enthalpies H and of Gibbs free energies G are defined in analogous fashion.

Chapter 4 Aqueous Phase Processing of 1-Propanol over Pt

4.1. Indroduction

Starting from this chapter, this thesis will focus on the results obtained from computational studies. The first catalytic system to be addressed is the Pt-catalyzed aqueous phase processing of alcohols as modeled by 1-propanol.

Despite of the high material cost, Pt was one of the first metals to be successfully tested for the aqueous phase processing of alcohols.[52] The success of Pt catalysts is partly related to their high selectivity for the reforming path yielding H_2.[52] Depending on the nature of the feed molecule, H_2 selectivities of more than 90% can be achieved,[52] rendering Pt, aside from Pd, one of the most selective catalysts for reforming in the aqueous phase.[22] In addition, Pt was shown to be the catalytically most active monometallic catalyst for reforming.[22]

Yet, there are various experimental studies which also report the formation of alkanes as side products, especially when the reactions run under acidic conditions.[23,52,55,66] Based on experimental studies, an outline of a reaction network for the aqueous phase processes has been proposed (cf. Figure 2 in Chapter 2) which comprises both the reforming pathway and the alkane formation.[52] That reaction network has not been evaluated by quantum chemical calculations. As mentioned in Chapter 2, one of the first computational works dealing with the AP processing of alcohols on Pt addressed the competition between the C-C and the C-O scission of ethanol on Pt(111).[71,72] Furthermore, there are various theoretical studies which focus on the hydrogenation and dehydrogenation of hydrocarbons[145-147,201-203] as well as of organic oxygenates[204,205] over Pt, reflecting the high catalytic activity of Pt for hydrogen transfer reactions. In more recent studies, complete reaction pathways on Pt(111) have been explored computationally, e.g., for glycerol and other polyols.[78,82,91,93] However, many of the mentioned studies feature a certain model character as they do not account, among other things, for the influence of defect sites on the catalyst or the effect of acidic functionalities. These circumstances motivated efforts to clarify, on the example of 1-propanol, the mechanistic details of the Pt-catalyzed aqueous phase processing.[17-21] This chapter presents

results from Ref 21, which contributes to the study of the reaction network of 1-propanol by investigating the effect of stepped defect sites on the energetics of the alkane formation path.

As the present study is based on previous works, a more detailed review on these earlier experimental[16] and theoretical studies[17-21] addressing 1-propanol on Pt will be given in the following subsection.

4.1.1. Previous Studies

Experiments on the aqueous phase processing of 1-propanol over Pt supported on Al_2O_3 have been performed at 473 K and 20 bar total pressure.[16] The analysis of the gas phase and liquid products shows the formation of ethane, propionic acid, CO_2 and propanal. The formation of H_2 has not been analyzed, but its formation can safely be assumed, as the reaction of glycerol under the same reaction conditions leads to the formation of H_2.[16] From the experimentally detected products, a reaction mechanism has been proposed, that starts with the (oxidative) dehydrogenation of 1-propanol to form propanal, which in return disproportionates to propionic acid and 1-propanol.[16] The acid can further decarboxylate to CO_2 and a C_2 fragment, that is fully hydrogenated to form ethane (Figure 11a).

However, there are some issues to be considered. The detection of a formed species and the analysis of the yield as a function of reaction time cannot always prove beyond doubt that an observed species is an intermediate of the main reaction pathway. An observed species may also be a side product that is in equilibrium with an intermediate or the product species. In the present case, the acid may only be a side product, as CO_2 does not necessarily have to be formed via the decarboxylation of propionic acid. A possible alternative pathway for CO_2 formation that is consistent with the experimental observations is the decarbonylation of propanal yielding CO which is subsequently converted to CO_2 in a WGS step as mentioned in

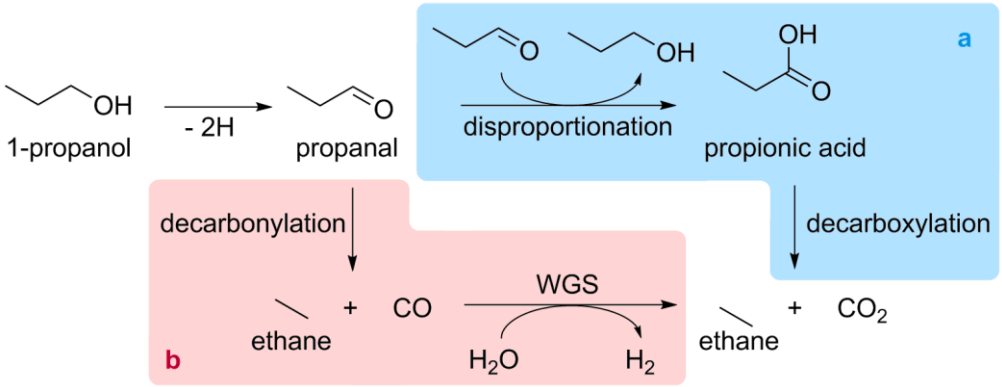

Figure 11: Possible reforming pathways for 1-propanol. a) disproportionation of propanal followed by decarboxylation, b) decarbonylation of propanal followed by a water gas shift reaction (WGS).

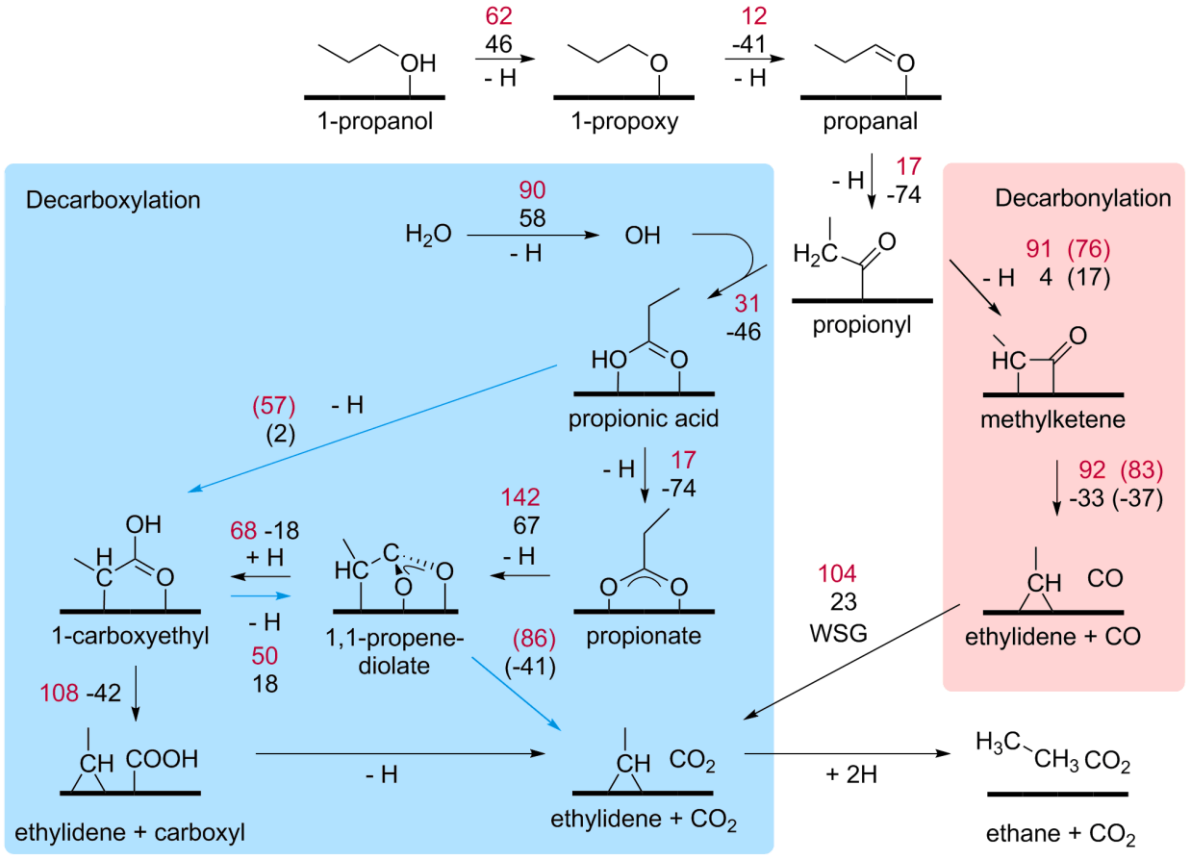

Figure 12: Reaction pathway for 1-propanol reforming over Pt as proposed by Refs 17 and 19. Reaction energies are shown in black, activation barriers in red. Energies referred to the reaction at step sites are shown in parentheses. The decarboxylation mechanism depends on the availability of steps. For the decarboxylation, the black arrows denote the mechanism on a flat Pt surface. Where the presence of steps induces a change in the decarboxylation mechanism, the corresponding reactions are marked by a blue arrow. In favor of a clearer representation, reaction energies and barriers are only shown for the reaction on terrace or for the reaction at step sites, where appropriate. All values in kJ mol^{-1}.

Section 2.2 (Figure 11b).[16]

Computational studies on the reforming pathway as shown in Figure 12 have demonstrated that 1-propanol can dehydrogenate easily on a Pt terrace to form propanal in an overall thermo-neutral process.[17] The highest barrier of 62 kJ mol^{-1} is associated with the dehydrogenation at the OH group.[17] However, the dehydrogenation will most likely not stop at the stage of propanal, as the C-H cleavage yielding the key intermediate propionyl is a strongly exothermic process with a low barrier of only 17 kJ mol^{-1}.[17] After a further dehydrogenation step at α-position, this species can undergo C-C cleavage to form ethylidene and CO.[19] Both steps of the decarbonylation pathway are associated with barriers of around 90 kJ mol^{-1}, if the reaction occurs on terrace sites.[19] An alternative reaction for propionyl is the insertion of a surface OH to yield the experimentally detected[16] species propionic acid.[19]

The OH insertion itself is a kinetically and thermodynamically easily accessible reaction.[19] However, this reaction requires the presence of surface OH groups formed from H_2O scission. Based on computational works using various solvent models,[206-209] the barrier for this endothermic process has been estimated to 90 kJ mol^{-1}.[19] However, note that the energetics of the H_2O scission step, is associated with a significant degree of uncertainty: Depending on the computational model, barriers of up to 130 kJ mol^{-1} have been reported.[207] The actual C-C scission of the acid formed from the OH insertion step, which leads to decarboxylation also proceeds via an α-dehydrogenated intermediate.[19] The highest barrier along this pathway is 142 kJ mol^{-1}, which indicates that on Pt terrace sites, the decarboxylation is less likely than the decarbonylation pathway.[19]

If the reactions are also allowed to proceed at step sites, the highest barrier for the decarbonylation pathway decreases slightly to 83 kJ mol^{-1}, but the mechanism is not changed.[19] At variance, the steps induce small changes to the mechanism of the decarboxylation pathway: While 1-carboxyethyl is the precursor for the decarboxylation step on terrace, CO_2 is formed from 1,1-propene-diolate at step sites, see Figure 12. Furthermore, the steps significantly reduce the highest barrier of the decarboxylation pathway to 86 kJ mol^{-1} only, i.e. even lower than the barrier of 90 kJ mol^{-1} estimated for the scission of a water molecule, which becomes rate-limiting.[19] The results indicate, under the assumption that the estimated energetics for the water scission step is reasonable, that the decarboxylation and the decarbonylation pathways can be considered as equally likely on a (realistic) Pt catalyst containing step sites. The CO formed in the decarbonylation pathway can be converted with water to CO_2 and H_2 in an endothermic water gas shift step that is associated with a barrier of 104 kJ mol^{-1} on Pt(111).[210]

Computational studies on the alkane formation pathway on Pt terrace sites have considered reactions under neutral and acidic conditions.[20,21] It has been shown that the alkane formation under neutral conditions, referred to as the alcohol hydrogenolysis (AH) pathway, is limited by the cleavage of the C-O bond of the alcohol.[20,21] Various mechanisms as shown in Figure 13 have been considered for the C-O cleavage step. The most likely mechanism is the activation of the C-O bond by the exothermic dehydrogenation at C1 (the C bonded to the OH group) followed by the C-O cleavage of the formed 1-hydroxypropyl (mechanism AH-I in Figure 13), consistent with earlier computational works on ethanol on Pt.[71] The corresponding C-O scission step is associated with a barrier E_a of 105 kJ mol^{-1}. This value is lower than the barriers associated with the direct C-O cleavage of propanol (AH-II)

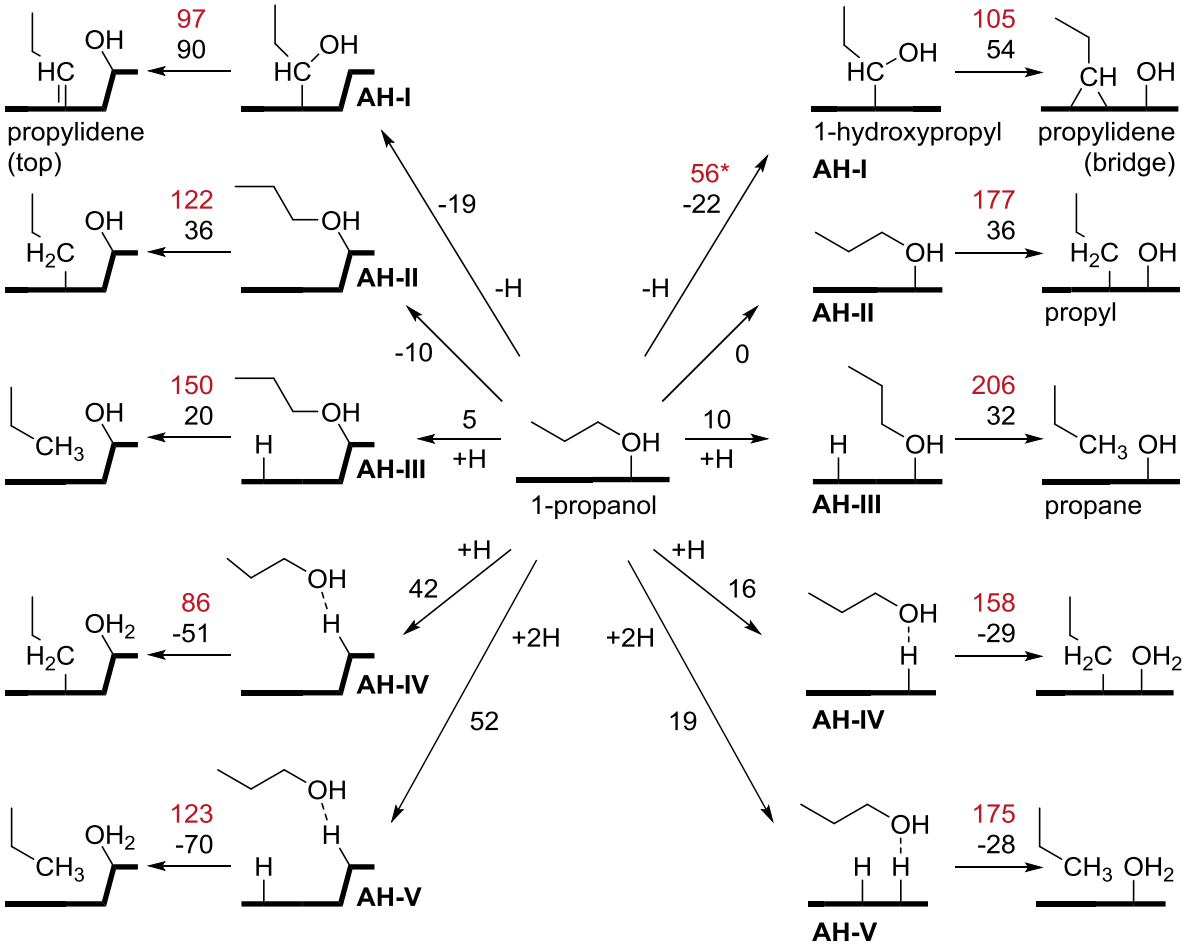

Figure 13: Direct reaction energies (black) and barriers (red) for the C-O cleavage step in the alcohol hydrogenolysis (AH) pathway for the conversion of 1-propanol to propane on terraces and at step sites of a Pt surface. The reaction energy required for the transformation of 1-propanol and H atoms adsorbed at (formally) infinite distance on a Pt(111) surface to those surface complexes, which serve as the ISs for the C-O cleavage steps is also given. Data for the reactions on terrace sites are taken from Refs 20 and 21. The barrier and the energy required for the formation of 1-hydroxyproyl (*) is, differing from the original works, referred to the most stable surface geometry of 1-propanol on Pt(111). The names of the organic substrates are given at the first appearance of a structure. All values in kJ mol^{-1}.

or any hydrogen-assisted mechanism that couples the C-O scission with the hydrogenation at C1 or / and at the O (AH-III to AH-V). Note that the mechanisms AH-III to AH-V can be understood as substitutions reactions, for which the direct barrier $E_{a,d}$ is not identical to E_a (Section 3.4). To account for the strongly differing initial state structures required for the different C-O cleavage mechanisms, $E_{a,d}$ and $E_{r,d}$ will be used for the discussion. The energy required to form the corresponding IS complexes from adsorbed H atoms and the most stable adsorption complex of propanol on a Pt(111) surface is given in Figure 13.

The formation of propane from 1-propanol in the presence of acidic protons follows a different pattern than the AH pathway.[20,21] The C-O bond scission occurs via an acidic

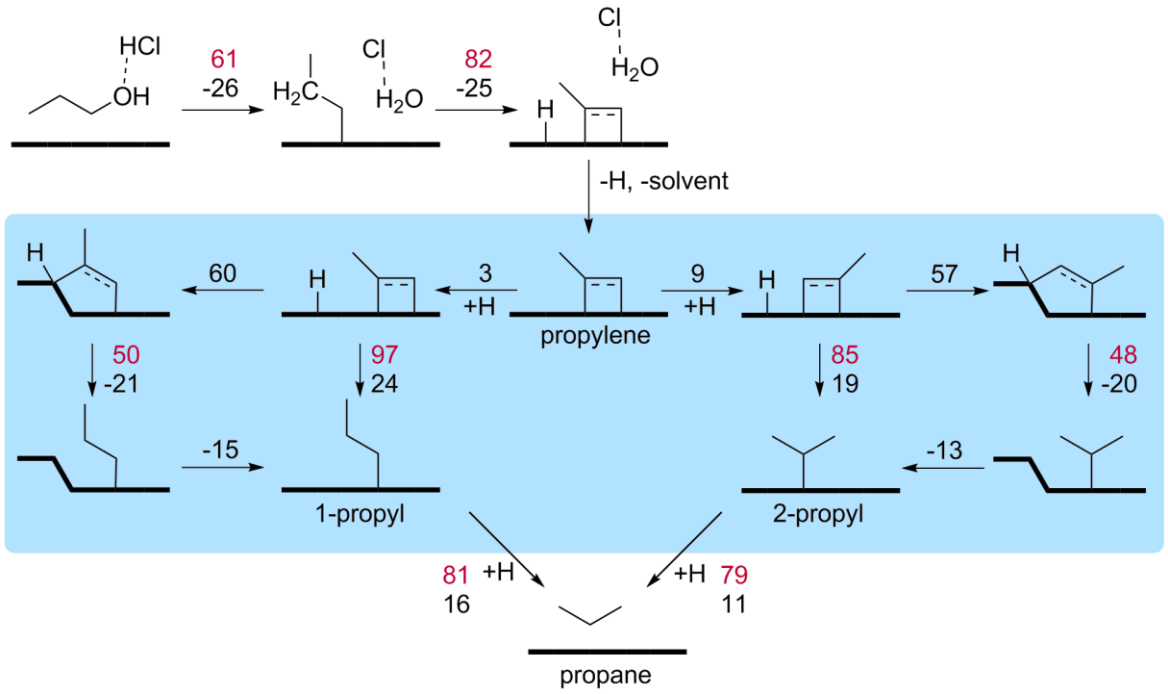

Figure 14: Reaction energies and barriers for the dehydration-hydrogenation (DH) pathway for the conversion of propanol to propylene on Pt. The energetics of the highlighted rate-limiting hydrogenation reaction is illustrated in greater detail. The energies for the formation of the initial state complexes as well as direct reaction energies and direct barriers are shown. Data for the reactions on terrace sites are taken from Refs 20 and 21. All values in kJ mol^{-1}.

dehydration step yielding propylene, which is rehydrogenated to form propane (Figure 14). This mechanism is thus referred as the dehydration–hydrogenation (DH) pathway. Using a simple model for the solvated proton, it has been shown that the highest direct barrier for the dehydration steps is only 82 kJ mol^{-1} on Pt(111).[20,21] At variance, the rehydrogenation of propylene yielding 1-propyl or 2-propyl as intermediates is the rate-limiting step of the DH pathway. The associated direct barriers are 97 kJ mol^{-1} and 85 kJ mol^{-1}.[20,21] The corresponding values for E_a are slightly higher, 100 kJ mol^{-1} and 94 kJ mol^{-1}.[20,21]

4.2. Results and Discussion

4.2.1. Effect of Steps on the Propane Formation Pathway

It is reasonable to study the effect of step sites on the propane formation, in order to achieve comparability with the data on the reforming pathway,[18,19] for which the reactions at Pt step sites have been modeled by a Pt(221) surface. This section will re-evaluate the rate-limiting steps of the AH pathway and of the DH pathway at step sites. The results from modeling the Pt-catalyzed C-O cleavage steps as well as the hydrogenation of propylene on a Pt(221) surface are presented below.

4.2.1.1. C-O Cleavage of the Alcohol-Hydrogenolysis Pathway

All C-O cleavage mechanisms (AH-I to AH-V) which have been considered for the reaction on the Pt terrace site,[20,21] have been re-evaluated with the stepped surface. For C-O cleavage of 1-propanol at step sites (AH-II to AH-V) it is assumed that the hydroxyl group interacts with a Pt atom at the step edge or with an H atom adsorbed at the step edge, as schematically shown in Figure 13. In case of AH-I, the IS for the C-O scission is a 1-hydroxypropyl moiety adsorbed on a top site at the lower terrace of the step; the OH group of the adsorbate is pointing to the step edge with a Pt-O distance of 270 pm (Figure 15). All IS geometries at step sites are chosen such that the C-O cleavage reaction yields an oxygen functionality (water or hydroxyl) at the step edge and a carbon-moiety (propylidene, propyl or propane) at the lower terrace of the step site (Figure 13).

An overview of the energetics for the C-O cleavage at Pt step sites is provided in Figure 13. The comparison with the reactions on terrace shows that the influence of the steps differs from mechanism to mechanism. The IS complexes at step sites for the C-O cleavage according to the mechanisms AH-I to AH-III are of similar stability with their counterparts at the terrace site. In contrast, the IS complexes at step sites for the pathways AH-IV and AH-V,

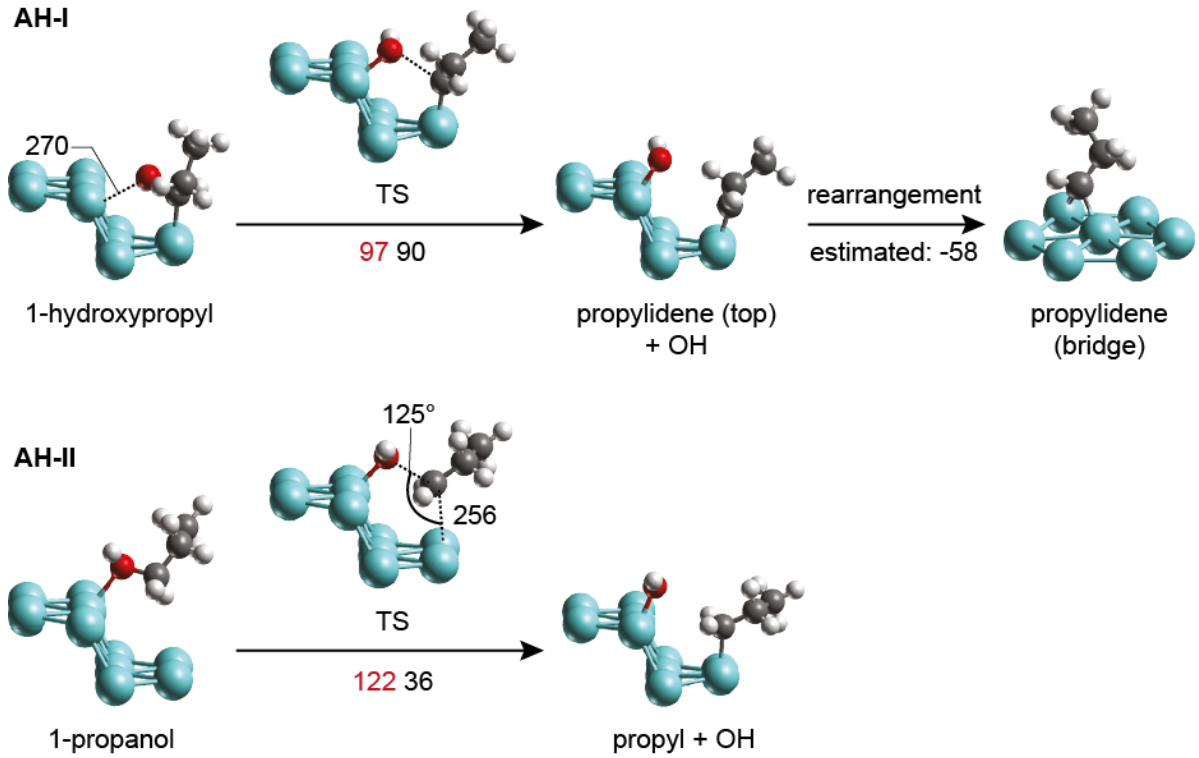

Figure 15: Stationary point structures involved in the C-O cleavage at Pt step sites according to the mechanisms AH-I and AH-II. The stabilizing rearrangement of top adsorbed propylidene to a bridge site is also shown. The direct reaction energies $E_{r,d}$ (black) and the direct barriers $E_{a,d}$ (red) are given in kJ mol^{-1}. Where appropriate, interatomic distances (pm) and bond angles (degree) are shown. Black: C, red: O, white: H, cyan: Pt.

in which the propanol molecule interacts with a H at the step edge, are significantly less stable, by > 26 kJ mol^{-1}, than the corresponding structures on a Pt terrace.

The comparison of the direct barriers for the C-O cleavage reactions as displayed in Figure 13 shows that the presence of steps decreases the direct barriers $E_{a,d}$ in all cases. While the direct barrier for the C-O scission according to AH-I is lowered by only 8 kJ mol^{-1} upon introducing step sites, the barrier reducing effect of the steps on the mechanisms AH-II to AH-V is in the range between 52 kJ mol^{-1} and 77 kJ mol^{-1}. At variance to AH-I, the organic adsorbate in the ISs of the latter four mechanisms interact only via the OH group with the surface or with H centers on the surface. During the reaction, the carbon group forms a new bond with the Pt surface or with H atoms on the surface. The strong reduction of the direct barriers for the reactions AH-II to AH-V at steps compared to the corresponding reactions on terrace sites will be rationalized here on the example of AH-II. The corresponding TS structure (Figure 15) features a C-Pt distance of 256 pm and an O-C-Pt angle of 125°. At variance, values of 260 pm and 81° have been reported for the corresponding TS structure on the Pt terrace.[21] In view of the shorter C-Pt distance at the step site, the ethyl moiety interacts stronger with the Pt surface than in the corresponding TS on a terrace. The interaction with the Pt surface is expected to have a stabilizing effect on the ethyl moiety, as its C1 center is under-coordinated if it would not interact with the metal catalyst. The C-O cleavage step discussed here can be understood as a (nucleophilic) substitution reaction at the reactant 1-propanol. Within this interpretation, the OH group may be understood as the leaving group that is replaced by a bond to the Pt surface, which acts as a nucleophile. For electronic reasons, the nucleophile typically attacks a reactant from the "back side", i.e. opposite to the direction in which the leaving group is pointing.[211] For the reactions under study, the O-C-Pt angle introduced here can be used as an indicator whether reactions proceed as a substitution from the back side. A O-C-Pt angle smaller than 90°, as found in the terrace site TS structure, indicates that the Pt surface attacks from the same side in which the OH group is directed. An O-C-Pt angle > 90°, as found in the TS at the steps, indicates the preferred "back-side approach" of the Pt surface, which rationalizes the lower C-O cleavage barrier for the reaction at the step site.

The situation for the C-O scission in AH-I differs from to the reaction mechanisms AH-II to AH-V. In AH-I the presence of the steps results in a changed geometry of the C-O cleavage product. As schematically depicted in Figure 13, the reaction on a terrace yields propylidene adsorbed on a bridge site. At variance, the reaction at the step yields top

adsorbed propylidene as an intermediate, which is significantly less stable than the conformer at the bridge site.[20] This results in the relatively endothermic $E_{r,d}$ value of 90 kJ mol^{-1} for the C-O cleavage in mechanism AH-I at a step site. Note that the $E_{r,d}$ value represents a lower limit for the direct barrier $E_{a,d}$. Due to this, the barrier $E_{a,d}$ the C-O cleavage step in AH-I is only reduced by 8 kJ mol^{-1} from 105 kJ mol^{-1} for the reaction on the terrace to 97 kJ mol^{-1} for the reaction at step sites, close to the lower limit of 90 kJ mol^{-1}.

At the Pt step site, there are only two AH mechanisms that involve direct barriers for the C-O cleavage that are below 100 kJ mol^{-1}, AH-I and AH-IV. The other mechanisms can be ruled out as the main AH pathway, due to their high barriers (Figure 13). Although the hydrogen assisted C-O cleavage mechanism at a step site according to mechanism AH-IV features the lowest C-O cleavage barrier of all AH type mechanisms under study, only 86 kJ mol^{-1}, this reaction is not likely to be the most preferred C-O cleavage mechanism under neutral conditions. The formation of the IS complex required for this mechanism is rather endothermic, E_r = 42 kJ mol^{-1}, which is a major obstacle for this mechanism. At variance, the formation of 1-hydroxypropyl at a Pt step site, the IS complex required for the mechanism AH-I, is an exothermic process. Thus, similar to the situation at terrace sites, AH-I is considered the most likely AH type mechanism at Pt step sites. The previously mentioned endothermicity of the C-O cleavage step in the step site variant of AH-I is most likely not a problem. Calculations on a Pt(111) surface showed that the unstable top adsorbed propylidene, as formed in the AH-I mechanism at the steps, can easily rearrange to form the more stable bridge site complex of propylidene, a process that stabilizes the C-O cleavage products by approximately 60 kJ mol^{-1}.[21]

In summary, C-O cleavage on Pt under neutral conditions will proceed via the mechanism AH-I. The effect of the steps on the barrier height is relatively small in this case, less than 10 kJ mol^{-1}. The preference for a mechanism that involves a dehydrogenation step may rationalize, why alkane formation is hardly observed in the aqueous phase processing of oxygenates over Pt, even if high H_2 pressure is applied.[53,66] The overall process to form an alkane and water from an alcohol requires H_2 and thus should benefit from high H_2 pressure. However, the high H_2 pressure will hinder the dehydrogenation step yielding 1-hydroxypropyl, which is essential for the C-O cleavage under neutral conditions.

4.2.1.2. Propylene Hydrogenation in the Acidic Dehydration-Hydrogenation Pathway

This section will discuss the hydrogenation of propylene to yield 1-propyl and 2-propyl at the Pt(221) step site. As seen from Figure 14, both reactions feature comparable energetics. Therefore, this section will mainly discuss the process on the example of the reaction yielding 2-propyl, which is the slightly favored reaction pathway on a Pt terrace. The reactions yielding 1-propyl is only addressed if it shows significant differences to the 2-propyl pathway.

Previous works gave reason to assume that the high barrier for the reaction on terraces may be partly related to the weak interaction between the carbon center to be hydrogenated and the Pt surface.[20,21] This is particularly pronounced for the TS of the hydrogenation at the central propylene C, for which a C-Pt distance of 321 pm has been calculated.[20] One may expect that Pt centers at a convex step edge can interact better with the adsorbate at the TS than metal centers of a close-packed terrace do. This circumstance should induce a lower barrier for the hydrogenation reaction at step sites. To study the effect of the corrugated surface structure, it is assumed that propylene is adsorbed in a di-σ fashion at the step site; one C atom of the (formal) olefinic double bond is bound to a top site at the step edge, while the other C center of the double bond interacts with a top site on the terrace, as shown exemplarily for the reaction to yield 2-propyl (Figure 16). The effect of the concave step edge described above should only play a role if the hydrogenation occurs at the C center at the step edge. At variance, the hydrogenation of the terrace site C center is expected to resemble the reaction on the Pt(111) surface, due to the similarity in the local geometry. Thus the hydrogenation at the C center at the terrace site is not considered in this work. For the hydrogenation at a step edge, two ISs are required when exploring the hydrogenation at C1 and at C2 of propylene. In the propylene absorption complex for the reaction yielding 2-propyl (Figure 16), the methyl group of propylene is at the C center on the terrace site. At variance, the methyl group is required to be at the C center at the step edge, when considering the hydrogenation step to yield 1-propyl, as schematically illustrated in Figure 14. Transferring a propylene molecule from a Pt terrace to form a step site complex as shown in Figure 16 is by 41 kJ mol^{-1} endothermic. This is partly related to the substrate structure in the step site complex. On a terrace, the C-C-Ru angles are 110° and 105°, comparable to the tetrahedral angle of 109.5° that is typically found for four-fold coordinated carbon centers (Figure 16). The coordination of propylene to the Pt step site induces significantly larger C-C-Ru angles of 115° and 124° (Figure 16). This atypical adsorbate geometry likely

destabilizes the complexes at step sites.

The hydrogenation at the step edge as considered is this study requires an IS in which a hydrogen atom is co-adsorbed with the propylene at a step edge. The optimized IS structures for the reactions yielding 1-propyl and 2-propyl both feature a H atom that is adsorbed to the same step edge Pt atom, to which the propylene C atom is also bound (Figure 16). Note that in the analogue ISs for the reactions on Pt(111), the H atom and the C atoms of propylene are adsorbed at different Pt atoms (Figure 16). It was not possible to identify stable structures at terrace sites in which the H and a C center of propylene adsorb at the same Pt center. Figure 16 illustrates the formation of the IS complexes for the hydrogenation step on Pt(111) and at the Pt(221) step site as a process in which the propylene molecule is initially adsorbed at a terrace site and at a step site, respectively. An H center adsorbed on a terrace site at formally infinite distance is then transferred to the direct vicinity of the propylene to form the IS complexes. While this process is endothermic only by 9 kJ mol^{-1} at a terrace, the analogous process at the step site is endothermic by 24 kJ mol^{-1}. The stronger endothermicity at the steps is related to the co-adsorption of the H and the C center at the same Pt atom.

The direct barrier $E_{a,d}$ and the reaction energy $E_{r,d}$ for the formation of 2-propyl starting from the IS described above are 48 kJ mol^{-1} and -20 kJ mol^{-1} (Figure 16). Very similar values

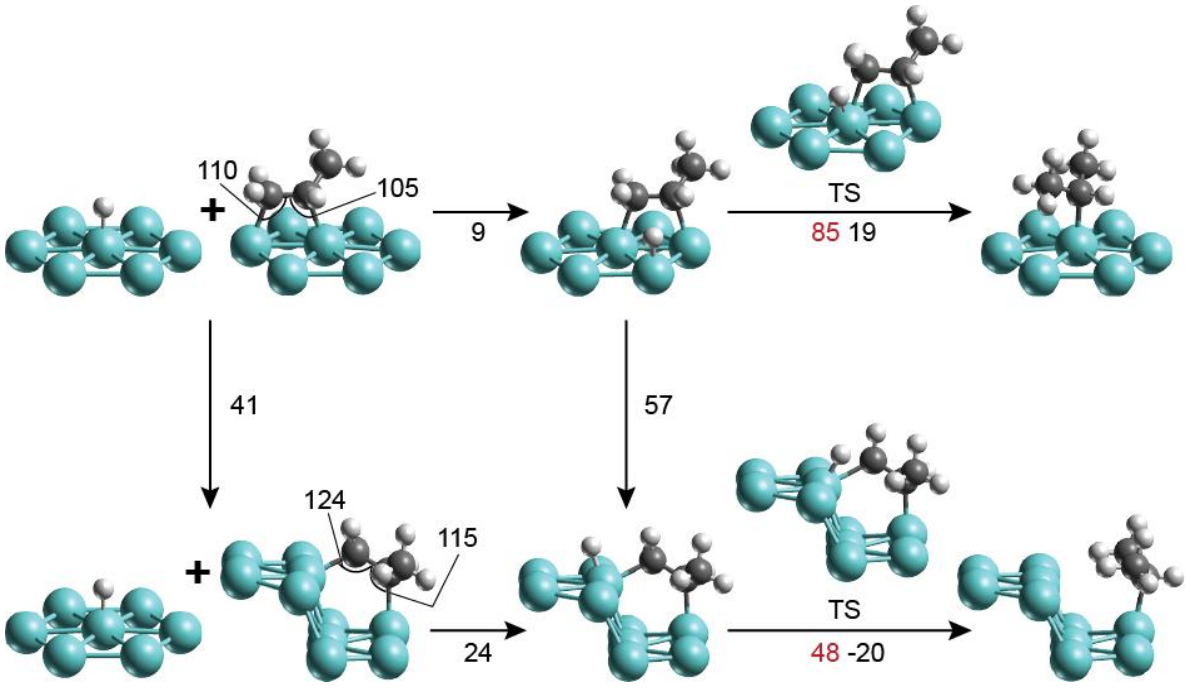

Figure 16: Structures of stationary points involved in the hydrogenation of propylene to form 2-propyl on Pt terrace and step sites. The direct reaction energies $E_{r,d}$ (black) and the direct barriers $E_{a,d}$ (red) are given in kJ mol^{-1}. Where appropriate, the C-C-Pt angle is given in degree. Black: C, white: H, cyan: Pt.

are calculated for the hydrogenation to yield 1-propylene, 50 kJ mol^{-1} and -21 kJ mol^{-1}, respectively (Figure 14). The presence of the steps obviously decreases the barriers for the hydrogenation of propylene, which were computed to be 85 kJ mol^{-1} (yielding 2-propyl) and 97 kJ mol^{-1} (1-propyl) on Pt(111).[20,21] However, the lower barrier at the steps is partly related to the fact that the ISs for the reactions at step sites are energetically less stable than the corresponding IS structures on a terrace (Figure 14). This also rationalizes why the hydrogenation step on a terrace is endothermic but exothermic at the step edge. Therefore, it is difficult to determine ultimately whether steps have a noticeable effect on the overall rate for the DH pathway. This issue has been left open here because it does not affect the interpretation of the total reaction network as the next section will show. However, it seems worthwhile to address questions regarding the DH pathway by future kinetic modeling.

4.3. Conclusion

The study of the formation of propane from 1-propanol on Pt shows that the effect of steps varies strongly from reaction to reaction. At step sites, the various C-O cleavage steps in an AH type mechanism feature direct barriers that are by up to 72 kJ mol^{-1} lower than the corresponding barriers of reactions at terrace sites. However, the effect on the barrier for the most likely AH pathway, AH-I, which proceeds via 1-hydroxypropyl as intermediate, is rather weak. While the C-O cleavage of 1-hydroxypropyl on Pt(111) is 105 kJ mol^{-1}, the presence of the steps reduces the barrier to only 97 kJ mol^{-1}. The AH mechanism thus is only slightly facilitated by the step sites.

In the case of the acid-catalyzed dehydration-hydrogenation, the situation is less clear, how the presence of steps affects the overall kinetics of that reaction pathway. The direct barrier of the hydrogenation of propylene, which is rate determining if the reaction occurs on terraces sites, decreases from 85 kJ mol^{-1} (reaction yielding 2-propyl) and 97 kJ mol^{-1} (1-propyl) to 48 kJ mol^{-1} and 50 kJ mol^{-1}, respectively, when the reaction can occur at step sites. However the hydrogenation reaction at step sites also involves energetically high lying IS complexes which are less stable than the corresponding structures on terrace sites. Thus the presence of the steps induces counter acting effects. To determine ultimately the impact of step sites on the overall reaction rate of the DH mechanism, a modeling of the kinetics, e.g. by micro-kinetic simulations, seems to be necessary.

Although some details of the kinetics of the DH mechanism are not completely understood, an interpretation of the overall reaction network for the AP processing of 1-propanol is still possible. Under neutral reaction conditions, the two possible reactions for

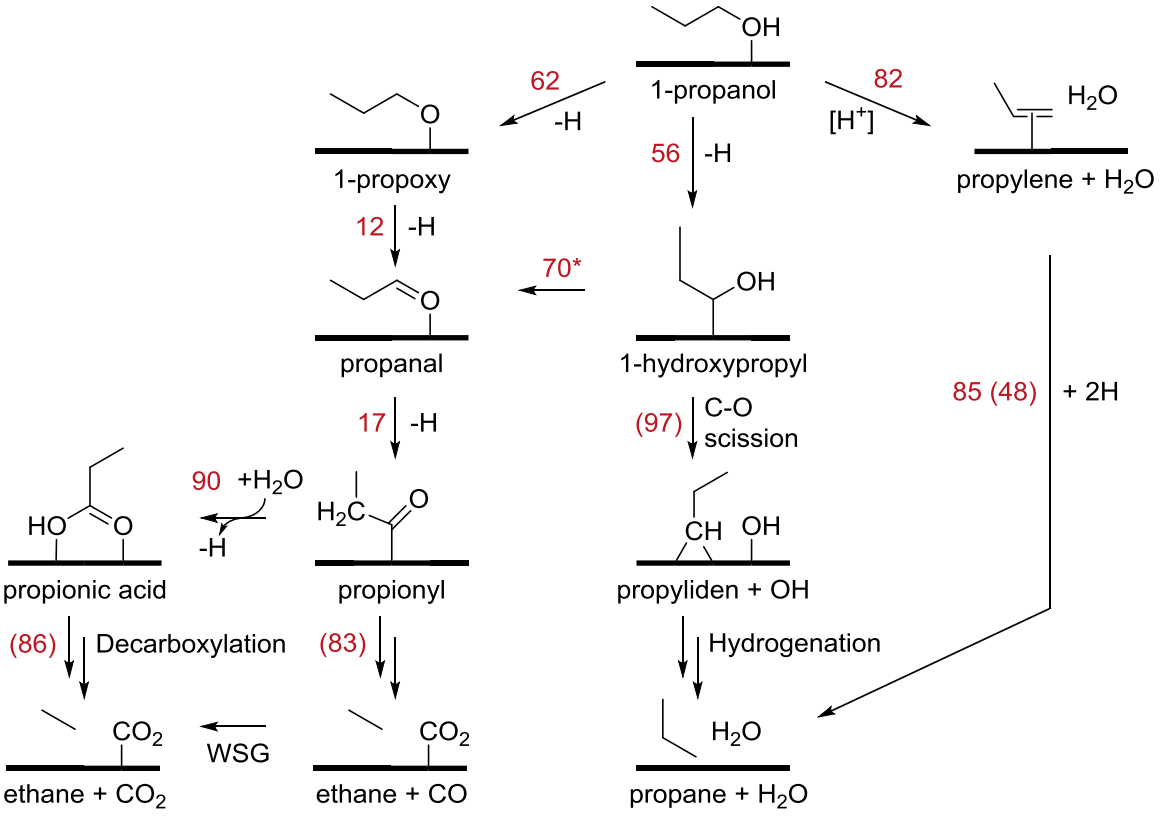

Figure 17: Overview on the reaction network involved in the aqueous phase processing of 1-propanol over Pt. Relevant barrier heights in kJ mol^{-1} are shown as red numbers. Barriers for reactions at step sites are shown in parenthesis to distinguish them from barrier calculated for reactions at terrace sites. The barrier for the dehydrogenation of 1-hydroxypropyl (*) is estimated from the barrier for the analogous reaction of 1-hydroxymethyl. [H^+] marks the presence of acidic protons which act as a catalyst.

1-propanol are the dehydrogenation at O with a barrier of 62 kJ mol^{-1} and the dehydrogenation at C1 with a barrier of 56 kJ mol^{-1} (Figure 17). While the former reaction leads to the formation of surface propoxy that is only associated with the reforming pathway, the latter reaction yields 1-hydroxypropyl. From this latter intermediate the system may take the AH pathway, resulting in a C-O cleavage at Pt step sites with a barrier of 97 kJ mol^{-1}. However, the more likely reaction of 1-hydroxypropyl is a further dehydrogenation at C1 to yield propanal, also an intermediate on the reforming pathway (Figure 17). Based on the data for the reaction of hydroxymethyl,[205] the barrier for this dehydrogenation step is estimated to be 70 kJ mol^{-1}, i.e. significantly lower than the barrier for the competing C-O cleavage. Therefore, under neutral conditions, the reaction is directed towards the reforming route. Under acidic conditions, a third reaction is possible for 1-propanol, the acidic dehydration which has a barrier of 82 kJ mol^{-1} (Figure 17). The acidic dehydration is kinetically less favored than the initial dehydrogenation steps of the reforming pathway. Once the hydrogen

at the hydroxyl group of 1-propanol is removed, the acidic dehydrogenation mechanism is not possible any more. Thus, the computational results indicate, even under acidic conditions, the preferred path for 1-propanol processing over Pt is the reforming path, consistent with experiments.[23,55,56]

Chapter 5 Decomposition of Ethanol over Ru

5.1. Introduction

After having presented the reactions of alcohols on a late and weakly oxophilic transition metal, such as Pt, this chapter will turn to the reaction of alcohols over more oxophilic metals, such as Ru,[212] which is found further left in the periodic table of elements. This chapter follows the presentation of the results in Ref 213.

As elaborated in Section 2.1, a more oxophilic catalyst may be expected to favor the C-O cleavage, which is associated with the alkane formation pathway, over the C-C cleavage that is related to the reforming pathway. In fact, experiments on the catalytic processing of alcohols over Ru have reported high selectivity for the production of alkanes.[22,23] Although the formation of alkanes can be rationalized with the argument above, the mechanism at the molecular level for the Ru-catalyzed reaction is yet to be explored. It has been suggested that oxygenates decompose to H_2 and CO / CO_2 in a first step.[23,52] Afterwards, alkanes are formed from them via a Fischer-Tropsch (FT) like mechanism,[23,52] for which Ru is known to be an active catalyst.[214] However, such a mechanism requires the cleavage of the C≡O triple bond, which is substantially more difficult to break than a C-O single bond as found in alcohols, a typical feedstock for the aqueous phase processes. Thus, is seems reasonable to ask whether a mechanism is possible or even likely, in which the C-O bond is directly cleaved before an alcohol decomposes to CO or CO_2. After all, it has been reported for various metals including Ru that hydrogenated or alkylated CO species have lower C-O scission barriers than carbon monoxide.[73,215-219]

Due to the importance of Ru for FT synthesis, various reactions on Ru, which are also relevant for the aqueous phase processing of organic oxygenates, have been studied computationally, e.g. the C-O cleavage of CO and species derived from CO hydrogenation,[219,220] (de)hydrogenation of CO and C_1 species,[219,221-224] and the coupling of C_1 species.[225] However, a systematical study of the reaction pathways of oxygenates over Ru has been lacking so far.

Table 2: Geometric characteristics and adsorption energies E_{ads} (kJ mol^{-1}) of various adsorption complexes[a] on Ru(0001).

Species		adsorption geometry	E_{ads}	Species	adsorption geometry	E_{ads}
CH_3CH_2OH	**1**	O-top	-39	CH_3CH_2	hollow	-170
CH_3CH_2O	**2**	O-hollow	-272	CH_3CH	hcp	-397
CH_3CHOH	**3**	O-top, C1-hollow	-169	CH_2CH_2	C1-hollow, C2-top	-92
CH_2CH_2OH	**4**	O-top, C2-bridge	-208	CH_3C	hcp	-579
CH_3CHO	**5**	O-bridge, C1-top	-70	CH_2CH	C1-hcp, C2-top	-318
CH_3COH	**6**	O-top, C1-hollow	-261	CH_2C	C1-hcp, C2-top	-451
CH_2CH_2O	**7**	O-bridge, C2-top	-149	CHCH	C1,C2 –hollow	-266
CH_2CHOH	**8**	O-top, CC-π	-86	CHC	C1-hcp, C2-fcc	-565
CH_3CO	**9**	O,C1-top	-233	CH_2OH	O-top, C-bridge	-189
CH_2CHO	**10**	O-top, CC-π	-238	CH_2O	O-bridge, C-top	-102
CH_2COH	**11**	O-top, CC-π	-297	CHOH	O-top, C-bridge	-301
CHCHOH	**12**	O,C1-top, C2-hollow	-327	CHO	O,C-top	-245
CH_2CO	**13**	O,C2-top, C1-hollow	-150	COH	hcp	-455
CHCHO	**14**	O-top, C2-bridge	-461	CO	top	-172
CHCO	**15**	O-top, C1,C2-hollow	-352	CH_3	hollow	-210
CCO	**16**	C2-hcp	-547	CH_2	hcp	-430
				CH	hcp	-671
				C	hcp	-730
				OH	hollow	-342
				O	hcp	-603

[a] Designators as introduced in Section 5.2 are shown for the species of formula $CH_kCH_lOH_m$.

The study in the present chapter explores the reaction pathways of organic oxygenates on Ru catalysts as modeled by the flat Ru(0001) surface. A focus is placed on the competition between the C-O and C-C scission. Ethanol, the smallest alcohol that contains a C-O and a C-C bond is chosen as a model for organic oxygenates. Reaction barriers E_a and reaction energies E_r as defined in Section 3.4 have been evaluated for the scission of C-O, C-C, O-H, and C-H bonds of ethanol and various intermediates derived by dehydrogenation of the alcohol.

5.2. Nomenclature

This chapter deals with reactions of adsorption complexes formed by species described by the general formula $CH_kCH_lOH_m$. (k = 0–3; l = 0–2; m = 0,1). The adsorption complexes under study will be denoted by labels **1** to **16** as shown in Table 2. No designators have been assigned to species, which are only considered as bond cleavage products. Labels of the form **x-y** refer to reactions in which a species **x** is dehydrogenated to yield the product **y**. C-O and

C-C scissions for a given species **x** are referred to as **x-CO** and **x-CC**, respectively. The TS structures associated with the reactions will be denoted as **TSx-y**, **TSx-CO**, and **TSx-CC**, respectively.

When addressing the C atoms in species of type $CH_kCH_lOH_m$, the C atom bonded to the oxygen functionality will be referred to, according to IUPAC rules, as C1, the other C center as C2. For carbonaceous adsorbates CH_kCH_l without any oxygen, C1 denotes the C center carrying fewer H atoms.

5.3. Results and Discussion

This section starts with discussing the structures of the adsorption complexes on the Ru(0001) surface. Afterwards, the reactions for the surface structures and the corresponding energetics will be presented. Based on these results the decomposition pathways of ethanol on a Ru terrace will be evaluated.

5.3.1. Adsorption Geometries

Table 2 gives a brief overview of the geometries of the surface complexes under study. The discussion in this section will focus on structural motifs for various typical functional groups, rather than discussing the adsorption geometries of all species studied. Figure 18 shows the optimized structure of the adsorption complexes considered here.

R-O(H), OH, O. The surface complexes of ethanol **1** and ethoxy **2** are prototypical structures when considering the adsorption modes of species with hydroxyl groups and alkoxy groups, respectively, as the hydrocarbon moieties of the two adsorbates are fully saturated and do not interact with the Ru surface. Hydroxyl groups as in alcohols adsorb on top sites of Ru(0001), similar to the situation on the close-packed surfaces of Pt and Pd.[17,71,75] Top adsorption is determined for R-OH groups of almost all species listed in Table 2. However, if the hydrocarbon moiety R is not saturated, deformation of the top adsorbed geometry around the OH group may occur to allow better interaction between the moiety R and the Ru surface. This can be for instance seen from the Ru-O-C1 angles of the adsorption complexes **1**, **3**, **8**, **9**, and **11** (Figure 18). In **1**, the adsorption complex of ethanol, this angle is 123°, but in those complexes where the adsorbates are singly (e.g. **3**, **8**) or doubly dehydrogenated at C1 (e.g. **9**, **11**), the corresponding angle is at most 96°. Furthermore, the Ru-O bonds in **3**, **8**, **9**, and **11** are tilted from the surface normal by 25–30°. At variance, the Ru-O bond in **1** is nearly parallel to the surface normal, tilted by 3° only. These distortions in the structures **3**, **8**, **9**, and **11** indicate the presence of structural strain in the four-member rings formed by O, C1 and two of the coordinating Ru atoms. The C-O bonds in **3** and **9**,

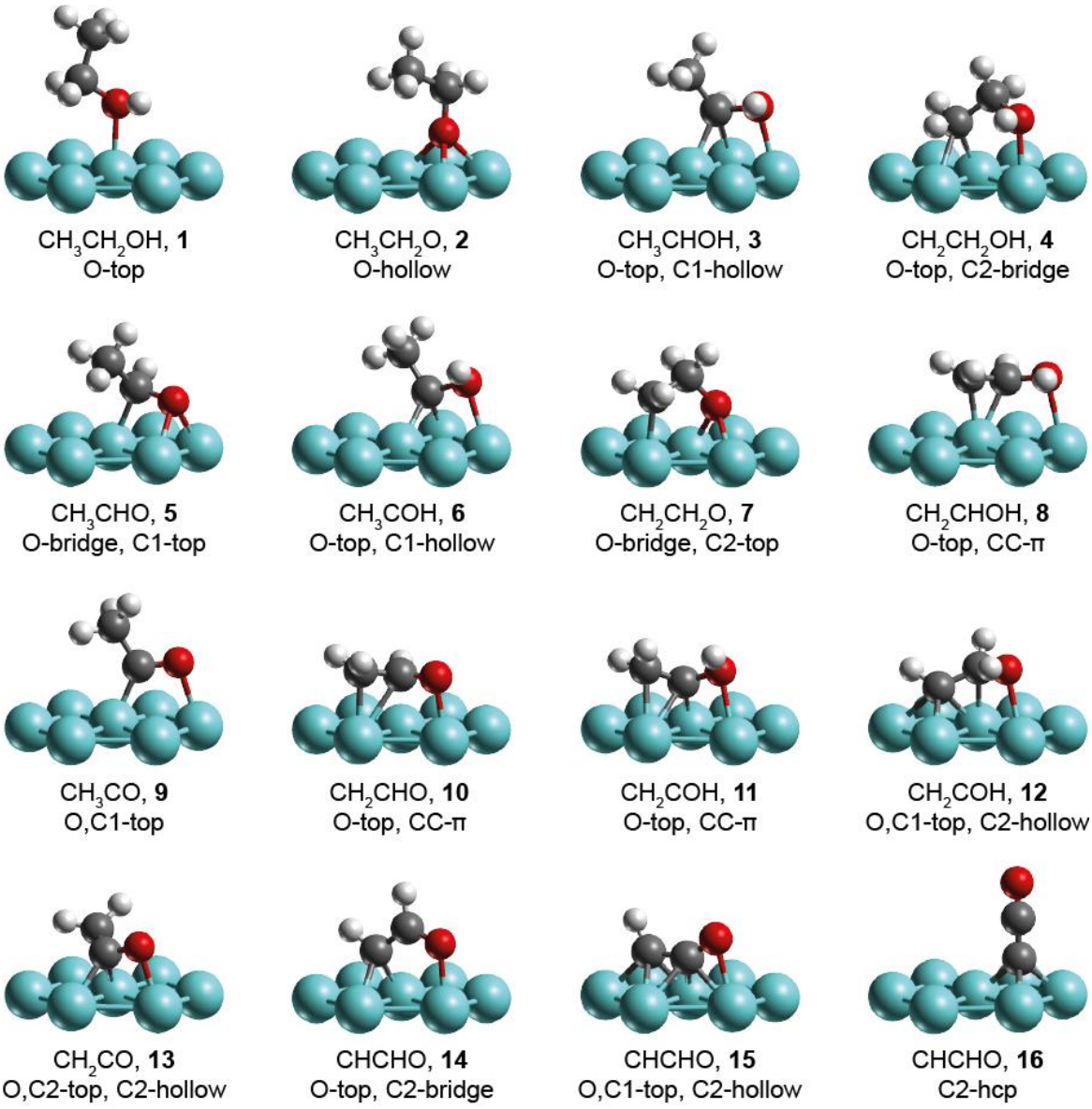

Figure 18: Optimized structures of various adsorption complexes on Ru(0001); see Table 2. Black: C, red: O, white: H, cyan: Ru.

structures with adsorbates dehydrogenated at C1 only, are 2 pm longer than in the surface complex of ethanol **1** which has been calculated at 146 pm. This elongation of the C-O bond may also be related to structural strain. The situation in the adsorption complexes **8** and **11**, which feature adsorbates dehydrogenated at C1 and C2, is slightly different. The C-O bonds in **8** and **11** are 142 pm, i.e. 4 pm shorter than in **1**. This finding is similar to the situation for species in the gas phase: the shorter C-O bond in **8** and **11** is related to the presence of a C=C double bond geminal to the OH group.[71] The adsorption complex **4**, which contains an adsorbate that is dehydrogenated at C2 only, exhibits a Ru-O-C1 angle of 114°, i.e. an angle that is larger than the ones in **3**, **8**, **9**, and **11.** The Ru-O bond is tilted from the surface normal

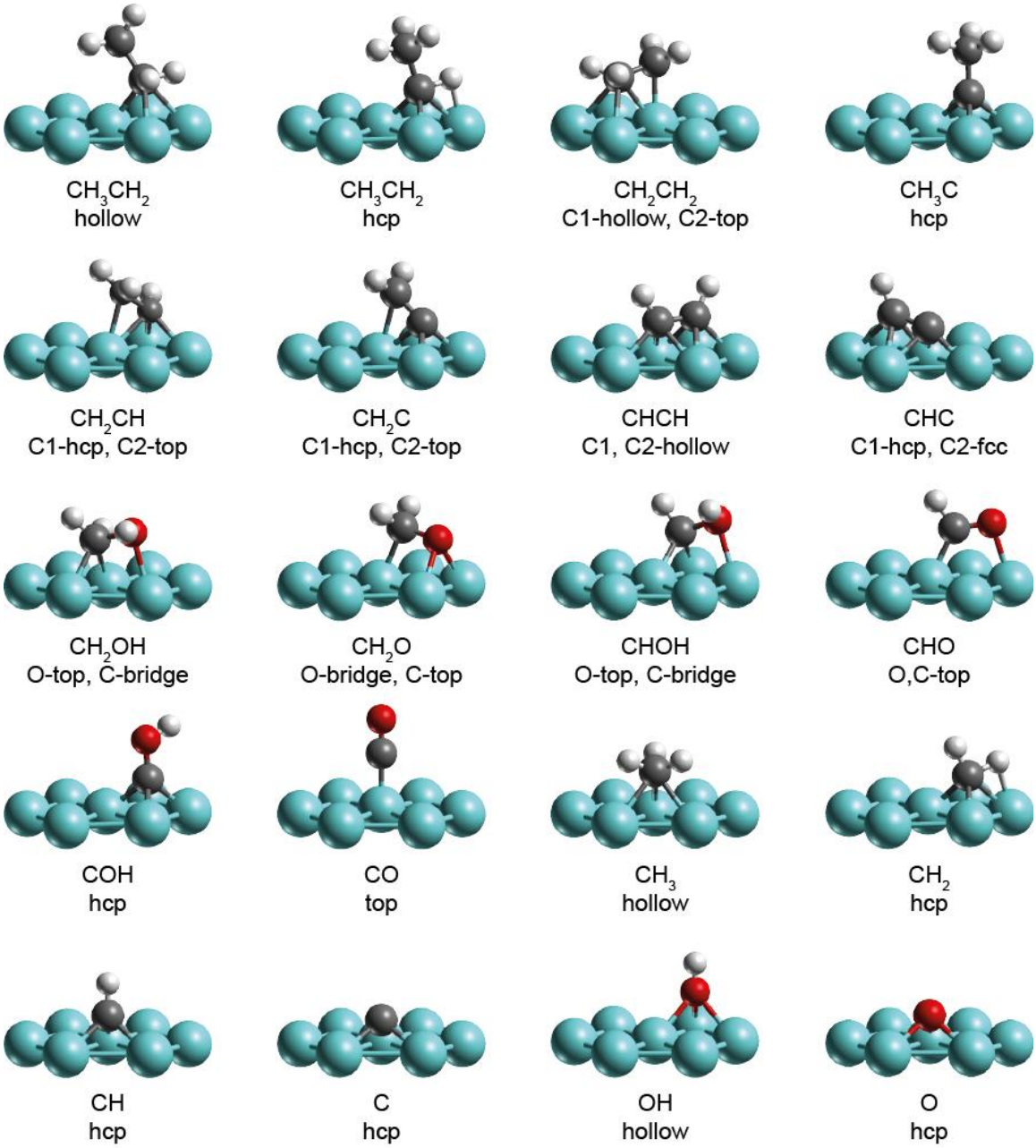

Figure 18 (continued)

by 3° only, similar to the situation of ethanol. Apparently, five-member ring structures as in **4** are less prone to distortion and steric stress than four-member rings.

In the adsorption complex of ethoxy **2**, the adsorbate is bound via the O center to a hollow site on Ru(0001), similar to the structure of methoxy on the (111) facet of Pd clusters.[73] However, the site preference of ethoxy on Ru(0001) differs from analogous adsorption complexes of ethoxy or propoxy on Pt(111) and Pd(111) surfaces which are reported to favor top sites.[17,71,75] Not all alkoxy groups prefer hollow sites on Ru(0001); for example, structure **7**, the adsorption complex of CH_2CH_2O, features an oxa-metalla-cycle

with the O center at a bridge site. R-O species with an unsaturated C1 center will be discussed separately below as species featuring a carbonyl group. Similar to alkoxy groups, isolated O centers and surface hydroxyl groups are also adsorbed at hollow sites. Note that only in case of the isolated O centers, there is a strong preference for hcp sites over fcc sites, by $\Delta E_{ads} = E_{ads}(fcc) - E_{ads}(hcp) = 34$ kJ mol^{-1}.

R-CH$_k$ (R = CH$_3$ or H; k = 0–2) and C. The interaction of carbon moieties with the Ru surface can be explored on the example of alkyl, alkylidene, alkylidyne groups and an isolated C atom. In the most stable adsorption complexes of all these species, the adsorbate is located at a hollow site. This leads to C coordination numbers (CN) of up to 6 for alkyl groups, different to the situation on the late transition metals Pt, Pd, Rh, Ni, on which the CN for carbon centers does not exceed 4.[203,226,227] While R-CH$_2$ complexes on fcc and hcp sites of Ru(0001) are of comparable stability [$\Delta E_{ads} = E_{ads}(fcc) - E_{ads}$ (hcp) < 10 kJ mol^{-1}], complexes at hcp sites become thermodynamically more favored with decreasing number of hydrogen atoms at C1 of the adsorbate, consistent with the results of earlier studies on hydrocarbons on Ru.[221] For the series of the surface C$_1$ species CH$_3$ to C, the ΔE_{ads} values as defined above increases with the number of H atoms in the adsorbate, from -7, to 15, 38, and 63 kJ mol^{-1}.

Other species of the type C$_2$H$_x$. At variance with the adsorbate structures addressed in the preceding paragraph, which only feature one unsaturated C center, the present paragraph addresses those species C$_2$H$_x$, which exhibit two unsaturated C centers. In other words, both C atoms of the structures under study are able to form C-Ru bonds. In the adsorption complexes of all C$_2$H$_x$ species discussed here, there is at least one C center that adsorbs at a hollow site, similar to alkyl, alkylidene and alkylidyne discussed above. The most stable surface complex of ethylene, CH$_2$CH$_2$, has one C center at a hollow site and the other C at a top site ("C1-hollow, C2-top"). A complex adsorbed in di-σ fashion, which is reported to be the most stable structure for ethylene on Pd and Pt,[203,227-229] has not been identified on Ru(0001). The "C1-hollow, C2-top" adsorption geometry is favored for all species of the formula CH$_2$CH$_k$ (k = 0–2). For k < 2, the more strongly dehydrogenated C1 center occupies the hollow site, while the C2 center of the methylene group interacts with the top site, consistent with earlier studies.[225] Similar to the situation of the C$_1$ species in the preceding paragraph, the C1 center of CH$_2$CH$_k$ (k = 0, 1) prefers hcp over fcc sites. At variance, for the adsorption complexes of the less strongly dehydrogenated species ethylene (k = 2) in "C1-hollow, C2-top" geometry, the nature of the hollow site, i.e. fcc type or hcp type, only has an weak impact on the stability of the structure.

In the adsorption complexes of acetylene (CHCH) and ethinyl (CHC), one C center adsorbs at an hcp and the other one at the neighboring fcc site ("C1-hcp, C2-fcc"). In case of the asymmetric adsorbate ethinyl, the most stable structure features the completely dehydrogenated C1 center at the hcp and C2 at the fcc site, consistent with the previously determined preference of strongly dehydrogenated C centers for the hcp site.

R-C=O. Carbonyl groups are usually described as C=O double bonds, as justified by the calculated C-O bond length of 122 pm for ethanal in the gas phase. In contrast, most adsorption complexes with a carbonyl group have longer C-O bonds, > 124 pm, indicating a somewhat activated double bond character. The carbonyl moiety can adsorb over a hollow site, with the C center at a top site and the O center at a bridge site formed by the other two neighboring metal atoms, as for instance visible in structure **5**, the surface complex of ethanal. Depending on the interaction of the C2 center with the surface, the carbonyl C1 center may be shifted towards the top or the hollow site, or even lifted from the surface as in **14**, the adsorption complex of CHCHO. Furthermore, C1 and O of the carbonyl group can also both adsorb at top sites, as seen in the adsorption complexes of acetyl (CH_3CO, **9**) or formyl (HCO).

5.3.2. Reaction Energies

Having discussed the adsorption geometries, this section turns to the reaction energies E_r of the various reactions as shown in Table 3. In addition, the reaction energies of the C-O and C-C cleavage reactions are compared in Figure 19.

Dehydrogenation. The calculations show that the dehydrogenation reactions at the carbon moiety can be divided into two groups. In one group, the carbon moiety of the IS is a saturated ethyl group (**1-3**, **1-4**, **2-5** and **2-7**). These reactions are endothermic or thermo-neutral. The other group of reactions, consisting of all other C-H dehydrogenation steps, involves IS structures that feature at least one unsaturated carbon center. These reactions are all exothermic. The difference between the two groups of reactions is related to the fact that partially strained four- or five-member metalla rings, respectively, are formed upon dehydrogenation at the saturated ethyl group (**1-3**, **1-4**, **2-5** and **2-7**) as discussed for the R-OH species in Section 5.3.1. At variance, there are already ring structures in the initial states of the other C-H cleavage reactions as the unsaturated C centers are already bonded to the Ru surface, so the dehydrogenation at these structures does not introduce significantly more structural strain.

In contrast to dehydrogenation reactions at C centers, all O-H bond scissions studied are

Table 3: Reaction energies E_r and barriers E_a (kJ mol^{-1}) for C-O cleavage, C-C cleavage, C-H cleavage at C1 and C2 as well as the dehydrogenation reactions at the OH group under study.

Initial state	C-O			C-C			O-H			C1-H			C2-H		
		E_r	E_a		E_r	E_a		E_r	E_a		E_r	E_a		E_r	E_a
CH_3CH_2OH	**1-CO**	-32	167	**1-CC**	24	255	**1-2**	-58	69	**1-3**	0	91	**1-4**	3	77
CH_3CH_2O	**2-CO**	-42	136	**2-CC**	41	236				**2-5**	11	77	**2-7**	33	94
CH_3CHOH	**3-CO**	-71	55	**3-CC**	5	135	**3-5**	-48	66	**3-6**	-26	35	**3-8**	-23	29
CH_2CH_2OH	**4-CO**	-67	80	**4-CC**	7	127	**4-7**	-28	68	**4-8**	-25	39			
CH_3CHO	**5-CO**	-91	80	**5-CC**	-3	103				**5-9**	-55	12	**5-10**	-35	32
CH_3COH	**6-CO**	-110	33	**6-CC**	-56	92	**6-9**	-76	43				**6-11**	-20	53
CH_2CH_2O	**7-CO**	-107	43	**7-CC**	-6	101									
CH_2CHOH	**8-CO**	-68	70	**8-CC**	11	72									
CH_3CO	**9-CO**	-101	94	**9-CC**	-52	102							**9-13**	-3	58
CH_2COH	**11-CO**	-85	66	**11-CC**	-50	92									
CHCHOH	**12-CO**	-77	63	**12-CC**	-3	59									
CH_2CO	**13-CO**	-94	103	**13-CC**	-64	38							**13-15**	-25	72
CHCHO	**14-CO**	-99	45	**14-CC**	-14	104									
CHCO	**15-CO**	-68	152	**15-CC**	-90	40									
CCO				**16-CC**	-39	57									

exothermic, by up to -76 kJ mol^{-1} (Table 3). However, O-H cleavage on Ru does not seem to be exothermic in general. For instance, dehydrogenation at the OH group of methanol on a Ru_8 cluster has been reported to be endothermic with a reaction enthalpy of 46 kJ mol^{-1}.[69] At variance, the analogous reaction for ethanol **1-2** presented here is of exothermic character, E_r = -58 kJ mol^{-1}.

C-O cleavage. All C-O cleavage reactions under study are calculated to be exothermic (Table 3), which reflects the oxophilic nature of Ru.[212] With the exception of the C-O scission for ethanol and ethoxy (**1-CO** and **2-CO**), all reactions are strongly exothermic, by at least -67 kJ mol^{-1}. Thus, C-O bonds, once broken, are unlikely to be re-formed on the Ru(0001) surface. Although still exothermic, the C-O scission reactions of **1** and **2** are thermodynamically less favored than the corresponding reactions of other intermediates, similar to the situation of C-H dehydrogenation reactions. Different from the present findings for reactions on Ru, C-O cleavage on close-packed surfaces of the less oxophilic metals Pd and Pt were calculated to be endothermic in most cases.[71,73]

C-C cleavage. Exothermic C-C cleavage reactions (**x-CC** with **x** = **6**, **9**, **11**, **13**, **15**, **16**), with E_r values ranging from -39 kJ mol^{-1} to -90 kJ mol^{-1}, all start from an IS with a fully dehydrogenated C1 center and yield CO or C-OH as product. These are the only COH_x

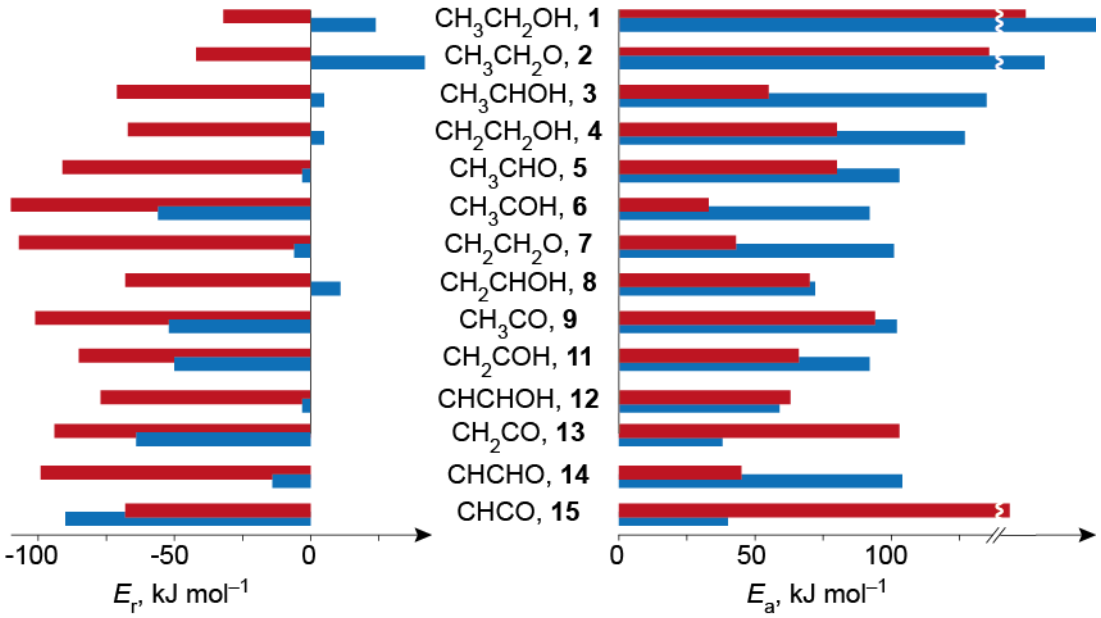

Figure 19: Reaction energies E_r and activation barriers E_a for the C-O (red) and C-C cleavage reactions (blue) under study. Numerical values are given in Table 3.

fragments where solely the C center, but not the O center is interacting with the Ru surface. Clearly endothermic C-C bond breaking steps are only associated with the surface complexes **1** and **2**, which have a saturated adsorbate. These species are generally rather unreactive as corroborated by the fact that the C-O cleavage and dehydrogenation reactions for these two species are also less exothermic than analogous reactions of other intermediates. The other C-C cleavage reactions not addressed so far, are associated with E_r values between -14 kJ mol^{-1} and 11 kJ mol^{-1}. Thus these reactions can be considered as approximately thermo-neutral. They are characterized by moderately dehydrogenated C centers in the IS.

For all intermediates considered (except CHCO **15**), C-O cleavage is thermodynamically favored over the C-C scission, by at least 31 kJ mol^{-1} (Figure 19). For **15**, C-C cleavage was calculated by 21 kJ mol^{-1} more exothermic than the competing C-O bond scission. This exception may be related to the formation of two very stable species upon C-C cleavage, CO and methine, the most stable CH_k species on Ru(0001).[221]

5.3.3. Reaction Barriers

Dehydrogenation. Earlier studies on the dehydrogenation of alkanes on Ru have shown that the first dehydrogenation step is associated with a high barrier, while the majority of the succeeding dehydrogenation steps are kinetically easier accessible.[222,223] The current study reveals that this also holds for the C-H dehydrogenation of alcohols. The dehydrogenation reactions at the saturated ethyl group in the adsorption complexes of ethanol **1** and ethoxy **2**

have barriers in the range of 77–94 kJ mol^{-1}. At variance, breaking the C-H bonds in the structures **3**, **4**, and **5**, which involve singly and doubly dehydrogenated adsorbates, required significantly lower activation energies, 12–39 kJ mol^{-1}. However, for adsorption complexes, which feature an adsorbate with a completely dehydrogenated C1, e.g. the surface complexes of hydroxyethylidene **6**, acetyl **9**, and ketene **13**, higher C-H dehydrogenation barriers are determined, between 53 kJ mol^{-1} and 72 kJ mol^{-1}. This finding is comparable to the situation of ethylene transformation on Pd, Pt, Rh, and Ni, where high dehydrogenation barriers were calculated for the reactions of CH_kC species that have one completely dehydrogenated C center.[226,227,229]

The dehydrogenation at the hydroxyl group has been studied for the species **1**, **3**, **4** and **6**, i.e. adsorbed ethanol and structures that can be derived by dehydrogenating the ethyl group of ethanol up to two times. The E_a values for these O-H cleavage reactions fall into a rather narrow range, indicating that the barrier heights depend only weakly on the number of H atoms in the carbon moiety. The O-H scission barrier for the singly dehydrogenated species **3** and **4** are determined to be 66 kJ mol^{-1} and 68 kJ mol^{-1}, respectively, in good agreement with the corresponding value for reaction **1-2,** the dehydrogenation of ethanol to yield ethoxy, 68 kJ mol^{-1}. Only reaction **6-9**, dehydrogenation of 1-hydroxyethylidene yielding acetyl, has a lower barrier, 43 kJ mol^{-1}, compared to the other O-H dehydrogenations under study. This finding may be related to the somewhat stronger exothermicity of this reaction, E_r = -74 kJ mol^{-1}, compared to the other O-H cleavage reactions studied here, which feature E_r values between -28 kJ mol^{-1} and -58 kJ mol^{-1}.

C-O cleavage. Due to the important role of the C-O cleavage (and of the C-C cleavage discussed below) for the selectivity of biomass processing as mentioned in Section 2.1,[12,23-25] the C-O cleavage will be discussed in more detail than it is done for the dehydrogenation steps above. To establish trends for the C-O cleavage barriers, it seems appropriate to search for common structural features in the IS and TS structures of reactions with comparable barriers. Features of interest are (*i*) whether the atoms in the ISs are saturated, (*ii*) the lengths of the C-O bond as an indicator for its bond order, and (*iii*) distances between the metal surface and the adsorbate(s) in the TS geometry. The distances described in (*iii*) can be used to identify molecular moieties in the TS structures that are well separated from the Ru surface, and hence do not interact with the surface. By doing so, one may rationalize the instability of certain TS structures and the high barrier for the corresponding reactions.

It will be demonstrated in the following that C-O cleavage reactions are only accessible,

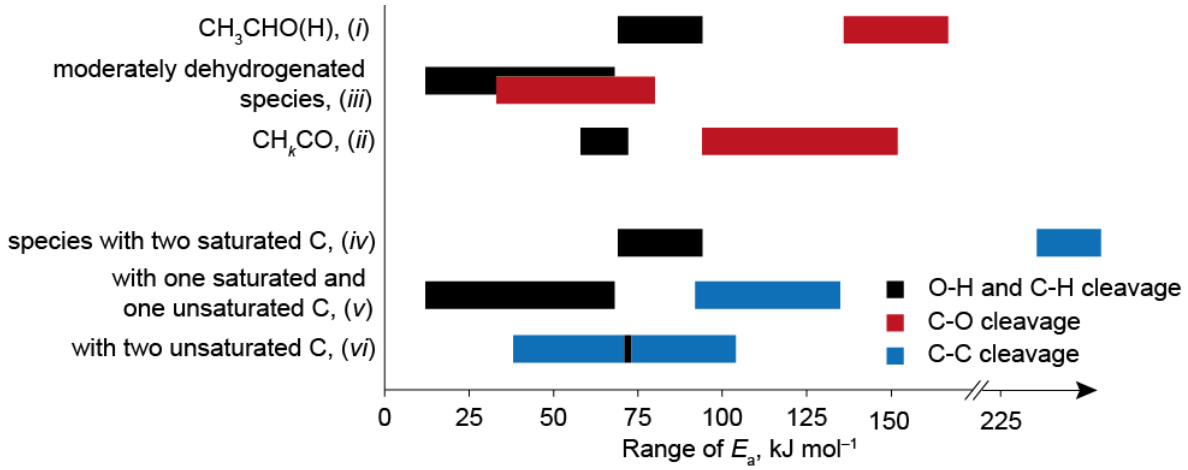

Figure 20: Ranges of reaction barriers E_a associated with the C-O cleavage [(*i*)–(*iii*), red] and the C-C cleavage reactions [(*iv*)–(*vi*), blue] for different types of ISs. The classification of the reactions is introduced in Section 5.3.3. Note that the C-O cleavage reactions have been sorted by the decreasing hydrogen content in the ISs. For comparison, the range of the barriers associated with the competing dehydrogenation reactions in shown in black.

if the adsorbate in the IS has at least one unsaturated C center. It shall further be illustrated that there is a correlation between the formal bond order of the C-O bond and the barrier for its cleavage. The latter effect is especially pronounced for the reactivity of the highly dehydrogenated species of the type CH_kCO, k = 3–1.

The C-O cleavage steps under study can be separated into three classes based on their ISs. There are reactions starting from (*i*) species that feature an adsorbate with a saturated carbon moiety, i.e. the surface complexes of ethanol **1** or ethoxy **2**. These reactions have high barriers of at least 136 kJ mol^{-1}, see Figure 20. A second group of C-O cleavage reactions (*ii*) features strongly dehydrogenated IS species with an adsorbate of type CH_kCO, k = 3–1. In other words, the C1 and O centers in the ISs are completely dehydrogenated as in the structures **9**, **13**, and **15**. The C-O scission reactions of these species also have high barriers, ranging from 94 kJ mol^{-1} to 152 kJ mol^{-1} (Figure 20). The last group of C-O scission reactions (*iii*) contains the reactions of all other species under study. The corresponding IS structures all feature at least one unsaturated C center. The barriers associated with the reactions of group (*iii*) are at most 80 kJ mol^{-1}, i.e. lower than the barriers for reactions of groups (*i*) and (*ii*), see Figure 20. The lowest barrier for a C-O cleavage step under study is 33 kJ mol^{-1} and is calculated for the C-O scission of surface hydroxyethylidene, CH_3COH **6**, a reaction from group (*iii*).

Analyzing the TSs of C-O cleavage, one notes that the kinetically accessible reactions of group (*iii*) are characterized by TS structures, which feature C-Ru distances of less than

~240 pm. Therefore, the carbonaceous fragment is close enough to the Ru surface to interact with it in the TS. In contrast, long C-Ru distances, over 265 pm, are found in the TS structures associated with the kinetically inaccessible reactions of group (*i*): **TS1-CO** and **TS2-CO**. As group (*i*) is characterized by reactants with saturated C centers, it seems likely that the presence of unsaturated C centers, as found in the IS of the reactions of group (*iii*), is a prerequisite for accessible C-O cleavage barriers. However, the barrier heights do not correlate with the numbers of removed H atoms, as shown by the high barriers of the reactions of group (*ii*), i.e. by the C-O cleavage of strongly dehydrogenated species.

In the following, the C-O bond lengths in ISs containing unsaturated C1 centers shall be compared. The C-O bond distance in the ISs roughly increases with the increasing number of H atoms at the C1-O moiety hence with the decrease of the formal C-O bond order. This can be illustrated on the example of the C-O distances in the adsorption complexes of CH_3CO **9**, 128 pm, CH_3CHO **5**, 135 pm, and CH_3CHOH **3**, 148 pm. The barriers for the C-O cleavage of these three intermediates rise with the formal bond order: E_a(**3-CO**) = 55 kJ mol^{-1}, E_a(**5-CO**) = 80 kJ mol^{-1}, and E_a(**9-CO**) = 94 kJ mol^{-1}. The correlation between increasing C-O bond order and increasing activation barriers is also in line with the rather high barriers for reactions of group (*ii*), E_a > 94 kJ mol^{-1}. Recall that the ISs of these latter reactions are characterized by a fully dehydrogenated C1-O moiety and thus feature a formal C-O bond order of 2, the highest value for intermediates considered in this study. A similar correlation between bond orders and cleavage barriers has been reported for the catalytic dissociation of CO and O_2;[215-218,230] these reactions are kinetically less favorable than the corresponding reactions of hydrogenated CO and O_2, respectively.

C-C cleavage. Similar to the discussion of C-O scission above, a (qualitative) correlation between the saturation of the carbon moieties and the C-C cleavage barriers will be discussed here. Based on the ISs, C-C scission reactions can also be classified in three groups, distinguishing reactions with ISs (*iv*) where both C centers are saturated (**1-CC**, **2-CC**; E_a > 200 kJ mol^{-1}); (*v*) where only one C center is saturated (**x-CC**, **x** = **3**–**7**, **9**; E_a from 92 kJ mol^{-1} to 135 kJ mol^{-1}); and (*vi*) where both C centers are unsaturated (**x-CC**, **x** = **8**, **11**–**16**; E_a between 38 kJ mol^{-1} and 104 kJ mol^{-1}). This classification reflects that the C-C cleavage barriers roughly decrease with the increasing number of dehydrogenated C-centers in the IS structure, Figure 20. A similar relation between the number of H atoms and the reaction barrier has been reported for the C-C coupling of CH_k species; the highest barriers were calculated for coupling steps involving methyl.[231]

The C-Ru distances of C-C scission TSs have also been analyzed in analogy to the investigation of the C-O cleavage. In reactions involving a substrate with unsaturated C centers, groups (*v*) and (*vi*), C-Ru distances of 240 pm or shorter are calculated, indicating that the C centers are bound or almost bound to the Ru surface. In contrast, C1-Ru distances larger than 250 pm are determined only in the TSs associated with group (*iv*), **TS1-CC** and **TS2-CC**. Similar to the situation for C-O cleavage reactions, the longest C-Ru distances in the TS structures are associated with reactions featuring the highest C-C cleavage barriers. In contrast to the C-O bond lengths, the C-C distances in the IS structures do not change significantly when the number of H atoms of the adsorbate is varied, as long as the number of unsaturated C atoms remains constant. For IS structures that have one or two fully saturated C centers, i.e. ISs for the reactions of groups (*iv*) or (*v*), C-C distances of 151±1 pm are calculated. In intermediates dehydrogenated at both C centers, i.e. ISs of group (*vi*) reactions, one finds C-C = 142±1 pm with the exception of surface adsorbed CCO **16**, where C-C = 133 pm. Therefore, different from the situation of C-O cleavages, low C-C bond breaking barriers are associated with IS structures with *shorter* C-C bonds.

It has been shown above that the C-C cleavage barriers decrease with the degree of saturation (going along with shorter C-C bonds in ISs). A similar trend has also been reported for the C-C scission of symmetric species described by the formula CH_kCH_k, k = 0–2, on Pd(111).[227] Summing up for the C-C scission, C-C barrier heights correlate best with the number of unsaturated C centers, whereas, different from C-O cleavage reactions, the barrier heights of C-C scission do not even roughly correlate with the C-C bond distance in the ISs.

For most intermediates, the C-C cleavage barrier is comparable or higher than the competing C-O scission barrier (Figure 19). Only for the highly dehydrogenated species **13** and **15** is C-C cleavage clearly kinetically favored over C-O bond breaking. The preference of the C-C scission over the C-O cleavage in **13** and **15** is related to two trends discussed above: (*i*) C-O cleavage barriers increase with dehydrogenation at the C1-O moiety, and (*ii*) C-C scission barriers decrease with increasing number of unsaturated C centers in the IS.

5.3.4. Reaction Pathways

With the energetics of the individual reactions steps discussed in the preceding sections, the most likely reaction pathways can be derived by following the reactions with the lowest barrier for each intermediate. This most likely path leads to the formation of ketene, which is a precursor for the C-C scission to yield CO and methylene. In addition, the lowest path that

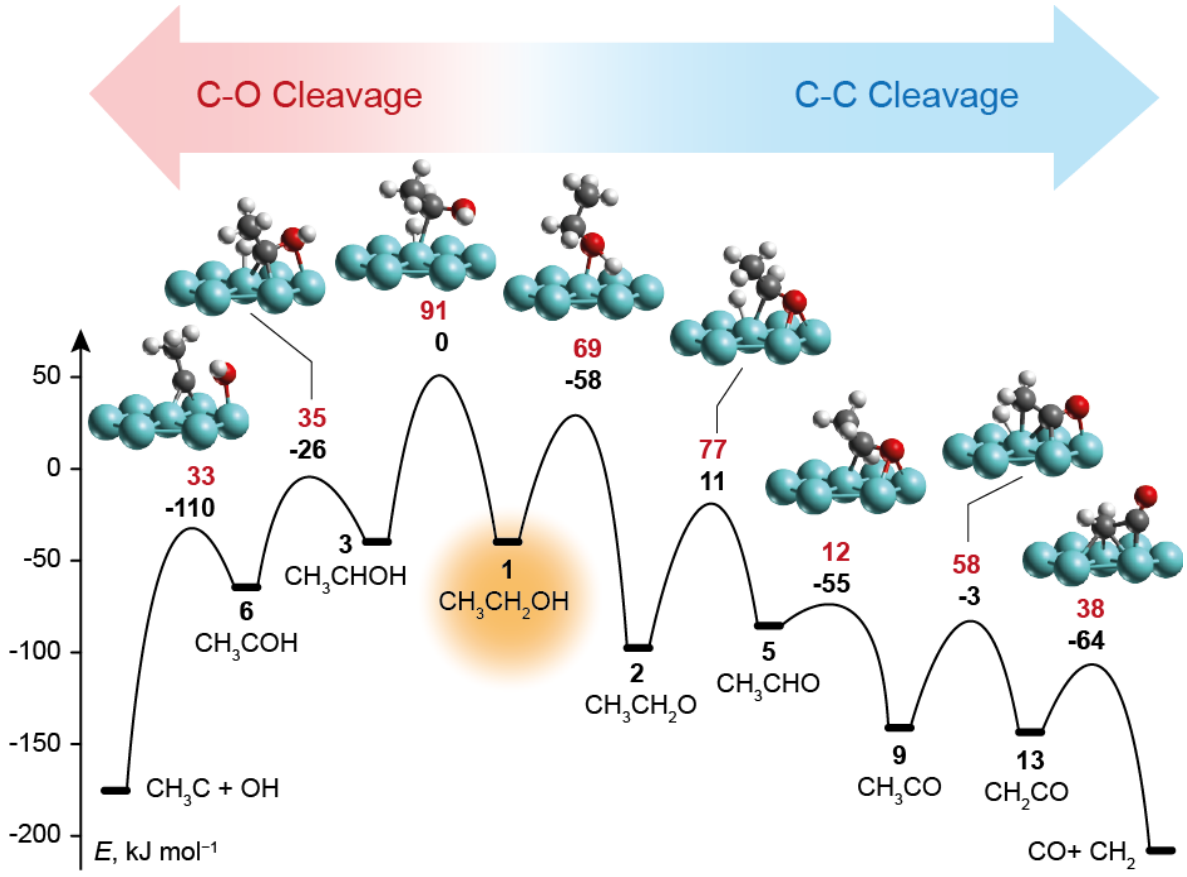

Figure 21: Energy profile for the most likely pathways leading to C-C cleavage and to C-O cleavage, respectively. The bars represent minimum structures, arcs stand for TSs. The numbers at the arcs denote the reaction barriers E_a (red) and reaction energies E_r (black), in kJ mol^{-1}. All energies are referenced to ethanol in the gas phase and a clean Ru(0001) surface. TS structures of the involved reactions are also shown. Black: C, red: O, white: H, cyan: Ru.

leads to C-O cleavage will be addressed. Both pathways are illustrated in Figure 21.

Most likely pathway. The reaction pathway starts with the adsorption complex of ethanol **1**, for which only dehydrogenation steps are likely to occur. The competing C-C and C-O cleavage reactions are associated with barriers that are by at least 76 kJ mol^{-1} higher than the highest dehydrogenation barrier, 91 kJ mol^{-1} for reaction **1-3**. The thermodynamically and kinetically most favored reaction of **1** is the dehydrogenation **1-2** at O to yield ethoxy, E_r = -58 kJ mol^{-1} and E_a = 69 kJ mol^{-1}. The most likely reactions for adsorbed ethoxy **2** is also a dehydrogenation step, the reaction **2-5** at C1 with E_a = 77 kJ mol^{-1} that yields ethanal in a weakly endothermic process.

The C-O and C-C cleavage barriers for adsorbed ethanal **5** are 80 kJ mol^{-1} and 103 kJ mol^{-1}, respectively. Thus, for the first time along this reaction route, either step may be considered kinetically accessible. C-O cleavage **5-CO** yielding ethylidene and O is a

strongly exothermic process, E_r = -91 kJ mol^{-1}, thermodynamically favored over all possible dehydrogenation reactions of **5**, for which E_r have been determined to be -55 kJ mol^{-1} or less exothermic. However, neither the C-O scission nor the C-C cleavage of **5** is likely because the dehydrogenation reactions of **5** exhibit significantly lower barriers, 12 kJ mol^{-1} (**5-9**) and 32 kJ mol^{-1}(**5-10**) for the C-H scission at C1 and C2, respectively. The reaction route till here is analogous to the reaction path reported for 1-propanol reforming on Pt.[17]

After three dehydrogenation steps on Ru, first at O, then twice at C1, the reaction pathway arrives at the intermediate acetyl **9**, which features H atoms only at C2. Yet, also for this structure, the kinetically most preferred reaction is the further dehydrogenation **9-13** with a barrier of 58 kJ mol^{-1}. Alternative reactions are associated with activation barriers that are at least 20 kJ mol^{-1} higher.

Along the reaction path discussed here, acetyl **9** is the first intermediate of type CH_kCO and thus the first IS for a reaction of group (*ii*), as defined above when discussing C-O scission reactions in Section 5.3.3. As mentioned there, C-O cleavage barriers for this group of reactions are high due to the high order of the C-O bond. Thus, with E_a(**9-CO**) = 94 kJ mol^{-1}, this is the first time that the of C-O scission barrier is higher than the corresponding C-O cleavage barrier for a preceding intermediate along the reaction pathway. Prior to **9**, the C-O scission barriers have been falling steadily, from 167 kJ mol^{-1} to 80 kJ mol^{-1} (Table 3).

The barrier for the dehydrogenation of the next intermediate, ketene **13**, to yield ketenyl **15**, is relatively high, 72 kJ mol^{-1}, and is comparable to the barriers for the dehydrogenation at the ethyl group in the structures **1** or **2**. The activation energy required for the C-O scission follows the increasing trend just mentioned and rises to 103 kJ mol^{-1}. The most facile transformation of **13** is the cleavage of the C-C bond, with E_a =38 kJ mol^{-1}, yielding methylene and CO. This barrier is by at least 56 kJ mol^{-1} lower than the C-C scission barriers for any preceding intermediate along this pathway. This is in line with ketene being the first intermediate where both carbon centers are dehydrogenated, a prerequisite for easy C-C bond breaking, as discussed in Section 5.3.3.

Similar to C-C bond breaking in ethylene on Pd[227] and the decomposition of glycerol or glycol on Pt,[78,82,91,93] the cleavage of the ethanol C-C bond on Ru(0001) is only accessible if the reactant is first dehydrogenated several times. Although C-O bond scission over Ru(0001) is favored over C-C cleavage for the majority of intermediates derived from ethanol dehydrogenation, the most likely reaction pathway for ethanol on Ru terrace sites leads to the

scission of the C-C bond and the formation of CO. This is a consequence of the dehydrogenation barriers being lower than the barriers of C-O cleavage which ultimately leads to the formation of highly dehydrogenated species such as ketene **13**, which favor C-C cleavage, Figure 20. The highest barrier along the most likely pathway discussed thus far is determined for the dehydrogenation at the ethyl group of ethoxy, **2-5**. That reaction features a barrier of 77 kJ mol^{-1} and yields ethanal as product.

As mentioned in Chapter 4, the decomposition of alcohols may proceed via the intermediate formation of carboxylic acids. The formation of carboxylic acids via OH insertion into acetyl or its derivatives, have been discussed for the reactions on various metals,[19,76,88,89,94-96] thus the corresponding reaction on Ru has also been considered here. In line with the oxophilic character of Ru, the transfer of hydroxyl from the metal surface to the acetyl moiety to yield acetic acid is a relatively endothermic process, E_r = 70 kJ mol^{-1}, with a moderate barrier, 79 kJ mol^{-1}. The reverse exothermic reaction has a barrier of only 9 kJ mol^{-1}. Thus, should acetic acid be formed, it is expected to decompose immediately to acetyl and OH. Therefore, the formation of acetic acid (and subsequent decarboxylation) can be ruled out as a relevant pathway for the decomposition of ethanol on Ru.

Pathway to C-O cleavage. As mentioned previously, the majority of intermediates favor the C-O cleavage over the C-C cleavage. Thus, it is of interest to identify in a similar fashion the most likely reaction pathway leading to C-O scission, and to evaluate, whether it may co-exist, as a side reaction, with the C-C cleavage pathway. The C-O cleavage pathway requires the formation of a key intermediate, for which the C-O cleavage is the most preferred reaction. A potential candidate for the key intermediate is structure **6,** surface hydroxyethylidene, CH_3COH, which features a C-O cleavage barrier of only 33 kJ mol^{-1}, the lowest C-O cleavage barrier for all intermediates under study. The C-O cleavage yielding ethylidyne (CH_3C) and OH is the kinetically most favored reaction for **6**. However, the dehydrogenation of **6** at the hydroxyl group and at C2 are only slightly disfavored, with E_a of 43 kJ mol^{-1} and 53 kJ mol^{-1}, respectively.

To further evaluate whether a C-O cleavage pathway via the intermediate **6** is possible, it has to be clarified whether the formation of **6** from adsorbed ethanol **1** is kinetically and thermodynamically accessible. As both the oxygen center and C2 of **6** are saturated, dehydrogenation of **1** may only occur at C1 (**1-3**) in order to yield **6**. Such a reaction has been reported to be the preferred reaction on close-packed Pd.[75] On Ru(0001), the barrier for this reaction is 91 kJ mol^{-1}, i.e. by 22 kJ mol^{-1} and 14 kJ mol^{-1} higher than the barriers for the

competing dehydrogenation reactions at O (**1-2**) and at C2 (**1-4**) of ethanol, respectively. The product of the dehydrogenation **1-3** at C1, 1-hydroxyethyl **3**, has to be dehydrogenated further at C1 to yield 1-hydroxyethylidene **6**. The barrier of this step, 35 kJ mol^{-1}, is slightly higher than the barrier for the competing dehydrogenation at C2 of structure **3**, 29 kJ mol^{-1}. Other transformations of **3** are associated with higher barriers, 55 kJ mol^{-1} or more. Finally, the most favorable reaction of **6** is the C-O cleavage. Among all possible reactions for **6**, this transformation is the most exothermic reaction, E_r = -110 kJ mol^{-1}, and has the lowest barrier, E_a = 33 kJ mol^{-1}.

The highest barrier along this C-O cleavage pathway, as illustrated in Figure 21, is the initial dehydrogenation **1-3** of ethanol at C2 with E_a = 91 kJ mol^{-1}. This value is only 14 kJ mol^{-1} higher than the barrier of reaction **2-5**, the highest barrier along the most likely pathway leading to C-C cleavage. However, the competition among the reactions of ethanol, in particular between the thermo-neutral reaction **1-3** and the kinetically preferred exothermic reaction **1-2** (dehydrogenation at O), E_a = 79 kJ mol^{-1} and E_r = -58 kJ mol^{-1}, directs the most likely pathway toward the C-C cleavage.

Possible alternative pathways leading to C-O cleavage may proceed via intermediates of the most likely pathway that can be hydrogenated to yield the adsorption complex of hydroxyethylidene **6** or of 1-hydroxyethyl **3**, which can be dehydrogenated to form **6**. **6** and **3** may be formed via the hydrogenation at the O center of adsorbed acetyl **9** and ethanal **5**. However, these reactions, reversed **6-9** and reversed **3-5**, are rather endothermic, E_r > 48 kJ mol^{-1}, and also kinetically challenged with E_a > 100 kJ mol^{-1}. Therefore two-fold dehydrogenation of ethanol at C1 as shown in Figure 21 seems to be the only reasonable pathway that leads to the formation of intermediate **6** and the successive C-O cleavage, ultimately yielding the adsorbates ethylidyne and hydroxyl.

5.4. Conclusions

The study described in this chapter shows that the most likely pathway for ethanol decomposition on Ru(0001) starts with four successive dehydrogenation steps: one time at the OH group, twice at the C1 center, and one time at C2, to yield the adsorption complex of ketene CH_2CO. This intermediate ultimately undergoes C-C bond scission to yield CO and methylene. Thus, C-O cleavage from a species other than CO, as discussed in Section 5.1 as a possible pathway for the alkane formation, seems unlikely over the close-packed Ru(0001) surface. It is more likely that the alkanes are formed in a FT-type mechanism from CO, methylene and surface hydrogen, all products of the most favored decomposition pathway

discussed in Section 5.3.4.

The identified reaction pathway leading to C-C cleavage is supported by the experimental observation that ethanol processing with H_2 over Ru mainly yields CO and CH_4,[68] both products that can only be formed if a C-C cleavage step occurs. Aqueous phase processing of glycerol with excess H_2 mainly produces glycol, a C-C cleavage product, and propylene glycol, a species obtained from C-O cleavage, in the ratio of approximately 2:1, and some methane.[61,62] This experiment indicates that C-C cleavage is preferred over the C-O cleavage when oxygenates are brought to reaction over Ru. On the other hand, these experimental results also show that C-O cleavage is a side reaction which competes with C-C cleavage. The product spectrum observed in the experiment[61,62] is thus in line with the results of the present study.

The results of the current chapter also demonstrate that C-O scission is favored over C-C cleavage for a large number of intermediates. Thus Ru does have the potential to cleave the C-O bond of ethanol if the formation of highly dehydrogenated species as ketene can be avoided. In order to avoid the formation of such highly dehydrogenated species one would need to the control the selectivity of the dehydrogenation steps to enhance the formation of moderately dehydrogenated intermediates which exhibit C-O scission as the most likely reaction, e.g. intermediate **6,** the adsorption complex of hydroxyethylidene. A possibility to influence the distribution of the formed intermediates is to vary the size of the catalyst particles because, in this way, the availability of the various types of surface sites on a catalyst will be changed. It is for instance known that the ethanol decomposition pathway on a close-packed Rh surface[77,80] differs from the reaction at Rh step sites.[81] While the close-packed surface models, as also used in the present study, are suitable for studying the reactions on wide, flat facets of large catalyst particles; reactions on small particles, which feature more defect sites, seem to be described better by stepped surface models. It may also be interesting to explore how the ethanol decomposition pathway, derived here for the Ru(0001) model surface, is affected by the presence of stepped defect sites and whether the presence of steps can enhance the formation of moderately dehydrogenated intermediates.

Chapter 6 Hydrodeoxygenation of Guaiacol over Ru

6.1. Introduction

The preceding chapters dealt with the processing of aliphatic oxygenates. The present chapter focuses on reactions of aromatic oxygenates which can be derived from lignin by pyrolysis. As mentioned in Section 2.2, such pyrolysis products often contain too many oxygen functionalities to be suitable for the direct usage as fuel.[110,128] Therefore, the pyrolysis products have to be upgraded in a hydrodeoxygenation (HDO) step, in which the O groups are partially removed. This chapter addresses the Ru-catalyzed HDO of aromatic oxygenates and follows in part the presentation of the results in Ref 232.

Experimental works on this topic have used, among others, guaiacol (2-methoxyphenol), a typical product of lignin pyrolysis, to study the reactions of aromatic oxygenates.[26-29] These studies showed that, in the presence of hydrogen, guaiacol can be transformed over carbon-supported Ru nanoclusters to phenol[27-29] or benzene[26]. The reactions are typically carried out at temperatures between 523 K and 673 K[26-29] and at varying pressures.[26-29] While the processes at 1 bar mainly yields phenol,[27-29] benzene has been reported as the main product for the reaction under 40 bar pressure.[26] The difference in the total pressure is mainly a result of the difference in H_2 pressure.[26-29]

Based on experimental observations, it has been suggested that the HDO of guaiacol proceeds via the intermediates catechol and phenol,[26,28] similar to the mechanism originally proposed for the reaction on CoMo and NiMo alloys.[102,103] Yet, the detailed mechanism of the HDO process, especially the atomistic processes at the catalyst surface, are not well understood. This is partly related to the fact that theoretical works on the HDO of aromatic species are still rare. Only a small number of computational works have addressed the elementary reactions of HDO, e.g. the very recently published studies of the process on flat surfaces of Ru,[137,138], Pt[139], Pd[140] and Fe.[140] For some time, the majority of theoretical works addressing HDO only examined the adsorption of reactants on the catalyst.[28,112,121,129] A related reaction which has been investigated computationally is the dissociation of arylic

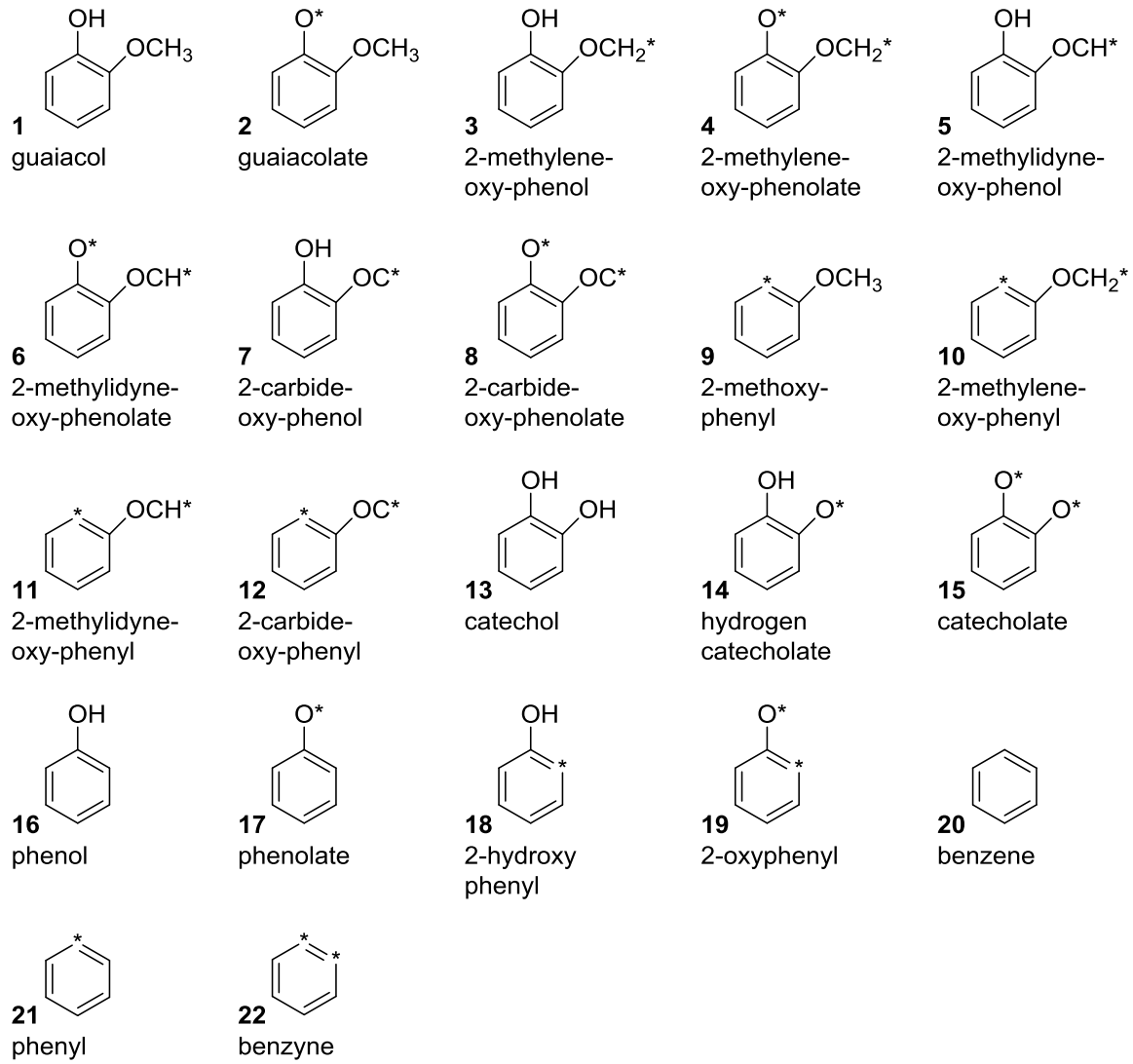

Figure 22: Structure formulas of all adsorbates under study. The structures are first sorted by the number of C atoms, then by the number of O atoms, and finally by the number of H atoms. An asterisk indicates the bond of a (poly-) radical site to the metal surface.

ethers via C-O bond cleavage over Ni based catalysts or acidic catalysts.[141,142]

In this thesis, the HDO of guaiacol over a Ru surface is first modeled using a close-packed Ru(0001) surface, similar to the study presented in Chapter 5. This should deliver an overview of the potential energy surface for guaiacol HDO and allow the identification of the rate-limiting reactions. In a second step, it will be examined how the presence of step sites on the Ru catalyst influences the overall kinetics of the HDO process. It is expected that the presence of such structural defect sites will facilitate the reaction as shown for various Ru-catalyzed processes.[220,231,233] Using the computationally determined energetics, an interpretation of the experiments[26-29] will be provided with special focus on the pressure dependent selectivity for the formation of phenol and benzene.

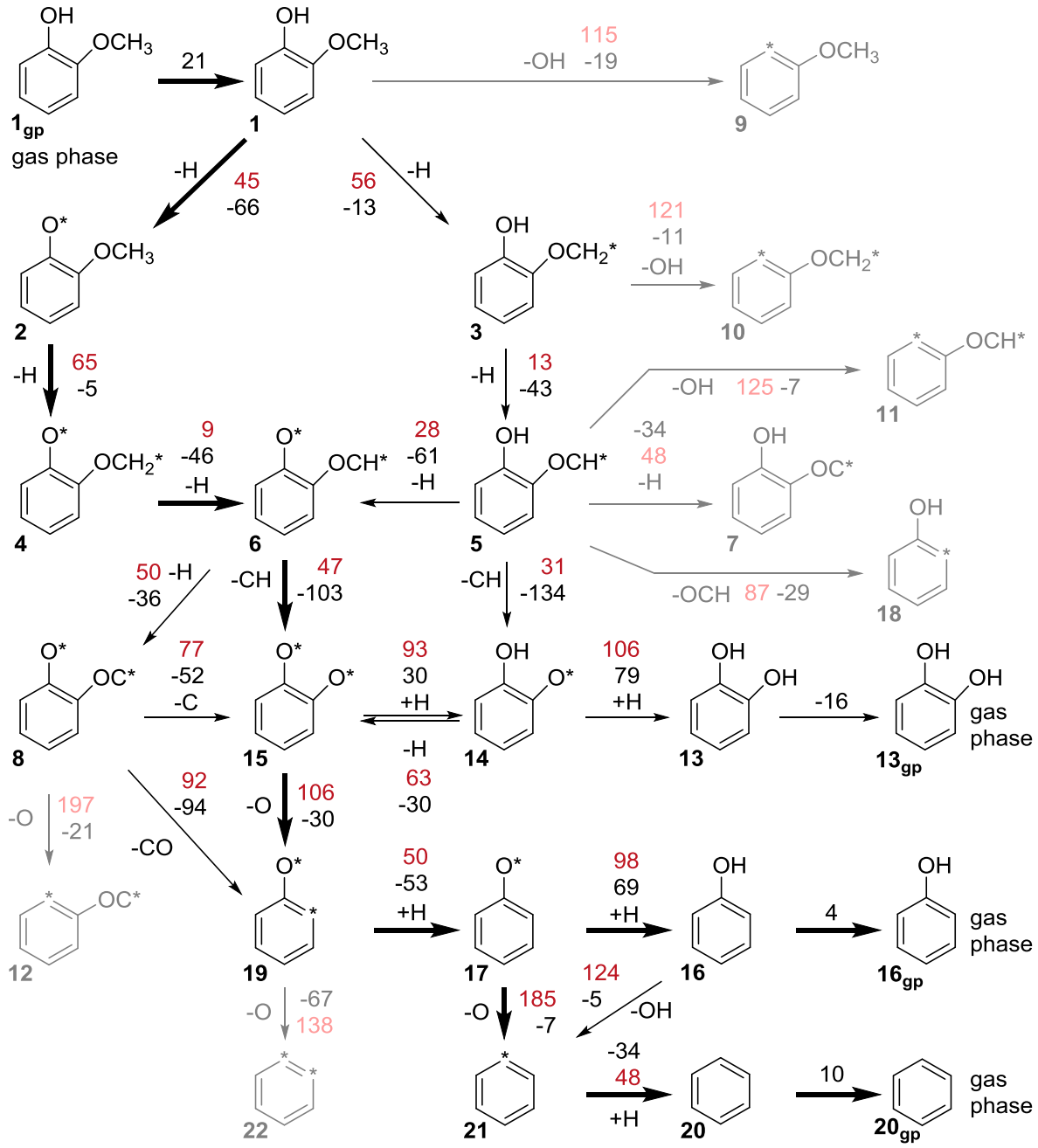

Figure 23: Reaction network of guaiacol HDO. Bold black arrows denote the main reaction pathway discussed in Section 6.3.1.5. The kinetically accessible alternative pathways are marked by thin black arrows. Numerical values at the arrows denote Gibbs free energies of reaction (black) and of activation (red) at 673 K and 1 bar for the reactions on Ru(0001). Species that are not on a kinetically accessible pathway are shown in gray.

6.2. Nomenclature

The adsorption complexes of all aromatic substrate species under study will be denoted by labels **x**, **x** = **1**–**22** (Figure 22). Note that the labels used in this chapter are independent of those introduced in Chapter 5. Labels of the form $\mathbf{x}_{gp}$ denote the species **x** in the gas phase. For ease of reading, no identifiers have been introduced for non-aromatic fragments like

OCH_k or CH_k. Reactions from an IS **x** to a product **y** (and a non-aromatic fragment) will be denoted as **x-y**, the corresponding TS as **x_y**.

Figure 23 provides an overview of all species and the reaction network under study. Table 4 displays the calculated Gibbs free energies of reaction G_r and of activation G_a for all surface reactions studied. The reactions are shown in the direction of the bond cleavage, although some reactions may occur in reverse direction along the reaction pathways to be discussed later on.

For the discussion of the reactions at the step site, some extension to the present nomenclature rules is required. These will be introduced when dealing with those reactions in Section 6.3.2.

6.3. Results and Discussion

This section will start with the results obtained by modeling the Ru catalyst with the close-packed Ru(0001) surface. First, some structural aspects of the adsorption complexes under study will be discussed. Subsequently, the energetic properties of pertinent elementary

Table 4: Calculated Gibbs free energies of reaction G_r and Gibbs free energies of activation G_a for the reactions under study on Ru(0001) at 673 K. The reactions are presented in the direction of the bond cleavage.[a] All values in kJ mol^{-1}.

IS	O-H			C_{alkyl}-H			C_{alkyl}-O			C_{aryl}-O(H)			C_{aryl}-OR		
	P	G_r	G_a	P	G_r	G_a	P	G_r	G_a	P	G_r	G_a	P	G_r	G_a
1	**2**+H	-66	45	**3**+H	-13	56	**14**+CH_3	-110	167[b]	**9**+OH	-19	115	**18**+OCH_3	-38	100
2				**4**+H	-5	65	**15**+CH_3	-74		**9**+O	-24	174	**19**+OCH_3	-14	135
3	**4**+H	-58	39	**5**+H	-43	13	**14**+CH_2	-105	48	**10**+OH	-11	121	**18**+OCH_2	-14	138
4				**6**+H	-46	9	**15**+CH_2	-76	56	**10**+O	-24	198	**19**+OCH_2	3	155
5	**6**+H	-61	28	**7**+H	-34	48	**14**+CH	-134	31	**11**+OH	-7	125	**18**+OCH	-29	87
6				**8**+H	-36	50	**15**+CH	-103	47	**11**+O	-17	177	**19**+OCH	-9	95
8							**15**+C	-52	77	**12**+O	-21	197	**19**+CO	-94	92
13	**14**+H	-79	27												
14	**15**+H	-30	63							**19**+OH	12	130			
										18+O	-18	181			
15										**19**+O	-30	106			
				C_{aryl}-H								184			
16	**17**+H	-69	29	P	G_r	G_a				**21**+OH	-5	124			
17				**19**+H	53	103				**21**+O	-7	185			
19										**22**+O	-67	138			
20				**21**+H	34	82									

[a] For each reaction, the initial state (IS) and the cleavage product (P) are listed; in some cases various products have been examined. [b] Estimated; see Section 6.3.1.2.

Table 5: Calculated reaction energies E_r and activation energies E_a of the surface reactions understudy on Ru(0001). The reactions are presented in the direction of the bond cleavage.[a] All values in kJ mol^{-1}.

IS	O-H			C_{alkyl}-H			C_{alkyl}-O			C_{aryl}-O(H)			C_{aryl}-OR		
	P	E_r	E_a	P	E_r	E_a	P	E_r	E_a	P	E_r	E_a	P	E_r	E_a
1	**2**+H	-62	51	**3**+H	-11	62	**14**+CH_3	-104	171[b]	**9**+OH	-14	115	**18**+OCH_3	-33	102
2				**4**+H	-5	69	**15**+CH_3	-64		**9**+O	-22	180	**19**+OCH_3	-7	143
3	**4**+H	-55	49	**5**+H	-34	21	**14**+CH_2	-91	58	**10**+OH	-7	120	**18**+OCH_2	-5	145
4				**6**+H	-34	20	**15**+CH_2	-58	67	**10**+O	-21	207	**19**+OCH_2	15	168
5	**6**+H	-55	37	**7**+H	-22	61	**14**+CH	-127	35	**11**+OH	1	128	**18**+OCH	-13	95
6				**8**+H	-27	63	**15**+CH	-93	58	**11**+O	-13	177	**19**+OCH	7	107
8							**15**+C	-45	82	**12**+O	-19	205	**19**+CO	-72	101
13	**14**+H	-72	47												
14	**15**+H	-21	78							**19**+OH	20	135			
										18+O	-14	184			
15										**19**+O	-28	106			
				C_{aryl}-H								185			
16	**17**+H	-68	37	P	E_r	E_a				**21**+OH	-2	124			
17				**19**+H	66	118				**21**+O	-3	189			
19										**22**+O	-58	149			
20				**21**+H	40	92									

[a] For each reaction, the initial state (IS) and the cleavage product (P) are listed.
[b] Estimated; see discussion in Section 6.3.1.2.

reactions on the Ru terrace will be addressed to work out general trends for G_a and G_r. Based on these results, the most likely reaction pathways as well as their rate-limiting steps are determined. In a second part, the kinetic and thermodynamic properties of the rate-limiting steps are re-evaluated for Ru catalysts with defects, using the stepped S3-Ru(10$\bar{1}$5) and S4-Ru(10$\bar{1}$5) surfaces as models. The discussion in the present section will focus on the Gibbs free energies evaluated for 673 K and 1 bar, i.e. for the reaction conditions reported in Ref 27, if not stated otherwise. The sub-sections 6.3.1.3 and 6.3.1.4 will illustrate that variation of temperature and pressure within the range of values reported for the experiment (523 K to 673 K; 1 bar to 40 bar)[26-29] does not change the overall picture of the thermodynamic and kinetic properties of the HDO process. For comparison, the temperature and pressure independent reaction energies E_r and activation energies E_a for the surface reactions are provided in Table 5. Note that this study does not consider C-C cleavage steps, in view of the stability of aromatic ring systems.

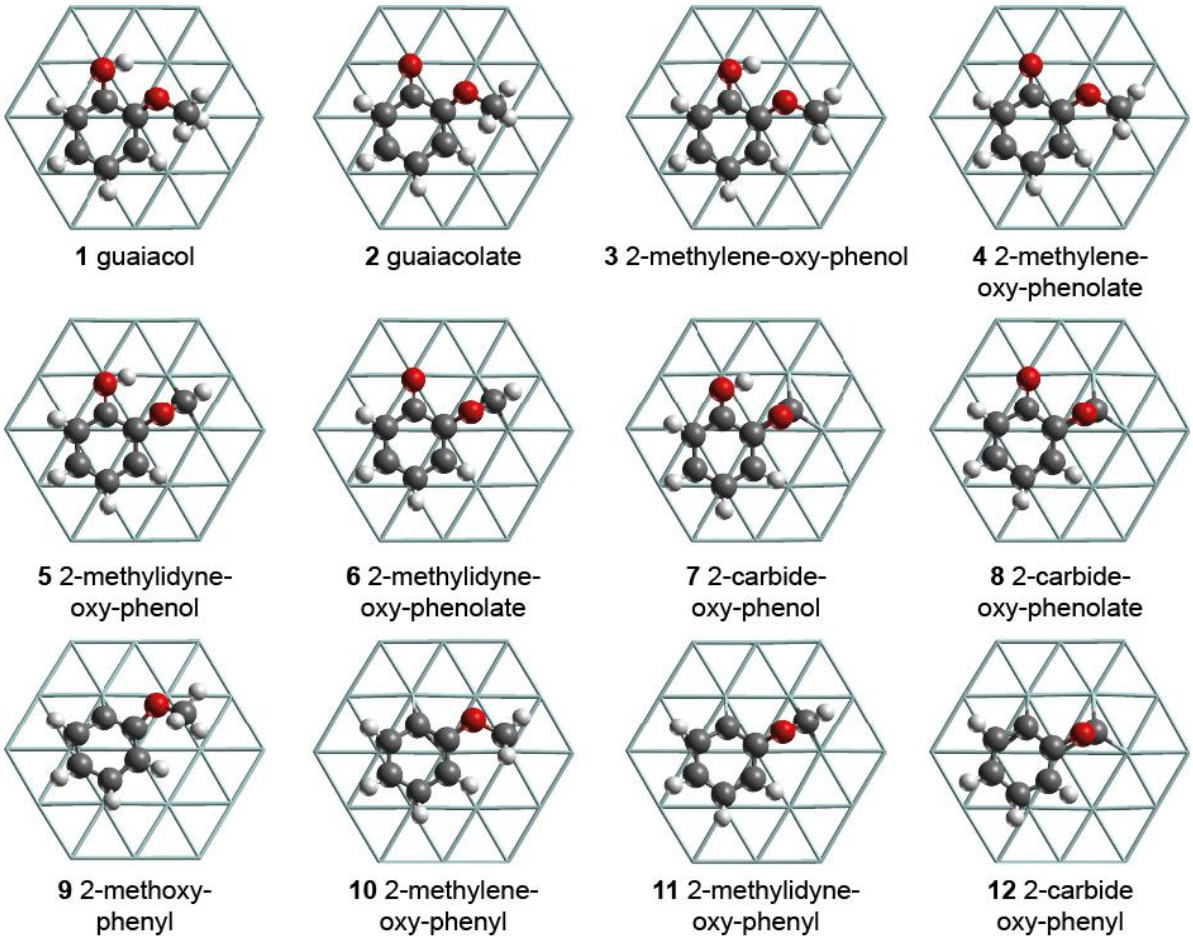

Figure 24: Top view on the optimized structures of all considered minimum state adsorption complexes on Ru(0001). Black: C, red: O, white: H, cyan: Ru. For the sake of a clearer view, the Ru-Ru bonds are displayed as sticks.

6.3.1. Adsorption and Reactions on Close-Packed Ru(0001)

6.3.1.1. Adsorption Geometries

This section addresses the most stable adsorption complexes formed by selected intermediates of guaiacol HDO on Ru(0001) (Figure 24). Preferred adsorption geometries of the various functional groups determined for the adsorbate structures will be identified here.

The prototypic species of an aromatic C_6 ring is benzene that forms the adsorption complex **20**, a system, which is also well characterized by experiment.[234-236] The GGA calculations of the present work indicate that benzene prefers to adsorb at hcp sites, i.e., with the center of the C_6 ring over an hcp-hollow site. Every second C center of benzene binds to a top site, C-Ru ~218 pm, while the other three centers are located over fcc-hollow sites with notably longer C-Ru distances, 257–278 pm. This leads to a corrugated structure of the adsorbed C_6 ring. For easier orientation and discussion of the structure, an average plane for

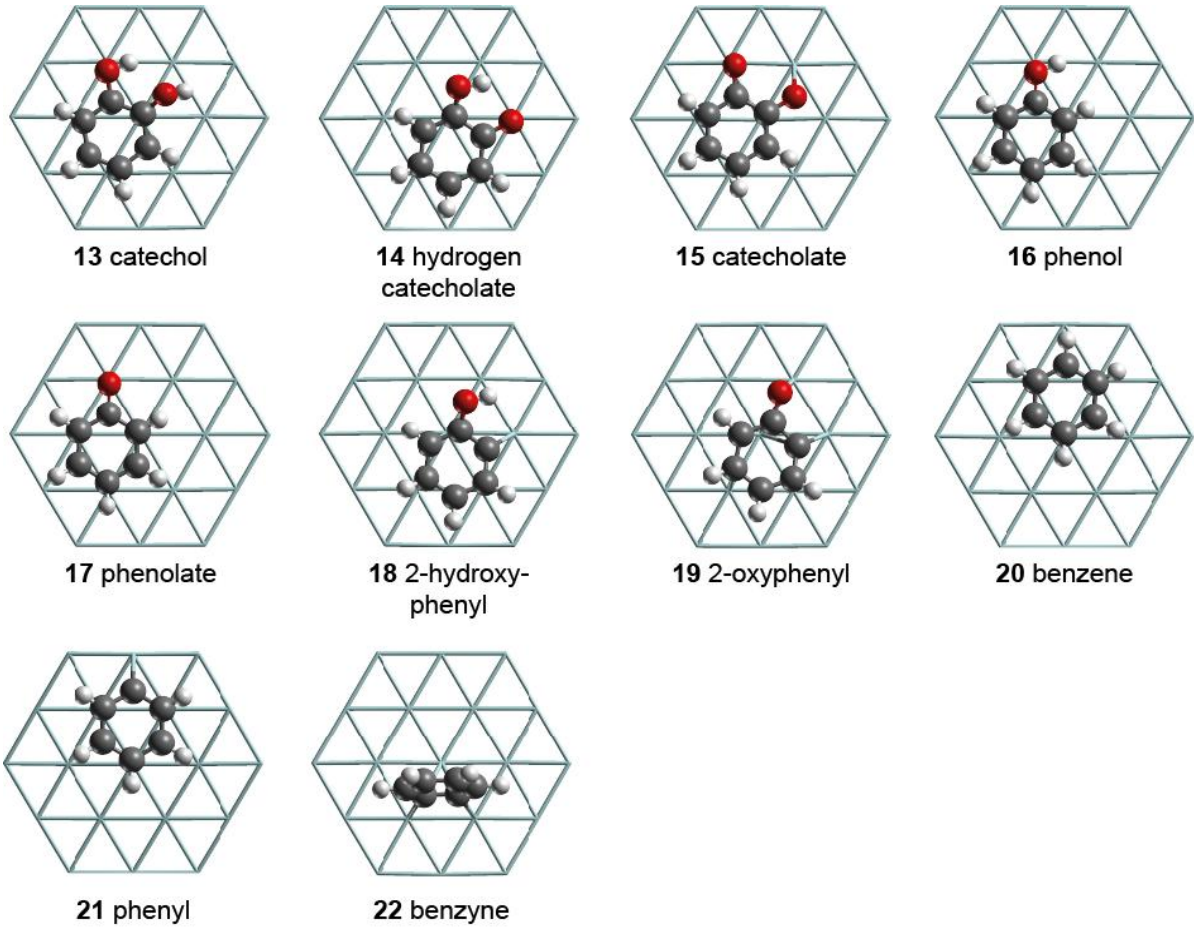

Figure 24 (continued)

the carbon ring shall be introduced here. This average plane is defined by a least-squares fit to the locations of the six carbon centers of the adsorbed benzene ring. The average plane is oriented parallel to the Ru(0001) surface. The C atoms on top and hollow sites are located 3 pm below and above the average plane, respectively. Different from the structure of benzene in the gas phase, the six H atoms in the benzene adsorption complex **20** are not in the average plane defined by the C atoms. Rather, the C-H bonds are pointing away from the metal surface. The C-H bonds associated with the hollow site C atoms form angles of 14–15° with the average plane of the C atoms. Larger angles, 22–23°, are found for those C-H bonds at the top adsorbed C centers. The distortion of the planar geometry of benzene upon adsorption on the Ru surface can be rationalized with the rehybridization of the C centers. The structure of the adsorption complex and the calculated adsorption *energy* E_{ads} of -136 kJ mol^{-1} are consistent with earlier results from GGA-DFT calculations[236] and LEED experiments.[234-236] Note that the hollow-adsorbed structure is not typical for benzene adsorbed on all close-packed metal surfaces. Besides Ru, preferred adsorption at hollow sites

has only been calculated for Group 11 metals where the adsorption energies E_{ads} at GGA level are calculated to be -5 kJ mol^{-1} or less exothermic.[237,238] Adsorption energies comparable to the E_{ads} value computed here for benzene on Ru(0001) have been reported for the close-packed surfaces of Pt,[145,239] Pd,[147,240,241] and Rh;[240] these energies range from 117 kJ mol^{-1} to 145 kJ mol^{-1}. Note that the value of -136 kJ mol^{-1} for E_{ads} on Ru is shown here for easier comparison with earlier studies, which only reported adsorption energies. In anticipation of the up-coming Section 6.3.1.4 it is mentioned already here that the inclusion of entropy is necessary for a reasonable description of the adsorption and desorption processes under typical HDO process conditions.

The presence of OH and OCH_3 substituents at the C_6 ring does not affected the preference of the aromatic ring for hollow sites on the Ru(0001) surface. Adsorbed guaiacol **1**, catechol **13** and phenol **16** (Figure 24) also favor the adsorption over hcp or fcc sites. However, the presence of OH and / or OCH_3 has an influence on the adsorption energies E_{ads}. Adsorption becomes less exothermic with increasing number of substituents featuring oxygen centers (benzene **20**: -136 kJ mol^{-1}, phenol **16**: -130 kJ mol^{-1}, catechol **13**: -116 kJ mol^{-1}, guaiacol **1**: -107 kJ mol^{-1}), in line with results reported for group 10 metals.[241-244] This trend is still present if Gibbs free energies of adsorption G_{ads} are considered instead of E_{ads} as will be shown in Section 6.3.1.4. The O centers of the OH and OCH_3 moieties in the adsorption complexes **1**, **13**, and **16** hardly interact with the Ru surface, as indicated by Ru-O distances of 246 pm or longer, albeit Ru is known to be oxophilic.[212] The C_{aryl}-O bonds in the mentioned adsorption complexes are tilted away from the Ru(0001) surface, by 11–35°, similar to the C-H bonds in the adsorption complex of benzene **20**. Similarly tilted C_{aryl}-O bonds have been reported for phenol on Pt, Ni, and Rh.[150,242-244]

Even if the OCH_k group at aromatic substrates is dehydrogenated and thus forms a bond with the Ru surface, as in the adsorption complexes **3**, **5**, or **7** (Figure 24), the preference for hollow sites by the aromatic C_6 ring remains unchanged. In the structures of **3**, **5**, and **7**, the dehydrogenated, aliphatic C center adsorbs at top, bridge, and hollow sites of the Ru(0001) surface, respectively. This is remarkable, as previous calculations, including those discussed in Chapter 5, have shown that all isolated CH_k species, k = 0–3, prefer hollow sites on Ru(0001).[221,245] This difference between isolated CH_k species and OCH_k groups in aromatic adsorbates is related to the competition between the OCH_k and the aromatic ring for the preferred adsorption sites.

A dehydrogenated aromatic C center as in the surface complex of phenyl **21**, is another

structural motif encountered several times in this study. As notable in structure **21** (Figure 24) the dehydrogenated aromatic C adsorbs preferentially at hollow sites. This invokes a slight shift of the center of the C_6 ring in **21** towards a bridge site, by 45 pm. On the close-packed surface of Ru, the C_6 ring of phenyl in structure **21** lies essentially parallel to the metal surface. At variance, phenyl was calculated to adsorb upright or tilted on the Cu(100) and Pt(111) surfaces.[145,149]

Another recurring functional group is the C-O moiety of oxo groups at the aromatic C_6 ring as in the adsorption complex of phenolate **17**. In structure **17**, the C_6 ring is at an hcp site, the C-O moiety adsorbs to the neighboring fcc site. In particular, the C atom is close to the center of the fcc site, while the O center interacts in top fashion with one Ru atom of the fcc site. The corresponding Ru-O distance, 212 pm, indicates a significantly stronger metal-O interaction than in the absorption complex of phenol **16**, the hydrogenated analogue with Ru-O = 267 pm. An alternative conformer for the adsorption complex of phenolate **17** with the oxo group over hollow or bridge sides could not be identified. In general, oxo functionalities at aromatic rings seem to prefer the local geometry as described for structure **17**. Similar local geometries are also determined for other adsorption structures featuring an oxo group, among others the structures **2**, **4**, and **6** (Figure 24). However, there are other surface complexes, like catecholate **15** or 2-oxyphenyl **19**, in which the intrinsic structures of the adsorbate prevent oxo groups to interact with the Ru(0001) surface in the preferred fashion.

In the adsorption complex **15** of catecholate (Figure 24), which features two vicinal oxo groups, one O adsorbs at the preferred top site, while the second O center can only be located over a less favorable bridge site (or rather a skewed top site). The resulting unequal Ru-O distances at this bridge site, 231 pm and 245 pm, as well as the fact that the center of the aromatic ring in **15** is shifted by 58 pm from the center of a hollow site (Figure 24), indicate that the adsorbate structure is under strain. The strain can be rationalized by the competition between the two oxo groups and the aromatic ring for their respective ideal adsorption sites. The C-O distances also reflect the presence of strain in the adsorption complex **15**. The distances $C\text{-}O_{top}$ = 131 pm and $C\text{-}O_{bridge}$ = 135 pm indicate that the latter bond is more activated. Similarly, the surface structure of 2-oxyphenyl **19** exhibits strain, as the dehydrogenated C center and the oxo group in *ortho* position compete for optimum sites. As the former adsorbs at a preferred hollow site, the C-O moiety of the oxo group is forced to align along a bridge site (Figure 24). This atypical local geometry around the C-O moiety has

not been found for any other adsorption complex under study.

Finally, a more exotic structure shall be addressed, namely the adsorption complex of benzyne **22** (Figure 24) which is included as a possible intermediate in the reaction network (Figure 23). Benzyne formally derives from the further dehydrogenation of phenyl at *ortho* position to the dehydrogenated C. At variance with the surface structure of phenyl, the benzyne moiety in **22** is located over a hollow site, with the ring oriented *perpendicular* to the Ru surface. Similar benzyne adsorption complexes have previously been identified computationally on Pt(111) and Cu(100).[145,149]

6.3.1.2. Energetics of Reactions

The energetics, in particular the G_r and G_a values of the reactions under study, is discussed in this section (Table 4). For the discussion the reactions are grouped, based on the bond being broken, into six categories: bond cleavages of (*i*) O–H, (*ii*) C_{alkyl}–H, (*iii*) C_{aryl}–H, (*iv*) C_{alkyl}–O, (*v*) C_{aryl}–OH, and (*vi*) C_{aryl}–OCH_k. To facilitate comparison with earlier works which often report only electronic energies *E* instead of Gibbs free energies *G*, the electronic energies will be mentioned where appropriate (Table 5).

O–H cleavage. The dehydrogenation of an OH group at aromatic C_6 rings has been studied for the species **1**, **3**, **5**, **13**, **14** and **16**, which differ only in the substituent in *ortho* position to the OH group. The corresponding reactions, **1-2**, **3-4**, **5-6**, **13-14**, **14-15**, and **16-17**, are all determined to be exothermic. With the exception of **14-15**, which will be discussed separately, all reactions have similar energetic properties (Table 4). The calculated Gibbs free energies of reaction G_r are in the range from -58 kJ mol^{-1} to -79 kJ mol^{-1}. The exothermic character of these reactions is related to the formation of a stable bond between an O center and the surface of an oxophilic metal, Ru. The corresponding barriers G_a are between 28 kJ mol^{-1} and 45 kJ mol^{-1}. Hence the O-H scission reactions addressed here can be considered as easily accessible under the typical HDO conditions, 523–673 K and 1–40 bar.[26-29] The reactions have in common that the OH group in the corresponding ISs does not interact with the Ru surface (or does so only weakly), while the oxo group of the product adsorbs at a top site. The similarity in the G_r and G_a values can be rationalized by the fact that the various substituents in *ortho* position hardly affect the local structure around the hydroxyl group where the actual reaction occurs.

In order to compare with similar reactions, the reaction energies E_r and activation energies E_a of the above mentioned reactions (**1-2**, **3-4**, **5-6**, **13-14**, and **16-17**) should be introduced (Table 5). The values for E_r lie between -55 kJ mol^{-1} and -72 kJ mol^{-1}; these

values are slightly less exothermic than the corresponding G_r values, -58÷-79 kJ mol^{-1}. The activation energies E_a are generally higher than the Gibbs free energies of activation (G_a: 28–45 kJ mol^{-1}) and fall in the range from 37 kJ mol^{-1} to 51 kJ mol^{-1}.These values are somewhat lower than E_a results of 69 kJ mol^{-1} and 63 kJ mol^{-1} reported for the O-H scission of phenol on Pt(111) and Rh(111), respectively.[150]

The activation energies E_a for the dehydrogenation at the OH substituents of aromatic compounds are slightly lower than the E_a reported for aliphatic OH groups (42–78 kJ mol^{-1});[246] see also Chapter 5. A direct comparison between the thermodynamic properties for aromatic and aliphatic O-H cleavage steps is not straightforward. The reaction energies E_r for the cleavage of aliphatic O-H groups scatter much stronger, from -22 kJ mol^{-1} to -64 kJ mol^{-1} (cf. Chapter 5),[246] than the E_r or G_r values associated with the scission of aromatic O-H groups.

Reaction **14-15** has a higher barrier (63 kJ mol^{-1}) and is less exothermic (-30 kJ mol^{-1}) than the other aromatic OH cleavage reactions on Ru mentioned above. This difference can be related to the structure of product **15**. At variance with all other O-H cleavage steps discussed above, the O center of the OH group adsorbs at an unfavorable bridge site upon dehydrogenation, which is related to the competition between the two oxo functionalities in the product **15**. As discussed in Section 6.3.1.1, this atypical adsorption geometry for the oxo group in **15** comes along with structural strain which renders the reaction **14-15** slightly less favorable than the other O-H scission steps discussed before.

C_{alkyl}–H cleavage. This category addresses the dehydrogenation at the methoxy group. These reactions can be divided into two groups, based on the IS structure. There is either a hydroxyl group (**1-3**, **3-5**, **5-7**) in *ortho* position to the OCH_k moiety (k = 3–1) being dehydrogenated, or an oxo group (**2-4**, **4-6**, **6-8**). Similar to the O-H cleavage reactions discussed above, the influence of the substituent in *ortho* position on the energetics is negligible. The G_r and G_a values of analogous reactions in the two groups differ by at most 9 kJ mol^{-1}. The barriers G_a for the removal of the first H atom from the methoxy group are determined to be 56 kJ mol^{-1} (**1-3**) and 65 kJ mol^{-1} (**2-4**). The corresponding values for G_r are slightly exothermic, -13 kJ mol^{-1} and -5 kJ mol^{-1}, respectively. The C-H scission for the second hydrogen, **3-5** and **4-6**, is both kinetically and thermodynamically more favored, with G_r of -43 kJ mol^{-1} and -46 kJ mol^{-1}, respectively, and G_a of at most 13 kJ mol^{-1}. The third and last dehydrogenation steps leading to the formation of a –OC moiety (**5-7**, **6-8**) are associated with barriers of 48 kJ mol^{-1} and 50 kJ mol^{-1}, respectively, that are slightly lower

than those of the first dehydrogenation step **1-3** (56 kJ mol^{-1}) and **2-4** (65 kJ mol^{-1}). These reactions are exothermic as well, by -34 kJ mol^{-1} and -36 kJ mol^{-1}, respectively.

The Gibbs free energies of reaction presented here indicate a picture that differs from the situation for ethanol dehydrogenation on Ru(0001) as discussed in Chapter 5. Recall that the first dehydrogenation at the ethyl moiety of ethanol was determined to be endothermic. In contrast, the thermodynamic properties for the reactions at the methoxy group of guaiacol presented here resemble more the potential energy surface reported for methane dehydrogenation on Ru(0001), whose first three dehydrogenation steps are all exothermic.[221,222,245] Note that the O center in the OCH_k (k =0–3) group of the aromatic species studied here does not interact at all with the Ru surface, whereas the O-Ru interaction plays an important role in the case of ethanol (cf. Chapter 5). This may rationalize why the thermodynamic properties for the reaction at the guaiacol methoxy group resembles those for the reaction of methane, which does not contain any oxygen centers.

As mentioned before, the barriers associated with the removal of the first H from the methoxy group (**1-3**, **2-4**) are higher than those for the dehydrogenation at an already dehydrogenated $–OCH_2$ moiety (**3-5**, **4-6**). This can be rationalized by noting that in the IS structures **1** and **2**, the methyl group interacts only weakly with the surface, thus the methyl C-H bonds are essentially not activated. At variance, in structures **3** and **4** the aliphatic C atom binds notably to the Ru surface. This argument is supported by results of earlier computational studies on the reactions of aliphatic species on Ru; the highest dehydrogenation barriers were determined for the reaction at saturated C moieties (cf. Chapter 5).[221,223]

C_{aryl}-H cleavage. The prototypical C_{aryl}–H cleavage reaction is the dehydrogenation **20-21** of adsorbed benzene to form adsorbed phenyl **21**, which is an endothermic process, G_r = 34 kJ mol^{-1} with a barrier of 82 kJ mol^{-1}. Slightly higher values are obtained when thermodynamic corrections are not considered: E_r = 40 kJ mol^{-1} and E_a = 92 kJ mol^{-1} (Table 5). Analogous reactions on other transition metal surfaces have been reported to be endothermic as well, E_r of 75 kJ mol^{-1} and 71 kJ mol^{-1} have been determined for the reactions on Pt(111)[145] and Cu(100),[149] respectively. A noteworthy fact is that the adsorption complex of the product phenyl on Ru shows a different structure than the corresponding complexes on Pt and Cu. As mentioned in Section 6.3.1.1, the phenyl moiety lies flat on the Ru(0001) surface (Figure 24), but is adsorbed upright or tilted on the surfaces Cu(100) and Pt(111). The second reaction in this category is reaction **17-19**, the dehydrogenation in *ortho*

position to the oxo group of phenolate. This reaction is both thermodynamically (G_r = 53 kJ mol^{-1}) and kinetically (G_a = 103 kJ mol^{-1}) less favored than **20-21** (Table 4). This can be rationalized by the strained structure of the product **19**, which was addressed in Section 6.3.1.1.

C_{alkyl}-O cleavage. This category of reactions comprises the cleavages of the H_kC-O bond with k = 0–3 (Table 4). Similar to the C_{alkyl}-H cleavage reactions, the C_{alkyl}-O scissions can also be divided into two groups, recognizing that the ISs have either a hydroxyl substituent or an oxo group in *ortho* position to the OCH_k group. The former group of reactions yields adsorbed hydrogen catecholate **14** as product, whereas the latter group leads to the formation of surface catecholate **15**.

For the reactions yielding **14**, the bond scission barrier G_a decreases with k, from 167 kJ mol^{-1} estimated for **1-14** (k = 3),[*] to 48 kJ mol^{-1} for **3-14** (k = 2), and 31 kJ mol^{-1} for **5-14** (k = 1). The corresponding G_r values are generally strongly exothermic, ranging from -105 kJ mol^{-1} (**3-14**) to -134 kJ mol^{-1} (**5-14**), but do not show any obvious correlation with k. The analogous reactions from the group yielding catecholate **15** are less exothermic than the reactions yielding **14**, by 29–36 kJ mol^{-1} (Table 4). This is related to the steric strain due to the two oxo groups in the product structure **15**; cf. Section 6.3.1.1. In line with the less exothermic G_r values for the reactions of the oxo-substituted ISs (yielding **15**), the barriers of **4-15** and **6-15** are also higher than those of the reactions of the OH-substituted reactants (yielding **14**), by 8 kJ mol^{-1} (**4-15** vs. **3-14**) and 16 kJ mol^{-1} (**6-15** vs.**5-14**). Reaction **2-15** has been omitted, as it is expected to be a kinetically inaccessible reaction with a barrier larger than G_a(**1-14**) = 167 kJ mol^{-1}. Similar to the reactions of the first group yielding **14**, the barriers for the reactions of the oxo-substituted ISs yielding **15**, the cleavage of the HC-O bond (**6-15**) is kinetically easier accessible than the scission of the H_2C-O bond (**4-15**). In addition, reaction **8-15** has been studied. The corresponding IS has no H at the aliphatic C center (k = 0). For this reaction, G_a = 77 kJ mol^{-1} has been calculated, i.e. the barrier of **8-15** is higher than those for **4-15** and **6-15**. Therefore, the barriers of the C_{alkyl}-O cleavages do not

[*] The force on the TS structure **1_14** could only be converged to 2.7×10^{-4} eV, i.e. slightly above the standard convergence criteria of 2.0×10^{-4} eV. The corresponding structure shows two imaginary vibrational modes: 547i cm^{-1} for the stretching mode of the methoxy C-O bond, and a significantly smaller frequency of 96i cm^{-1} related to the movement of the methyl group towards the Ru surface. The barrier of G_a =167 kJ mol^{-1} is estimated under the assumption that this structure is a reasonable approximation for the "real" TS structure. Due to the small residual forces, the error on G_a introduced by the above mentioned approximation is expected to be negligible.

fall synchronously with the decreasing value of *k*. Instead, there is a minimum at $k = 1$. A similar trend with a rough minimum has also been found for the activation *energies* E_a associated with the C-O cleavage of ethanol and its dehydrogenation products on Ru(0001) (cf. Chapter 5).

C_{aryl}-O(H) cleavage. The removal of an oxo or a hydroxyl group from the aromatic C_6 ring will be addressed here. These reactions are generally characterized by barriers higher than 100 kJ mol^{-1} (Table 4). With the exceptions of the reactions **15-19** and **19-22**, which will be discussed separately, a clear trend can be identified. Cleavage reactions of C_{aryl}-OH bonds are associated with barriers ranging from 115 kJ mol^{-1} to 130 kJ mol^{-1}, whereas removal of an oxo group is kinetically even less favored, with barriers between 174 kJ mol^{-1} and 198 kJ mol^{-1}. At variance, thermodynamics tends to prefer the removal of an oxo group over the elimination of an OH group. All reactions eliminating an oxo group are exothermic, with G_r from -7 kJ mol^{-1} to -24 kJ mol^{-1}. On the other hand, the analogous OH removal reactions from an O-hydrogenated intermediate are less exothermic or even endothermic in all cases where the data allow a direct comparison (Table 4).

In the special case of the reaction **15-19**, there are two oxo groups in the IS structure **15**. As mentioned in Section 6.3.1.1, one catecholate oxo group is adsorbed at a top, the other at a bridge site. The barrier associated with the removal of the top-adsorbed O is 184 kJ mol^{-1}, well comparable to values found for other oxo removal steps (**2-9**, **4-10**, **6-11**, **8-12**, **14-18**, **17-21**) in which the pertinent oxygen center is also attached to a top site. The C-O scission barrier associated with O at the bridge site is by 78 kJ mol^{-1} lower, G_a = 106 kJ mol^{-1}. Obviously, the local geometry around the oxo group to be eliminated notably affects the barrier height. This is a consequence of the strain in the adsorbate moiety of **15** leading to a stronger activation of the C-O_{bridge} bond as discussed in Section 6.3.1.1.

The second special case, **19-22**, also involves an IS structure that is under strain. The IS **19** is the only adsorption complex under study, in which a dehydrogenated, aromatic C center in the C_6 ring competes with the oxo group for the ideal adsorption site on the Ru surface (cf. Section 6.3.1.1). In addition, the product structure, the adsorption complex of benzyne **22**, is the only surface structure in this study which features a C_6 moiety oriented upright on the metal surface (Figure 24). G_r of -67 kJ mol^{-1} and the barrier of 138 kJ mol^{-1} indicate that this reaction is both thermodynamically and kinetically more favorable than the "typical" oxo removal steps discussed above, **2-9**, **4-10**, **6-11**, **8-12**, **14-18**, and **17-21**. Obviously reaction **19-22** is not comparable to these oxo-removal steps.

C_{aryl}-OR cleavage. Similar to the C_{aryl}-O(H) cleavage just discussed, this category of reactions also has rather high barriers, between 87 kJ mol^{-1} and 155 kJ mol^{-1}. Although the G_a values for the C_{aryl}-OR cleavage tend to be lower than the barriers associated with the C_{aryl}-O(H) cleavage, the scission of any C_{aryl}-O bond is still kinetically challenging, irrespective of the substitution pattern at the O center. Similar to the C_{alkyl}-O cleavage, the nature of the substituent in *ortho* position to the OCH_k group of the ISs has a notable effect on the energetics.

For ISs with an OH group in *ortho* position, one yields intermediate **18** as the product of exothermic reactions, with G_r from -14 kJ mol^{-1} to -38 kJ mol^{-1}. The corresponding barriers fall into the range from 87 kJ mol^{-1} to 138 kJ mol^{-1}. Neither G_r nor G_a show a clear correlation with the number of H centers at the aliphatic C. However, the highest barrier is calculated for the least exothermic reaction **3-18** with R = CH_2. The reactions of the intermediates featuring an oxo group instead of the OH group yield the strained structure **19** as product (cf. Section 6.3.1.1). Such reactions are thermodynamically and kinetically less favored than the analogue reactions yielding **18**. The G_a for the reactions forming **19** range from 92 kJ mol^{-1} to 155 kJ mol^{-1}, i.e. are by at least by 8 kJ mol^{-1} higher than the barriers of the reactions starting from the corresponding O-hydrogenated ISs. With the exception of reaction **8-19**, all reactions yielding **19** are weakly exothermic or thermo-neutral. **8-19** is a rather exothermic reaction, -94 kJ mol^{-1}; note that it involves the formation of the relatively stable side product CO. Similar to the situation of C_{alkyl}-O cleavages, the general preference for reactions of intermediates with an OH group (**x-18**) over the reactions of their O-dehydrogenated analogues (**x-19**) is related to the structural strain in the product **19**.

6.3.1.3. Comment on the Temperature and Pressure Dependency

The reactions discussed above and displayed in Table 4 are all reactions of species adsorbed on a Ru surface. When evaluating the Gibbs free energies of such species, one can treat, as a rough approximation, the frustrated translation modes and frustrated rotation modes as harmonic vibrational modes.[188,189] Therefore, the translational contribution to the entropy, the only pressure dependent term in the Gibbs free energy, is set to zero. Thus, the G_r and G_a values for *surface* reactions are independent of the pressure. In contrast, for the evaluation of the Gibbs free energies of gas phase species, which can move and rotate freely, it is not possible to treat the rotational and translational modes as vibrational modes. Therefore, the energetics of *adsorption* processes, which are discussed separately in the next section, *is* pressure dependent.

Table 6: Calculated Gibbs free energies of reaction G_r and Gibbs free energies of activation G_a at 523 K for reactions on Ru(0001).[a] All values in kJ mol^{-1}.

IS	O-H			C_{alkyl}-H			C_{alkyl}-O			C_{aryl}-O(H)			C_{aryl}-OR		
	P	G_r	G_a	P	G_r	G_a	P	G_r	G_a	P	G_r	G_a	P	G_r	G_a
1	**2**+H	-68	43	**3**+H	-16	53	**14**+CH_3	-111	164[b]	**9**+OH	-19	113	**18**+OCH_3	-38	99
2				**4**+H	-8	62	**15**+CH_3	-74		**9**+O	-24	173	**19**+OCH_3	-13	134
3	**4**+H	-60	37	**5**+H	-44	12	**14**+CH_2	-104	46	**10**+OH	-11	119	**18**+OCH_2	-13	137
4				**6**+H	-47	8	**15**+CH_2	-74	56	**10**+O	-24	198	**19**+OCH_2	5	155
5	**6**+H	-62	25	**7**+H	-34	48	**14**+CH	-133	31	**11**+OH	-6	124	**18**+OCH	-26	87
6				**8**+H	-37	50	**15**+CH	-101	48	**11**+O	-17	176	**19**+OCH	-6	96
8							**15**+C	-51	76	**12**+O	-22	197	**19**+CO	-89	93
13	**14**+H	-80	27												
14	**15**+H	-31	61							**19**+OH	13	128			
										18+O	-18	179			
15										**19**+O	-30	104			
				C_{aryl}-H								182			
16	**17**+H	-72	27	P	G_r	G_a				**21**+OH	-6	122			
17				**19**+H	53	103				**21**+O	-7	184			
19										**22**+O	-65	140			
20				**21**+H	32	81									

[a] For each reaction, the initial state (IS) and the cleavage product (P) are listed.
[b] Estimated; see Section 6.3.1.2.

Whereas the energetics of the surface reactions is independent of the pressure, it *does* depend on the temperature. As various experimental works on guaiacol HDO have been performed at temperatures between 523 K and 673 K,[26-29] it is appropriate to ask whether G_r and G_a values evaluated for 673 K (Table 4) still give a reasonable description of the HDO experiments done at lower temperatures. Table 6 shows G_r and G_a evaluated for 523 K, which deviate by at most 5 kJ mol^{-1} from the corresponding values at 673 K. Thus, the Gibbs free energies of the surface reactions under study depend only weakly on the temperature. Therefore, the energetics evaluated for *surface* reactions at 673 K can be used safely for the interpretation of reactions at somewhat lower temperatures. At variance, the *adsorption* processes, which involve species in the gas phase, behave differently: their corresponding Gibbs free energies depend more strongly on the temperature, as the discussion in the next section will show.

6.3.1.4. Adsorption Processes

As already mentioned, adsorption processes are pressure dependent, as the Gibbs free energy, in particular, the translational contribution to the entropy, of gas phase species is pressure

dependent. The temperature dependency of the Gibbs free energy of adsorption G_{ads} will be briefly addressed here. Upon adsorption, an adsorbate is limited in its rotational and translational degrees of freedom, which leads to a significant decrease in entropy. In the case of guaiacol, the entropy change S_{ads} associated with the adsorption process is as large as -156 J K^{-1} mol^{-1}. As the Gibbs free energy of adsorption is calculated as $G_{ads} = H_{ads} - S_{ads}T$, with H_{ads} and T being the adsorption enthalpy and the temperature, respectively, a large value (in absolute terms) for S_{ads} directly leads to a strong temperature dependency of G_{ads}.

Table 7 shows G_{ads} values for all closed-shell intermediates under study, evaluated at pertinent reaction conditions (523 K, 673 K; 1 bar, 40 bar). At 673 K and 1 bar, the adsorption of guaiacol and catechol on the Ru(0001) surface yielding the surface structures **1** and **13** are endothermic processes, while the adsorption of phenol and benzene forming **16** and **20** are slightly exothermic. These results indicate that all four aromatic structures considered can easily desorb from the Ru surface. The importance of considering the entropy for the adsorption processes can be illustrated best by comparing G_{ads} with the adsorption energy E_{ads} (Table 7). In contrast to the G_{ads} values, the E_{ads} results for the species under study are -107 kJ mol^{-1} or more exothermic, which may misleadingly suggest that the adsorbates can hardly desorb. The data in Table 7 further show that G_{ads} becomes thermodynamically more favorable at lower temperature and higher pressures. Thus, within the considered temperature and pressure range, the most exothermic values of G_{ads} are calculated for 523 K and 40 bar, between -23 kJ mol^{-1} and -53 kJ mol^{-1}. The values in Table 7 indicate that the desorption of the aromatic adsorbates is thermodynamically accessible at all reaction conditions relevant for the HDO process.

There is one final issue to be commented on in this section. Despite G_{ads} depending strongly on temperature and pressure, the relative order of the G_{ads} values does not change,

Table 7: Calculated adsorption energies E_{ads} and Gibbs free energies of adsorption G_{ads} of relevant adsorbates, in kJ mol^{-1}.

		E_{ads}	G_{ads}			
			523 K, 1 bar	523 K, 40 bar	673 K, 1 bar	673 K, 40 bar
1	guaiacol	-107	-7	-23	21	0
13	catechol	-116	-14	-30	16	-5
16	phenol	-130	-32	-48	-4	-25
20	benzene	-136	-37	-53	-10	-30

independent of the reaction conditions. The adsorption becomes more favorable in the order guaiacol, catechol, phenol, benzene. The same trend is also found for E_{ads}, as mentioned in Section 6.3.1.1.

6.3.1.5. Reaction Pathways

This section presents possible pathways that are derived from the Gibbs free energies discussed in the preceding sections. The discussion starts with the most likely pathway (Figure 25) which has been deduced by choosing for each intermediate the reaction with the lowest activation barrier. In the second part of this section, alternative pathways that are kinetically accessible are discussed. These alternative pathways feature barriers that are

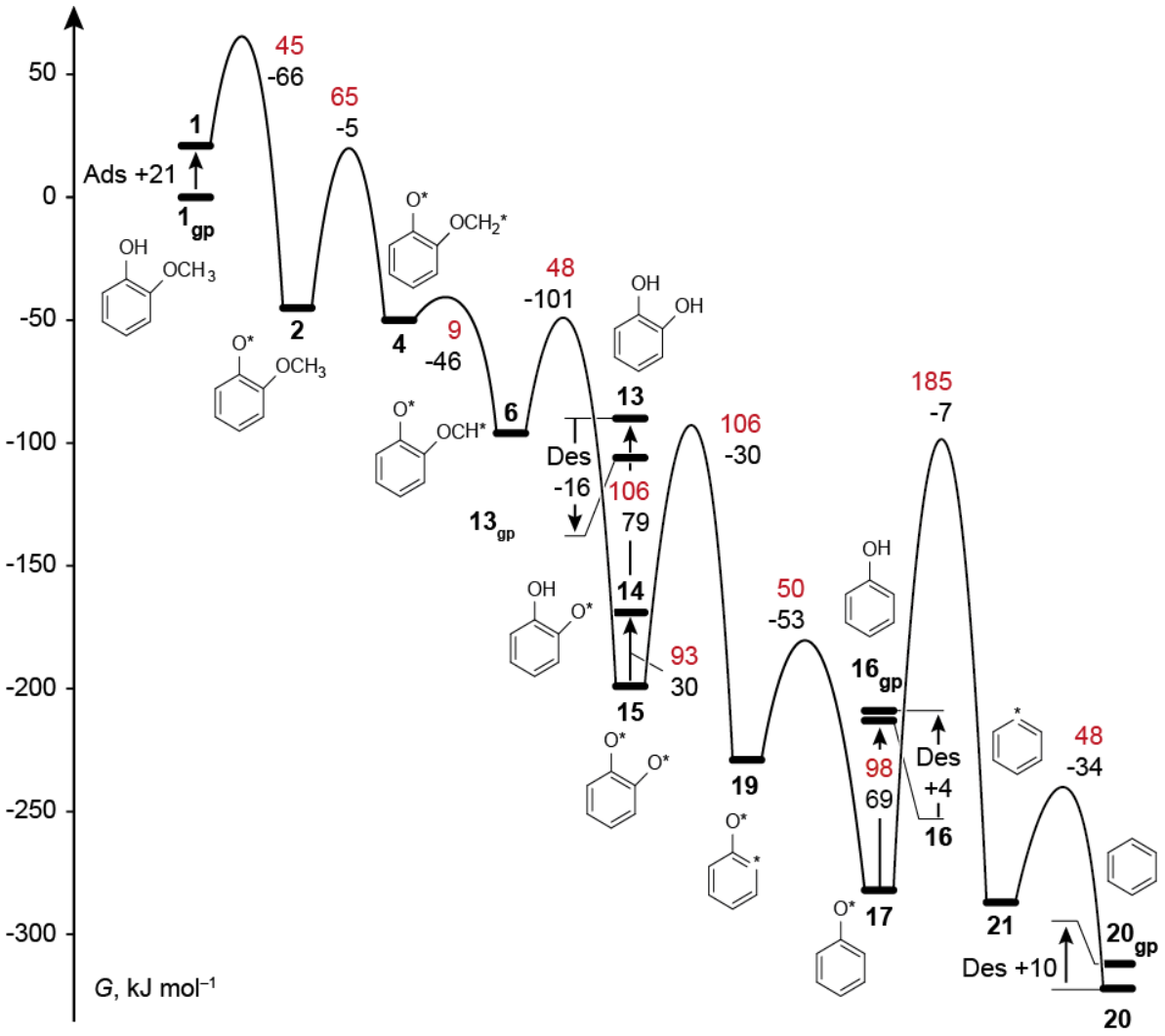

Figure 25: Gibbs free energy profile at 673 K and 1 bar for the most likely reaction pathway on Ru(0001). Intermediate states are represented by bars, TS states by arches. Numerical values at the arcs denote the Gibbs free energies of activation (red) and of reaction (black). Also shown are Gibbs free energies of reaction and of activation for hydrogenation steps that yield catechol and phenol.

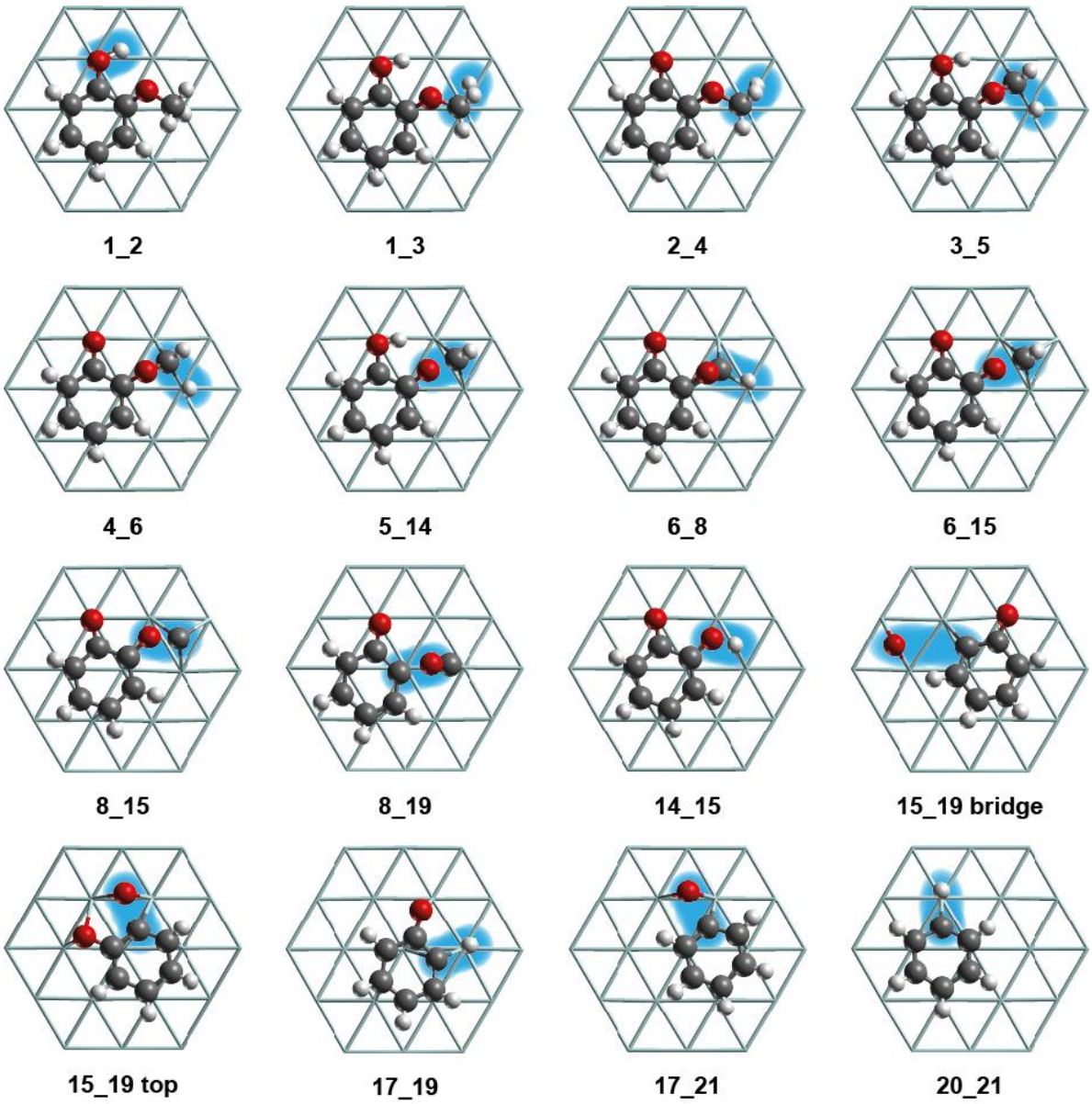

Figure 26: Top view on the optimized structures of all adsorption complexes of TS structures encountered along the reaction pathways on Ru(0001) discussed in Section 6.3.1.5. Black: C, red: O, white: H, cyan: Ru. For the sake of a clearer view, the Ru-Ru bonds are displayed as sticks. The blue background highlights the cleaving / forming bond.

slightly higher (typically by up to 10 kJ mol^{-1}) than those of the most likely pathway. Recall that the discussion refers to reactions at 673 K and 1 bar. The TS structures involved in the discussed pathways are displayed in Figure 26.

The most likely pathway. Starting from gas phase guaiacol $\mathbf{1_{gp}}$ and an empty Ru(0001) surface, the initial step of this pathway is the endothermic formation of the adsorption complex of guaiacol **1** on the metal surface, with G_{ads} = -21 kJ mol^{-1}. For adsorption complex **1**, only two reactions with G_a < 100 kJ mol^{-1} have been identified, the exothermic

dehydrogenation reactions at the hydroxyl group (**1-2**, G_a = 45 kJ mol^{-1}) and at the methyl group (**1-3**, G_a = 56 kJ mol^{-1}). The most preferred reaction is the O-H scission to form adsorbed guaiacolate **2**, a process that stabilizes the system by -66 kJ mol^{-1}. Note that this is not the most exothermic reaction of **1**. The most exothermic reaction of **1** is the removal of the methyl group (**1-14**) with G_r = -110 kJ mol^{-1}. However, this reaction can be considered as kinetically hindered due to the high estimated barrier of around 170 kJ mol^{-1}. Due to the relatively low lying barrier for the reaction **1-3**, an alternative pathway proceeding with **3** will be discussed later. After the dehydrogenation at the hydroxyl group, the most likely pathway continues with two consecutive exothermic dehydrogenation steps at the methyl group, **2-4** and **4-6**, with barriers of 65 kJ mol^{-1} and 9 kJ mol^{-1}, respectively. All other reactions for intermediate **2** can be ruled out as possible side reactions due to their high barriers, $G_a \geq$ 135 kJ mol^{-1}.

The dehydrogenation at the methyl group **2-4** activates the bonds at the aliphatic substituent in the product structure **4**. This is not only reflected in the low barrier of the further dehydrogenation as just mentioned. The barrier of the H_2C-O bond cleavage (**4-15**) can also be considered as accessible, 56 kJ mol^{-1}. Recall the high barrier of ~170 kJ mol^{-1} for the H_3C-O bond scission (**1-14**), i.e. the analogue reaction at the *saturated* methoxy group. The barriers for all cleavage reactions of any C_{aryl}-O bond in **4** were calculated far above 100 kJ mol^{-1}, and thus need not be considered as side reactions (Table 4).

The most likely pathway thus proceeds with the formation of **6** from **4**. At the stage of **6**, the reactions with the lowest barriers are **6-8**, the removal of the (last) H from the aliphatic carbon center, G_a = 50 kJ mol^{-1}, and **6-15**, the cleavage of the C_{alkyl}-O bond, G_a = 47 kJ mol^{-1}. All other reactions of intermediate **6** are kinetically hindered due to their significantly higher barriers of at least 95 kJ mol^{-1}. Structure **6** is the first intermediate along this pathway, for which the C_{alkyl}-O scission is kinetically competitive to the C_{alkyl}-H scission. In view of the slightly lower barrier of the C_{alkyl}-O scission and its significantly stronger exothermicity, G_r = -103 kJ mol^{-1}, **6** will likely react to form catecholate in reaction **6-15**. The alternative path proceeding with the less exothermic dehydrogenation step **6-8**, G_r = -36 kJ mol^{-1}, will be discussed later on.

There are two possible reactions for adsorbed catecholate **15**: rehydrogenation at one O site **15-14** (reversed **14-15**) or reaction **15-19**, the cleavage of the C_{aryl}-O bond. The two reactions have comparable barriers, 93 kJ mol^{-1} and 106 kJ mol^{-1}, respectively. The kinetically slightly more preferred hydrogenation step is endothermic by 30 kJ mol^{-1},

whereas the C-O cleavage step is exothermic, by -30 kJ mol^{-1}. After a second endothermic hydrogenation step with a high barrier (reversed **13-14**, G_r = 79 kJ mol^{-1}, G_a = 106 kJ mol^{-1}) and the exothermic desorption (G_{des} = -16 kJ mol^{-1}), the rehydrogenation path ultimately leads to the formation of catechol in the gas phase $\mathbf{13_{gp}}$ (Figure 25), the primary intermediate product observed in experiment.[26,27] Due to the endothermic nature of the overall reaction from **15** to $\mathbf{13_{gp}}$, this reaction is most likely only a side reaction for **15**. Thus, the more preferred reaction for **15** is the C-O cleavage **15-19** to form 2-oxyphenyl on the Ru surface. The corresponding intermediate product **19** can either be rehydrogenated at the aromatic ring (reverse **17-19**) to form the adsorption complex of phenolate **17** or undergo a second C-O cleavage step **19-22** to form benzyne. Although thermodynamics slightly favors **19-22**, G_r(**19-17**) = -53 kJ mol^{-1} vs. G_r (**19-22**)= -67 kJ mol^{-1}, the reaction is ruled out due to the significantly higher barrier, G_a(**19-17**) = 50 kJ mol^{-1} vs. G_a(**19-22**) = 138 kJ mol^{-1}. Therefore, the main reaction path continues with the formation of phenolate **19-17**.

Adsorbed phenolate **17** is a very stable species which renders any transformation a challenge. The rehydrogenation at the oxygen, with G_r = 69 kJ mol^{-1} and G_a = 98 kJ mol^{-1}, yields adsorbed phenol **16**, which in return can desorb in a quasi thermo-neutral process. This is the most preferred reaction for **17,** as the only alternative reaction is **17-21,** the thermo-neutral C-O cleavage, which features a very high barrier of 185 kJ mol^{-1}.

Thus the calculated results predict that the HDO of guaiacol over Ru(0001) ends with the formation of phenol, which agrees with the experiment over Ru/C, carried out under H_2 pressures below 1 bar.[27-29] However, as benzene is observed as product under elevated H_2 pressure of around 40 bar,[26] a further reaction of the C-O cleavage product phenyl **21** to benzene **20** should be included in the current discussion, despite of the high barrier associated with the formation of **21**. The final step from phenyl to benzene is the exothermic rehydrogenation **21-20** (reversed **20-21**) at the C_6 ring, G_r = -34 kJ mol^{-1}, which has a barrier of 48 kJ mol^{-1}. After its formation, the benzene adsorbate can easily desorb from the Ru(0001) surface in a weakly endothermic step.

Because of the high C-O cleavage barrier for phenolate (**17-21**), it is reasonable to consider an alternative mechanism, in which phenolate is hydrogenated to form phenol (reverse **16-17**) before the C-O bond cleaves to yield phenyl and OH in reaction **16-21**, which has a lower barrier of 124 kJ mol^{-1} (Figure 27). However, **16_21**, the highest lying TS for this alternative mechanism, is by 193 kJ mol^{-1} less stable than the phenolate adsorption complex **17**. Thus TS **16_21** is of comparable stability as TS **17_21** which is by 185 kJ mol^{-1} less

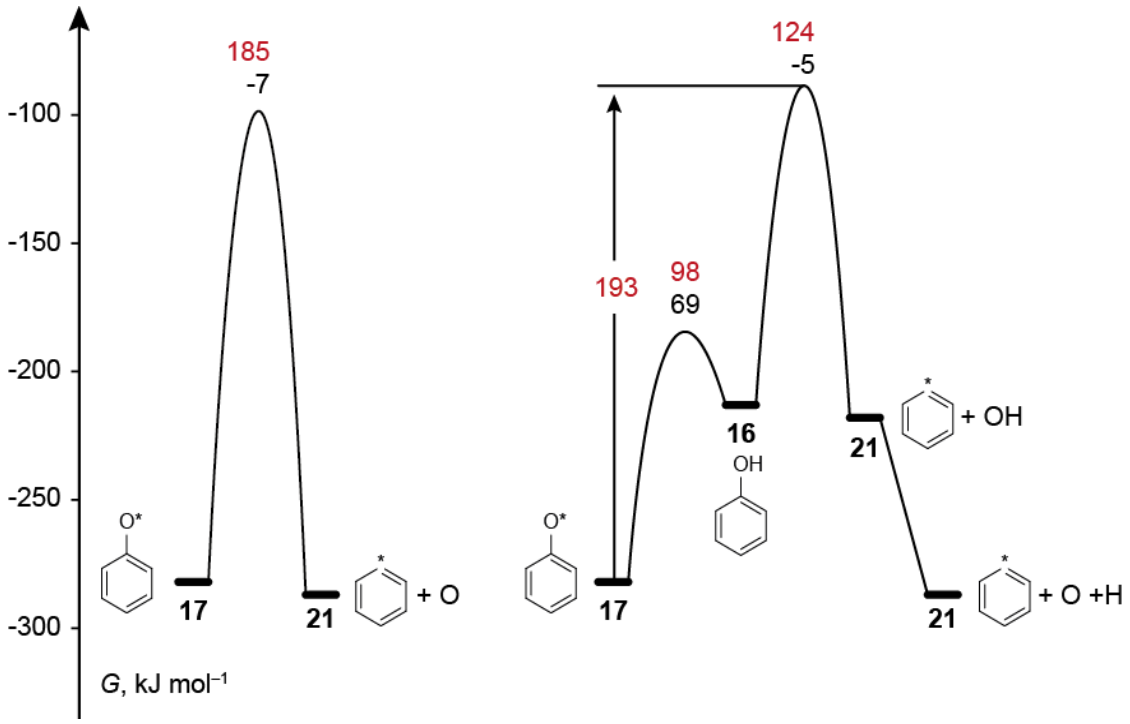

Figure 27: Gibbs free energy profile at 673 K for the two pathways possible for the cleavage of the phenolate C-O bond on Ru(0001), as discussed in Section 6.3.1.5. Layout as in Figure 25.

stable than structure **17**. Therefore, one can conclude that the C-O cleavage mechanism via the intermediate formation of surface phenol **16** is as unfavorable as the "direct" scission of the C-O bond via reaction **17-21**. Recall also that once phenol is formed on the Ru(0001) surface, it would rather desorb in a thermo-neutral process than undergo the C-O cleavage reaction with a high barrier.

The main reaction path discussed above is consistent with the mechanism formulated by *Laurent* and *Delmon* for the reaction of guaiacol over CoMo and NiMo alloys,[102,103] which has recently also been suggested for the reaction on Ru.[26] The present study revealed details of the reactions at the Ru surface which previously have not been addressed. Indeed, the C_{alkyl}-O bond cleaves prior to the two C_{aryl}-O bonds. However, the cleavage steps do not occur from guaiacol, catechol and phenol as originally suggested,[102,103] but from the adsorption complexes formed by their dehydrogenated analogues which are significantly more stable. Due to their radical nature, the dehydrogenated species are unable to desorb and thus cannot be detected in the product mixture. Another aspect, which has not been covered in the original mechanism,[102,103] is the activation of the methoxy group prior to the actual cleavage of the C_{alkyl}-O bond. The aliphatic C center is not removed as a methyl group because the cleavage of the C-O bond is kinetically accessible only after the CH_3 group has

been dehydrogenated, which allows the formation of a bond between the C center and the catalyst surface leading to the activation of the C_{alkyl}-O bond.

Alternative pathways. As mentioned above, in the initial step, guaiacol does not necessarily have to be dehydrogenated at the OH group (**1-2**). The dehydrogenation step **1-3** at the methoxy group is also accessible (Figure 28) as the associated barrier is only by 11 kJ mol^{-1} higher than the barrier of **1-2**. As on the most likely pathway, the methoxy group is activated by the removal of the first H in reaction **1-3**. The methoxy group continues to dehydrogenate (**3-5**) yielding intermediate **5** which features an –OCH moiety. The Gibbs free energy profile of the reactions from **1** to **5** (Figure 28) is similar to the profile from **2** to **6** discussed for the most likely pathway (Figure 25). G_a and G_r of the corresponding reactions differ by only **9** kJ mol^{-1} or less. Intermediate **5** may undergo two reactions. One option is the dehydrogenation **5-6** at the OH group, yielding **6** (Figure 28), an intermediate on the main reaction pathway. The highest barrier along the discussed reaction path from **1** via **3** to **6** is 56 kJ mol^{-1}, even slightly lower than the highest barrier, 65 kJ mol^{-1}, on the path discussed as

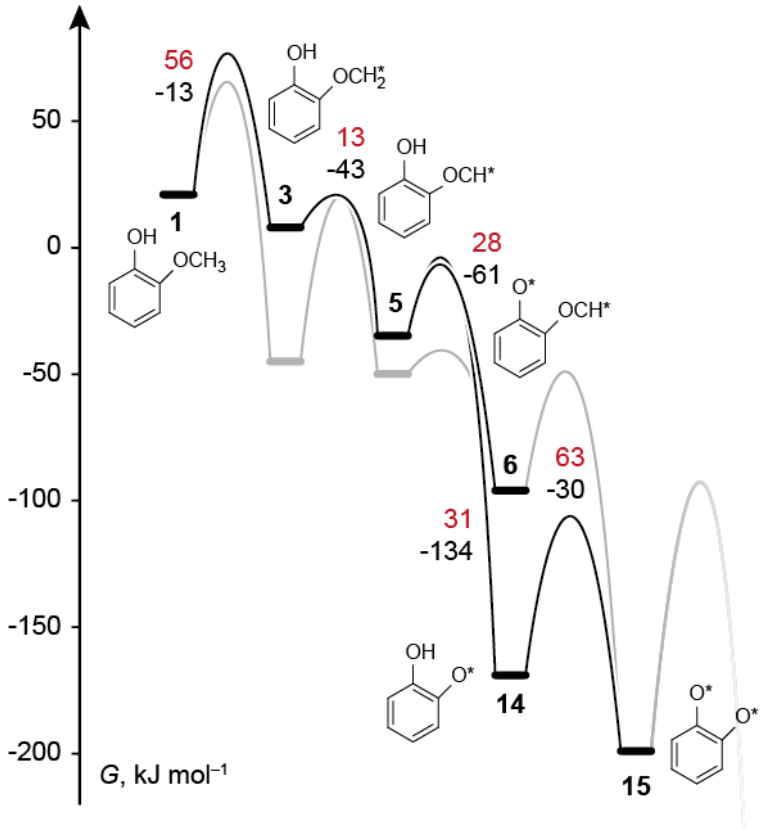

Figure 28: Gibbs free energy profile at 673 K for reaction pathways on Ru(0001) via intermediate **3**, which are alternatives to the most likely path shown in Figure 25. Lay-out as in Figure 25. For easier comparison, a part of the most likely pathway shown in Figure 25 is displayed here in gray.

the most likely route (**1** via **2** to **6,** Figure 25). However, as visible from Figure 28, the first reaction of the most likely pathway, **1-2**, is by -53 kJ mol^{-1} more exothermic than **1-3**, the initial step of the alternative pathway discussed here. In consequence, the stationary points along the main path are always more stable than or nearly degenerated (**2_4** vs. **3_5**) with the stationary points along the alternative path.

The second kinetically accessible reaction for **5** is the strongly exothermic scission of the C_{alkyl}-O bond **5-14**, G_r = -134 kJ mol^{-1}; its barrier, 31 kJ mol^{-1}, is comparable to that of **5-6** (Figure 28). As addressed in Section 6.3.1.2, reaction **5-14** is both thermodynamically and kinetically more favored than the analogous reaction **6-15**, which is part of the most likely pathway. The only difference between **5-14** and **6-15** is that the IS and the product in **5-14** feature an OH group, while the IS and product of **6-15** is dehydrogenated, displaying an oxo group. As **5-14** is kinetically easily accessible, the competing reaction **5-7**, the removal of the last H form the OCH group, which features a barrier of 61 kJ mol^{-1}, is unlikely to occur. Recall that the removal of the last H from the C_{alkyl} center of **6** (**6-8**) was discussed to be competitive to the C_{alkyl}-O scission step **6-15** of the most likely pathway.

As discussed in the context of the most likely pathway, the surface complex of hydrogen catecholate **14** obtained from C_{alkyl}-O bond scission can either be hydrogenated at the oxo group to form surface catechol **13**, which can desorb, or it can dehydrogenate at the remaining OH group to form catecholate **15** that continues to react as described for the most likely reaction path.

A similar reaction path as the one described above was proposed in a computational study addressing HDO of guaiacol over Ru[137] where species **5** was proposed to occur as intermediate on the main pathway.[137] Then, instead of continuing with the cleavage of the C_{alkyl}-O bond **5-14** as shown here in Figure 28, the C_{aryl}-O bond cleavage **5-18** was suggested to occur, which is reported to require an activation *energy* E_a of 102 kJ mol^{-1},[137] slightly higher than the G_a and E_a values of 87 kJ mol^{-1} and 95 kJ mol^{-1}, respectively, calculated in the present study. Recall that reaction **5-18** has been ruled out in the discussion of the present work, in view of to the significantly lower barrier, only 28 kJ mol^{-1}, determined for the competing reaction **5-14**.

Along the most likely pathway, there is a second intermediate besides guaiacol **1** which does not have a single clearly preferred reaction. Also intermediate **6** is associated with two reactions of similar barriers, the C_{alkyl}-O scission **6-15**, as discussed for the main pathway, and the less exothermic removal of the last H from the aliphatic carbon center, reaction **6-8**

(Figure 29). Three reactions may be discussed for the corresponding product **8**. The kinetically most favored reaction **8-15** is the cleavage of the C_{alkyl}-O bond with G_a = 77 kJ mol^{-1} and G_r = -52 kJ mol^{-1}. The difference between this alternative path and the most likely path is only the precursor for the C_{alkyl}-O cleavage step, intermediate **6** with the singly hydrogenated –OCH moiety or intermediate **8** with the completely dehydrogenated –OC moiety. Experiment could help with discriminating the two variants if the surface species were analyzed, e.g., by RAIRS (reflection-absorption infrared spectroscopy).

Another reaction to be considered for **8** is **8-19**, the scission of the C_{aryl}-OC bond which is by 42 kJ mol^{-1} more exothermic than **8-15**, but kinetically less favorable due to the higher activation barrier of 92 kJ mol^{-1}. This less likely route would lead to the direct formation of intermediate **19**, which is an intermediate of the most likely pathway. Note that neither the surface complexes of catecholate **15** nor any of its O-hydrogenated analogues **13** or **14** is formed on that pathway, which seems to contradict the experimental detection of catechol as

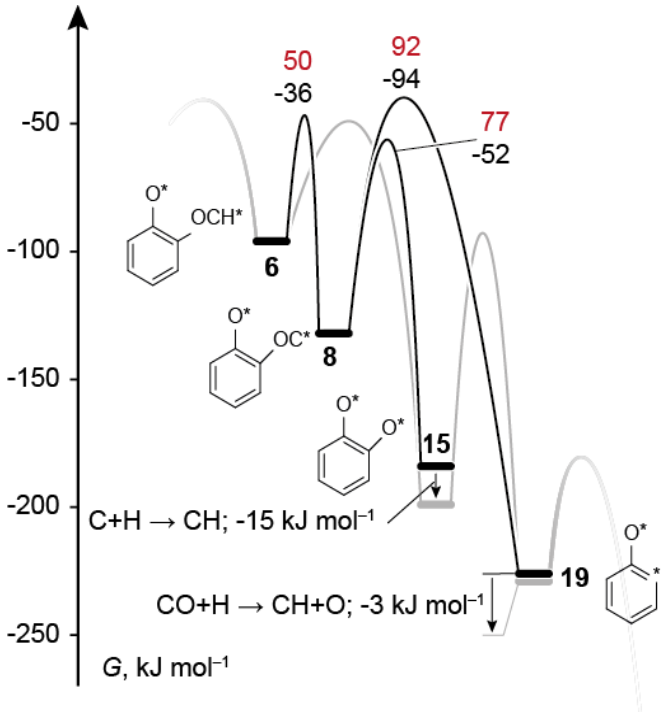

Figure 29: Gibbs free energy profile at 673 K for reaction pathways on Ru(0001) starting from intermediate **6**, which are alternative to the most likely path shown in Figure 25. Lay-out as in Figure 25. For easier comparison, a part of the most likely pathway shown in Figure 25 is displayed here in gray. The Gibbs free energies associated with the intermediates **15** and **19** in the alternative path in black differ from those values shown for the main path in gray. This is related to a variation of the side products. On the alternative path, **15** is co-adsorbed with C and H, **19** with CO and H. On the main path, **15** is co-adsorbed with methine, **19** with methine and O. The Gibbs free energies required for converting these co-products into each other are also shown.

intermediate.[26,27] This finding is consistent with categorizing this pathway as a mechanism of minor importance based on the high activation barrier of **8-19**. Nevertheless, a very recent study, which did not consider the competing reaction **8-15**, proposed a mechanism via **8-19** as the dominating HDO path.[138] The third reaction for intermediate **8**, the removal of the oxo group in reaction **8-12**, can be easily ruled out because of its high barrier of 197 kJ mol^{-1}.

6.3.2. Reaction on Stepped S3-Ru(10$\bar{1}$5) and S3-Ru(10$\bar{1}$5) Surfaces

The study of the reactions on the close-packed Ru(0001) surface has demonstrated that the guaiacol HDO process is limited by the scission of the C-O bonds of the intermediates catecholate (**15-19**) and phenolate (**17-21**). The energetics of the two C-O cleavage reactions was studied in addition at the stepped surfaces S4-Ru(10$\bar{1}$5) and S3-Ru(10$\bar{1}$5) (Section 3.2) to evaluate how step sites on the Ru catalyst affect the kinetics of the HDO process.

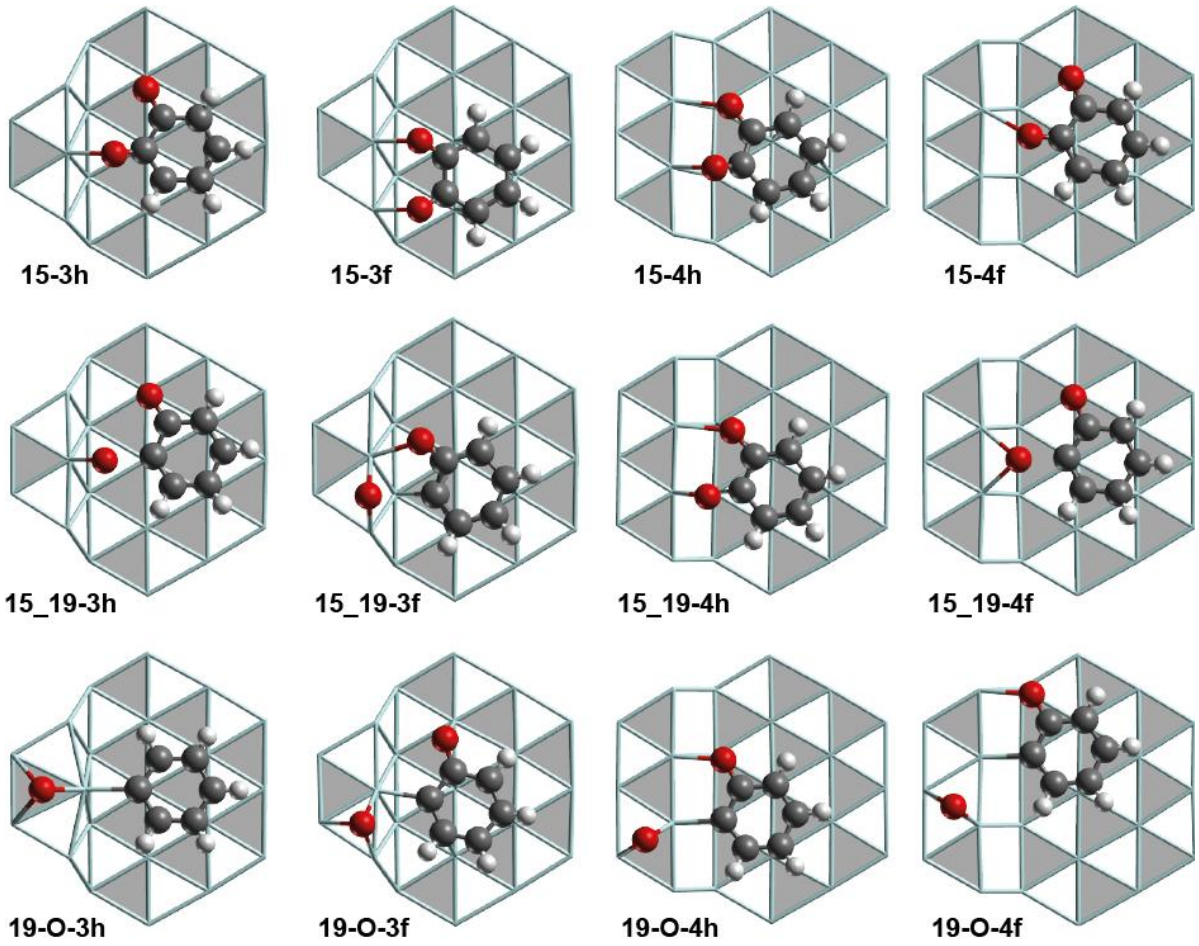

Figure 30: Optimized structures of adsorption complexes **15-yz** (**z = h, f**) of catecholate at step sites of Ru and the associated TSs **15_19-yz** as well as product structures **19-O-yz** of C-O cleavage reactions. Black: C, red: O, white: H, cyan: Ru. For the sake of a clearer view, the Ru-Ru bonds are displayed as sticks. hcp sites are marked in gray, fcc sites in white.

Subsequently, the adsorption complexes of catecholate and phenolate at step sites and their stability are discussed. Afterwards, the energetics of the C-O scission steps, also in the context of the complete HDO process, is addressed. The presented Gibbs free energies refer here again to reactions at 673 K. As adsorption processes are not studied in this section, all energetic properties are independent of the pressure.

6.3.2.1. Extension to Nomenclature Rules

In order to address the reactions and structures at step sites, the nomenclature introduced in Section 6.2 will be extended. Recall that identifiers of type **x** and $\mathbf{x_{gp}}$ (**x = 1** to **22**) refer to adsorption complexes on Ru(0001) and structures in the gas phase of the corresponding adsorbates. The complexes of catecholate (Figure 30) and phenolate (Figure 31) at step sites will be referred by identifiers of the form **x-yz** (**x** = **15**, **17**). **y** can be **3** or **4** indicating that the

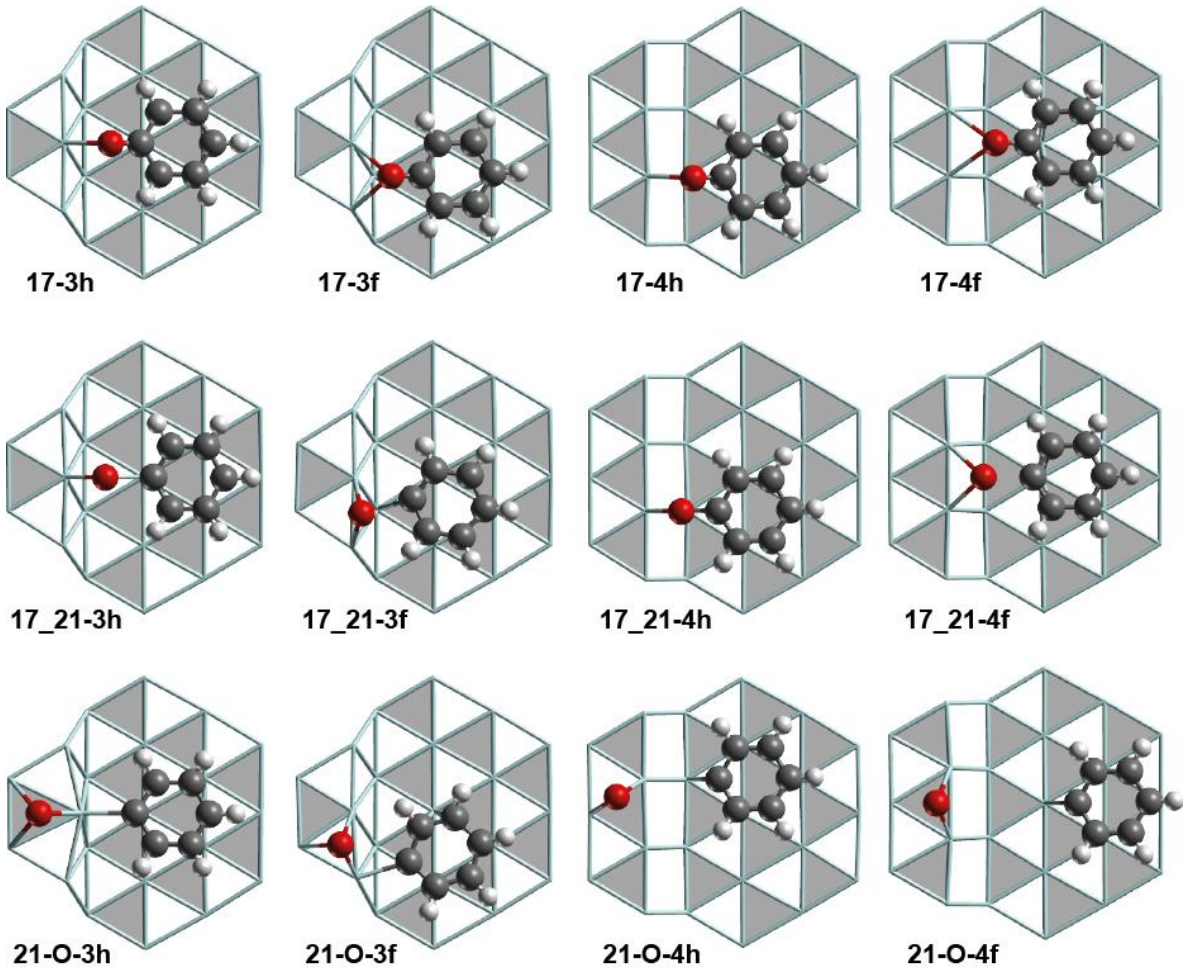

Figure 31: Optimized structures of adsorption complexes **17-yz** (**z = h, f**) of phenolate at step sites of Ru and the associated TS **17_21-yz** as well as product structures **21-O-yz** of C-O cleavage reactions. Black: C, red: O, white: H, cyan: Ru. For the sake of a clearer view, the Ru-Ru bonds are displayed as sticks. hcp sites are marked in gray, fcc sites in white.

complex is located at an S3 type or an S4 type step, respectively. The location of the center of the C_6 ring at an hcp or an fcc site is indicated by **z** = **h**, **f**, respectively.

The step-site variant of the C-O cleavage reactions of catecholate **15-19** and of phenolate **17-21** discussed in this section will be referred to as **15-19-yz** and **17-21-yz**. The corresponding TSs are labeled as **15_19-yz** (Figure 30) and **17_21-yz** (Figure 31), respectively. The various product structures are referred to as **19-O-yz** (Figure 30) and **21-O-yz** (Figure 31). The identifier **O** indicates that an oxygen atom is co-adsorbed with the cleavage product 2-oxyphenyl (**19-O-yz**) or phenyl (**19-O-yz**). The labels designate the IS state, the associated C-O cleavage TS, and the corresponding product structure. However, the **yz** labels do not necessarily imply the position of the C_6 ring in the TS and the product structures correctly, as the C_6 ring may move during C-O cleavage.

As indicated in Figure 32a on the example of the C-O cleavage of catecholate, the C-O cleavage at a step site is studied as a process of three phases: (*i*) diffusion of the reactant from its most stable adsorption site on a terrace (**15**, **17**) to a step site yielding the adsorption complexes **x-yz** (**x** = **15**, **17**); (*ii*) the actual C-O cleavage yielding the product structure of type **19-O-yz** or **21-O-yz**, in which the scission products are co-adsorbed at the step; and (*iii*) diffusion of the C-O cleavage products to their most stable adsorption sites at formally infinite separation on a Ru(0001) surface. The corresponding changes in the Gibbs free

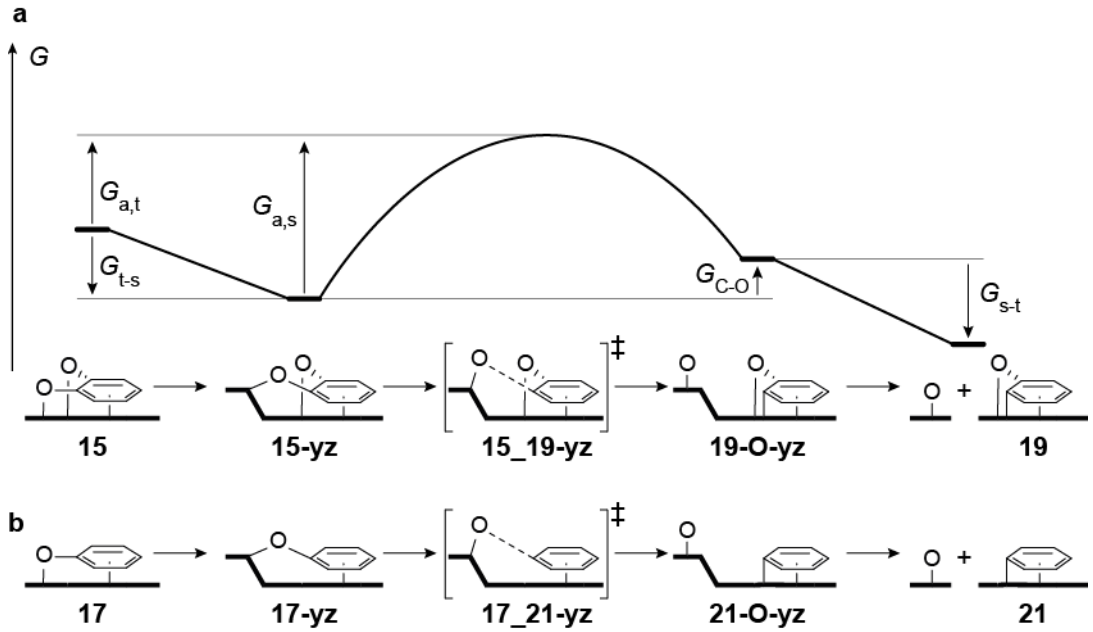

Figure 32: a) Schematic representation of the definitions of the free energy values $G_{t\text{-}s}$, $G_{C\text{-}O}$, $G_{s\text{-}t}$, $G_{a,t}$, and $G_{a,s}$ on the example of the C-O scission of catecholate at step sites. b) Schematic representation of the processes considered for the C-O scission of phenolate at step sites.

energy associated with the three phases are referred to as $G_{t\text{-}s,}$ $G_{C\text{-}O}$, and $G_{s\text{-}t}$, respectively (Figure 32). Note that $G_{C\text{-}O}$ can be understood as the *direct* Gibbs free energy of reaction for the C-O cleavage step according to the definition in Section 3.4. For the C-O cleavage step, two different types of activation barriers will be discussed (Figure 32). One is the *direct* barrier $G_{a,s}$ that is the difference between the Gibbs free energies of a TS and of the directly preceding *local* minimum state at the step site. The other type of barrier is $G_{a,t}$, calculated as the difference between the Gibbs free energies of a TS at a step site and the IS at the terrace site: $G_{a,t} = G_{t\text{-}s} + G_{a,s}$. As $G_{a,t}$ is always referred to the IS at the terrace site, differences in $G_{a,t}$ directly reflect differences in stability of isomeric TS structures.

6.3.2.2. Adsorption of Catecholate and Phenolate at Step Sites

Four adsorption complexes each at step sites have been identified for catecholate (Figure 30) and phenolate (Figure 31). In each of these structures, the C_6 ring is adsorbed on the *lower* terrace while at least one C-O moiety is bonded to the edge of the *ascending* step. The present study only considers such structures as the scission of carbon monoxide and its hydrogenated derivatives at structurally comparable Ru step sites have been reported to yield product structures in which the O center is localized at the *upper* terrace while the C moiety remains at the *lower* terrace.[97,247-249] The following discussion starts with the structurally less complex phenolate adsorption complexes **17-yz**, and later on will be extended to the catecholate complexes **15-yz**.

The four identified phenolate complexes differ significantly in their stability, as notable from the large range, from -9 kJ mol^{-1} to +57 kJ mol^{-1}, spanned by the associated $G_{t\text{-}s}$ values (Table 8). In the two more stable structures **17-4h** and **17-3f**, characterized by $G_{t\text{-}s}$ values of -9 kJ mol^{-1} and 16 kJ mol^{-1}, the C atom of the C-O group is located over a hollow site (Figure 31), similar to the structure of the phenolate complex **17** on a terrace, discussed in Section 6.3.1.1 (Figure 24). $G_{t\text{-}s}$ for the other two, less stable phenolate complexes **17-3h** and **17-4f** at step sites are 30 kJ mol^{-1} and 57 kJ mol^{-1} (Table 8). In these latter structures, the C-O carbon center binds to a top site (Figure 31).

The different stability of the various step-site complexes of phenolate can be partially related to the distortion of the adsorbate structure relative to the structure of phenolate in the gas phase. Table 8 shows the elongation of the C-O bond relative to the gas phase structure as well as the O-C-C_6 angle between the C-O bond vector and the C_6 plane that is defined by a least-squares fit to the positions of the atoms in the C_6 ring. The more stable complexes **17-4h** and **17-3f** feature shorter C-O bonds and smaller O-C-C_6 angles than the less stable structures

Table 8: Gibbs free energies of reaction $G_{t\text{-}s}$, $G_{C\text{-}O}$, and $G_{s\text{-}t}$ as well as the activation barriers $G_{a,t}$ and $G_{a,s}$ of the C-O scission of adsorbed catecholate and phenolate.[a] Also shown are the changes Δ(C-O) of the C-O bond length relative to the structure in the gas phase[b] and the angle formed by the C-O bond vector and the plane of the C_6 ring in the IS complexes. Energies in kJ mol^{-1}, distances in pm, angles in degree.

	Reaction	$G_{t\text{-}s}$	$G_{C\text{-}O}$	$G_{s\text{-}t}$	$G_{a,t}$	$G_{a,s}$	IS	Δ(C-O)	O-C-C_6
catecholate							**15_{gp}**		0, 0
	15-19		-30		106		**15**	13, 8	2, 4
	15-19-3h	-11	35	-54	135	147	**15-3h**	11, 8	27, 1
	15-19-3f	-24	64	-70	52	76	**15-3f**	9, 9	19, 19
	15-19-4h	-27	2	-5	63	90	**15-4h**	9, 13	31, 5
	15-19-4f	27	-55	-2	132	105	**15-4f**	11, 8	19, 1
phenolate							**17_{gp}**		0
	17-21		-7		185		**17**	4	2
	17-21-3h	30	51	-88	176	146	**17-3h**	7	27
	17-21-3f	16	47	-70	93	77	**17-3f**	6	16
	17-21-4h	-9	83	-81	95	104	**17-4h**	4	18
	17-21-4f	57	-15	-49	171	114	**17-4f**	7	19

[a] Definition according to Section 6.3.2.1 and Figure 32. [b] C-O bond length for gas phase catecholate **15_{gp}**: 123 pm for both C-O bonds; C-O bond length for gas phase phenolate **17_{gp}**: 127 pm.

17-3h and **17-4f**. In other words, the distortion is less pronounced for the more stable complexes. However, the distortion of the adsorbate is only one factor that influences the stability of a phenolate complex and provides only a rough rationalization for the stability trends. For instance, the distortion argument cannot explain why **17-4f** is less stable than **17-3h**, the phenolate complex with the largest O-C-C_6 angle.

The relative stability of the catecholate complexes shows a similar pattern as the stability of the phenolate complexes. Again, the complex **15-3f** at the fcc site close to a S3 type step and the hcp adsorbed complex **15-4h** next to a S4 type step ($G_{t\text{-}s}$ = -24 kJ mol^{-1} and -27 kJ mol^{-1}) are thermodynamically more preferred than the complexes **15-3h** and **15-4f**. While all phenolate complexes feature their only C-O bond perpendicular to the edge of the step site, the structures of the catecholate complexes are not as uniform. In the optimized structures of the catecholate adsorption complexes, one C-O bond is always bound to the step edge; the second C-O group either interacts with Ru centers of a terrace site or at the step edge. The latter case is found for the more stable structures **15-3f** and **15-4h**. The O-Ru interaction induces a slight rotation of the C_6 ring compared to the phenolate complexes at analogous adsorption sites. This rotation allows both O centers of the substrate to interact

with the Ru atoms at the step edge. In the less stable catecholate complexes **15-3h** and **15-4f**, only one O center interacts with the step edge, while the other O center binds to a top site on the terrace. The C atom carrying the O center at the terrace site adsorbs over a hollow site, similar to the complex of phenolate **17** at terrace sites (Figure 24). Recall that such a structure with the C-O carbon center over a hollow site was discussed to be the most preferred adsorption geometry for aromatic C-O groups on close-packed Ru surfaces (Section 6.3.1.1). It has been attempted to relate the stability of the various catecholate complexes to the distortion of the adsorbate geometry, as done for the phenolate complexes. However, the data in Table 8 do not show any obvious correlation between the stability and the distortion of the catecholate adsorbates.

6.3.2.3. Energetics of the C-O Cleavage Process at Step Sites

Table 8 provides an overview of the energetics of the various C-O cleavage reactions at step sites. The $G_{a,t}$ values indicate that the lowest lying TSs of catecholate C-O scission are associated with the reactions **15-19-3f** ($G_{a,t}$ = 52 kJ mol^{-1}) and **15-19-4h** (63 kJ mol^{-1}) which proceed via the energetically low lying catecholate complexes **15-3f** and **15-4h**. The corresponding TS structures **15_19-3f** and **15_19-4h** are by 53 kJ mol^{-1} and 43 kJ mol^{-1}, respectively, more stable than **15_19**, the TS of the analogous reaction on Ru(0001). A discussion of the reaction pathways via the reactions **15-19-3h** and **15-19-4f** will be omitted in view of their high barriers $G_{a,t} \geq$132 kJ mol^{-1}.

The kinetically more accessible C-O cleavage reactions **15-19-3f** and **15-19-4h** start with the exothermic formation of the catecholate complexes **15-3f** and **15-4h** at step sites that are of similar stability, $G_{t\text{-}s}$ = -24 kJ mol^{-1} and -27 kJ mol^{-1}, respectively. The direct barriers $G_{a,s}$ of the actual C-O cleavages at a step site are 76 kJ mol^{-1} for **15-19-3f** and 90 kJ mol^{-1} for **15-19-4h**, indicating that reaction **15-19-3f** is kinetically slightly preferred. While the kinetically more preferred pathway is associated with $G_{C\text{-}O}$ = 64 kJ mol^{-1}, the C-O cleavage on the alternative path **15-19-4h** is thermo-neutral and thus thermodynamically preferred. The difference in $G_{C\text{-}O}$ is related to the interaction of the O atoms with the metal centers at the step edge. During the thermo-neutral C-O cleavage in reaction **15-19-4h**, both O atoms remain bound to the step edge (Figure 30). In contrast, in the endothermic C-O scission **15-19-3f**, both O centers are bound to the step edge in the IS **15-3f** and the TS **15-19-3f**, but not in the corresponding product structure **19-O-3f** (Figure 30). The missing interaction between the not reacting C-O group and the step edge in the product structure **19-O-3f** rationalizes the destabilization of that structure with respect to **19-O-4h**, the C-O cleavage

product of the thermo-neutral C-O cleavage of **15-19-4h**. When discussing the $G_{C\text{-}O}$ values, one should keep in mind that the product structures **19-O-3f** and **19-O-4h** are *local* minimum structures that are directly reached from the TSs. In other words, the co-adsorbed 2-oxophenyl and O moieties in those structures are *not necessarily* in their most preferred adsorption geometry. Rather, diffusion of these molecular fragments to their most stable adsorption sites on a Ru terrace entails (in part considerable) stabilization, as indicated by the $G_{s\text{-}t}$ values of -70 kJ mol^{-1} (**15-19-3f**) and -5 kJ mol^{-1} (**15-19-4h**, Table 8).

On a close-packed Ru terrace, the C-O cleavage product 2-oxophenyl can undergo rehydrogenation in an exothermic process with a barrier of 52 kJ mol^{-1} to yield phenolate, as discussed in Section 6.3.1.5. This reaction directly leads to the second C-O scission reaction under study. Also for phenolate, the reactions **17-21-3f** and **17-21-4h** are kinetically preferred compared to the reaction **17-21** on a terrace, as can be seen from the $G_{a,s}$ values around 95 kJ mol^{-1} (Table 8). At variance, similar to the reaction **17-21** on a terrace, the reactions **17-21-3h** and **17-21-4f** can be considered as kinetically inaccessible and thus will be omitted in the following discussion. The diffusion of phenolate **17** adsorbed on a terrace to the step sites to form **17-3f** or **17-4h** is characterized by $G_{t\text{-}s}$ of 16 kJ mol^{-1} and -9 kJ mol^{-1}, respectively. The $G_{t\text{-}s}$ values show that diffusion of phenolate from the terrace to the step sites is generally thermodynamically less favored than the corresponding process of catecholate (Table 8). One can rationalize this by the strained structure of the adsorption complex **15** of catecholate on the terrace (Section 6.3.1.1). This strain is released by the diffusion to the step site, which renders the diffusion of catecholate to the step site a thermodynamically favorable process. At variance, there is no such effect for the diffusion of phenolate, as the adsorption complex **17** of phenolate on a terrace site is not under strain.

The actual cleavage of the phenolate C-O bond is associated with direct barriers $G_{a,t}$ of 77 kJ mol^{-1} (**17-21-3f**) and 104 kJ mol^{-1} (**17-21-4h**), comparable to the values for catecholate. Both C-O cleavage steps are endothermic processes with $G_{C\text{-}O}$ = 47 kJ mol^{-1} and 83 kJ mol^{-1}, respectively. The product species phenyl and O are again considerably stabilized by their diffusion to the preferred adsorption sites on a Ru(0001) surface. The phenyl formed can easily be rehydrogenated to form the experimentally observed benzene[26] as discussed in Section 6.3.1.5.

Although the lowest $G_{a,s}$ values of catecholate (76 kJ mol^{-1}, **15-19-3f**) and phenolate (77 kJ mol^{-1}, **17-21-3f**) agree very well, there are some differences between the reactions of the two types of adsorbates that are worth commenting on. One issue is the relative stability

of the IS complexes at step sites. While the catecholate complexes **15-3f** and **15-4h** are of similar stability, the phenolate complex **17-4h** is by 25 kJ mol^{-1} more stable than its isomer **17-3f**. The difference between catecholate and phenolate may be related to the orientation of the aromatic substrates. While the two catecholate complexes display slight differences in the orientation of the C_6 ring (Figure 30), the C_6 moiety in both phenolate complexes show the same orientation (Figure 31). A second issue to be addressed here are the Gibbs free energies $G_{C\text{-}O}$ of the actual C-O cleavage step which are notably endothermic for both reactions of phenolate, **17-21-3f** and **17-21-4h**. At variance, only one reaction of catecholate, **15-17-3f**, is endothermic while the other one, **15-17-4h**, is thermo-neutral. As previously discussed, the different energetics of the reactions of catecholate can be related to the interaction (or the absence of it) between the spectator (not reacting) C-O group and the Ru centers at the step edge. In the case of phenolate, there is no second C-O group that is able to interact with the Ru step and thus induce such a difference in $G_{C\text{-}O}$.

Inspection of all TS structures at step sites reveals that energetically low-lying TSs, as characterized by the $G_{a,t}$ values, feature the C center of the cleaving C-O bond over a (three-fold) hollow site. In contrast, all TSs with the C atom over a (one-fold) top site are energetically inaccessible. In other words, in the more stable TS structures, more metal atoms are coordinated to the adsorbate. This is in line with what has been discussed for the N_2 scission on Ru[233] where more Ru centers are involved in the TS at a step site than at a terrace site and thus help to stabilize the N centers that become under-coordinated upon bond scission.[233] In that case, the improved stabilization of the TS at a step site has been discussed as the reason for the lower barrier of the reaction at the step.[233] A similar argument can be used to rationalize why steps on a Ru catalyst are able to decrease the C-O scission barrier as illustrated on the example of phenolate. Similar to the situation of N_2 scission,[233] in the C-O cleavage TS of phenolate **17_21** on a terrace site (Figure 26) the C and the O centers interact with two neighboring bridge sites. These bridge sites share a common Ru atom which induces a repulsive interaction that destabilizes the TS.[250] In the structure of the step-site TSs **17_21-3f** and **17_21-4h** (Figure 31), the hollow site of the C center does *not* share any atoms with the top or the bridge site to which the O is bound. In consequence, repulsive interactions are absent, which leads to the stabilization of the TS structures and decreases the corresponding activation barrier.

In summary, on a Ru catalyst with step sites, C-O cleavage of catecholate and phenolate can proceed with direct barriers $G_{a,s}$ of 76 kJ mol^{-1} and 77 kJ mol^{-1}, respectively. Thus, not

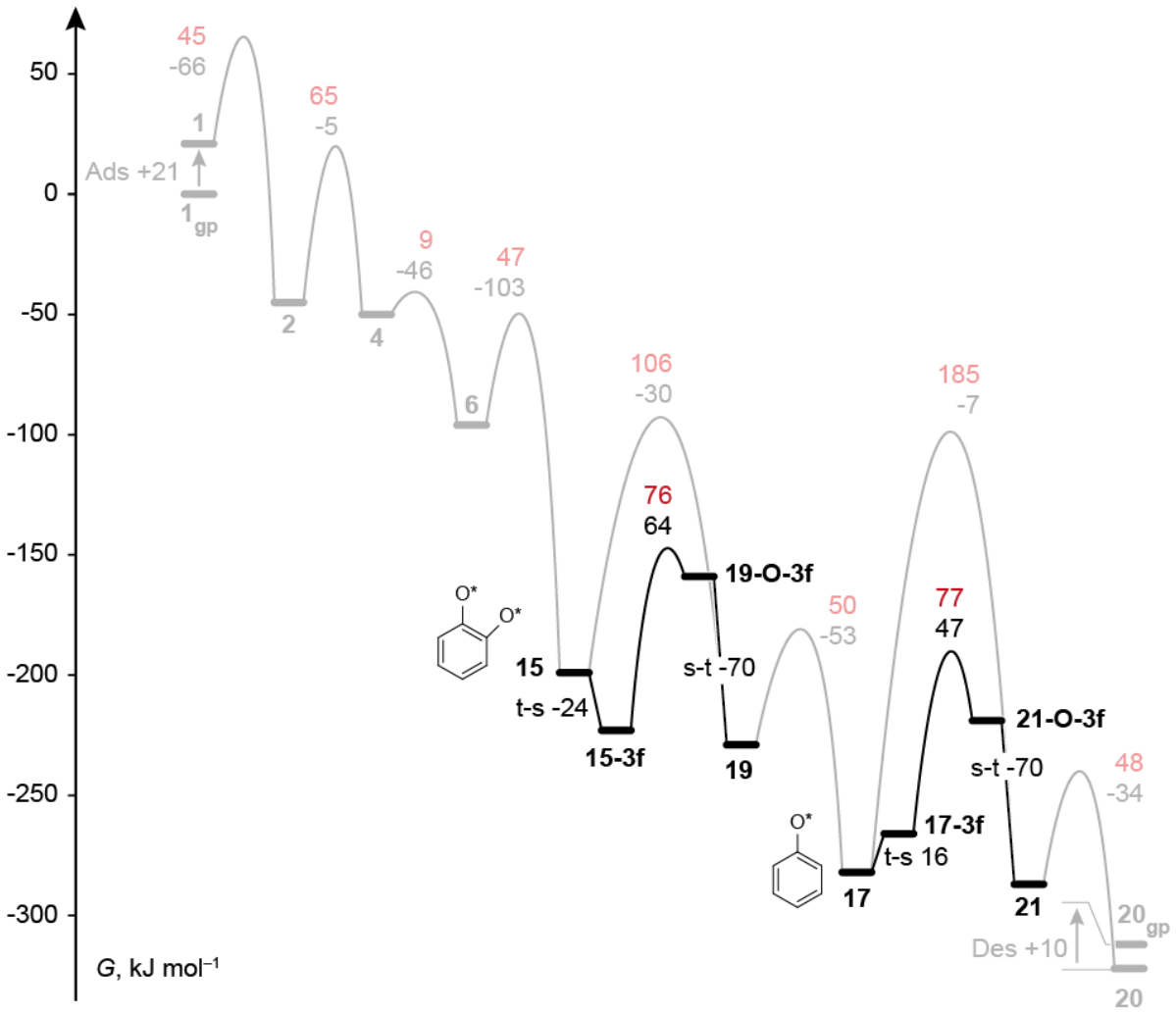

Figure 33: Gibbs free energy profile for the most preferred C-O cleavage of catecholate and phenolate on an fcc site at a S3 type step. The $G_{a,s}$ and $G_{C\text{-}O}$ values are displayed as red and black numbers, respectively. In addition, Gibbs free energies of diffusion $G_{t\text{-}s}$ and $G_{s\text{-}t}$ are shown. The Gibbs free energy profile for the most likely guaiacol HDO path on Ru(0001) is shown in the background, see Figure 25.

only the C-O cleavage of catecholate, but also the scission of the phenolate C-O bond is kinetically accessible (Figure 33), in agreement with the formation of benzene in the Ru-catalyzed guaiacol HDO experiment under elevated H_2 pressure.[26] Figure 33 shows the energetics of the C-O cleavage steps in the context of the most likely reaction pathway on Ru(0001) discussed in Section 6.3.1.3 (Figure 25). Figure 33 also shows that on a Ru surface with steps *and* terrace sites, the rate of the guaiacol HDO process is controlled by the kinetics of the scission of the aromatic C_{aryl}-O bonds, consistent with the experimental observation of catechol and phenol as intermediates and products.[26,27]

It is not necessary to discuss how the presence of steps affect the energetics of the other reactions involved in guaiacol HDO, as all reactions on Ru(0001) other than C_{aryl}-O cleavage

are associated with barriers of 65 kJ mol^{-1} or lower (Figure 33). If the steps increase the barrier associated with any of these other reactions, these transformation will rather occur on the terraces with barriers of at most 65 kJ mol^{-1}. Turned around, if steps have a barrier decreasing effect for these reactions, the corresponding barriers would have to be lower than 65 kJ mol^{-1}, the maximum value for a non-C_{aryl}-O-cleavage step on Ru terrace sites. In that case, these barriers would also be lower than $G_{a,s}$(**15-19-3f**) = 76 kJ mol^{-1}, the lowest barrier associated with the C_{aryl}-O cleavage at Ru step sites. Hence, independent of how the presence of steps affects the barriers of the non-C_{aryl}-O-cleavage reactions, one may safely assume that these reactions are not likely to have a significant impact on the overall HDO kinetics.

6.3.2.4. Interpretation of the Experimental Results

With the C-O cleavage reactions at step sites of Ru one is able to rationalize the formation of benzene. However, the arguments presented thus far are not able to explain how the H_2 pressure affects the selectivity of the reactions, mentioned in the introduction (Section 6.1), with phenol or benzene as final products.[26-29] One possibility would be that hydrogen plays a role in the mechanism for the C-O cleavage of phenolate, as benzene formation is only observed when the HDO process is carried out under elevated hydrogen pressure of around 40 bar.[26] However, there is no evidence for such a mechanism that may rationalize the experimental finding.[138] Yet, there is the possibility that hydrogen only plays an "indirect" role for the C_{aryl}-O cleavage as elaborated in the following.

The results discussed in the present chapter show that the cleavage of the phenolate C-O bond, which is necessary for the formation of benzene, is only possible at step sites of a Ru catalyst. In contrast, catecholate may undergo C-O scission at steps *and* on the terrace site of Ru. From these results and the experimental observation that benzene only forms at 40 bar H_2 pressure,[26] one may speculate that Ru step sites are only available under elevated hydrogen pressure. It is possible that carbon depositions form at step sites under lower H_2 pressure, which ultimately leads to the blocking of the only sites that are catalytically active for the C-O cleavage of phenolate. Formation of carbon deposits during the HDO process may be assumed to be reduced or even inhibited at elevated H_2 pressure, similar to the situation reported for the methanation process and for steam reforming over Ni.[251]

This hypothesis is supported by the fact that the experimental studies on guaiacol HDO mention coke formation as a possible reason for the deactivation of the catalyst.[26,27,29] Analysis of the published experimental data indicates that the deactivation proceeds faster at lower H_2 pressure. In the experiment at 1 bar H_2 pressure yielding phenol, the guaiacol

conversion rate drops continuously from 100% at the start of the process to about 30% after 3 to 4 hours time on stream.[27] In contrast, in the experiment at 40 bar yielding benzene, in which the formation of carbon deposition is assumed to be inhibited, the conversion rate drops within the first two hours time on stream from initially 50% to about 35% but stays constant for the next 4 hours.[26]

It is well known that carbonaceous species tend to form at step sites of metal surfaces,[73,248,252-255] which in return *may* lead to the inhibition of catalytic reactions.[248,252-254] In the particular case of Ru-catalyzed reactions, TPD (temperature programmed desorption) experiments have demonstrated that C atoms at steps suppress the scission of carbon monoxide,[248,253] which is kinetically accessible only at step sites.[219,248,253] However, carbon depositions do not generally lead to a reduced catalytic activity; for instance, the hydrogenation of olefins on Pd benefits from the presence carbon depositions.[256,257] The assumption that an elevated H_2 pressure can reduce carbon deposition is supported by experimental studies which report that Ni or Ru based catalysts can be regenerated with H_2, once they are deactivated due to coke formation.[251,258]

6.4. Conclusions

This computational study provides substantial new insight into the mechanism of the Ru-catalyzed HDO of guaiacol. It was shown that the reactions at the aliphatic side groups (OH, methoxy) of guaiacol follow similar patterns as the reactions of ethanol studied in Chapter 5. Also for guaiacol, the dehydrogenation at the aliphatic carbon activates the C_{alkyl}-O bond, so that its scission becomes kinetically easily accessible. This rationalizes the formation of catechol as an experimentally observed intermediate of guaiacol HDO on Ru.[26,27] A very recent work[139] has shown that the formation of catechol in guaiacol HDO over Pt[28,29,111,116,117] follows a comparable reaction pattern.[139]

It was further shown that the overall kinetics of the Ru-catalyzed guaiacol HDO is determined by the cleavage of the C_{aryl}-O bonds, in particular the C-O scission of the intermediates catecholate and phenolate. The calculations modeling the crucial C-O scission reaction at terrace sites and at step sites demonstrated that the reaction of catecholate may occur on terrace sites and at step sites. At variance, the C-O scission of phenolate is only kinetically accessible at steps.

Based on this new insight, this study provides a rationalization for the experimentally observed H_2 pressure dependency of the product selectivity of guaiacol HDO where the elevated H_2 pressure is crucial for the availability of step sites that otherwise are poisoned at

low H_2 pressure. In other words, at low H_2 pressure, the reaction can only occur at terrace sites where the catecholate C-O scission is associated with a barrier of 106 kJ mol^{-1} whereas the cleavage of the phenolate C-O bond, ultimately leading to the formation of benzene, is hindered due to a high barrier of 185 kJ mol^{-1}. At variance, under elevated H_2 pressure, the HDO reaction can also occur at step sites which allows the C-O scission of both catecholate and phenolate to proceed with decreased barriers of 76 kJ mol^{-1} and 77 kJ mol^{-1}, respectively. Of course, this interpretation is merely a hypothesis based on computational results. A confirmation by new experiments is highly desirable, e.g., by experiments that address the reaction on Ru single crystals with clearly defined surface structures, whose steps sites can selectively be blocked by thermal decomposition of deposited ethylene or CO.[248,253]

Chapter 7 Benchmark of DFT Strategies to Address van der Waals Interactions in Zeolites

7.1. Introduction

As mentioned in Chapter 1, zeolites are of eminent importance for various technical applications,[30,31] e.g., as catalyst for the conversion of methanol or ethanol to hydrocarbons as outlined in Section 2.3. Therefore, zeolites and their chemical properties have been the subject of many studies applying quantum chemical methods and models.[14,259] There are some specific issues that need to be accounted for when modeling zeolites. One issue is the correct description of the zeolite framework and its structural and electronic properties. The other and more challenging issue is the reasonable treatment of van der Waals (vdW) interactions between the zeolite framework and the adsorbates, which are incorrectly described by standard semi-local exchange-correlation functionals.[48] A possible DFT-based approach for reliably describing vdW interactions in zeolites is the hybrid MP2:DFT approach proposed by *Sauer* and co-workers.[37,40] In this approach, one evaluates the difference between the MP2 energy and the DFT energy for zeolite cluster models of varying sizes. Those energy differences are then extrapolated to clusters of infinite size and transferred as a reliable correction to the DFT energy calculated for a periodic model.[37] However, this method is computationally very demanding which limits its applicability as a routine method. A more economic alternative is to use QM/MM (quantum mechanics/molecular mechanics) methods in which only the reactive center is represented by quantum mechanical methods, while its surrounding is described by a force field that ideally accounts for vdW interactions. A QM/MM method that features periodic boundary conditions is the QM-Pot method;[260,261] it will be addressed in the discussion of the present chapter. Many other QM/MM methods have been developed for cluster model calculations, e.g., the ONIOM method („our own n-layered integrated molecular orbital and molecular mechanics“)[262] or the covEPE scheme (covalent elastic polarizable environment).[263] Also

these methods have been successfully applied for investigating various processes in zeolites.[264-267]

This chapter follows the presentation of Ref 268 where a benchmark study was carried out on the performance of selected DFT-based computational methods for weak interactions of various adsorbates in zeolites cavities. This work examined how well adsorption processes are described in H-ZSM5 and Silicalite, both zeolites of MFI structure type. In this study, a 3D periodical model is used to evaluate the adsorption energies of alkanes, alcohols, and water at the PBE-D2[49] level and with the vdW-DF2 functional.[50] As addressed in the methods section in Section 3.1, the PBE-D2 approach is a special case of the DFT-D2 scheme that accounts for vdW interactions by adding an empirical correction term to the energy at the PBE-DFT level.[49] At variance, vdW-DF2 denotes an exchange-correlation functional with a non-local correlation part that does not employ empirical parameters.[50] As vdW interactions are known to play an important role in adsorption processes in zeolites,[32-35,37-45] the comparison of calculated adsorption energies with experimental data[32-36] allows one to judge how well the explored methods describe the vdW interactions.

Several studies have been reported in which adsorption energies for zeolite systems have been evaluated using the DFT-D approach,[39-44,46,47] i.e. the DFT-D2 method or its more refined variant referred as "DFT-D3".[269] Cluster models and periodic models have been applied to study the adsorption of water,[40,41,43,44] alcohols,[40,41,43,44] nitriles,[44] olefins,[39,40,42] aromatics,[42] and alkanes[46,47] in zeolites. However, no work has systematically compared the interactions of alkanes as alcohols as done in this work. At variance with DFT-D, the vdW-DF2 functional is not yet a routine method for modeling adsorbates in zeolites.

7.2. Results and Discussion

This study reports the computed adsorption energies for a set of test molecules, for which experimental data are available: C_3 to C_6 *n*-alkanes, water, and primary C_1 to C_3 alcohols. The resulting adsorption complexes will be illustrated with the cluster extracts as shown in Figure 34. The following discussion starts with the calculated adsorption energies E_{ads} obtained with the PBE-D2 approach. Recall that the PBE-D2 approach allows a straightforward analysis of the dispersive interaction, as mentioned in Section 3.1. The additive correction, the D2 term, in the energies at PBE-D2 level can be interpreted as the energy contribution arising from the vdW interactions. Subsequently, the results calculated with the vdW-DF2 functional will be discussed. The experimental works this study refers to report adsorption enthalpies H_{ads},[32-36] whereas the calculations of this work yield adsorption energies E_{ads}. Formally, the

calculated E_{ads} values are used as an approximation for H_{ads}. This issue will be discussed in Subsection 7.2.1.3, which illustrates that this approximation is reasonable.

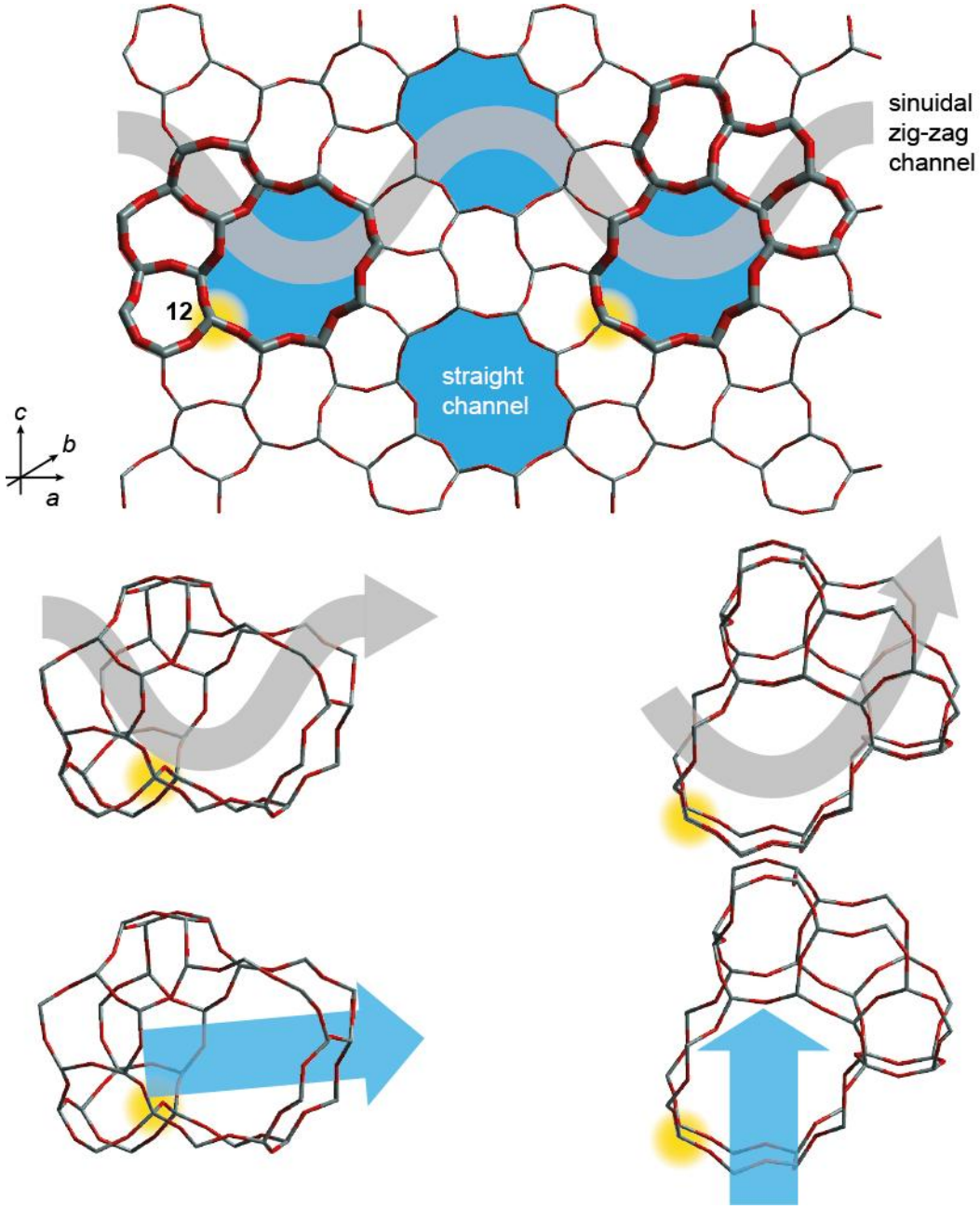

Figure 34: Structure models of MFI-type zeolites (H-ZSM5 and Silicalite) viewed along the crystallographic *b* direction. O centers are shown in red, Si in gray. The site Al12 in H-ZSM5 is highlighted. The straight (blue) and sinuidal zig-zag channels (gray) are indicated. Also shown are cluster cut-outs from the zeolite framework to illustrate the substrate-zeolite interactions. A larger figure of the super cell is provided in Figure 9 of Section 3.3.

7.2.1. Adsorption Energies from PBE-D2 Calculations

7.2.1.1. Adsorption of Alkanes

Two types of adsorption geometries have been considered for each alkane in MFI type zeolites: the "S conformation" and the "Z conformation", in which the alkane is oriented along a straight channel and along a sinuidal zig-zag channel, respectively (Figure 35). The calculated value E_{ads} of propane in the straight channel of Silicalite, -43 kJ mol^{-1}, agrees well with the experimental result,[36] -38 kJ mol^{-1} (Table 9 and Figure 36a). Similar agreement between theory and experiment is also found for *n*-hexane in S conformation. The calculated and the experimental[32] results for the adsorption energy / enthalpy are -75 kJ mol^{-1} and -72 kJ mol^{-1}, respectively. Experimental data for *n*-butane and *n*-pentane adsorption in Silicalite are not available. The calculated results for the S conformers agree quite well with the available experimental data. The adsorption of all alkanes under study is calculated to be more exothermic in the zig-zag channel (Z conformation). The differences in E_{ads} for the two conformers are between 5 kJ mol^{-1} and 24 kJ mol^{-1}. Therefore, the adsorption energies calculated for the most stable adsorption position of each alkane overestimate the experimental values by more than 20 kJ mol^{-1} (Table 9 and Figure 36a). It is unlikely that the discrepancy between theory and experiment is due to differences in coverage, as experiments have demonstrated that the adsorption enthalpies for alkanes in both Silicalite and H-ZSM5 are independent of the coverage.[32,33]

The calculated E_{ads} values for alkanes in H-ZSM5 are very similar to those in Silicalite, consistent with the experimental finding (cf. ΔE_{ads} in Table 9 and E_{ads} in Table 10). The largest difference ΔE_{ads} (in absolute terms) between calculated E_{ads} for the same adsorbate in the two zeolites is about 10 kJ mol^{-1}. This difference has been determined for propane in Z conformation and *n*-butane in S and Z conformation. For propane and *n*-butane in Z conformation, the adsorption in H-ZSM5 is slightly more favored, the difference is mainly related to the difference in the PBE contributions $E_{ads,PBE}$ to the adsorption energies. On the other hand, butane oriented along the straight channel (S conformation) is more stable in Silicalite than in H-ZSM5, which is mainly related to a change in the dispersion part $E_{ads,D2}$ of the calculated adsorption energy.

As shown in Table 10, two sets of experimental data have been reported for the adsorption enthalpies of C_3 to C_6 *n*-alkanes in H-ZSM5; corresponding values in the two sets differ by 5–10 kJ mol^{-1}.[32,33,35] The adsorption energies calculated at the PBE-D2 level overestimate the results of the earlier experiment[32,33] by 17−25 kJ mol^{-1}. The discrepancy to

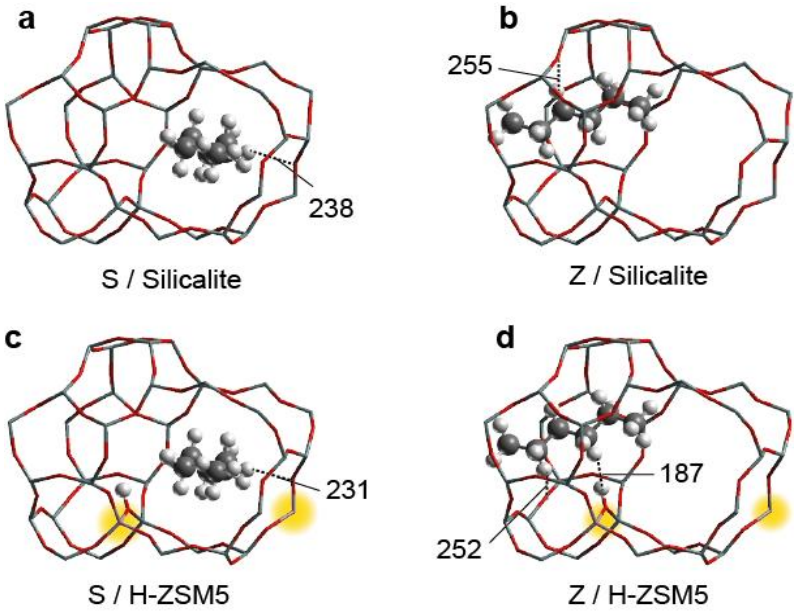

Figure 35: Sketches of adsorption complexes of *n*-hexane in Silicalite and H-ZSM5 in S and Z conformation. Structures are optimized at PBE-D2 level. Selected interatomic distances are shown in pm. The zeolite framework is represented as sticks, hexane is displayed in a ball-and-stick representation. Black: C, white: H. Al sites of the zeolite highlighted in yellow.

Table 9: Comparison of experimentally determined adsorption enthalpies H_{ads} with calculated adsorption energies E_{ads} for *n*-alkanes in Silicalite (kJ mol^{-1}).[a]

	Conformation[b]	H_{ads}	E_{ads}[c]				ΔE_{ads}[c]	
		Exp.	vdW-DF2	PBE-D2	PBE	D2	vdW-DF2	PBE-D2
propane	S	-38[d]	-50	-43	10	-53	-5	-2
	Z		-75	-59	2	-62	8	-9
butane	S		-69	-68	-3	-64	0	10
	Z		-82	-73	6	-79	3	-10
pentane	S		-83	-69	9	-78	8	1
	Z		-105	-85	19	-103	7	-6
hexane	S	-72[e]	-109	-78	21	-98	-6	2
	Z		-112	-102	23	-125	-5	-2

[a] $E_{ads,PBE}$ and $E_{ads,D2}$ denote the two contributions of the adsorption energy calculated at the PBE-D2 level. ΔE_{ads} is the difference between adsorption energies in H-ZSM5 and in Silicalite: $\Delta E_{ads} = E_{ads}$(H-ZSM5) - E_{ads}(Silicalite). [b] Adsorbates oriented along a straight (S) and a sinuidal zig-zag (Z) channel. [c] This work. [d] Ref 36, T = 273–232 K. [e] Ref 32, T = 373 K.

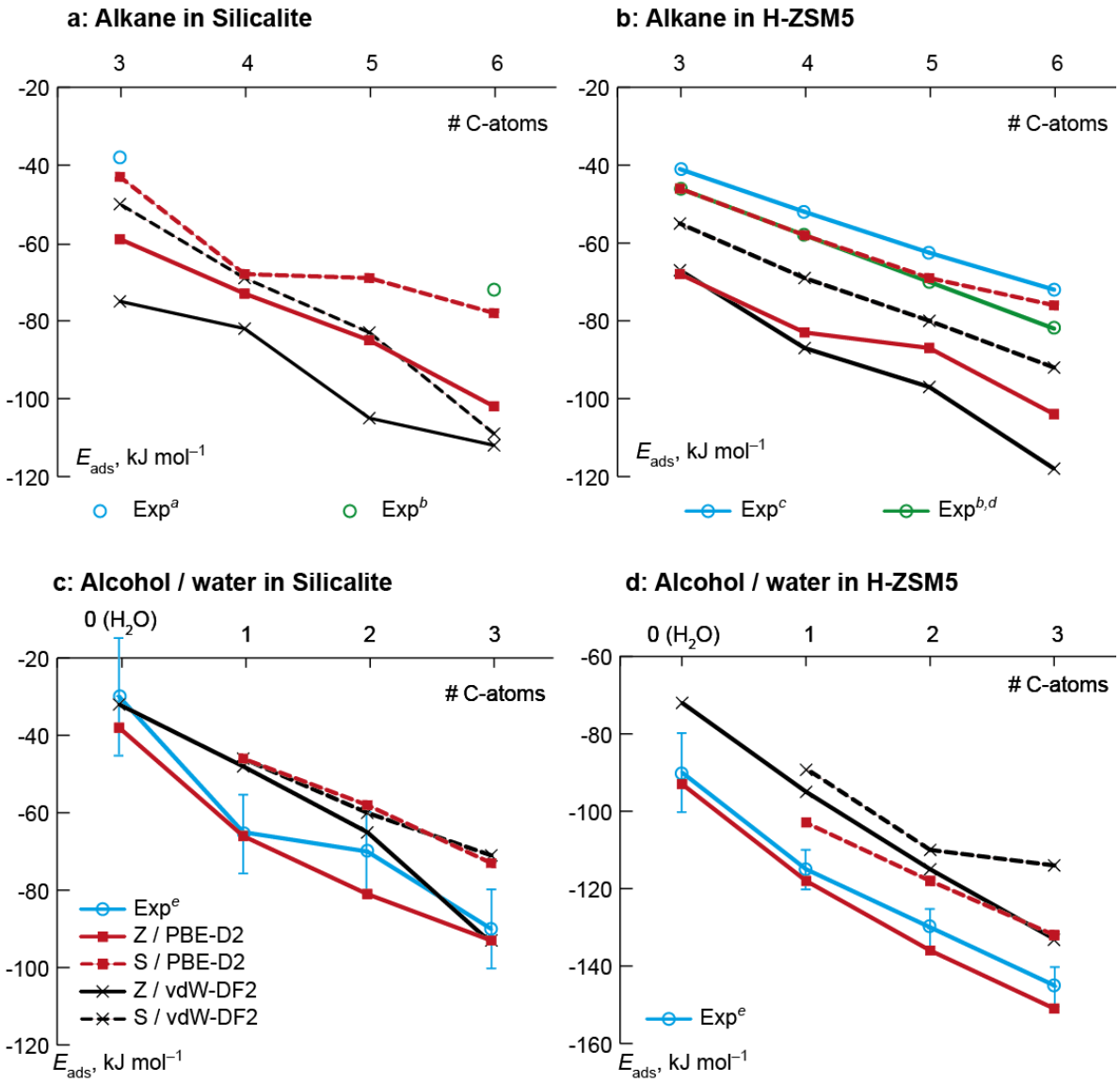

Figure 36: Calculated values E_{ads} for various adsorbates in Silicalite and in H-ZSM5: a) *n*-alkanes in Silicalite b) *n*-alkanes in H-ZSM5 c) alcohols and water in Silicalite d) alcohols and water in H-ZSM5. Results for adsorption complexes with the adsorbate in Z conformation are marked by continuous lines; those in S conformation are marked by dashed lines. Experimental adsorption enthalpies are shown where available. [a] Ref 36. [b] Ref 32. [c] Ref 35. [d] Ref 33. [e] Ref 34.

the more recent measurements[35] is even larger, 25−32 kJ mol^{-1}. Similarly to the situation in Silicalite, E_{ads} evaluated for alkanes in the thermodynamically less favored straight channels of H-ZSM5 agree very well, within 0−7 kJ mol^{-1}, with the reference of the earlier experiment.[32,33]

These results suggest that the DFT-D2 method tends to overestimate the exothermicity of alkane adsorption in zeolites. A similar trend has previously been reported for the adsorption of olefinic and aromatic species in both all-Si and Al-substituted zeolites.[39,42] Interestingly, adsorption energies obtained with the QM-Pot method mentioned in Section 7.1 also

overestimate the experimental data, but agree well with the results of the present study.[35] The differences between E_{ads} for adsorption complexes in Z conformation calculated at the QM-Pot level and the corresponding values at PBE-D2 level are at most 5 kJ mol^{-1}.[35] A theoretical study addressing the cracking of alkanes in H-ZSM5 reported adsorption energies for alkanes in the sinuidal zig-zag channel, obtained from periodic DFT calculations at the PBE-D2 level.[46] Although those methods[46] differ only in minor ways from the method used in the present work, the reported adsorption energies[46] are by 11 kJ mol^{-1} to 20 kJ mol^{-1} less exothermic than the results of the current study (Table 10). In fact, the results of these previous PBE-D2 calculations[46] agree better with experiment than the values of the present work. However, the geometries of the adsorption complexes reported in Ref 46 show some differences to the structures optimized for this thesis; the alkane moieties are located closer to the spacious area at the channel intersection.[46] In light of the results of the present study, it seems reasonable to assume that those earlier geometries[46] do not represent the most stable minimum structures.

The interaction of alkanes with the lattice of both Silicalite (Table 9) and H-ZSM5 (Table 10) is dominated by the dispersion contribution $E_{ads,D2}$, which amounts to more than 90% of the total adsorption energy $E_{ads,PBE-D2}$ at the PBE-D2 level. The PBE contribution $E_{ads,PBE}$ is typically thermo-neutral or endothermic and becomes more endothermic with increasing size of the alkane.

The structures of the alkane adsorption complexes in Silicalite and H-ZSM5 are

Table 10: Comparison of experimentally determined adsorption enthalpies H_{ads} with calculated adsorption energies E_{ads} for *n*-alkanes in H-ZSM5 (kJ mol^{-1}).[a]

	Conformation[b]	H_{ads}		E_{ads}		E_{ads}[c]			
		Exp.[d]	Exp.[e]	QM-Pot[f]	PBE-D2[g]	vdW-DF2	PBE-D2	PBE	D2
propane	S	-41	-46±1	-52		-55	-46	-3	-43
	Z			-63	-48	-67	-68	-8	-61
butane	S	-52	-58±1	-65		-69	-58	-2	-56
	Z			-84	-63	-87	-83	-4	-79
pentane	S	-63	-70±1	-85		-80	-69	4	-74
	Z			-96	-80	-97	-91	10	-101
hexane	S	-72	-82±1	-101		-92	-75	17	-93
	Z			-106	-92	-118	-104	22	-126

[a] $E_{ads,PBE}$ and $E_{ads,D2}$ denote the two contributions of the adsorption energy calculated at the PBE-D2 level. [b] Adsorbates oriented along a straight (S) and a sinuidal zig-zag (Z) channel. [c] This work. [d] Ref 35, T = 301–400 K, Si/Al = 35. [e] Refs 32 and 33, T = 323 K, Si/Al = 35. [f] Ref 35, periodical model. [g] Ref 46, periodical model.

illustrated on the example of *n*-hexane, the largest alkane under study (Figure 35). The closest distances from a hydrogen atom of an alkane H_{alkane} to an oxygen center of the zeolite framework O_{zeo} is 238 pm for alkanes in Silicalite and 231 pm in H-ZSM5. These O_{zeo}-H_{alkane} distances, both determined for hexane located in the straight channel, are substantially shorter than the sum of the van der Waals radii of O and H, 272 pm.[270] The shortest O_{zeo}-H_{alkane} distances determined for the adsorption complexes formed by the smaller alkanes under study are in the range 249–276 pm, i.e. also smaller than or comparable to the sum of the van der Waals radii of O and H. Not unexpectedly, for the majority of the studied alkane adsorption complexes in the straight channel of H-ZSM5, the shortest O_{zeo}-H_{alkane} distance involves an O center bound to an Al center.

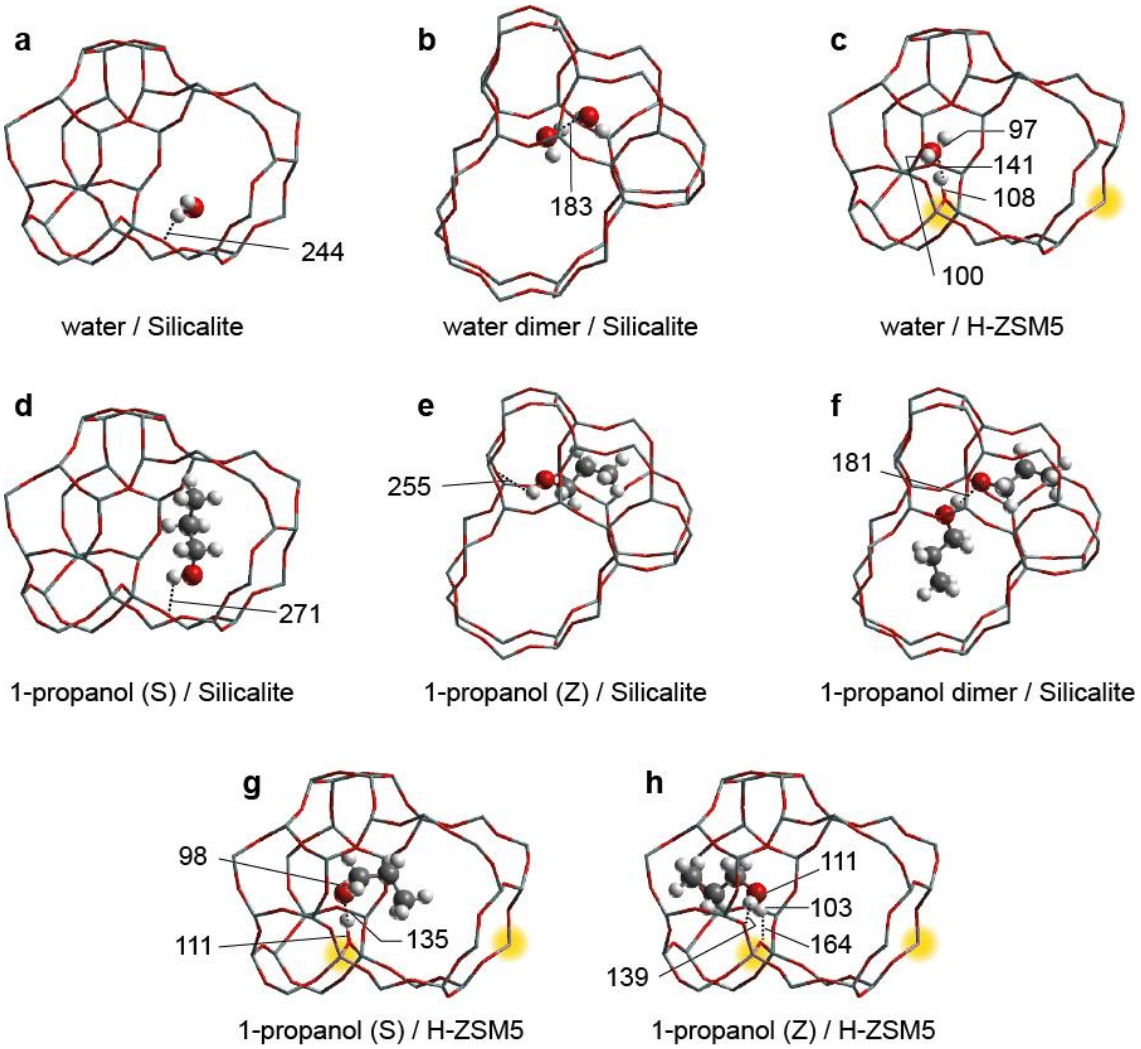

Figure 37: Sketches of the adsorption complexes of water and 1-propanol in Silicalite and H-ZSM5. Structures are optimized at the PBE-D2 level. Selected interatomic distances are shown in pm. The zeolite framework is represented as sticks, the adsorbates are displayed in a ball-and-stick representation. Black: C, red: O, white: H. Al sites of the zeolite highlighted in yellow.

7.2.1.2. Adsorption of Alcohols and Water

The calculated adsorption energy for a single water molecule in Silicalite (Table 11 and Figure 37a), -38 kJ mol^{-1}, and in H-ZSM5 zeolite (Table 12 and Figure 37c), -93 kJ mol^{-1}, agree with the experiment within the corresponding error margins, -30±15 kJ mol^{-1} and -90±10 kJ mol^{-1}.[34] The relatively large experimental error for the adsorption in Silicalite was rationalized by the formation of water clusters inside the zeolite.[34] This is consistent with the adsorption energy calculated for a water dimer in Silicalite (Table 12 and Figure 37b), which is found to be slightly more exothermic than the value for a single adsorbed water, -43 kJ mol^{-1} per adsorbed water molecule; also this result agrees, within the corresponding error margin, with the experiment.

The computed adsorption energies for methanol, ethanol and 1-propanol in the straight channel of Silicalite ("S conformation", see the structure of 1-propanol in Figure 37d) are generally by 10−20 kJ mol^{-1} less exothermic than the corresponding experimental values (Table 11). However, similarly to the situation for alkanes and the results of a previous computational study on alcohol adsorption,[41] the calculations indicate that alcohols in the zig-zag channel of the zeolite ("Z conformation", Figure 37e) are by about 20 kJ mol^{-1} more stable than the corresponding adsorption complexes in S conformation. Thus, the computed E_{ads} values for alcohols in the more favored zig-zag channels of Silicalite agree well with the

Table 11: Comparison of experimentally determined adsorption enthalpies H_{ads} with calculated adsorption energies E_{ads} for water and alcohols in Silicalite (kJ mol^{-1}).[a]

	Conf.[b]	H_{ads}[c]	E_{ads}[d]	E_{ads}[e]				ΔE_{ads}[e]	
		Exp.	PBE-D2	vdW-DF2	PBE-D2	PBE	D2	vdW-DF2	PBE-D2
water		-30±15		-32	-38	-11	-26	-40	-55
	dimer				-43	-18	-25		
methanol	S	-65±10	-33	-46	-46	-9	-37		
	Z		-42	-48	-66	-22	-44	-47	-52
ethanol	S	-70±10	-43	-60	-58	-14	-44		
	Z		-55	-65	-81	-20	-61	-50	-55
	dimer				-77	-25	-53		
1-propanol	S	-90±10	-57	-71	-73	-15	-58		
	Z		-69	-93	-93	-11	-82	-53	-58
	dimer				-81	-13	-68		

[a] $E_{ads,PBE}$ and $E_{ads,D2}$ denote the two contributions of the adsorption energy calculated at the PBE-D2 level. ΔE_{ads} is the difference between adsorption energies in H-ZSM5 and in Silicalite: $\Delta E_{ads} = E_{ads}$(H-ZSM5) - E_{ads}(Silicalite). [b] Adsorbates oriented along a straight (S) and sinuidal a zig-zag (Z) channel and as water / alcohol dimer. [c] Ref 34, T = 350 K. [d] Ref 41, periodical model. [e] This work.

experiments.[34] The difference between theory at the PBE-D2 level and experiment is only 1 kJ mol^{-1} for methanol, 11 kJ mol^{-1} for ethanol, and 3 kJ mol^{-1} for 1-propanol, i.e. below or comparable to the experimental error of ±10 kJ mol^{-1} (Table 11).[34] In analogy to the water dimer, the formation of alcohol dimers in Silicalite has also been considered for ethanol and 1-propanol (Figure 37f). The E_{ads} value per adsorbate molecule is calculated to be slightly less exothermic, at most by 12 kJ mol^{-1}, than the corresponding value for the adsorption complexes in Z conformation (Table 11). Also here, the difference between the adsorption energies (per adsorbate molecule) for an adsorbed alcohol dimer and a single alcohol molecule in Z conformation is comparable to the experimental error, indicating that the alcohols may form dimers in Silicalite.

In the most stable geometry of the studied alcohol molecules in H-ZSM5 (Table 12, Figure 37h), the hydrocarbon chains of the alcohols point to the zig-zag channel ("Z conformation"), while the hydroxyl group of the alcohols simultaneously acts as proton acceptor for the proton of the zeolite OH group at the Al12-O-Si12' site and as proton donor for an oxygen center of the zeolite framework. E_{ads} values calculated at the PBE-D2 level for these adsorption complexes agree well with the reported experimental H_{ads} values;[34] the differences are at most 6 kJ mol^{-1}, i.e., comparable to experimental uncertainty (Table 12). The alcohol molecules in H-ZSM5 can also adsorb with the carbon moiety oriented towards the straight channel (S conformation). These structures are calculated to be by 16–19 kJ mol^{-1} less stable than their isomers in Z conformation. The adsorption energies computed in this

Table 12: Comparison of experimentally determined adsorption enthalpies H_{ads} with calculated adsorption energies E_{ads} for alkanes in H-ZSM5 (kJ mol^{-1}).[a]

	Conformation[b]	H_{ads}		E_{ads}[c]	E_{ads}[d]			
		Exp.[e]	PBE-D2[f]	PBE-D2	vdW-DF2	PBE-D2	PBE	D2
water		-90 ± 10	-87		-72	-93	-75	-18
methanol	S	-115 ± 5	-108	-113	-89	-102	-70	-32
	Z			-116	-95	-118	-82	-36
ethanol	S	-130 ± 5	-124	-125	-110	-117	-71	-47
	Z			-132	-115	-135	-78	-58
1-propanol	S	-145 ± 5	-140	-135	-115	-131	-70	-61
	Z			-147	-133	-151	-72	-78

[a] $E_{ads,PBE}$ and $E_{ads,D2}$ denote the two contributions of the adsorption energy calculated at the PBE-D2 level. [b] Adsorbates oriented along a straight (S) and a sinuidal zig-zag (Z) channel. [c] Ref 41, periodical model. [d] This work. [e] Ref 34, T = 400 K, Si/Al =25 (estimated from Al bulk content of 630 μmol/g). [f] Ref 44, cluster model, T = 400 K.

study are in good agreement with data obtained from earlier calculations using a periodical model and the same method, PBE-D2.[40,41,44]

The formation of hydrogen bonds by adsorbed alcohols and water is reflected in the density functional term $E_{ads,PBE}$ of the calculated adsorption energies $E_{ads,PBE\text{-}D2}$ (Table 11 and Table 12). For adsorption complexes in H-ZSM5, the pure DFT contribution is significant, from -70 kJ mol^{-1} to -81 kJ mol^{-1}; in most cases it represents the dominating term of $E_{ads,PBE\text{-}D2}$. In Silicalite, where framework OH groups are missing, the values of $E_{ads,PBE}$ are significantly less exothermic, ranging from -9 kJ mol^{-1} to -25 kJ mol^{-1}. The $E_{ads,PBE}$ contributions for alcohol and water molecules in Silicalite and H-ZSM5 can be considered as independent of the size of the adsorbate; at variance, $E_{ads,D2}$, the empirical dispersion term, increases notably with the size of the adsorbate. For the largest alcohol molecule under study, 1-propanol, $E_{ads,D2}$ is even slightly more exothermic than $E_{ads,PBE}$, -78 kJ mol^{-1} vs. -72 kJ mol^{-1}, taking the values calculated for the H-ZSM5 adsorption complex in the most stable Z configuration.

In the less stable S conformers of the adsorption complexes formed by methanol, ethanol and 1-propanol in H-ZSM5 (Figure 37g), the alcohol OH group interacts with the zeolite proton H_{zeo} at the Al12-O-Si12' site. In these structures, the oxygen center of the alcohol $O_{alcohol}$ is bound via a hydrogen bond to the OH group of the zeolite, with $O_{alcohol}$-H_{zeo} distances of 135−140 pm. These bonds are quite a bit longer than the O_{zeo}-H_{zeo} distances within the bridging hydroxyl groups of the zeolite framework, 109−111 pm. The difference between these two types of O-H distances decreases with the size of the alcohol molecule, from 31 pm (for methanol) to 24 pm (for 1-propanol), consistent with the higher proton affinity of heavier alcohols.[41] In the adsorption complexes in S conformation, the proton $H_{alcohol}$ of the alcohol hydroxyl group does not interact with the zeolite framework.

In the more stable Z conformation for alcohols in H-ZSM5, exemplarily depicted for 1-propanol in Figure 37g, the alcohol OH group is protonated by the zeolite's acidic hydroxyl group, as indicated by the $O_{alcohol}$-H_{zeo} distances of 102−103 pm. These distances are shorter than the corresponding O_{zeo}-H_{zeo} distances of 164−166 pm, which shows that the proton H_{zeo} has been transferred from the zeolite to the alcohol. The proton of the alcohol hydroxyl group $H_{alcohol}$ interacts with a further O_{zeo} center adjacent to Al12 with O_{zeo}-$H_{alcohol}$ distances of 127−139 pm, which are significantly longer than the $O_{alcohol}$-$H_{alcohol}$ bonds, 111−117 pm. Thus, the adsorption complexes in Z conformation represent a positively charged alkyloxonium ion that interacts with a deprotonated, negatively charged Al-O-Si moiety

originating from the bridging hydroxyl group at Al12-O-Si12'.

7.2.1.3. Comparison of Adsorption Enthalpies and Adsorption Energies

As mentioned previously, the computed data presented in this work are adsorption energies E_{ads} derived from electronic energies. Technically speaking, it is not correct to compare those values with the experimentally determined adsorption enthalpies H_{ads}, as the energies E_{ads}

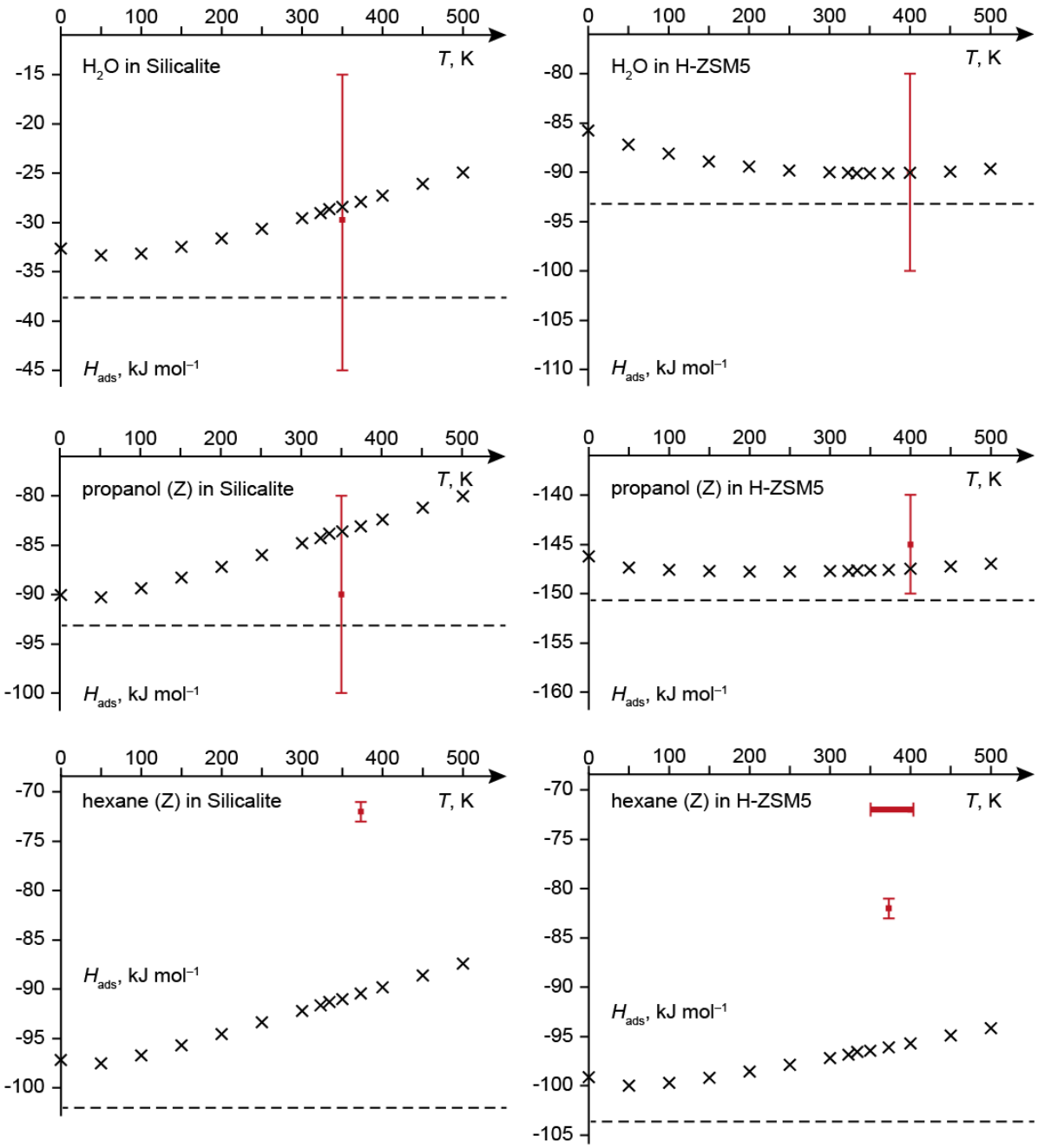

Figure 38: Enthalpy values H_{ads} calculated at the PBE-D2 level for selected systems at various temperatures (black crosses). For comparison, the experimental values are shown in red. Experimental errors are given where available. The dashed black line denotes the calculated adsorption energy E_{ads}. See Table 13 for the numerical results.

Table 13: Comparison of the calculated adsorption energies with calculated and experimentally determined adsorption enthalpies (kJ mol^{-1}) at temperature T (K).[a]

Zeolite	Adsorbate	Conformation[b]	E_{ads}	H_{ads}		T
			PBE-D2	PBE-D2	Exp	
Silicalite	water		-38	-28	-30 ± 15[c]	350[c]
	1-propanol	Z	-93	-84	-90 ± 10[c]	350[c]
	n-hexane	Z	-102	-91	-72 ± 1[d]	373[d]
H-ZSM5	water		-93	-90	-90 ± 10[c]	400[c]
	1-propanol	Z	-151	-148	-145 ± 5[c]	400[c]
	n-hexane	Z	-104	-97	-82 ± 1[e]	323[e]
				-97÷ -96	-72[f]	301 – 400[f]

[a] Calculated values evaluated at PBE-D2 level. [b] Adsorbates oriented along the sinuidal zig-zag (Z) channel. [c] Ref 34. [d] Ref 32. [e] Refs 32 and 33. [f] Ref 35.

neglect the contribution of the internal energy to H_{ads}. However, both computational and experimental methods are associated with uncertainties. As long as the contribution of the internal energy is not significantly larger than the uncertainties of the methods, H_{ads} can be approximated by E_{ads} as done in the present work.

To estimate the contribution of the internal energy, H_{ads} has been evaluated computationally for the Z conformers of the adsorption complexes of water, 1-propanol and *n*-hexane in Silicalite and H-ZSM5 (Table 13 and Figure 38). The adsorption enthalpies have been evaluated for temperatures T between 0 K and 500 K, a range that covers all temperatures considered in the corresponding experiments.[32-35]

In case of the oxygen containing adsorbates, water and 1-propanol, the difference between calculated H_{ads} at experimental T and E_{ads} is slightly smaller than the experimental uncertainty, < 10 kJ mol^{-1}. This justifies the exclusive focus on E_{ads} in this study. As visible from Figure 38 the calculated enthalpy results agree slightly better with the experiment than the straightforwardly calculated energies.

In the case of the *n*-hexane adsorption complexes, the difference between computed H_{ads} (at the temperature of the experiment) and E_{ads} is 11 kJ mol^{-1} in Silicalite and 7 kJ mol^{-1} in H-ZSM5. The differences are comparable to the values calculated for water and 1-propanol, but larger than the experimental uncertainty of 1 kJ mol^{-1}.[32,33] Also in the case of *n*-hexane adsorption complexes, the experimental H_{ads} is closer to the calculated H_{ads} than to E_{ads}. However, neglecting the thermal corrections is not likely to be the main reason for the poor agreement between experiment and theory at PBE-D2 level. As shown in Figure 38, the H_{ads}

values calculated for adsorption complexes of *n*-hexane are still by 15–19 kJ mol^{-1} more exothermic than the experimental reference.[32,33,35] Thus, also in the case of the alkane adsorption complexes, the discussion of calculated E_{ads} results instead of H_{ads} values does not bias the interpretation of the results.

7.2.2. Adsorption Energies from vdW-DF2 Calculations

As the non-local correlation functional of type vdW-DF2[196] is designed to account also for vdW interactions, the adsorption energies have also been evaluated with this functional using the same model and otherwise the same computational procedure as described for the calculations with the PBE-D2 method. Where necessary, the adsorption energies at the vdW-DF2 level will be referred as $E_{ads,vdW\text{-}DF2}$ in order to distinguish them from the results at the PBE-D2 level, $E_{ads,PBE\text{-}D2}$.

7.2.2.1. Adsorption of Alkanes

This section will start with the adsorption complexes formed by *n*-alkanes in Silicalite. $E_{ads,vdW\text{-}DF2}$ = -75 kJ mol^{-1} has been calculated for the propane complex in Z conformation, i.e. the computed value is by 37 kJ mol^{-1} more exothermic than the experiment. The corresponding values for *n*-hexane are -112 kJ mol^{-1} and 40 kJ mol^{-1}, respectively (Table 9). For adsorption complexes in S conformation, the value of $E_{ads,vdW\text{-}DF2}$ for propane and *n*-hexane are -50 kJ mol^{-1} and -109 kJ mol^{-1}, respectively. Thus, similarly to the PBE-D2 approach, the alkane-zeolite interaction of propane and *n*-hexane oriented along the straight channel (S conformation) is calculated to be weaker than for the isomers in Z conformation (Table 9). Different from the results at the PBE-D2 level, even the less exothermic $E_{ads,vdW\text{-}DF2}$ values associated with the adsorption complexes in S conformation overestimate the measured exothermicity.[32,36]

The vdW-DF2 results for the interaction of *n*-alkanes with H-ZSM5 (Table 10) also overestimate the exothermicity of the adsorption processes when the most stable adsorption complexes in Z conformation are considered. The overestimation ranges from 26 kJ mol^{-1} to 46 kJ mol^{-1} or 21 kJ mol^{-1} to 36 kJ mol^{-1}, depending on the experimental reference.[32,33,35] $E_{ads,vdW\text{-}DF2}$ values for *n*-alkanes oriented along the straight channel (S conformation) are by 12−26 kJ mol^{-1} less exothermic than those in the zig-zag channel (Z conformation). In general, the difference between theory an experiment increases with the size of the molecule (Figure 36b). Similar to the situation in Silicalite, the $E_{ads,vdW\text{-}DF2}$ values calculated for both the Z conformers and the S conformers of the alkane adsorption complexes in H-ZSM5 are more exothermic than the experimental reference. Comparable to the results at PBE-D2 level,

the $E_{ads,vdW\text{-}DF2}$ associated with the adsorption complexes in S conformation agree better with the experiment than the values for the complexes in Z conformation do. However, the differences between $E_{ads,vdW\text{-}DF2}$ for the S conformers and the experimental references[32,33] are about 10 kJ mol^{-1} *at best*. Recall that the PBE-D2 results $E_{ads,PBE\text{-}D2}$ for the analog structures are *at most* 7 kJ mol^{-1} less exothermic than the experimentally determined H_{ads} values from the same references (Refs 32 and 33) as used for assessing the vdW-DF2 results.

7.2.2.2. Adsorption of Alcohols and Water

For most studied oxygen-containing adsorbates in Silicalite, the adsorption energies calculated at the vdW-DF2 level agree very well with the measured adsorption enthalpies, as can be seen from Table 11. With the exception of methanol, the differences between $E_{ads,vdW\text{-}DF2}$ and the experimental data are less than 5 kJ mol^{-1}, significantly smaller than the uncertainty of the experiment which is estimated at 10 kJ mol^{-1} or more.[34] Only for methanol, $E_{ads,vdW\text{-}DF2}$ = -48 kJ mol^{-1}, the adsorption is calculated noticeably less exothermic than the corresponding experimental reference, -65±10 kJ mol^{-1}. The vdW-DF2 adsorption energies of water and alcohols in H-ZSM5 zeolite (Table 12) are more exothermic, by 12–20 kJ mol^{-1}, than the experimental values. The largest deviations are determined for the systems with the smallest adsorbates, methanol and water.

7.2.3. Comparison of the Two Types of Zeolites

The calculated adsorption energies allow one to determine the differences ΔE_{ads} between the adsorption energies in Silicalite and in H-ZSM5 (Table 10 and Table 12). The difference is mainly related to the formation of strong hydrogen bonds (especially for water and alcohols) in H-ZSM5, which contains acidic OH groups. The calculated results for alkanes do not exhibit a general trend whether adsorption in H-ZSM5 or Silicalite is more exothermic (Table 10). Both at PBE-D2 level and at vdW-DF2 level, the absolute values of ΔE_{ads} for alkane adsorption complexes are 10 kJ mol^{-1} or smaller (Table 10). In contrast, ΔE_{ads} for complexes formed by water or alcohols are, as expected, significantly larger, 40–53 kJ mol^{-1} (PBE-D2) and 52–58 kJ mol^{-1} (vdW-DF2), in favor of H-ZSM5 (Table 12).

To estimate the contribution of the hydrogen bond in alcohol adsorption complexes to the overall adsorption energy, E_{ads} values calculated for molecules with the same number of "heavy" atoms are compared, i.e., ethanol vs. propane as well as 1-propanol vs. *n*-butane (Figure 39). In the most stable adsorption geometries, the interaction of H-ZSM5 with an alcohol of formula $C_kH_{2k+1}OH$ (k = 2, 3) is by ~68 kJ mol^{-1} (PBE-D2) and ~47 kJ mol^{-1} (vdW-DF2) more exothermic than the interaction between H-ZSM5 and the corresponding

alkane of formula $C_{k+1}H_{2k+4}$. Analysis of the PBE and D2 contributions shows that the PBE-D2 approach mainly attributes the difference between the adsorption energies of alcohols and of alkanes, i.e., the strength of the hydrogen bonds, to the difference in $E_{ads,PBE}$ (Figure 39). In contrast, for the compared pairs of adsorbates with the same number of "heavy" atoms, the $E_{ads,D2}$ contributions do not differ by more than 3 kJ mol^{-1}.

For the adsorption in Silicalite, the calculations at PBE-D2 level and at vdW-DF2 level give somewhat different results. The PBE-D2 results indicate a more exothermic adsorption of the alcohols, by ~20 kJ mol^{-1}. Similarly to the situation in H-ZSM5, the stronger exothermicity for the alcohol adsorption is related to the more exothermic $E_{ads,PBE}$ term. At variance to the PBE-D2 results for adsorption complexes in Silicalite, results obtained with the vdW-DF2 method do not exhibit a clear trend. The $E_{ads,vdW-DF2}$ value for *n*-butane is by 11 kJ mol^{-1} *less* exothermic than the corresponding value for 1-propanol. In contrast, $E_{ads,vdW-DF2}$ associated with the propane adsorption complex is by 10 kJ mol^{-1} *more* exothermic than the value for the adsorption complex of ethanol. The reason for this is not fully understood. However, it may be related to the finding that compared to the experiment, the vdW-DF2 method underestimates the exothermicity of alcohol adsorption while it

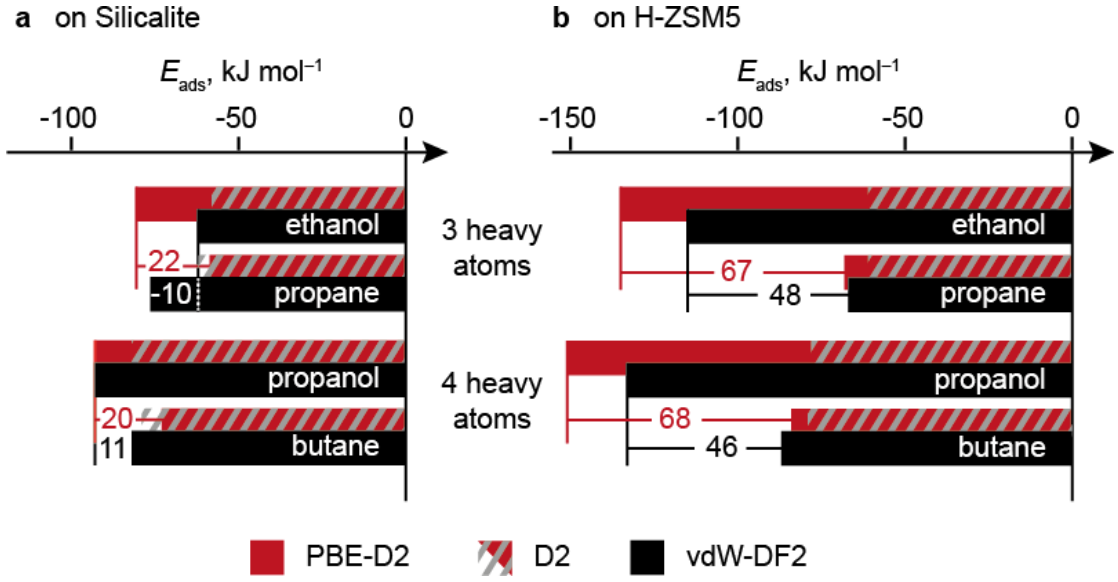

Figure 39: Comparison of calculated E_{ads} values for alkane and alcohol molecules with equal number of heavy (non-H) atoms. The displayed energies refer to the most stable conformer of each adsorbate in Silicalite and on HZSM-5. The numerical values shown are the differences [$E_{ads}(C_kH_{2k+1}OH)$ - $E_{ads}(C_{k+1}H_{2k+4})$], between E_{ads} calculated for the alcohol and for the alkane in the same zeolite. The bars and values in red denote the results at the PBE-D2 level, the hatched area represents the contribution of the dispersive correction $E_{ads,D2}$ to $E_{ads,PBE-D2}$. Note that the dispersive correction $E_{ads,D2}$ can be larger than $E_{ads,PBE-D2}$. The PBE contribution $E_{ads,PBE}$ to $E_{ads,PBE-D2}$ corresponds to the difference between the PBE-D2 result and the D2 contribution and is not explicitly marked. The results at the vdW-DF2 level are shown in black.

overestimates the heat of adsorption for alkanes. As a result, $E_{ads,vdW\text{-}DF2}$ for alkanes and for alcohols in Silicalite come closer than the corresponding $E_{ads,PBE\text{-}D2}$ values do. This may lead to variations in the order of the $E_{ads,vdW\text{-}DF}$ for alkanes and alcohols. Similarly, the difference in $E_{ads,vdW\text{-}DF2}$ for alcohols and alkanes with the same number of heavy atoms in H-ZSM5 is also generally smaller than the difference between the corresponding PBE-D2 values.

7.2.4. Analysis of PBE-D2 Adsorption Energies and Comparison with vdW-DF2 Results

As discussed in the preceding Sections 7.2.1 and 7.2.2, both approaches tested to account for weak interactions in zeolites, either by adding an empirical correction term (PBE-D2), or by a non-local correlation component of the functional (vdW-DF2), yielded results in acceptable agreement with experimental adsorption enthalpies of alcohols and water. However, adsorption energies of *n*-alkanes in both Silicalite and H-ZSM5 were notably overestimated, by 17–32 kJ mol^{-1} (PBE-D2) and 21–46 kJ mol^{-1} (vdW-DF2). Within the PBE-D2 approach (Table 9 and Table 10), the exothermic adsorption of alkanes in zeolites is essentially a result of the dispersion contribution $E_{ads,D2}$, while the pure DFT contribution $E_{ads,PBE}$ is in most cases negligible or repulsive. In other words, single-point calculations at the pure PBE level on the optimized PBE-D2 geometries, would describe the adsorption of alkanes in both Silicalite and H-ZSM5 as a thermodynamically unfavorable or thermo-neutral process. Only the adsorption complex of propane in H-ZSM5 in Z conformation displays a small exothermic contribution from the PBE-DFT energy, $E_{ads,PBE}$ = -8 kJ mol^{-1}, to the total adsorption energy $E_{ads,PBE\text{-}D2}$. Yet, even in this case, $E_{ads,PBE}$ is only 11% of $E_{ads,PBE\text{-}D2}$. In other words, the GGA contribution is mostly repulsive and prevents potential adsorbates to come too close to the zeolite walls.

To reach a more detailed understanding of the two methods applied for describing the dispersive interactions between the adsorbate and the zeolite framework, it is worth examining how $E_{ads,PBE\text{-}D2}$ and its components, $E_{ads,D2}$ and $E_{ads,PBE}$, vary when an adsorbate is moved inside the zeolite. For this purpose, $E_{ads,PBE\text{-}D2}$ values have been evaluated for various structural arrangements where the adsorbate is shifted by Δ from its equilibrium position (Figure 40). The value $E_{ads,PBE\text{-}D2}$ and its components at $\Delta = 0$ corresponds to the values shown in Tables 9–12, which had been obtained by geometry optimizations at the PBE-D2 level. When evaluating $E_{ads,PBE\text{-}D2}$ for $\Delta \neq 0$, the adsorbate is rigidly moved from the position in the reference structure ($\Delta = 0$) by Δ along the *c*-axis. The zeolite framework (including the OH groups in HZSM-5) was kept fixed in the positions optimized for $\Delta = 0$. The analysis as described above has been done for adsorption complexes of *n*-hexane in the straight and the

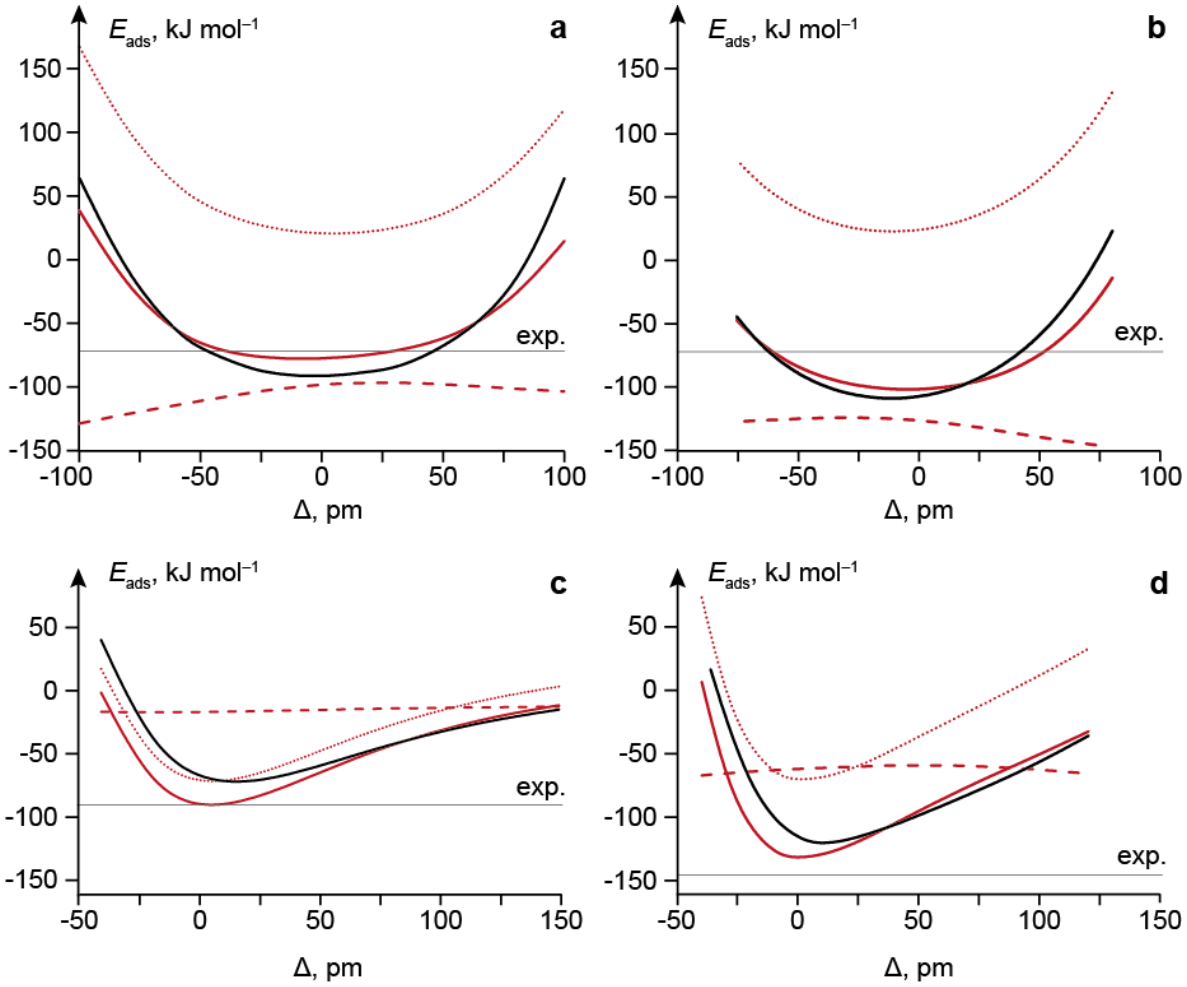

Figure 40: Adsorption energies E_{ads} from PBE-D2 (red, solid line) and vdW-DF2 calculations (black) for shifts Δ of the adsorbate along the crystallographic c-axis away from the minimum position determined at the PBE-D2 level. Negative values of Δ indicate a shift of the adsorbate towards the wall of a channel. The PBE (dotted) and D2 contributions (dashed) to $E_{ads,PBE-D2}$ are also shown. Experimental H_{ads} values are indicated. a) *n*-hexane (S conformation) in Silicalite, b) *n*-hexane (Z) in Silicalite, c) water in H-ZSM5, d) 1-propanol (S) in H-ZSM5.

zig-zag channels of Silicalite as well as for the adsorption complexes of water and 1-propanol (S conformation) in H-ZSM5 (Figure 40). The S conformer of 1-propanol in H-ZSM5 is chosen here instead of the more stable Z conformer, as in the latter structure the zeolite proton is transferred to the alcohol to form an alkyloxonium ion. In that case, the variation of the adsorption energy will be affected by the implied charge separation, making an interpretation of the data less straightforward. For comparison, vdW-DF2 adsorption energies have also been evaluated in single-point fashion at the *same* geometries (Figure 40). In other words, the values $E_{ads,vdW-DF2}$ at $\Delta = 0$ do *not* correspond the values discussed in Section 7.2.2, as $\Delta = 0$ refers to the minimum structure optimized at the PBE-D2 level.

Figures 40a and 40b show the analysis for the largest alkane under study, *n*-hexane, in Silicalite. The PBE contribution $E_{ads,PBE}$ is, for both S and Z conformers, always repulsive. At variance, the dispersion contribution is attractive and remains essentially constant over the range of Δ studied. For values $|\Delta| < 40$ pm, $E_{ads,D2}$ varies by at most by 10%. For water and 1-propanol in H-ZSM5 (Figures 40c and 40d), the $E_{ads,D2}$ contribution also remains essentially constant in the range of shifts Δ studied. It is not surprising that the value $E_{ads,D2}$ for water, about -20 kJ mol^{-1}, is (in absolute values) relatively small compared to the other systems under study, where $E_{ads,D2}$ values are -60 kJ mol^{-1} or even more exothermic. This is a direct consequence of the different sizes of the adsorbate molecules. In contrast to *n*-hexane in Silicalite, the $E_{ads,PBE}$ contributions for 1-propanol and water in H-ZSM5 are attractive over a range of Δ values that vary by more than 200 pm. This behavior is related to the hydrogen bonds between the zeolite and the adsorbates.

The four adsorption systems in MFI type zeolites displayed in Figure 40 show that the empirical correction $E_{ads,D2}$ to the adsorption energy is largely independent of how the adsorbate is located within a channel. The dispersion term $E_{ads,D2}$ is a large, quasi constant, additive correction to the potential energy surface calculated at the PBE level. Note that for alkanes in Silicalite, whose GGA-DFT contribution to $E_{ads,PBE-D2}$ is repulsive over the complete range of Δ, the PBE-D2 approach fails to predict adsorption energies with chemical accuracy. In contrast, for water and alcohols in H-ZSM5, where $E_{ads,PBE}$ is attractive for a large range of Δ values, the $E_{ads,PBE-D2}$ values agree well with experiment.

For the adsorption systems of *n*-hexane in Silicalite, the total adsorption energies calculated with the PBE-D2 and the vdW-DF2 approaches give quite similar results when the adsorbate molecules are moved in the channel. In other words, the vdW-DF2 functional with its non-local correlation part yields adsorption energies similar to the result that one gets when one applies the empirical D2 type dispersion correction to the GGA-PBE functional. Recall that the PBE-D2 and vdW-DF2 energies reported here are evaluated at the identical geometries, i.e. for a unit cell size optimized at the PBE-D2 level. In other words, adsorption energies consistently determined at the vdW-DF2 level may deviate more from the results consistently determined at the PBE-D2 level.

7.2.5. General Comments

In view of the fact that the dispersion term dominates the attractive interaction in the adsorption complexes under study, it is worth commenting on its origin. According to the original parameterization of the DFT-D2 method,[49] the Si-C interaction is the strongest of all

pair-wise interactions that occur in adsorption complexes of alkanes in Silicalite. This specific interaction is still significant at large interatomic distances where contributions from other atom pairs (O-H, O-C, and Si-H) are already negligible. This feature of the DFT-D2 approach is to some extend incompatible with the general perception of the chemistry of zeolites, where the framework oxygen centers exhibit a large polarizability due to their partially anionic character. Therefore, the O centers are expected to contribute the strongest of all elements to the dispersive interactions. In contrast, the polarizability of the silicon centers, and thus their contribution to dispersive interactions, is expected to be rather limited in view of their cationic character.[259,271] This discrepancy between the DFT-D2 parameterization and the expected chemical behavior of zeolites is not surprising because the empirical interaction parameters of the DFT-D2 approach are obtained, among others, from the polarizability α for *isolated* atomic species,[49] a quantity which approximately increases proportional to the volume of an atom.[272] However, it seems necessary to account also for the "physical" (less than "formal") charges of the atomic centers within a molecule or solid, to obtain reliable parameters for the empirical correction. Theoretical studies have demonstrated that the electrostatic potential in zeolite cavities is best reproduced by O centers with a charge of 0.6–1.0 e, depending on the level of theory.[263,273,274] Auger electron spectroscopy has demonstrated for such systems that the polarizability (or rather the polarizability volume) of the O centers, 1.2 $Å^3$, is indeed significantly larger than that of Si centers, 0.38 $Å^3$.[271,275]

There are some more elaborate methods to account for dispersive interactions, e.g. the DFT-D3 variant, recently developed by *Grimme* and co-workers,[269] or a related correction scheme proposed by *Tkatchenko* and *Scheffler* (TS-vdW)[276] which accounts for the chemical environment of a system. It is of interest to know whether such methods allow a more accurate description of the vdW interactions in zeolites than the DFT-D2 and the vdW-DF2 approaches do. In the context of this thesis, both the DFT-D3 methods (as PBE-D3) and the TS-vdW method were used to evaluate the adsorption energy for the Z conformer of *n*-hexane in Silicalite in single-point fashion using the geometries optimized at the PBE-D2 level. However, results of these two approaches did not improve the PBE-D2 adsorption energy. Note that within the TS-vdW method the polarizability of the zeolite Si centers is determined to be larger than the polarizability of zeolite O centers. Seemingly, both the DFT-D2 approach and the TS-vdW method suffer from a similar issue.

Next, a comment on the overall accuracy of the computational approaches applied in this study is given. In case of the PBE-D2 method, the failure to deliver results of chemical

accuracy for the systems examined may be related to the parameterization procedures used to generate the empirical inter-atomic interaction parameters.[49] The results of the present study suggest that proper modeling of the adsorption of saturated hydrocarbons in zeolites (as well as on other silicate surfaces) requires a specific parameterization. However, it is a non-trivial task to obtain suitable reference values for such a parameterization strategy; currently high-level multi-reference calculations with sufficiently flexible basis sets for zeolites still require far too much computational resources and the database of reliable experimental values simply is not large enough.

At variance with the PBE-D2 approach, the usage of non-local correlation functionals like vdW-DF2 is a non-empirical approach to address dispersive interactions. Such functionals have originally been designed to address layered systems, such as graphite,[277] and were later on generalized to all kinds of systems as in the vdW-DF2 variant employed in this work.[196,278] Despite of the claim to address all kinds of chemical systems, the accuracy of the vdW-DF2 approach was so far mainly assessed for molecular systems.[196] The only system with a porous material considered is the interaction of H_2 with aromatic C_6 rings in MOFs (metal organic frameworks), which is not really comparable to the interactions in zeolites. It seems that the vdW-DF2 approach, despite the claim of universal applicability, has a problem with silicates, as recent studies report that the exothermicity of the adsorption of methane on quartz[279] as well as of the adsorption of C_1 to C_3 alkanes in Chabazite[280] are also overestimated. While the vdW-DF2 functional is not able to describe reliably the adsorption of alkanes in zeolites, one should not necessarily dismiss non-local correlation functionals as unsuitable for describing zeolites. It seems worthwhile to consider other non-local correlation functional, e.g. optB88-vdW,[50] which are based on an exchange functional that has been optimized for use in combination with the non-local correlation part.[50]

One should also keep in mind that the interaction of alkanes (simple but rather unreactive species) in general is hard to describe. This is also notable from the benchmark calculations carried out to evaluate the accuracy of the DFT-D2 and the vdW-DF2 methods.[49,196] The DFT-D2 method overestimates the formation energy of a methane dimer by 0.25 kJ mol^{-1} (or 11%), as judged by the more accurate RI-MP2 results. One may argue that the relative error is only high as the absolute values of the target quantity are small, only -2.34 kJ mol^{-1} (DFT-D2) and -2.09 kJ mol^{-1} (RI-MP2), respectively.[49] However, this error increases with the size of the system. The formation energy of a butane dimer is overestimated even stronger by the DFT-D2 method, both in absolute and relative terms: 3.89 kJ mol^{-1} and 32%,[49]

respectively, compared to MP2 results.[281] The formation energy of a methane dimer at the vdW-DF2 level has also been compared to CCSD(T) results.[196,282,283] The vdW-DF2 results overestimate the formation energy by 0.68 kJ mol^{-1} (30%). These findings are in line with our results where the exothermic interaction of alkanes with a zeolite wall is generally overestimated. Recently it has been pointed out that the vdW-DF2 approach as well as the empiric dispersion correction (in the more recent DFT-D3 fashion) yield binding energies which deviate on average from the values at the CCSD(T) level by approximately 7% and 12% (in *absolute* terms), respectively.[284] For the special case of pure vdW dominated interactions, the deviation of the vdW-DF2 values from the CCSD(T) is similar to the general case, 7%, while the error of the DFT-D3 results is about 15%.[284]

7.3. Conclusions

The present study addressed the performance of periodic density functional calculations using a gradient-corrected density functional with empirical dispersion corrections (PBE-D2) and a non-local correlation functional (vdW-DF2). It has been explored how well the two approaches describe the adsorption processes of water, alcohols and alkanes in Silicalite and H-ZSM5. The adsorption energies of water and alcohol molecules calculated at the PBE-D2 level agree in acceptable fashion with the experimental values. In contrast, adsorption energies of *n*-alkanes in both the all-Si zeolite and the Al-substituted zeolite were significantly overestimated, by 21 kJ mol^{-1} or more.

Analysis of the PBE-D2 results showed that the pure DFT component $E_{ads,PBE}$ and the empirical dispersion term $E_{ads,D2}$ give rather different contributions to the total adsorption energies $E_{ads,PBE-D2}$. The attractive interaction of alkanes with the zeolite lattice is almost exclusively due to the empirical dispersion term, whereas the GGA-DFT part is mainly repulsive, preventing the adsorbates to come too close to the zeolite walls. Adsorption energies obtained with the vdW-DF2 method are comparable to those of the PBE-D2 method, with the latter results agreeing slightly better with experiment in most cases.

The two tested approaches reproduce available experimental adsorption enthalpies of alkanes in Silicalite and H-ZSM5 only in a limited fashion, and certainly not at chemical accuracy. In consequence, with either of the evaluated methods, modeling of chemical reactions that involve alkanes and oxygenates in zeolites will result in a systematic over-stabilization of the deoxygenated species. The PBE-D2 approach may be amenable to more accurate results if the empirical dispersion correction is based on atomic polarizabilities that are more adequate for silicates. For the vdW-DF2 approach (or rather the non-local

correlation approach), benchmarking of further functionals together with more fundamental revision and re-evaluation of the method seems necessary to render such functionals useful for describing chemical transformations in zeolites.

Chapter 8 Summary

This thesis addressed the conversion of biomass derived feedstock by heterogeneous catalysis and related chemical processes. On the one hand periodic DFT calculations at the GGA level were used to study reaction mechanisms that are involved in the metal-catalyzed processing of organic oxygenates. On the other hand this thesis also presented a benchmark study to evaluate how well DFT-based methods such as the DFT-D2 approach and the vdW-DF2 functional are able to describe dispersive interactions, which play an important role for the chemistry of zeolites and zeolite catalyzed reactions.

The application results of this thesis were presented in four chapters. Chapter 4 dealt with the alkane formation pathways in the aqueous phase processing of 1-propanol over Pt and is focused on the effect of Pt step sites on these reactions. The alcohol-hydrogenolysis pathway, which under neutral conditions is the dominating mechanism of alkane formation, is only weakly affected by the presence of steps. Both at steps and on terrace sites, the alcohol-hydrogenolysis mechanism proceeds via the intermediate 1-hydroxypropyl, which is derived from the dehydrogenation of propanol at C1. The rate-limiting step here is the C-O cleavage of 1-hydroxypropyl. On a Pt terrace, this step is associated with a barrier of 105 kJ mol^{-1}. The presence of steps decreases the barrier only slightly, to 97 kJ mol^{-1}. The effect of the steps on the hydrogenation of propylene, which has previously been determined to be the rate-limiting step of the acidic dehydration-hydrogenation mechanism on Pt(111), has also been considered. Step sites lower the direct barrier of propylene hydrogenation from 85–97 kJ mol^{-1} to around 50 kJ mol^{-1}. However, it is not clear whether the reaction really prefers to occur at step sites, as the reaction at the steps involves, in contrast to the reaction on terrace sites, energetically high lying ISs. An explicit modeling of the kinetics may help to solve this issue. Despite of this open question, the results presented here provide, together with earlier works, a complete overview over the reaction network of the aqueous phase processing of 1-propanol on Pt. The high selectivity for the reforming pathway on Pt is related to the kinetically easily accessible dehydrogenation at C1 and at the OH group, which leads to the formation of propionyl, the key intermediate of the reforming pathway. The complete

dehydrogenation at the C1-O moiety strengthens the C-O bond, as the single bond in propanol formally becomes a double bond, which hinders the C-O cleavage required for alkane formation.

Chapter 5 showed a systematic study of the decomposition of ethanol on the closed-packed Ru(0001) surface. The C-O cleavage was shown to be both thermodynamically and kinetically more favored than the analogue reaction on Pt. Therefore, the formation of C-O bonds, e.g. the OH insertion into surface acyl groups (R-C=O), which is essential for the aqueous phase processing of alcohols on Pt, are not favored. Despite of these differences between the reactions on Ru and Pt, the reaction pathways on both metals are not fundamentally different. Similar to the reactions of 1-propanol on Pt(111), ethanol also dehydrogenates various times before it ultimately undergoes C-C cleavage. In particular, the preferred ethanol decomposition pathway on Ru(0001) proceeds via the intermediate ketene whose C-C bond cleaves with a relatively low barrier of only 38 kJ mol^{-1} to form carbon monoxide and methylene on the Ru surface. The highest barrier along this path is calculated at 77 kJ mol^{-1}; it is associated with the dehydrogenation at the C1 center of the intermediate ethoxy. This indicates that the alkanes observed in experiments on the aqueous phase processing of alcohols over Ru are most likely formed from methylene, CO and surface hydrogen in a reaction similar to the Fischer-Tropsch process, for which Ru is known to be catalytic active. The "direct" C-O cleavage without the preceding C-C scission requires the formation of 1-hydroxyethylidene. This species is associated with a C-O cleavage barrier of only 33 kJ mol^{-1}. However, the formation of 1-hydroxyethylidene, the key intermediate for the *direct* C-O cleavage pathway, is not favored as the competing undesired dehydrogenation at the hydroxyl group is a strongly exothermic reaction with an easily accessible barrier of around 70 kJ mol^{-1}. At variance, the dehydrogenation of ethanol at C1, which is required for the formation of 1-hydroxyethylidene, has a higher barrier of 91 kJ mol^{-1} and thus is less favored than the dehydrogenation at the OH group.

Having studied the comparably simple system of ethanol on Ru, Chapter 6 addressed the Ru-catalyzed hydrodeoxygenation of guaiacol. A most likely reaction path was proposed based on a systematic exploration of the potential energy surface, together with various alternative kinetically also accessible pathways. The proposed main reaction path proceeds via the formation of the key intermediates catecholate and phenolate; this finding is consistent with the experimental detection of catechol and phenol as intermediate products. The rate-limiting steps of the HDO process are cleavage reactions of the C_{aryl}-O bonds of

catecholate and phenolate. At terrace sites, only the C_{aryl}-O bond scission of catecholate, associated with a barrier of 106 kJ mol^{-1}, can be considered as kinetically accessible. At variance, the C_{aryl}-O cleavage barrier of 185 kJ mol^{-1} for phenolate indicates that this reaction is strongly hindered. The difference in the activation barrier for the reactions of catecholate and phenolate is related to the strained structure of the catecholate surface complex on the close-packed Ru surface. At step sites, both C_{aryl}-O cleavage steps are more easily accessible; they are associated with barriers of only 76 kJ mol^{-1} and 77 kJ mol^{-1}, respectively. Based on the calculated results, this thesis proposed a possible rationalization for the experimental observation that benzene is only formed under elevated H_2 pressure, while hydrodeoxygenation at reduced H_2 pressure mainly yields phenol. The availability of step sites on the Ru catalyst is likely linked to the H_2 pressure, as at high H_2 pressure step sites can be kept free of carbon depositions, which otherwise would poison the only site of a Ru catalyst that is active in the C_{aryl}-O scission of phenolate.

Chapter 7 focuses on quantum chemical tools to explore catalytic processes, rather than on the catalytic processes themselves. The performance of the DFT-D2 approach in the PBE-D2 variant and of the vdW-DF2 functional for representing dispersive interactions in MFI type zeolites has been evaluated. Both methods describe the adsorption of water and short-chain, primary alcohols reasonably well. In these systems, the adsorption process is dominated by the formation of hydrogen bonds between the adsorbate and the zeolite framework, while the contribution of the dispersive interactions to the adsorption energy is mostly of minor importance. The differences between theoretically determined adsorption energies and the experimental references are either smaller or comparable to the uncertainty of the experiment, which is 5–15 kJ mol^{-1}. However, both methods under study show the general tendency to overestimate the exothermicity of alkane adsorption. Discrepancies between theory and experiment of up to 46 kJ mol^{-1} demonstrate that “chemical accuracy” is not reachable for such adsorption interactions, which are dominated by dispersive interactions. Therefore, in such calculations, unfunctionalized hydrocarbons tend to be over-stabilized with respect to functionalized species such as oxygenates. This is an important issue to be kept in mind when one intends to deal with reactions involving both functionalized and unfunctionalized species like the transformation of ethanol to higher hydrocarbons.

In summary, this thesis, via its application results, provided new insight into the mechanistic details of metal-catalyzed transformations of aliphatic and aromatic oxygenates.

Especially the work on guaiacol hydrodeoxygenation has been one of the first detailed studies addressing the reaction network of metal-catalyzed hydrodeoxygenation of aromatics. The usage of stepped surfaces as catalyst models allowed taking into account the effect of the catalyst surface topology, amending the simplifications of flat surface models which still are very popular. The method-oriented work, evaluating recently proposed DFT-based methods for representing dispersive interactions, showed that, despite of notable methodological progress, a reliable description of reactions in zeolites, e.g. for biomass processing, is still challenging issue.

Appendix: List of Abbreviations

AH	alcohol hydrogenolysis
AP	aqueous phase
BEP	Brønsted-Evans-Polanyi (relation)
CCSD(T)	coupled-cluster with singles, doubles and perturbative triples
CN	coordination number
covEPE	covalent elastic polarizable environment (scheme)[263]
D2, DFT-D2	Empirical dispersion correction to DFT methods[49]
D3, DFT-D3	Empirical dispersion correction to DFT methods[269]
DFT	density functional theory
DH	dehydration-hydrogenation
DOS	density of states
exp	experiment
fcc	face-centered cubic
FT	Fischer-Tropsch (synthesis)
GGA	generalized gradient approximation
hcp	hexagonal close-packed
HDO	hydrodeoxygenation
H-ZSM5	proton form of Zeolite Socony Mobil-5
IS	initial state
LEED	low-energy electron diffraction
MFI	structure type ZSM-five
MOF	metal-organic framework
NEB	nudged elastic band
ONIOM	„our own n-layered integrated molecular orbital and molecular mechanics“ (method)[262]
optB88-vdW	non-local correlation van der Waals density functional based on the optimized Becke 88 type exchange functional[50]

PAW	projector-augmented wave (method)
PBE	Perdew-Burke-Ernzerhof type GGA functional[191,192]
PW91	Perdew-Wang type GGA functional[190]
QM/MM	quantum mechanics/molecular mechanics
RAIRS	reflection-absorption infrared spectroscopy
RI-MP2	resolution of identity second-order Møller-Plesset perturbation theory
SCF	self-consistent field
Si/Al	molar silicon to aluminum ratio in mol/mol
T	temperature
TPD	temperature programmed desorption
TS	transition state
TS-vdW	Tkatchenko-Scheffler vdW correction scheme[276]
VASP	Vienna Ab initio Simulation Package
vdW	van der Waals
vdW-DF2	non-local correlation van der Waals density functional[196]
WGS	water gas shift

References

1. Shafiee, S.; Topal, E., *Energ Policy* **2009,** *37*, 181-189.
2. Sorrell, S.; Miller, R.; Bentley, R.; Speirs, J., *Energ Policy* **2010,** *38*, 4990-5003.
3. Chapman, I., *Energ Policy* **2014,** *64*, 93-101.
4. Hallock Jr, J. L.; Wu, W.; Hall, C. A. S.; Jefferson, M., *Energy* **2014,** *64*, 130-153.
5. Miller, R. G.; Sorrell, S. R., *Phil Trans R Soc A* **2014,** *372*, 20130179-27.
6. Davis, S. C.; Diegel, S. W.; Boundy, R. G., Transportation Energy Data Book. 33rd ed.; 2014. http://cta.ornl.gov/data/tedb33/Edition33_Full_Doc.pdf (accessed 06.08.2014).
7. Matar, S.; Hatch, L. F., *Chemistry of Petrochemical Processes*. 2nd ed.; Gulf Professional Publishing: Houston, Texas, USA, 2000.
8. Stanier, C.; Hutchinson, J., A Sustainable Global Society - How Can Materials Chemistry Help? - A white paper from the Chemical Sciences and Society Summit (CS3) 2010 http://www.rsc.org/images/sustainable-global-society-full-report_tcm18-221431.pdf (accessed 06.08.2014).
9. Bull, T. E., *Science* **1999,** *285*, 1209.
10. Serrano-Ruiz, J. C.; Luque, R.; Sepulveda-Escribano, A., *Chem Soc Rev* **2011,** *40*, 5266-5281.
11. Bozell, J. J.; Petersen, G. R., *Green Chem* **2010,** *12*, 539-554.
12. Chheda, J. N.; Huber, G. W.; Dumesic, J. A., *Angew Chem Int Ed* **2007,** *46*, 7164-7183.
13. Greeley, J.; Norskov, J. K.; Mavrikakis, M., *Annu Rev Phys Chem* **2002,** *53*, 319-348.
14. Nachtigall, P.; Sauer, J., Chapter 20 Applications of quantum chemical methods in zeolite science. In *Introduction to Zeolite Molecular Sieves, Studies in Surface Science and Catalysis*, Čejka, J.; van Bekkum, H.; Corma, A.; Schüth, F., Eds. Elsevier: Amsterdam, 2007; Vol. 168, pp 701-736.
15. Nørskov, J. K.; Abild-Pedersen, F.; Studt, F.; Bligaard, T., *Proc Natl Acad Sci USA* **2011,** *108*, 937-943.
16. Wawrzetz, A.; Peng, B.; Hrabar, A.; Jentys, A.; Lemonidou, A. A.; Lercher, J. A., *J Catal* **2010,** *269*, 411-420.

17. Basaran, D.; Genest, A.; Rösch, N., *J Catal* **2012,** *287*, 210-213.
18. Başaran, D., Theoretical Studies of Catalytic Transformations of Hydrocarbons over Transition Metals. PhD Thesis, Technische Universität München, Munich, Germany, 2013.
19. Basaran, D.; Genest, A.; Lercher, J. A.; Rösch, N., *ACS Catal* **2013,** *3*, 1730-1738.
20. Chiu, C.-c., Density Functional Studies on Catalysis on Noble Metal Surfaces. Master Thesis, Technische Universität München, Munich, Germany, 2010.
21. Chiu, C.-c.; Genest, A.; Rösch, N., *ChemCatChem* **2013,** *5*, 3299-3308.
22. Davda, R. R.; Shabaker, J. W.; Huber, G. W.; Cortright, R. D.; Dumesic, J. A., *Appl Catal B-Environ* **2003,** *43*, 13-26.
23. Davda, R. R.; Shabaker, J. W.; Huber, G. W.; Cortright, R. D.; Dumesic, J. A., *Appl Catal B-Environ* **2005,** *56*, 171-186.
24. Alonso, D. M.; Bond, J. Q.; Dumesic, J. A., *Green Chem* **2010,** *12*, 1493-1513.
25. Guo, N.; Caratzoulas, S.; Doren, D. J.; Sandler, S. I.; Vlachos, D. G., *Energy Environ Sci* **2012,** *5*, 6703-6716.
26. Chang, J.; Danuthai, T.; Dewiyanti, S.; Wang, C.; Borgna, A., *ChemCatChem* **2013,** *5*, 3041-3049.
27. Boonyasuwat, S.; Omotoso, T.; Resasco, D. E.; Crossley, S. P., *Catal Lett* **2013,** *143*, 783-791.
28. Sun, J.; Karim, A. M.; Zhang, H.; Kovarik, L.; Li, X. S.; Hensley, A. J.; McEwen, J.-S.; Wang, Y., *J Catal* **2013,** *306*, 47-57.
29. Gao, D.; Schweitzer, C.; Hwang, H. T.; Varma, A., *Ind Eng Chem Res* **2014,** *53*,18658-18667.
30. van Bokhoven, J. A., In *Ordered Porous Solids Recent Advances and Prospects*, Valtchev, V.; Mintova, S.; Tsapatsis, M., Eds. Elsevier: 2009; pp 651-668.
31. Bellussi, G.; Mizia, F.; Calemma, V.; Pollesel, P.; Millini, R., *Micropor Mesopor Mat* **2012,** *164*, 127-134.
32. Eder, F.; Lercher, J. A., *Zeolites* **1997,** *18*, 75-81.
33. Eder, F.; Stockenhuber, M.; Lercher, J. A., *J Phys Chem B* **1997,** *101*, 5414-5419.
34. Lee, C. C.; Gorte, R. J.; Farneth, W. E., *J Phys Chem B* **1997,** *101*, 3811-3817.
35. De Moor, B. A.; Reyniers, M.-F.; Gobin, O. C.; Lercher, J. A.; Marin, G. B., *J Phys Chem C* **2011,** *115*, 1204-1219.
36. Hampson, J. A.; Rees, L. V. C., *J Chem Soc Faraday T* **1993,** *89*, 3169-3176.
37. Tuma, C.; Sauer, J., *Phys Chem Chem Phys* **2006,** *8*, 3955-3965.

38. De Moor, B. A.; Reyniers, M.-F.; Sierka, M.; Sauer, J.; Marin, G. B., *J Phys Chem C* **2008,** *112*, 11796-11812.
39. Kerber, T.; Sierka, M.; Sauer, J., *J Comput Chem* **2008,** *29*, 2088-2097.
40. Svelle, S.; Tuma, C.; Rozanska, X.; Kerber, T.; Sauer, J., *J Am Chem Soc* **2009,** *131*, 816-825.
41. Nguyen, C. M.; Reyniers, M.-F.; Marin, G. B., *Phys Chem Chem Phys* **2010,** *12*, 9481-9493.
42. Hansen, N.; Kerber, T.; Sauer, J.; Bell, A. T.; Keil, F. J., *J Am Chem Soc* **2010,** *132*, 11525-11538.
43. Nguyen, C. M.; Reyniers, M.-F.; Marin, G. B., *J Phys Chem C* **2011,** *115*, 8658-8669.
44. Van der Mynsbrugge, J.; Hemelsoet, K.; Vandichel, M.; Waroquier, M.; Van Speybroeck, V., *J Phys Chem C* **2012,** *116*, 5499-5508.
45. Zazza, C.; Sanna, N.; Rutigliano, M.; Cacciatore, M.; Palma, A., *Comp Theor Chem* **2011,** *967*, 191-198.
46. Tranca, D. C.; Hansen, N.; Swisher, J. A.; Smit, B.; Keil, F. J., *J Phys Chem C* **2012,** *116*, 23408-23417.
47. Sukrat, K.; Tunega, D.; Aquino, A. J. A.; Lischka, H.; Parasuk, V., *Theor Chem Acc* **2012,** *131*, 1-12.
48. Cohen, A. J.; Mori-Sánchez, P.; Yang, W., *Chem Rev* **2011,** *112*, 289-320.
49. Grimme, S., *J Comput Chem* **2006,** *27*, 1787-1799.
50. Klimeš, J.; Bowler, D. R.; Michaelides, A., *Phys Rev B* **2011,** *83*, 195131-13.
51. Ma, F.; Hanna, M. A., *Bioresource Technol* **1999,** *70*, 1-15.
52. Cortright, R. D.; Davda, R. R.; Dumesic, J. A., *Nature* **2002,** *418*, 964-967.
53. Shabaker, J. W.; Davda, R. R.; Huber, G. W.; Cortright, R. D.; Dumesic, J. A., *J Catal* **2003,** *215*, 344-352.
54. Huber, G. W.; Shabaker, J. W.; Dumesic, J. A., *Science* **2003,** *300*, 2075-2077.
55. Shabaker, J. W.; Huber, G. W.; Davda, R. R.; Cortright, R. D.; Dumesic, J. A., *Catal Lett* **2003,** *88*, 1-8.
56. Davda, R. R.; Dumesic, J. A., *Angew Chem Int Ed* **2003,** *42*, 4068-4071.
57. Shabaker, J. W.; Huber, G. W.; Dumesic, J. A., *J Catal* **2004,** *222*, 180-191.
58. Shabaker, J. W.; Simonetti, D. A.; Cortright, R. D.; Dumesic, J. A., *J Catal* **2005,** *231*, 67-76.
59. Huber, G. W.; Chheda, J. N.; Barrett, C. J.; Dumesic, J. A., *Science* **2005,** *308*, 1446-1450.

60. Huber, G. W.; Shabaker, J. W.; Evans, S. T.; Dumesic, J. A., *Appl Catal B-Environ* **2006,** *62*, 226-235.
61. Maris, E. P.; Davis, R. J., *J Catal* **2007,** *249*, 328-337.
62. Maris, E. P.; Ketchie, W. C.; Murayama, M.; Davis, R. J., *J Catal* **2007,** *251*, 281-294.
63. Geboers, J. A.; Van de Vyver, S.; Ooms, R.; Op de Beeck, B.; Jacobs, P. A.; Sels, B. F., *Catal Sci Tech* **2011,** *1*, 714-726.
64. Van de Vyver, S.; Geboers, J.; Jacobs, P. A.; Sels, B. F., *ChemCatChem* **2011,** *3*, 82-94.
65. Weingarten, R.; Conner, W. C.; Huber, G. W., *Energy Environ Sci* **2012,** *5*, 7559-7574.
66. Huber, G. W.; Cortright, R. D.; Dumesic, J. A., *Angew Chem Int Ed* **2004,** *43*, 1549-1551.
67. Santen, R. A. v.; Neurock, M.; Shetty, S. G., *Chem Rev* **2009,** *110*, 2005-2048.
68. Ferrin, P.; Simonetti, D.; Kandoi, S.; Kunkes, E.; Dumesic, J. A.; Nørskov, J. K.; Mavrikakis, M., *J Am Chem Soc* **2009,** *131*, 5809-5815.
69. Kua, J.; Goddard, W. A., *J Am Chem Soc* **1999,** *121*, 10928-10941.
70. Zhang, C. J.; Hu, P., *J Chem Phys* **2001,** *115*, 7182-7186.
71. Alcalá, R.; Mavrikakis, M.; Dumesic, J. A., *J Catal* **2003,** *218*, 178-190.
72. Davda, R. R.; Alcalá, R.; Shabaker, J.; Huber, G.; Cortright, R. D.; Mavrikakis, M.; Dumesic, J. A., 11 DFT and experimental studies of C-C and C-O bond cleavage in ethanol and ethylene glycol on Pt catalysts. In *Studies in Surface Science and Catalysis*, Anpo, M.; Onaka, M.; Hiromi, Y., Eds. Elsevier: Amsterdam, 2003; Vol. 145, pp 79-84.
73. Yudanov, I. V.; Matveev, A. V.; Neyman, K. M.; Rösch, N., *J Am Chem Soc* **2008,** *130*, 9342-9352.
74. Ferrin, P.; Nilekar, A. U.; Greeley, J.; Mavrikakis, M.; Rossmeisl, J., *Surf Sci* **2008,** *602*, 3424-3431.
75. Li, M.; Guo, W.; Jiang, R.; Zhao, L.; Shan, H., *Langmuir* **2009,** *26*, 1879-1888.
76. Zope, B. N.; Hibbitts, D. D.; Neurock, M.; Davis, R. J., *Science* **2010,** *330*, 74-78.
77. Li, M.; Guo, W.; Jiang, R.; Zhao, L.; Lu, X.; Zhu, H.; Fu, D.; Shan, H., *J Phys Chem C* **2010,** *114*, 21493-21503.
78. Liu, B.; Greeley, J., *J Phys Chem C* **2011,** *115*, 19702-19709.
79. Grabow, L. C.; Mavrikakis, M., *ACS Catal* **2011,** *1*, 365-384.
80. Choi, Y.; Liu, P., *Catal Today* **2011,** *165*, 64-70.
81. Zhang, J.; Cao, X. M.; Hu, P.; Zhong, Z.; Borgna, A.; Wu, P., *J Phys Chem C* **2011,** *115*, 22429-22437.

82. Liu, B.; Greeley, J., *Top Catal* **2012,** *55*, 280-289.
83. Studt, F.; Abild-Pedersen, F.; Wu, Q.; Jensen, A. D.; Temel, B.; Grunwaldt, J.-D.; Nørskov, J. K., *J Catal* **2012,** *293*, 51-60.
84. Palo, D. R.; Dagle, R. A.; Holladay, J. D., *Chem Rev* **2007,** *107*, 3992-4021.
85. Klier, K., Methanol Synthesis. In *Advances in Catalysis*, Eley, D. D.; Pines, H.; Weisz, P. B., Eds. Academic Press: New York, 1982; Vol. 31, pp 243-313.
86. Sutton, J. E.; Vlachos, D. G., *Ind Eng Chem Res* **2014,** DOI: 10.1021/ie5043374.
87. Sutton, J. E.; Panagiotopoulou, P.; Verykios, X. E.; Vlachos, D. G., *J Phys Chem C* **2013,** *117*, 4691-4706.
88. Wang, H.-F.; Liu, Z.-P., *J Am Chem Soc* **2008,** *130*, 10996-11004.
89. Ma, Y.; Hernández, L.; Guadarrama-Pérez, C.; Balbuena, P. B., *J Phys Chem A* **2012,** *116*, 1409-1416.
90. Wang, J.-H.; Lee, C. S.; Lin, M. C., *J Phys Chem C* **2009,** *113*, 6681-6688.
91. Chen, Y.; Salciccioli, M.; Vlachos, D. G., *J Phys Chem C* **2011,** *115*, 18707-18720.
92. Liu, B.; Greeley, J., *Phys Chem Chem Phys* **2013,** *15*, 6475-6485.
93. Salciccioli, M.; Vlachos, D. G., *ACS Catal* **2011,** *1*, 1246-1256.
94. Wang, H.-F.; Liu, Z.-P., *J Phys Chem C* **2007,** *111*, 12157-12160.
95. Wang, E. D.; Xu, J. B.; Zhao, T. S., *J Phys Chem C* **2010,** *114*, 10489-10497.
96. Zhang, J.; Zhong, Z.; Cao, X. M.; Hu, P.; Sullivan, M. B.; Chen, L., *ACS Catal* **2014,** *4*, 448-456.
97. Nørskov, J. K.; Bligaard, T.; Logadottir, A.; Bahn, S.; Hansen, L. B.; Bollinger, M.; Bengaard, H.; Hammer, B.; Sljivancanin, Z.; Mavrikakis, M.; Xu, Y.; Dahl, S.; Jacobsen, C. J. H., *J Catal* **2002,** *209*, 275-278.
98. Roy, S.; Mpourmpakis, G.; Hong, D.-Y.; Vlachos, D. G.; Bhan, A.; Gorte, R. J., *ACS Catal* **2012,** *2*, 1846-1853.
99. Ishimoto, R.; Jung, C.; Tsuboi, H.; Koyama, M.; Endou, A.; Kubo, M.; Del Carpio, C. A.; Miyamoto, A., *Appl Catal A-Gen* **2006,** *305*, 64-69.
100. Ahmed, F.; Nagumo, R.; Miura, R.; Suzuki, A.; Tsuboi, H.; Hatakeyama, N.; Takaba, H.; Miyamoto, A., *J Phys Chem C* **2011,** *115*, 24123-24132.
101. Ahmed, F.; Miura, R.; Hatakeyama, N.; Takaba, H.; Miyamoto, A.; Salahub, D. R., *J Phys Chem C* **2013,** *117*, 5051-5066.
102. Laurent, E.; Delmon, B., *Appl Catal A-Gen* **1994,** *109*, 77-96.
103. Laurent, E.; Delmon, B., *Appl Catal A-Gen* **1994,** *109*, 97-115.
104. Elliott, D. C.; Hart, T. R., *Energ Fuel* **2008,** *23*, 631-637.

105. Wildschut, J.; Mahfud, F. H.; Venderbosch, R. H.; Heeres, H. J., *Ind Eng Chem Res* **2009,** *48*, 10324-10334.
106. Yakovlev, V. A.; Khromova, S. A.; Sherstyuk, O. V.; Dundich, V. O.; Ermakov, D. Y.; Novopashina, V. M.; Lebedev, M. Y.; Bulavchenko, O.; Parmon, V. N., *Catal Today* **2009,** *144*, 362-366.
107. Zhao, C.; Kou, Y.; Lemonidou, A. A.; Li, X.; Lercher, J. A., *Angew Chem Int Ed* **2009,** *48*, 3987-3990.
108. Zakzeski, J.; Bruijnincx, P. C. A.; Jongerius, A. L.; Weckhuysen, B. M., *Chem Rev* **2010,** *110*, 3552-3599.
109. Carlson, T. R.; Cheng, Y.-T.; Jae, J.; Huber, G. W., *Energy Environ Sci* **2011,** *4*, 145-161.
110. Mortensen, P. M.; Grunwaldt, J. D.; Jensen, P. A.; Knudsen, K. G.; Jensen, A. D., *Appl Catal A-Gen* **2011,** *407*, 1-19.
111. Nimmanwudipong, T.; Runnebaum, R. C.; Block, D. E.; Gates, B. C., *Energ Fuel* **2011,** *25*, 3417-3427.
112. Badawi, M.; Paul, J.-F.; Cristol, S.; Payen, E., *Catal Comm* **2011,** *12*, 901-905.
113. Zhao, C.; He, J.; Lemonidou, A. A.; Li, X.; Lercher, J. A., *J Catal* **2011,** *280*, 8-16.
114. He, Z.; Wang, X., *Catal Sustain Energy* **2012,** *1*, 28-53.
115. Lee, C. R.; Yoon, J. S.; Suh, Y.-W.; Choi, J.-W.; Ha, J.-M.; Suh, D. J.; Park, Y.-K., *Catal Comm* **2012,** *17*, 54-58.
116. Nimmanwudipong, T.; Aydin, C.; Lu, J.; Runnebaum, R.; Brodwater, K.; Browning, N.; Block, D.; Gates, B., *Catal Lett* **2012,** *142*, 1190-1196.
117. Runnebaum, R. C.; Nimmanwudipong, T.; Block, D. E.; Gates, B. C., *Catal Sci Tech* **2012,** *2*, 113-118.
118. Bykova, M. V.; Ermakov, D. Y.; Kaichev, V. V.; Bulavchenko, O. A.; Saraev, A. A.; Lebedev, M. Y.; Yakovlev, V. A., *Appl Catal B-Environ* **2012,** *113–114*, 296-307.
119. Ben, H.; Mu, W.; Deng, Y.; Ragauskas, A. J., *Fuel* **2013,** *103*, 1148-1153.
120. Mortensen, P. M.; Grunwaldt, J.-D.; Jensen, P. A.; Jensen, A. D., *ACS Catal* **2013,** *3*, 1774-1785.
121. Badawi, M.; Paul, J.-F.; Payen, E.; Romero, Y.; Richard, F.; Brunet, S.; Popov, A.; Kondratieva, E.; Gilson, J.-P.; Mariey, L.; Travert, A.; Maugé, F., *Oil Gas Sci Technol – Rev IFP* **2013,** *68*, 829-840.
122. Wang, X.; Rinaldi, R., *Angew Chem Int Ed* **2013,** *52*, 11499-11503.

123. Jongerius, A. L.; Bruijnincx, P. C. A.; Weckhuysen, B. M., *Green Chem* **2013,** *15*, 3049-3056.
124. Nie, L.; de Souza, P. M.; Noronha, F. B.; An, W.; Sooknoi, T.; Resasco, D. E., *J Mol Catal A-Chem* **2014,** *388–389*, 47-55.
125. Anex, R. P.; Aden, A.; Kazi, F. K.; Fortman, J.; Swanson, R. M.; Wright, M. M.; Satrio, J. A.; Brown, R. C.; Daugaard, D. E.; Platon, A.; Kothandaraman, G.; Hsu, D. D.; Dutta, A., *Fuel* **2010,** *89, Supplement 1*, S29-S35.
126. Mohan, D.; Pittman, C. U.; Steele, P. H., *Energ Fuel* **2006,** *20*, 848-889.
127. Huber, G. W.; Iborra, S.; Corma, A., *Chem Rev* **2006,** *106*, 4044-4098.
128. Resasco, D. E.; Crossley, S., *AIChE J* **2009,** *55*, 1082-1089.
129. Moon, J.-S.; Kim, E.-G.; Lee, Y.-K., *J Catal* **2014,** *311*, 144-152.
130. Ben, H.; Ferguson, G. A.; Mu, W.; Pu, Y.; Huang, F.; Jarvis, M.; Biddy, M.; Deng, Y.; Ragauskas, A. J., *Phys Chem Chem Phys* **2013,** *15*, 19138-19142.
131. Wan, H.; Chaudhari, R. V.; Subramaniam, B., *Top Catal* **2012,** *55*, 129-139.
132. Jin, S.; Xiao, Z.; Li, C.; Chen, X.; Wang, L.; Xing, J.; Li, W.; Liang, C., *Catal Today*, **2014**, *234*, 125-132.
133. Bui, V. N.; Toussaint, G.; Laurenti, D.; Mirodatos, C.; Geantet, C., *Catal Today* **2009,** *143*, 172-178.
134. Ohta, H.; Kobayashi, H.; Hara, K.; Fukuoka, A., *Chem Comm* **2011,** *47*, 12209-12211.
135. Girgis, M. J.; Gates, B. C., *Ind Eng Chem Res* **1991,** *30*, 2021-2058.
136. Furimsky, E., *Catal Today* **2013,** *217*, 13-56.
137. Lu, J.; Heyden, A., Theoretical Study of the Liquid-phase Deoxygenation of Guaiacol into Aromatic Chemicals over Ru Surfaces. At 23rd North American Catalysis Society Meeting, Louisville, Kentucky, USA. https://nam.confex.com/nam/2013/webprogram/Paper7915.html (accessed June 11, 2014).
138. Lu, J.; Heyden, A., *J Catal* **2015,** *321*, 39-50.
139. Lee, K.; Gu, G. H.; Mullen, C. A.; Boateng, A. A.; Vlachos, D. G., *ChemSusChem* **2015,** *8*, 315-322.
140. Hensley, A.; Wang, Y.; McEwen, J.-S., *ACS Catal* **2015,** *5*, 523-536.
141. He, J.; Zhao, C.; Mei, D.; Lercher, J. A., *J Catal* **2014,** *309*, 280-290.
142. He, J.; Lu, L.; Zhao, C.; Mei, D.; Lercher, J. A., *J Catal* **2014,** *311*, 41-51.
143. Hensley, A. J. R.; Hong, Y.; Zhang, R.; Zhang, H.; Sun, J.; Wang, Y.; McEwen, J.-S., *ACS Catal* **2014,** *4*, 3381-3392.

144. Mittendorfer, F.; Hafner, J., *J Phys Chem B* **2002,** *106*, 13299-13305.
145. Saeys, M.; Reyniers, M.-F.; Neurock, M.; Marin, G. B., *J Phys Chem B* **2003,** *107*, 3844-3855.
146. Saeys, M.; Reyniers, M. F.; Neurock, M.; Marin, G. B., *J Phys Chem B* **2004,** *109*, 2064-2073.
147. Morin, C.; Simon, D.; Sautet, P., *Surf Sci* **2006,** *600*, 1339-1350.
148. Ghiringhelli, L. M.; Caputo, R.; Delle Site, L., *Phys Rev B* **2007,** *75*, 113403-4.
149. Lesnard, H.; Bocquet, M.-L.; Lorente, N., *J Am Chem Soc* **2007,** *129*, 4298-4305.
150. Honkela, M. L.; Bjork, J.; Persson, M., *Phys Chem Chem Phys* **2012,** *14*, 5849-5854.
151. Yoon, Y.; Rousseau, R.; Weber, R. S.; Mei, D.; Lercher, J. A., *J Am Chem Soc* **2014,** *136*, 10287-10298.
152. Inoue, T.; Itakura, M.; Jon, H.; Oumi, Y.; Takahashi, A.; Fujitani, T.; Sano, T., *Micropor Mesopor Mat* **2009,** *122*, 149-154.
153. Song, Z.; Takahashi, A.; Mimura, N.; Fujitani, T., *Catal Lett* **2009,** *131*, 364-369.
154. Ermakov, R. V.; Plakhotnik, V. A., *Pet Chem* **2008,** *48*, 1-5.
155. Inaba, M.; Murata, K.; Saito, M.; Takahara, I., *Green Chem* **2007,** *9*, 638-646.
156. Gayubo, A. G.; Alonso, A.; Valle, B.; Aguayo, A. T.; Olazar, M.; Bilbao, J., *Fuel* **2010,** *89*, 3365-3372.
157. Gayubo, A. G.; Alonso, A.; Valle, B.; Aguayo, A. T.; Bilbao, J., *Appl Catal B-Environ* **2010,** *97*, 299-306.
158. Goto, D.; Harada, Y.; Furumoto, Y.; Takahashi, A.; Fujitani, T.; Oumi, Y.; Sadakane, M.; Sano, T., *Appl Catal A-Gen* **2010,** *383*, 89-95.
159. Inaba, M.; Murata, K.; Saito, M.; Takahara, I., *React Kinet Catal Lett* **2006,** *88*, 135-141.
160. Derouane, E. G.; Nagy, J. B.; Dejaifve, P.; van Hooff, J. H. C.; Spekman, B. P.; Védrine, J. C.; Naccache, C., *J Catal* **1978,** *53*, 40-55.
161. Anderson, J. R.; Foger, K.; Mole, T.; Rajadhyaksha, R. A.; Sanders, J. V., *J Catal* **1979,** *58*, 114-130.
162. Johansson, R.; Hruby, S.; Rass-Hansen, J.; Christensen, C., *Catal Lett* **2009,** *127*, 1-6.
163. Stöcker, M., *Micropor Mesopor Mat* **1999,** *29*, 3-48.
164. Stöcker, M., *Micropor Mesopor Mat* **2005,** *82*, 257-292.
165. Haw, J. F.; Song, W.; Marcus, D. M.; Nicholas, J. B., *Acc Chem Res* **2003,** *36*, 317-326.
166. Olsbye, U.; Svelle, S.; Bjørgen, M.; Beato, P.; Janssens, T. V. W.; Joensen, F.; Bordiga, S.; Lillerud, K. P., *Angew Chem Int Ed* **2012,** *51*, 5810-5831.

167. Lesthaeghe, D.; Horré, A.; Waroquier, M.; Marin, G. B.; Van Speybroeck, V., *Chem Eur J* **2009,** *15*, 10803-10808.
168. Inaba, M.; Murata, K.; Takahara, I.; Inoue, K.-i., *J Chem Technol Biot* **2011,** *86*, 95-104.
169. Gayubo, A. G.; Alonso, A.; Valle, B.; Aguayo, A. T.; Bilbao, J., *AIChE J* **2012,** *58*, 526-537.
170. Kresse, G.; Hafner, J., *Phys Rev B* **1993,** *47*, 558-561.
171. Kresse, G.; Hafner, J., *Phys Rev B* **1994,** *49*, 14251-14269.
172. Kresse, G.; Furthmüller, J., *Comp Mater Sci* **1996,** *6*, 15-50.
173. Kresse, G.; Furthmüller, J., *Phys Rev B* **1996,** *54*, 11169-11186.
174. Blöchl, P. E., *Phys Rev B* **1994,** *50*, 17953-17979.
175. Kresse, G.; Joubert, D., *Phys Rev B* **1999,** *59*, 1758-1775.
176. Jónsson, H.; Mills, G.; Jacobsen, K. W., Nudged elastic band method for finding minimum energy paths of transitions. In *Classical And Quantum Dynamics In Condensed Phase Simulations*, World Scientific: Singapore, 1998; pp 385-404.
177. Henkelman, G.; Jónsson, H., *J Chem Phys* **2000,** *113*, 9978-9985.
178. Henkelman, G.; Uberuaga, B. P.; Jónsson, H., *J Chem Phys* **2000,** *113*, 9901-9904.
179. Sheppard, D.; Terrell, R.; Henkelman, G., *J Chem Phys* **2008,** *128*, 134106-10.
180. Sheppard, D.; Henkelman, G., *J Comput Chem* **2011,** *32*, 1769-1771.
181. Sheppard, D.; Xiao, P.; Chemelewski, W.; Johnson, D. D.; Henkelman, G., *J Chem Phys* **2012,** *136*, 074103-8.
182. Chaffey-Millar, H.; Nikodem, A.; Matveev, A. V.; Krüger, S.; Rösch, N., *J Chem Theory Comput* **2012,** *8*, 777-786.
183. Nikodem, A.; Matveev, A. V.; Zheng, B.-X.; Rösch, N., *J Chem Theory Comput* **2012,** *9*, 588-599.
184. Henkelman, G.; Jónsson, H., *J Chem Phys* **1999,** *111*, 7010-7022.
185. Olsen, R. A.; Kroes, G. J.; Henkelman, G.; Arnaldsson, A.; Jónsson, H., *J Chem Phys* **2004,** *121*, 9776-9792.
186. Heyden, A.; Bell, A. T.; Keil, F. J., *J Chem Phys* **2005,** *123*, 224101-14.
187. Kästner, J.; Sherwood, P., *J Chem Phys* **2008,** *128*, 014106-6.
188. McQuarrie, D. A.; Simon, J. D., *Molecular Thermondynamics*. University Science Books: Sausalito, 1999.
189. Chang, C.-R.; Zhao, Z.-J.; Köhler, K.; Genest, A.; Li, J.; Rösch, N., *Catal Sci Tech* **2012,** *2*, 2238-2248.

190. Perdew, J. P.; Wang, Y., *Phys Rev B* **1992,** *45*, 13244-13249.
191. Perdew, J. P.; Burke, K.; Ernzerhof, M., *Phys Rev Lett* **1996,** *77*, 3865-3868.
192. Perdew, J. P.; Burke, K.; Ernzerhof, M., *Phys Rev Lett* **1997,** *78*, 1396-1396.
193. Methfessel, M.; Paxton, A. T., *Phys Rev B* **1989,** *40*, 3616-3621.
194. Monkhorst, H. J.; Pack, J. D., *Phys Rev B* **1976,** *13*, 5188-5192.
195. Moskaleva, L. V.; Chen, Z.-X.; Aleksandrov, H. A.; Mohammed, A. B.; Sun, Q.; Rösch, N., *J Phys Chem C* **2009,** *113*, 2512-2520.
196. Lee, K.; Murray, É. D.; Kong, L.; Lundqvist, B. I.; Langreth, D. C., *Phys Rev B* **2010,** *82*, 081101-4.
197. VASP manual, http://cms.mpi.univie.ac.at/vasp/guide/node124.html. (accessed 28.08.2013).
198. VASP manual, http://cms.mpi.univie.ac.at/vasp/guide/node161.html. (accessed 19.08.2014).
199. Baerlocher, C.; McCusker, L. B., Database of Zeolite Structures: http://www.iza-structure.org/databases/. (accessed 16.04.2012).
200. Schröder, K.-P.; Sauer, J.; Leslie, M.; Richard, C.; Catlow, A., *Zeolites* **1992,** *12*, 20-23.
201. Valcárcel, A.; Ricart, J. M.; Clotet, A.; Illas, F.; Markovits, A.; Minot, C., *J Catal* **2006,** *241*, 115-122.
202. Yang, M.-L.; Zhu, Y.-A.; Fan, C.; Sui, Z.-J.; Chen, D.; Zhou, X.-G., *Phys Chem Chem Phys* **2011,** *13*, 3257-3267.
203. Zhao, Z.-J.; Moskaleva, L. V.; Aleksandrov, H. A.; Basaran, D.; Rösch, N., *J Phys Chem C* **2010,** *114*, 12190-12201.
204. Alcala, R.; Greeley, J.; Mavrikakis, M.; Dumesic, J. A., *J Chem Phys* **2002,** *116*, 8973-8980.
205. Greeley, J.; Mavrikakis, M., *J Am Chem Soc* **2004,** *126*, 3910-3919.
206. Michaelides, A.; Hu, P., *J Am Chem Soc* **2001,** *123*, 4235-4242.
207. Wang, J. G.; Hammer, B., *J Chem Phys* **2006,** *124*, 184704-7.
208. Karp, E. M.; Campbell, C. T.; Studt, F.; Abild-Pedersen, F.; Nørskov, J. K., *J Phys Chem C* **2012,** *116*, 25772-25776.
209. Michel, C.; Goltl, F.; Sautet, P., *Phys Chem Chem Phys* **2012,** *14*, 15286-15290.
210. Grabow, L. C.; Gokhale, A. A.; Evans, S. T.; Dumesic, J. A.; Mavrikakis, M., *J Phys Chem C* **2008,** *112*, 4608-4617.

211. Carey, F. A.; Sundberg, R. J., *Advanced Organic Chemistry, Part A: Structures and Mechanisms*. Fifth Edition ed.; Springer Science+Business Media, LLC: New York, 2008.
212. Bligaard, T.; Nørskov, J. K.; Dahl, S.; Matthiesen, J.; Christensen, C. H.; Sehested, J., *J Catal* **2004,** *224*, 206-217.
213. Chiu, C.-c.; Genest, A.; Rösch, N., *Top Catal* **2013,** *56*, 874-884.
214. Dry, M. E., *Catal Today* **2002,** *71*, 227-241.
215. Ojeda, M.; Li, A.; Nabar, R.; Nilekar, A. U.; Mavrikakis, M.; Iglesia, E., *J Phys Chem C* **2010,** *114*, 19761-19770.
216. Ojeda, M.; Nabar, R.; Nilekar, A. U.; Ishikawa, A.; Mavrikakis, M.; Iglesia, E., *J Catal* **2010,** *272*, 287-297.
217. Zhuo, M.; Tan, K. F.; Borgna, A.; Saeys, M., *J Phys Chem C* **2009,** *113*, 8357-8365.
218. Inderwildi, O. R.; Jenkins, S. J.; King, D. A., *J Phys Chem C* **2008,** *112*, 1305-1307.
219. Shetty, S.; Jansen, A. P. J.; van Santen, R. A., *J Am Chem Soc* **2009,** *131*, 12874-12875.
220. Shetty, S.; Jansen, A. P. J.; van Santen, R. A., *J Phys Chem C* **2008,** *112*, 14027-14033.
221. Ciobîcă, I. M.; Frechard, F.; van Santen, R. A.; Kleyn, A. W.; Hafner, J., *Chem Phys Lett* **1999,** *311*, 185-192.
222. Ciobîcă, I. M.; Frechard, F.; van Santen, R. A.; Kleyn, A. W.; Hafner, J., *J Phys Chem B* **2000,** *104*, 3364-3369.
223. Ciobica, I. M.; van Santen, R. A., *J Phys Chem B* **2002,** *106*, 6200-6205.
224. Morgan, G. A.; Sorescu, D. C.; Zubkov, T.; Yates, J. T., *J Phys Chem B* **2004,** *108*, 3614-3624.
225. Ge, Q.; Neurock, M.; Wright, H. A.; Srinivasan, N., *J Phys Chem B* **2002,** *106*, 2826-2829.
226. Basaran, D.; Aleksandrov, H. A.; Chen, Z.-X.; Zhao, Z.-J.; Rösch, N., *J Mol Catal A-Chem* **2011,** *344*, 37-46.
227. Chen, Z.-X.; Aleksandrov, H. A.; Basaran, D.; Rösch, N., *J Phys Chem C* **2010,** *114*, 17683-17692.
228. Moskaleva, L. V.; Chen, Z.-X.; Aleksandrov, H. A.; Mohammed, A. B.; Sun, Q.; Rösch, N., *J Phys Chem C* **2009,** *113*, 2512-2520.
229. Moskaleva, L. V.; Aleksandrov, H. A.; Basaran, D.; Zhao, Z.-J.; Rösch, N., *J Phys Chem C* **2009,** *113*, 15373-15379.
230. Ford, D. C.; Nilekar, A. U.; Xu, Y.; Mavrikakis, M., *Surf Sci* **2010,** *604*, 1565-1575.
231. Liu, Z.-P.; Hu, P., *J Am Chem Soc* **2002,** *124*, 11568-11569.

232. Chiu, C.-c.; Genest, A.; Borgna, A.; Rösch, N., *ACS Catal* **2014,** *4*, 4178-4188.
233. Dahl, S.; Logadottir, A.; Egeberg, R. C.; Larsen, J. H.; Chorkendorff, I.; Törnqvist, E.; Nørskov, J. K., *Phys Rev Lett* **1999,** *83*, 1814-1817.
234. Stellwag, C.; Held, G.; Menzel, D., *Surf Sci* **1995,** *325*, L379-L384.
235. Braun, W.; Held, G.; Steinrück, H. P.; Stellwag, C.; Menzel, D., *Surf Sci* **2001,** *475*, 18-36.
236. Held, G.; Braun, W.; Steinrück, H.-P.; Yamagishi, S.; Jenkins, S.; King, D., *Phys Rev Lett* **2001,** *87*, 216102-4.
237. Schravendijk, P.; van der Vegt, N.; Delle Site, L.; Kremer, K., *ChemPhysChem* **2005,** *6*, 1866-1871.
238. Bilić, A.; Reimers, J. R.; Hush, N. S.; Hoft, R. C.; Ford, M. J., *J Chem Theory Comput* **2006,** *2*, 1093-1105.
239. Saeys, M.; Reyniers, M.-F.; Marin, G. B.; Neurock, M., *J Phys Chem B* **2002,** *106*, 7489-7498.
240. Morin, C.; Simon, D.; Sautet, P., *J Phys Chem B* **2004,** *108*, 5653-5665.
241. Orita, H.; Itoh, N., *Appl Catal A-Gen* **2004,** *258*, 17-23.
242. Delle Site, L.; Alavi, A.; Abrams, C. F., *Phys Rev B* **2003,** *67*, 193406-3.
243. Tan, Y. P.; Khatua, S.; Jenkins, S. J.; Yu, J. Q.; Spencer, J. B.; King, D. A., *Surf Sci* **2005,** *589*, 173-183.
244. Bonalumi, N.; Vargas, A.; Ferri, D.; Baiker, A., *J Phys Chem B* **2006,** *110*, 9956-9965.
245. Herron, J. A.; Tonelli, S.; Mavrikakis, M., *Surf Sci* **2013,** *614*, 64-74.
246. Sinha, N. K.; Neurock, M., *J Catal* **2012,** *295*, 31-44.
247. Ciobica, I. M.; van Santen, R. A., *J Phys Chem B* **2003,** *107*, 3808-3812.
248. Vendelbo, S. B.; Johansson, M.; Mowbray, D. J.; Andersson, M. P.; Abild-Pedersen, F.; Nielsen, J. H.; Nørskov, J. K.; Chorkendorff, I., *Top Catal* **2010,** *53*, 357-364.
249. Li, H.; Fu, G.; Xu, X., *Phys Chem Chem Phys* **2012,** *14*, 16686-16694.
250. Mortensen, J. J.; Morikawa, Y.; Hammer, B.; Nørskov, J. K., *J Catal* **1997,** *169*, 85-92.
251. Bartholomew, C. H., *Catal Rev* **1982,** *24*, 67-112.
252. Schauermann, S.; Hoffmann, J.; Johánek, V.; Hartmann, J.; Libuda, J.; Freund, H.-J., *Angew Chem Int Ed* **2002,** *41*, 2532-2535.
253. Zubkov, T.; Morgan Jr, G. A.; Yates Jr, J. T.; Kühlert, O.; Lisowski, M.; Schillinger, R.; Fick, D.; Jänsch, H. J., *Surf Sci* **2003,** *526*, 57-71.
254. Baumer, M.; Libuda, J.; Neyman, K. M.; Rösch, N.; Rupprechter, G.; Freund, H.-J., *Phys Chem Chem Phys* **2007,** *9*, 3541-3558.

255. Kozlov, S. M.; Cabeza, G. F.; Neyman, K. M., *Chem Phys Lett* **2011,** *506*, 92-97.
256. Schauermann, S.; Nilius, N.; Shaikhutdinov, S.; Freund, H.-J., *Acc Chem Res* **2012,** *46*, 1673-1681.
257. Freund, H. J.; Nilius, N.; Risse, T.; Schauermann, S., *Phys Chem Chem Phys* **2014,** *16*, 8148-8167.
258. Trimm, D. L., *Catal Rev* **1977,** *16*, 155-189.
259. van Santen, R. A.; van de Graaf, B.; Smit, B., Chapter 10 Introduction to zeolite theory and modelling. In *Introduction to Zeolite Science and Practice, Studies in Surface Science and Catalysis*, van Bekkum, H.; Flanigen, E. M.; Jacobs, P. A.; Jansen, J. C., Eds. Elsevier: Amsterdam, 2001; Vol. 137, pp 419-466.
260. Sierka, M.; Sauer, J., *Faraday Discuss* **1997,** *106*, 41-62.
261. Sauer, J.; Sierka, M., *J Comput Chem* **2000,** *21*, 1470-1493.
262. Svensson, M.; Humbel, S.; Froese, R. D. J.; Matsubara, T.; Sieber, S.; Morokuma, K., *J Phys Chem* **1996,** *100*, 19357-19363.
263. Nasluzov, V. A.; Ivanova, E. A.; Shor, A. M.; Vayssilov, G. N.; Birkenheuer, U.; Rösch, N., *J Phys Chem B* **2003,** *107*, 2228-2241.
264. Namuangruk, S.; Pantu, P.; Limtrakul, J., *J Catal* **2004,** *225*, 523-530.
265. McCann, D. M.; Lesthaeghe, D.; Kletnieks, P. W.; Guenther, D. R.; Hayman, M. J.; Van Speybroeck, V.; Waroquier, M.; Haw, J. F., *Angew Chem Int Ed* **2008,** *47*, 5179-5182.
266. Vayssilov, G. N.; Petrova, G. P.; Shor, E. A. I.; Nasluzov, V. A.; Shor, A. M.; Petkov, P. S.; Rösch, N., *Phys Chem Chem Phys* **2012,** *14*, 5879-5890.
267. Dinda, S.; Govindasamy, A.; Genest, A.; Rösch, N., *J Phys Chem C* **2014,** *118*, 25077-25088.
268. Chiu, C.-c.; Vayssilov, G. N.; Genest, A.; Borgna, A.; Rösch, N., *J Comput Chem* **2014,** *35*, 809-819.
269. Grimme, S.; Antony, J.; Ehrlich, S.; Krieg, H., *J Chem Phys* **2010,** *132*, 154104-19.
270. Bondi, A., *J Phys Chem* **1964,** *68*, 441-451.
271. Pellenq, R. J. M.; Nicholson, D., In-Crystal Oxygen Polarizability For Porous And Non-Porous Materials. In *Studies in Surface Science and Catalysis*, J. Rouquerol; Rodríguez-Reinoso, F.; Sing, K. S. W.; Unger, K. K., Eds. Elsevier: Amsterdam, 1994; Vol. 87, pp 31-39.
272. Atkins, P.; Friedman, R., *Molecular Quantum Mechanics, Fourth Edition*. Oxford University Press Inc.: New York, 2005; p 413.

273. Van Genechten, K. A.; Mortier, W. J.; Geerlings, P., *J Chem Phys* **1987,** *86*, 5063-5071.
274. Sherwood, P.; H. de Vries, A.; J. Collins, S.; P. Greatbanks, S.; A. Burton, N.; A. Vincent, M.; H. Hillier, I., *Faraday Discuss* **1997,** *106*, 79-92.
275. Pellenq, R. J. M.; Nicholson, D., *J Chem Soc Faraday T* **1993,** *89*, 2499-2508.
276. Tkatchenko, A.; Scheffler, M., *Phys Rev Lett* **2009,** *102*, 073005-4.
277. Rydberg, H.; Dion, M.; Jacobson, N.; Schröder, E.; Hyldgaard, P.; Simak, S. I.; Langreth, D. C.; Lundqvist, B. I., *Phys Rev Lett* **2003,** *91*, 126402-4.
278. Dion, M.; Rydberg, H.; Schröder, E.; Langreth, D. C.; Lundqvist, B. I., *Phys Rev Lett* **2004,** *92*, 246401-4.
279. Hermann, J.; Bludsky, O., *J Chem Phys* **2013,** *139*, 034115-6.
280. Göltl, F.; Grüneis, A.; Bučko, T.; Hafner, J., *J Chem Phys* **2012,** *137*, 114111-17.
281. Tsuzuki, S.; Honda, K.; Uchimaru, T.; Mikami, M., *J Chem Phys* **2006,** *124*, 114304-7.
282. Takatani, T.; Hohenstein, E. G.; Malagoli, M.; Marshall, M. S.; Sherrill, C. D., *J Chem Phys* **2010,** *132*, 144104-5.
283. Jurecka, P.; Sponer, J.; Cerny, J.; Hobza, P., *Phys Chem Chem Phys* **2006,** *8*, 1985-1993.
284. Tkatchenko, A.; DiStasio, R. A., Jr.; Car, R.; Scheffler, M., *Phys Rev Lett* **2012,** *108*, 236402-5.